

# A Study of the Undercutting of Woodwind Toneholes Using Particle Image Velocimetry



*Robert MacDonald*

A thesis submitted in fulfilment of the requirements  
for the degree of Doctor of Philosophy  
to the  
University of Edinburgh  
2009



# Abstract

The undercutting of toneholes has been practised for centuries with the aim of improving the tuning and playability of woodwind instruments. The influence of undercutting on tuning can be understood in terms of linear acoustic theory. Its effect on other playing characteristics is thought to lie in its reduction of local non-linear flow phenomena (boundary layer separation and the formation of jets and vortices) at the tonehole. Particle Image Velocimetry (PIV) is used to examine the oscillating airflow around a model woodwind tonehole. Velocity and vorticity information is obtained and compared for a square-edged tonehole and an undercut tonehole at a variety of sound levels. The upstream, internal edge of the tonehole is found to be the location of the most significant local non-linear flow behaviour. Undercutting is found to reduce the strength of local non-linear flow phenomena at a given sound level. Microphone measurements carried out in a reverberation chamber show that undercutting the tonehole also reduces the harmonic distortion introduced to the radiated pressure signal by the non-linear flow. Proper Orthogonal Decomposition (POD) is then applied to PIV data of oscillating flow at the end of a tube. It is used to approximately separate the acoustic field from the induced local non-linear flow phenomena. The POD results are then used to approximate the percentage of kinetic energy present in the non-linear flow. POD analysis is applied to the case of flow around the two toneholes. It shows a smaller transfer of kinetic energy to non-linear flow effects around the undercut tonehole at a given sound level. The dependence of the local non-linear flow kinetic energy on Strouhal number is considered.





# Declaration

This thesis was composed by myself and the work described within is my own, except where explicitly stated otherwise. This work has not been submitted for any other degree or professional qualification.

*Robert MacDonald*

September 2008



# Acknowledgements

I would like to thank the following people without whose contribution (either direct or indirect) this thesis would never have been written, or would have been a lot less enjoyable to write:

EPSRC for funding my studies. My supervisor Murray Campbell for always being approachable and for his infectious enthusiasm for musical acoustics. The guys in the mechanical workshop: Derek, Vince and especially Andrew, for making my equipment and helping with other projects which were not strictly legit. Julie and Tam for introducing me to bulgar wheat. Jean-Christophe Valière for introducing me to POD and encouraging me about my results. David Marx for providing me with the Matlab programmes to perform POD. Andreas Richter for providing simulation results. Lawrence Mitchell for being willing, at the drop of a hat, to be involved in ludicrous clarinet-related experiments. My fellow acousticians: Alan, Ali, Darren, Seona, Lin, Jonathan and Sam for making 4201 a great place to work. David Skulina for being an excellent mentor and always being willing to help. Mike Newton for being with me through it all, be it work or play (including floods, tidal waves, pitch & putt, clandestine Pancake Day observance, breakthroughs in syphoning technology and golf course subterfuge). Bob Akroyd for reminding me that axe-heads can float. My family: Ali for being a good flatmate; Doug for being a good band-mate; Vicky, Kath, Kieran, Julia and Niamh for being good mates. Mum and Dad for being my examples of taking pride in what you do and supporting me in everything I've done. Finally I would like to thank my wife Anne because, though she may not know all about my PhD, she knows all about me and she still loves me.



# Contents

<b>Abstract</b>	<b>i</b>
<b>Declaration</b>	<b>ii</b>
<b>Acknowledgements</b>	<b>iv</b>
<b>Contents</b>	<b>vi</b>
<b>List of figures</b>	<b>x</b>
<b>List of tables</b>	<b>xiv</b>
<b>1 Introduction</b>	<b>1</b>
1.1 Context . . . . .	1
1.2 Thesis Aims . . . . .	2
1.3 Thesis Outline . . . . .	2
<b>2 Background Acoustics and Fluid Dynamics</b>	<b>5</b>
2.1 Introduction . . . . .	5
2.2 Linear acoustics . . . . .	5
2.3 Acoustic Impedance . . . . .	6
2.3.1 Resonance . . . . .	7
2.4 Tube terminated by an open end . . . . .	8
2.4.1 Viscothermal losses in the tube . . . . .	9
2.5 Tube terminated by one open tonehole . . . . .	10
2.5.1 Effective acoustic length of a tonehole . . . . .	12
2.5.2 Series impedance . . . . .	13
2.5.3 Reflection and transmission . . . . .	13
2.6 Undercutting . . . . .	14
2.7 Non-linearity in woodwind instruments . . . . .	15
2.7.1 Boundary layer separation and reattachment in steady flow . . .	15
2.7.2 Steady flow at discontinuities in tubes . . . . .	17
2.7.3 Strouhal number . . . . .	18
2.7.4 Acoustic boundary layer . . . . .	19
2.7.5 Turbulence . . . . .	19
2.7.6 Quasi-steady approximation . . . . .	19

2.7.7	Energy losses due to non-linear flow effects . . . . .	20
2.7.8	Jet driven streaming . . . . .	20
<b>3</b>	<b>Particle Image Velocimetry</b>	<b>23</b>
3.1	Introduction . . . . .	23
3.2	Basic Principles . . . . .	24
3.2.1	Seeding particles . . . . .	24
3.2.2	Illumination . . . . .	26
3.2.3	Image capture . . . . .	27
3.3	Image analysis . . . . .	27
3.3.1	Cross-correlation . . . . .	28
3.3.2	Peak detection . . . . .	29
3.3.3	Vector validation and replacement . . . . .	29
3.4	Optimisation . . . . .	30
3.5	System Timing and Synchronisation . . . . .	31
<b>4</b>	<b>Experimental Apparatus and Method</b>	<b>35</b>
4.1	Introduction . . . . .	35
4.2	Clarinet model . . . . .	35
4.2.1	Main tube . . . . .	35
4.2.2	Excitation mechanism . . . . .	36
4.2.3	Tonehole section . . . . .	36
4.2.4	Tonehole pieces . . . . .	38
4.3	PCB transducer placement . . . . .	39
4.4	PCB transducer pressure calibration . . . . .	40
4.5	PIV experiment . . . . .	42
4.5.1	Enclosure . . . . .	42
4.5.2	Optical alignment . . . . .	42
4.5.3	Acoustic field . . . . .	44
4.5.4	Seeding . . . . .	44
4.5.5	Procedure . . . . .	44
4.5.6	Processing . . . . .	44
4.5.7	Timing . . . . .	45
4.6	Reverberation Chamber Measurements . . . . .	45
<b>5</b>	<b>PIV Applied to Oscillating Flow Around a Model Tonehole</b>	<b>49</b>
5.1	Introduction . . . . .	49
5.2	Background . . . . .	49
5.2.1	Visualisation . . . . .	49
5.2.2	Acoustic properties . . . . .	50
5.2.3	Toneholes . . . . .	51
5.3	PIV Results . . . . .	52
5.3.1	Square tonehole - level 1 . . . . .	55
5.3.2	Square tonehole - level 2 . . . . .	57
5.3.3	Square tonehole - level 3 . . . . .	57
5.3.4	Square tonehole - level 4 . . . . .	58

5.3.5	Square tonehole - level 5 . . . . .	59
5.3.6	Undercut tonehole - level 1 . . . . .	59
5.3.7	Undercut tonehole - level 2 . . . . .	60
5.3.8	Undercut tonehole - level 3 . . . . .	60
5.3.9	Undercut tonehole - level 4 . . . . .	60
5.3.10	Undercut tonehole - level 5 . . . . .	61
5.3.11	PIV results - summary . . . . .	112
5.3.12	2D finite element model . . . . .	114
5.4	Reverberation Chamber Results . . . . .	114
5.4.1	Power . . . . .	115
5.4.2	Harmonic generation . . . . .	117
5.5	Conclusions . . . . .	119
<b>6</b>	<b>POD Applied to PIV Data of Oscillating Flow at a Tube Termination</b>	<b>121</b>
6.1	Introduction . . . . .	121
6.2	Background . . . . .	122
6.3	Experimental apparatus . . . . .	124
6.3.1	PIV measurement procedure . . . . .	124
6.4	Analysis . . . . .	125
6.4.1	POD . . . . .	126
6.4.2	Energy transfer . . . . .	127
6.5	Results . . . . .	128
6.5.1	POD mode 1 . . . . .	128
6.5.2	Decomposition . . . . .	140
6.5.3	Energy . . . . .	142
6.6	Conclusion . . . . .	145
<b>7</b>	<b>POD Applied to PIV Data of Oscillating Flow at a Tonehole</b>	<b>147</b>
7.1	Introduction . . . . .	147
7.2	Data Presentation . . . . .	147
7.3	Jet Driven Streaming . . . . .	169
7.4	POD Mode 1 . . . . .	172
7.5	POD Mode 2 . . . . .	172
7.6	Energy Transfer . . . . .	174
7.6.1	$e_1$ and $e_2$ against $\bar{u}_{an}$ . . . . .	174
7.6.2	Strouhal number . . . . .	176
7.7	Conclusion . . . . .	179
<b>8</b>	<b>Conclusion</b>	<b>181</b>
8.1	Thesis Aims . . . . .	181
8.1.1	Clarinet model . . . . .	181
8.1.2	Undercutting and local non-linear flow effects . . . . .	181
8.1.3	Proper Orthogonal Decomposition . . . . .	182
8.1.4	Tonehole geometry . . . . .	183
8.2	Future work . . . . .	183

<b>Bibliography</b>	<b>185</b>
<b>Publications</b>	<b>191</b>



# List of Figures

2.1	Dimensions of main bore and tonehole. Excitation mechanism is situated to the left. . . . .	10
2.2	Definition of $L^x$ showing pressure standing wave pattern in tube during resonance. . . . .	11
2.3	Junction between tonehole and main bore showing matching volume. . .	12
2.4	$S_t/t_e$ against $b$ . $t + t_r = 7\text{mm}$ , $a = 7.5\text{mm}$ . From equations 2.34, 2.35 and 2.42. . . . .	14
2.5	Steady flow around a sharp $90^\circ$ bend in a tube. (a) Potential flow. (b) Flow with separation and reattachment. (c) Flow with separation. . . .	16
2.6	Steady flow through a sudden expansion in a tube. (a) Potential flow. (b) Flow with separation and reattachment. (c) Flow with separation. .	17
2.7	Steady flow through a sudden contraction in a tube. (a) Potential flow. (b) Flow with separation and reattachment. . . . .	18
2.8	(a) Diffuse inflow. (b) Jet outflow. (c) Jet driven steady flow. . . . .	21
3.1	Flow visualisation of boundary layer separation on inclined wing using tracer particles. Taken from [Visualisation 08]. . . . .	23
3.2	Basic PIV setup referred to in section 3.2. Taken from [Skulina 05a]. .	25
3.3	Oxford Lasers ‘Fibresheet’ light sheet optics. Taken from [Skulina 05a].	26
3.4	Example of the same $32 \times 32$ pixel interrogation area from a pair of PIV images and the resulting correlation plane. Magenta circle shows same group of particles. . . . .	28
3.5	Components of PIV synchronisation system. . . . .	32
3.6	PIV timing (not to scale). . . . .	33
4.1	Speaker box and pyramid adapter for coupling speaker to main tube. . .	36
4.2	(a) Tonehole section with tonehole inserted. (b) CAD drawing showing simplified tonehole section. . . . .	37
4.3	Important dimensions of toneholes used in clarinet model. Upper: square tonehole. Lower: undercut tonehole. The undercut tonehole has the same dimensions as the square tonehole, apart from those indicated. All length are in millimetres. . . . .	38
4.4	Effective acoustic lengths $L_e^{TH}$ , $L_e^{LS}$ and $L_e^M$ . . . . .	40
4.5	Aluminium enclosure used in experiment. Taken from [Skulina 05a]. . .	42

4.6	Alignment of model, light sheet and camera used for PIV of inside of clarinet model. . . . .	43
4.7	Points in acoustic velocity cycle at which PIV measurements are made, $t_i$ . . . . .	46
5.1	PIV data for the square tonehole at $\bar{p}_{an} = 207\text{Pa}$ . . . . .	62
5.2	PIV data for the square tonehole at $\bar{p}_{an} = 452\text{Pa}$ . . . . .	69
5.3	PIV data for the square tonehole at $\bar{p}_{an} = 760\text{Pa}$ . . . . .	76
5.4	PIV data for the square tonehole at $\bar{p}_{an} = 1067\text{Pa}$ . . . . .	82
5.5	PIV data for the square tonehole at $\bar{p}_{an} = 1703\text{Pa}$ . . . . .	87
5.6	PIV data for the undercut tonehole at $\bar{p}_{an} = 222\text{Pa}$ . . . . .	91
5.7	PIV data for the undercut tonehole at $\bar{p}_{an} = 463\text{Pa}$ . . . . .	95
5.8	PIV data for the undercut tonehole at $\bar{p}_{an} = 729\text{Pa}$ . . . . .	100
5.9	PIV data for the undercut tonehole at $\bar{p}_{an} = 1101\text{Pa}$ . . . . .	104
5.10	PIV data for the undercut tonehole at $\bar{p}_{an} = 1753\text{Pa}$ . . . . .	109
5.11	Comparison between simulated and PIV data for $i = 6$ . White areas mark location of tonehole walls. (a) $x$ velocity. Left: simulation. Right: PIV. (b) $y$ velocity. Left: simulation. Right: PIV. . . . .	113
5.12	Comparison between simulated and PIV data for $i = 16$ . White areas mark location of tonehole walls. (a) $x$ velocity. Left: simulation. Right: PIV. (b) $y$ velocity. Left: simulation. Right: PIV. . . . .	113
5.13	(a) Radiated acoustic power against AC loudspeaker power. (b) Power efficiency against AC loudspeaker power. (c) Power efficiency against RMS radiated pressure. (Blue) square. (Red) undercut. . . . .	115
5.14	(a) Radiated $SPL$ against AC loudspeaker power. (b) RMS radiated pressure against RMS pressure at antinode in tube. (c) $P_{rad}/\bar{p}_{an}^2$ against RMS pressure at antinode in tube. (Blue) square. (Red) undercut. . . . .	116
5.15	(a) Frequency spectra of radiated pressure for square tonehole at three values of $\bar{p}_{an}$ . Frequencies have been offset for the two lower values of $\bar{p}_{an}$ to allow comparison of amplitudes. (b) Total harmonic distortion of radiated pressure against RMS pressure at antinode in tube. (Blue) square. (Red) undercut. Dashed line is total harmonic distortion of pressure at antinode in tube. . . . .	117
5.16	(a) RMS radiated pressure against RMS pressure at antinode in tube using only fundamental component of signal. (b) $P_{rad}/\bar{p}_{an}^2$ against RMS pressure at antinode in tube using only fundamental component of signal. (Blue) square. (Red) undercut. . . . .	119
6.1	Geometry of tube termination used in this study, showing $r$ , the radius of curvature of the inside corner. . . . .	122
6.2	Real part of the radiation impedance as a function of the RMS acoustic velocity at the open end for the two different terminations. ( $\square$ ) $r = 0\text{mm}$ . ( $*$ ) $r = 0.3\text{mm}$ . ( $\triangle$ ) $r = 1\text{mm}$ . (---) linear theory, flanged. (- · -) linear theory, unflanged. From Atig [Atig 04a]. . . . .	123
6.3	Experimental apparatus for tube termination PIV experiments. Taken from [Skulina 05a]. . . . .	124
6.4	Points in cycle at which PIV measurements are made, $t_i$ . . . . .	125

6.5	Flow decomposition for $r = 0.3\text{mm}$ termination. Top left: Streaming flow $\tilde{\mathbf{u}}(x, y)$ . Top right: $a_m(t_i)$ of first 2 POD modes ( $-$ ) $a_1$ , ( $- - -$ ) $a_2$ . Bottom left: $\Phi_1(x, y)$ . Bottom right: $\Phi_2(x, y)$ . Spatial maps show left half of termination, with grey areas representing termination wall. .	129
6.6	Streamlines from the left inside edge of the $r = 0.3\text{mm}$ termination at a range of $\bar{p}_{an}$ . The displayed velocity field is $\Phi_1(x, y)$ for $\bar{p}_{an} = 203\text{Pa}$ . .	137
6.7	Comparison of $\mathbf{u}(x, y, t_4)$ with $\mathbf{u}_{nl}(x, y, t_4)$ at $2224\text{Pa}$ for $r = 0.3\text{mm}$ termination. . . . .	138
6.8	Comparison of $\mathbf{u}(x, y, t_4)$ with $\mathbf{u}_{nl}(x, y, t_4)$ at $7748\text{Pa}$ for $r = 0.3\text{mm}$ termination. . . . .	139
6.9	(a) $e_1$ against $\bar{u}_{an}$ for $r = 0\text{mm}$ , $r = 0.3\text{mm}$ and $r = 1\text{mm}$ terminations. (b) $e_2$ against $\bar{u}_{an}$ for $r = 0\text{mm}$ , $r = 0.3\text{mm}$ and $r = 1\text{mm}$ terminations. ( $\square$ ) $r = 0\text{mm}$ . ( $*$ ) $r = 0.3\text{mm}$ . ( $\triangle$ ) $r = 1\text{mm}$ . . . . .	143
6.10	$e_1$ against $St_r$ for $r = 0.3\text{mm}$ and $r = 1\text{mm}$ terminations. ( $*$ ) $r = 0.3\text{mm}$ . ( $\triangle$ ) $r = 1\text{mm}$ . . . . .	143
6.11	(a) Definition of $w$ , the distance from the start of the inside corner of the termination to the outside corner. (b) $e_1$ against $St_w$ for $r = 0\text{mm}$ , $r = 0.3\text{mm}$ and $r = 1\text{mm}$ terminations. ( $\square$ ) $r = 0\text{mm}$ . ( $*$ ) $r = 0.3\text{mm}$ . ( $\triangle$ ) $r = 1\text{mm}$ . . . . .	144
6.12	$e_2$ against $St_w$ for $r = 0\text{mm}$ , $r = 0.3\text{mm}$ and $r = 1\text{mm}$ terminations. ( $\square$ ) $r = 0\text{mm}$ . ( $*$ ) $r = 0.3\text{mm}$ . ( $\triangle$ ) $r = 1\text{mm}$ . . . . .	145
7.1	Flow decomposition for the square tonehole at $\bar{p}_{an} = 452\text{Pa}$ . . . . .	148
7.2	Flow decomposition for the square tonehole at $\bar{p}_{an} = 760\text{Pa}$ . . . . .	151
7.3	Flow decomposition for the square tonehole at $\bar{p}_{an} = 1067\text{Pa}$ . . . . .	154
7.4	Flow decomposition for the square tonehole at $\bar{p}_{an} = 1703\text{Pa}$ . . . . .	157
7.5	Flow decomposition for the undercut tonehole at $\bar{p}_{an} = 729\text{Pa}$ . . . . .	160
7.6	Flow decomposition for the undercut tonehole at $\bar{p}_{an} = 1101\text{Pa}$ . . . . .	163
7.7	Flow decomposition for the undercut tonehole at $\bar{p}_{an} = 1753\text{Pa}$ . . . . .	166
7.8	Vorticity sign of streaming flow. . . . .	170
7.9	Vorticity sign of POD mode 2. . . . .	172
7.10	$\Phi_3(x, y)$ for the square tonehole at $\bar{p}_{an} = 1067\text{Pa}$ . $a_1(t_i)$ , $a_2(t_i)$ and $a_3(t_i)$ are plotted inset into the vector map. (Black) $a_1(t_i)$ . (Magenta) $a_2(t_i)$ . (Cyan) $a_3(t_i)$ . . . . .	173
7.11	(a) $e_1$ against $\bar{u}_{an}$ for square and undercut toneholes. (b) $e_2$ against $\bar{u}_{an}$ for square and undercut toneholes. (Blue) square. (Red) undercut. . .	175
7.12	(a) $e_1$ against $\bar{u}_{an}$ for the area above the square and undercut toneholes. (b) $e_2$ against $\bar{u}_{an}$ for the area above the square and undercut toneholes. (Blue) square. (Red) undercut. . . . .	175
7.13	(a) $t^*$ , $b^*$ and $r^*$ for the square tonehole. (b) $t^*$ and $b^*$ for the undercut tonehole. . . . .	176
7.14	$e_1$ against $St_{r^*}$ for the square tonehole. . . . .	177
7.15	(a) $e_1$ against $St_{t^*}$ for the square and undercut toneholes. (b) $e_2$ against $St_{t^*}$ for the square and undercut toneholes. (Blue) square. (Red) undercut. . . . .	177

7.16	(a) $e_1$ against $St_{b^*}$ for the square and undercut toneholes. (b) $e_2$ against $St_{b^*}$ for the square and undercut toneholes. (Blue) square. (Red) undercut. . . . .	178
------	--	-----

# List of Tables

3.1	Timings on pulse generator relative to rising edge of triggering square wave for measurement of 180Hz acoustic signal. . . . .	33
5.1	Values of $\bar{p}_{an}$ , $SPL_{an}$ , $\bar{u}_{an}$ , $St_b$ , $Re_\delta$ and musical dynamic level used in the PIV experiments. . . . .	52
6.1	Description of non-linear flow constituents for $r = 0.3\text{mm}$ termination. .	140



# Chapter 1

## Introduction

### 1.1 Context

Undercutting is a method that has been used by woodwind makers for centuries to refine the playing characteristics of instruments. Greenham defines undercutting as, “the process of enlarging woodwind instrument toneholes in the region where they meet the bore whilst leaving the external hole size unchanged” [Greenham 03]. This enlarging can involve anything from a minimal amount of rounding of the internal edges of the tonehole, to introducing a flaring variation of the radius over a large part of the tonehole height. There are two main reasons for undercutting a tonehole: to adjust the pitch of the notes played with it as the first open hole, and to improve the quality of these notes. The quality of a note can describe its timbre, loudness or ease of playing.

A very small portion of the musical acoustics literature is devoted to the subject of undercutting. Benade states that rounding the inside edges of an instrument’s toneholes reduces turbulence in the oscillating flow through them [Benade 76]. Nederveen cites one of the results of undercutting to be a reduction of energy loss due to vortex formation in the flow through a tonehole [Nederveen 98a]. He also describes the effect of undercutting on the tuning of notes in different registers using linear acoustic theory. Greenham conducted a large survey of undercutting in clarinets [Greenham 03]. Input impedance measurements were used to assess tuning differences due to undercutting. Playing tests were also conducted on clarinets in which the only variable was the undercutting of the toneholes. The instruments with some degree of undercutting were judged to be superior to the instrument with none by a large majority of participants.

This study concentrates on the effect of undercutting proposed by Benade and Nederveen, namely its influence on local non-linear flow phenomena generated by an acoustic flow at a tonehole. Local non-linear flow phenomena, caused by the separation of the boundary layer at geometrical discontinuities in a flow, include the formation

of vortices, and the subsequent turbulence and steady streaming. The last of these phenomena can be felt outside the first open tonehole of any woodwind instrument during playing.

The main experimental technique employed in this study is Particle Image Velocimetry (PIV). This is an optical technique that simultaneously captures velocity information at a large number of points in a flow. PIV was first used to measure steady flows but has more recently been applied to acoustic velocity fields [Hann 97, Esposito 03, Tondast-Navæi 05, Berson 06]. Local non-linear flow effects generated by acoustic flows have been studied using PIV [Skulina 05a, Marx 08]. PIV is particularly useful in the context of these complex flow effects because, as well as providing information concerning their strength, PIV also gives insight into their form.

## 1.2 Thesis Aims

The primary objectives of this study are:

1. To construct an experimental clarinet model for which it is possible to perform PIV measurements on the entire flow in the region of the tonehole.
2. To answer the questions of whether undercutting reduces local non-linear flow effects and, if so, how does it achieve this.
3. To extend the use of Proper Orthogonal Decomposition in analysing PIV data of high amplitude oscillating flows, and to assess its usefulness for measuring the strength of local non-linear flow effects.
4. To investigate those aspects of tonehole geometry which are most significant in reducing local non-linear flow effects.

## 1.3 Thesis Outline

Chapter 2 outlines the theoretical acoustics and fluid dynamics relevant to the study of woodwind instrument toneholes. The linear acoustical description of sound waves in tubes with a sidehole is given, including a discussion concerning the effect of undercutting on tuning. This is followed by a section on the origin and nature of local non-linear flow phenomena.

Chapter 3 is a description of the PIV technique, and of the particular PIV apparatus used in this study to measure velocities at evenly spaced times in the cycle of an acoustic flow.



The subject of chapter 4 is the design of a model clarinet suitable for performing PIV measurements in the region around an open tonehole. The procedure used for obtaining the experimental results of chapters 5 and 7 is detailed.

Chapter 5 begins with a review of the experimental literature on local non-linear flow effects caused by oscillating flows. The velocity data obtained using PIV on the oscillating flow around a tonehole are then presented. Two toneholes are studied - one with square internal edges and another for which the internal edges are undercut - at a range of sound levels. The appearance and development of local non-linear flow effects at different points in the acoustic cycle are compared between the two geometries. The chapter ends with the results of an experiment measuring the differences in radiated sound pressure between the two toneholes.

Chapter 6 draws on PIV data of oscillating flow around the end of a tube which were previously obtained by a colleague [Skulina 05a]. These are used to evaluate whether it is possible to employ Proper Orthogonal Decomposition to separate the purely acoustic motion from the induced local non-linear flow in high amplitude sound fields. The kinetic energy in the non-linear flow relative to that in the acoustic flow is then calculated.

Proper Orthogonal Decomposition is then applied to the tonehole PIV data in chapter 7. The relative kinetic energy transferred to non-linear effects is compared for the two tonehole geometries. The last part of the chapter discusses which aspects of tonehole geometry are most significant for reducing the energy transfer

Chapter 8 assesses whether the aims outlined in this chapter have been met and suggests possible avenues of future research.



## Chapter 2

# Background Acoustics and Fluid Dynamics

### 2.1 Introduction

This chapter gives an overview of the areas of theoretical acoustics and fluid dynamics that are relevant to woodwind instrument toneholes. It begins by outlining the basic linear acoustic theory of low amplitude oscillations in tubes. The specific case of a tube with one open tonehole is discussed. The influence of undercutting on the pitch of the sounded note is then considered. Finally, the origin of local non-linear flow effects is described, as well as the non-dimensional numbers relevant to oscillating flow in a tube.

### 2.2 Linear acoustics

In the absence of external body forces, the Navier-Stokes equation [Kinsler 00] governing the relationship between pressure  $p$  and velocity  $\vec{u}$  in a fluid flow is

$$\rho \left( \frac{\partial \vec{u}}{\partial t} + (\vec{u} \cdot \nabla) \vec{u} \right) = -\nabla p + \left( \frac{4}{3}\eta + \eta_B \right) \nabla (\nabla \cdot \vec{u}) - \eta \nabla \times \nabla \times \vec{u} \quad (2.1)$$

where  $\rho$  is the density of the fluid,  $\eta$  is the coefficient of shear viscosity and  $\eta_B$  is the coefficient of bulk viscosity.  $p$  is the pressure variation about atmospheric pressure. If we consider acoustic flow (such as occurs inside a woodwind instrument) to be irrotational (so that the vorticity  $\vec{\omega} = \nabla \times \vec{u} \simeq 0$ ) and approximately free from viscous losses then the last two terms on the right hand side of equation 2.1 disappear. This kind of flow is described as potential flow [Tritton 99]. We consider the amplitude of the acoustic oscillations to be small such that  $\rho \simeq \rho_0$  (atmospheric density). If we also assume that the variation of velocity with respect to time is much greater than its

variation with respect to position ( $\frac{\partial \vec{u}}{\partial t} \gg (\vec{u} \cdot \nabla) \vec{u}$ ), then equation 2.1 reduces to

$$\rho_0 \frac{\partial \vec{u}}{\partial t} = -\nabla p, \quad (2.2)$$

the linear Euler's equation.

If a woodwind instrument is modelled as a cylindrical tube of radius  $a$  and length  $L$ , then an acoustic wave of wavelength  $\lambda$  propagating inside is considered a plane wave if  $\lambda \gg a$  (transverse modes are not present). In this case the acoustic properties are constant across a cross-section of the tube and equation 2.2 becomes 1-D:

$$\rho_0 \frac{\partial u}{\partial t} = -\frac{\partial p}{\partial x}. \quad (2.3)$$

It is possible to combine equation 2.3 with the continuity equation to obtain the 1-D linear wave equation [Kinsler 00]:

$$\frac{\partial^2 p}{\partial x^2} = \frac{1}{c^2} \frac{\partial^2 p}{\partial t^2} \quad (2.4)$$

where  $c$  is the speed of sound in air. This is solved by the complex pressure

$$\mathbf{p}(x, t) = \mathbf{A}e^{i(\omega t - kx)} + \mathbf{B}e^{i(\omega t + kx)} \quad (2.5)$$

where  $i = \sqrt{-1}$ ,  $\omega$  is the angular frequency and  $k$  is the wave number such that

$$k = \frac{\omega}{c} = \frac{2\pi}{\lambda}. \quad (2.6)$$

$\mathbf{A}$  is the complex amplitude of the pressure wave travelling in the positive  $x$ -direction and  $\mathbf{B}$  is the equivalent in the negative direction. According to equation 2.3 the complex acoustic particle velocity is given by

$$\mathbf{u}(x, t) = \frac{1}{\rho_0 c} \left[ \mathbf{A}e^{i(\omega t - kx)} - \mathbf{B}e^{i(\omega t + kx)} \right]. \quad (2.7)$$

## 2.3 Acoustic Impedance

It is useful to describe the behaviour of the resonator of a woodwind instrument in terms of acoustic impedance, defined for a cross-sectional plane in the resonator as

$$\mathbf{Z} = \frac{\mathbf{p}}{\mathbf{U}}. \quad (2.8)$$

$\mathbf{U}$  is the acoustic volume velocity and is defined as  $S\mathbf{u}$  where  $S = \pi a^2$  is the cross-sectional area of the tube. Combining equations 2.5, 2.7 and 2.8:

$$\mathbf{Z} = \frac{\rho_0 c}{S} \left[ \frac{\mathbf{A}e^{-ikx} + \mathbf{B}e^{ikx}}{\mathbf{A}e^{-ikx} - \mathbf{B}e^{ikx}} \right] = Z_c \left[ \frac{\mathbf{A}e^{-ikx} + \mathbf{B}e^{ikx}}{\mathbf{A}e^{-ikx} - \mathbf{B}e^{ikx}} \right]. \quad (2.9)$$

$Z_c = \rho_0 c/S$  is known as the characteristic acoustic impedance.

If the beginning of the tube is at  $x = 0$  then the acoustic impedance at this point, known as the input impedance is given by

$$\mathbf{Z}_{IN} = Z_c \left[ \frac{\mathbf{A} + \mathbf{B}}{\mathbf{A} - \mathbf{B}} \right]. \quad (2.10)$$

At the end of the tube,  $x = L$ , the radiation (or termination) impedance is given by

$$\mathbf{Z}_r = Z_c \left[ \frac{\mathbf{A}e^{-ikL} + \mathbf{B}e^{ikL}}{\mathbf{A}e^{-ikL} - \mathbf{B}e^{ikL}} \right]. \quad (2.11)$$

Combining equations 2.10 and 2.11 and eliminating  $\mathbf{A}$  and  $\mathbf{B}$  [Kinsler 00], we obtain the input impedance in terms of the radiation impedance

$$\mathbf{Z}_{IN} = Z_c \left[ \frac{\mathbf{Z}_r + iZ_c \tan(kL)}{i\mathbf{Z}_r \tan(kL) + Z_c} \right]. \quad (2.12)$$

### 2.3.1 Resonance

Generally, the impedance can be expressed in terms of a real part (the resistance) and an imaginary part (the reactance):

$$\mathbf{Z} = R + iX. \quad (2.13)$$

Assuming the tube to be open at  $x = 0$ , the resonances of the tube (those frequencies for which a standing wave will be most strongly supported) are those values of  $k$  for which  $X_{IN}$  goes to zero and for which  $R_{IN}$  is a minimum. In our present case these frequencies are dictated by  $L$  and  $\mathbf{Z}_r$ .

As an example, consider the purely theoretical case  $\mathbf{Z}_r = 0$ . Applying this to equation 2.12 we obtain

$$\mathbf{Z}_{IN} = iZ_c \tan(kL). \quad (2.14)$$

The reactance vanishes when

$$\tan(kL) = 0 \quad (2.15)$$

which occurs for

$$k_n L = n\pi \quad n = 1, 2, 3, \dots \quad (2.16)$$

These correspond to frequencies

$$f_n = \frac{nc}{2L} \quad n = 1, 2, 3, \dots \quad (2.17)$$

such that the resonance frequencies are harmonics of the fundamental. In the case that  $\mathbf{Z}_r = 0$  the effective length  $L_e$  (the length that dictates the resonance frequencies) is the same as the geometrical length  $L$ . If the tube is closed at  $x = 0$  then the resonance frequencies will be given by.

$$f_n = \frac{nc}{4L} \quad n = 1, 3, 5, \dots \quad (2.18)$$

The input impedance of a wind instrument can be measured over a range of frequencies using a number of methods [Dickens 07] and is a useful way of characterising its musical properties.

## 2.4 Tube terminated by an open end

At low acoustic pressure amplitudes and low frequencies (for which  $ka \ll 1$ ) the radiation impedance from an unflanged tube is given [Levine 48] by

$$\mathbf{Z}_r = Z_c \left[ \frac{(ka)^2}{4} + i0.61ka \right] \quad (2.19)$$

and for an infinite flange [Nomura 60] by

$$\mathbf{Z}_r = Z_c \left[ \frac{(ka)^2}{2} + i0.82ka \right]. \quad (2.20)$$

At the end of the tube, the radiation resistance  $R_r$  is associated with the acoustic power lost from the tube due to radiation. The average power radiated from the tube over one period  $T = 2\pi/\omega$  is [Atig 04a]

$$\langle P \rangle = \frac{R_r S u_{ac}^2}{2} \quad (2.21)$$

where  $u_{ac}$  is the velocity amplitude at the end of the tube.

The radiation reactance  $X_r$  describes the behaviour of the mass of air just outside the end of the tube. Its influence can be expressed as an increase in the resonating

length of the tube such that the effective acoustic length is given by

$$L_e = L + \frac{X_r}{Z_c k} \quad (2.22)$$

so that for the cases above

$$L_e = L + 0.61a \quad (\text{unflanged}) \quad (2.23)$$

$$L_e = L + 0.82a \quad (\text{flanged}). \quad (2.24)$$

$L_e - L$  gives the length correction associated with the radiation impedance. Then, ignoring radiated losses from the tube, the input impedance is given by

$$\mathbf{Z}_{IN} = iZ_c \tan(kL_e). \quad (2.25)$$

Real woodwind instruments, having walls of finite thickness, will have radiation impedances lying between the unflanged and infinitely flanged cases. Semi-empirical values of  $\mathbf{Z}_r$  have been calculated for a number of geometries relevant to woodwinds [Dalmont 01].

### 2.4.1 Viscothermal losses in the tube

Real fluids have a finite viscosity and a different temperature from the wall of the tube. In linear acoustics, energy losses due to the viscous nature of air are considered to be confined to a small region close to the wall called the viscous boundary layer. Similarly, thermal energy losses are considered to be limited to the thermal boundary layer. Viscothermal energy dissipation in these boundary layers is incorporated into linear acoustic theory as an attenuation of the speed of sound  $c$ . This leads to the wave number  $k$  being replaced by the complex propagation constant [Fletcher 98]

$$\mathbf{k} = \frac{\omega}{v} - i\alpha \quad (2.26)$$

where  $v$  is the new speed of sound and  $\alpha$  is known as the attenuation constant. Both  $v$  and  $\alpha$  are dependent on frequency such that viscothermal losses increase with frequency. The effect of the propagation constant is to increase the input resistance of the tube and to lower the resonance frequencies [Nederveen 98a]. This section will continue without considering viscothermal losses.

## 2.5 Tube terminated by one open tonehole

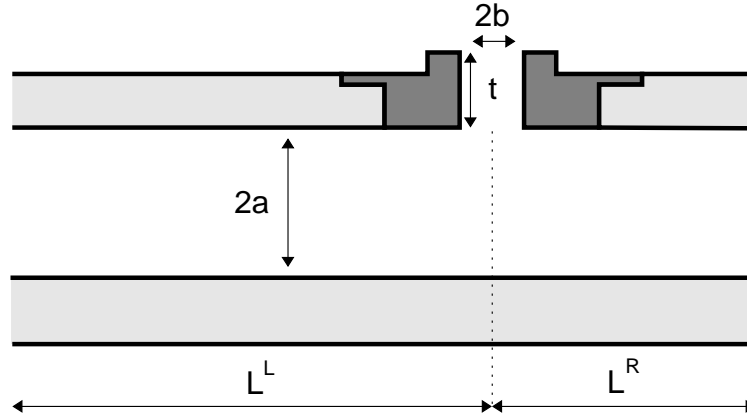


Figure 2.1: Dimensions of main bore and tonehole. Excitation mechanism is situated to the left.

Now we consider the case of an open tonehole near to the open end of the tube. The open end at  $x = L$  is replaced with a tonehole centred at  $x = L^L$  and a further length of tube  $L^R$ . This arrangement is shown in figure 2.1. The tonehole has length  $t$  and radius  $b$ . The radiation impedance is replaced in equation 2.12 with  $\mathbf{Z}_L$ , the acoustic impedance at  $x = L^L$ .  $\mathbf{Z}_L$  can be determined by stipulating that the admittances ( $\mathbf{Y} = 1/\mathbf{Z}$ ) of the three tubes at  $x = L^L$  obey

$$-\mathbf{Y}_L = \mathbf{Y}_R + \mathbf{Y}_t. \quad (2.27)$$

This gives

$$-\frac{1}{\mathbf{Z}_L} = \frac{1}{\mathbf{Z}_R} + \frac{1}{\mathbf{Z}_t}. \quad (2.28)$$

$\mathbf{Z}_R$  is the input impedance to the tube section to the right of the tonehole. This will be influenced by the size of  $L^R$  and the radiation impedance at the end of this section.

In most woodwind instruments at low frequencies, both the radius of the tonehole  $b$  and its length  $t$  are small compared to the wavelength of the sound. In this case the tonehole can be treated as a lumped acoustic element, meaning that acoustic variables are considered constant over its length [Kinsler 00, van Walstijn 02]. Therefore the input impedance of the tonehole  $\mathbf{Z}_t$  takes the form of a radiation impedance, with the effective acoustic length of the tonehole  $t_e$  appearing in the reactance term as a length correction

$$\mathbf{Z}_t = R_t + iX_t \quad (2.29)$$



$$= R_t + i \frac{t_e \rho_0 c k}{S_t} \quad (2.30)$$

where  $S_t = \pi b^2$  is the cross-sectional area of the tonehole. Assuming the losses in the tonehole are purely radiative then  $R_t$  takes the form of the resistance term in a radiation impedance (see section 2.4). There will also be increased viscothermal losses in the tonehole contributing to  $R_t$ . These are greater than in an equivalent length of the main bore because of the smaller value of tube radius and an increase in viscous losses at the discontinuity presented by the corners [Keefe 82a].

In the low frequency limit we assume that the resistive part for all three impedances is negligible compared to the reactive part. Then, using equations 2.25 and 2.28

$$-\frac{S}{i\rho_0 c \tan(kL_e^L)} = \frac{S}{i\rho_0 c \tan(kL_e^R)} + \frac{S_t}{i\rho_0 c \tan(kt_e)} \quad (2.31)$$

where  $L_e^L$  and  $L_e^R$  are the effective acoustic lengths of the left hand and right-hand tube sections. At a resonance of the system and when  $kL_e^R$  and  $kt_e \ll 1$  this relation becomes

$$\frac{S}{L^x} = \frac{S}{L_e^R} + \frac{S_t}{t_e} \quad (2.32)$$

where  $L^x$  is the length of tube which would have to be added at  $x = L^L$  to produce the same effective acoustic length as the combination of the tonehole and  $L_e^R$  [Nederveen 98a].  $L^x$  is shown in figure 2.2. The effective acoustic length of the tonehole  $t_e$  and its cross-sectional area are therefore significant parameters of the input impedance to the whole system.

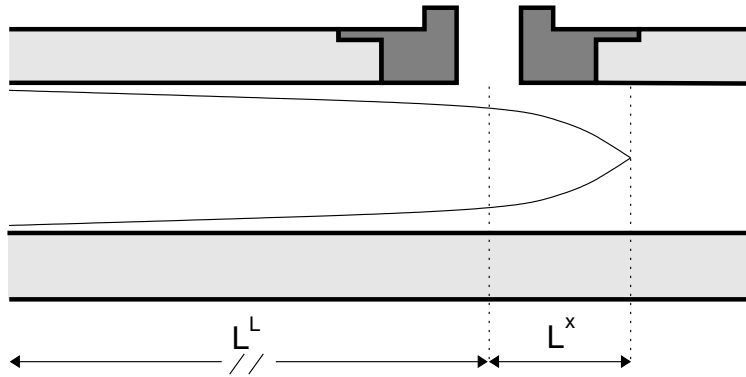


Figure 2.2: Definition of  $L^x$  showing pressure standing wave pattern in tube during resonance.

### 2.5.1 Effective acoustic length of a tonehole

The effective acoustic length of the tonehole differs from the geometrical length due to a number of factors. Firstly, there will be a length correction  $t_r$  due to the radiation impedance at the top of the tonehole. This can be obtained for the theoretical cases outlined in section 2.4.

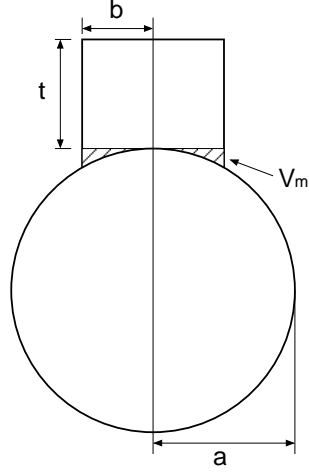


Figure 2.3: Junction between tonehole and main bore showing matching volume.

Secondly, there will be a correction due to the 3-dimensional nature of the junction between the tonehole and the main tube. Figure 2.3 shows this junction as a cross-section of the main bore.  $t$  corresponds to the shortest geometrical height of the tonehole. The remaining matching volume  $V_m$  defines the length correction

$$t_m = \frac{V_m}{S_t}. \quad (2.33)$$

$V_m$  can be calculated in terms of  $a$  and  $b$  [van Walstijn 02]:

$$\frac{t_m}{b} = \frac{b}{8a} \left( 1 + \frac{0.21b^3}{a^3} \right). \quad (2.34)$$

Lastly there will be a contribution to the effective acoustic length due to the discontinuity of the flow as it travels between the main bore and the tonehole. This is the internal length correction,  $t_i$ . Modal decomposition [Keefe 82b] and a 3-D finite difference method [Nederveen 98b] have been used to model  $t_i$  to a good agreement. The later method gives

$$\frac{t_i}{b} = 0.82 - 1.4 \left( \frac{b}{a} \right)^2 + 0.75 \left( \frac{b}{a} \right)^{2.7}. \quad (2.35)$$

The total effective length of the tonehole is then

$$t_e = t + t_r + t_m + t_i. \quad (2.36)$$

The effective length dictates the reactive part of the shunt impedance of the tonehole [Nederveen 98b].

### 2.5.2 Series impedance

As well as the shunt impedance of the tonehole acting at  $x = L^L$ , there will be a length correction to  $L_e^L$  and  $L_e^R$  due to the fact that the tonehole has a finite thickness in the  $x$ -direction.  $L_e^L$  and  $L_e^R$  have to be modified by the addition of an amount  $L_a/2$ , where  $L_a$  is the length correction associated with the series impedance of the tonehole  $\mathbf{Z}_a$ . The size of  $L_a$  depends on the extent to which the flow penetrates the tonehole so can again be investigated using a 3-D finite difference method model [Nederveen 98b]. In the low frequency limit

$$\frac{L_a}{a} = -0.28 \left( \frac{b}{a} \right)^3. \quad (2.37)$$

$L_e^L$  and  $L_e^R$  should incorporate this reduction when used in equation 2.31.

### 2.5.3 Reflection and transmission

To consider how sound is reflected and transmitted at an open tonehole, the section  $L^R$  is replaced by a section of infinite length and cross-sectional area  $S$ .  $\mathbf{Z}_R$  then becomes  $\rho_0 c/S$ . The fraction of acoustic power then reflected back to the left at the tonehole is then given by the power reflection coefficient [Kinsler 00]:

$$\mathcal{R} = \frac{(\rho_0 c/2S)^2}{(\rho_0 c/2S + R_t)^2 + X_t^2}. \quad (2.38)$$

The fraction of acoustic power transmitted to the right along the main tube is given by the power transmission coefficient [Kinsler 00]:

$$\mathcal{T} = \frac{R_t^2 + X_t^2}{(\rho_0 c/2S + R_t)^2 + X_t^2}. \quad (2.39)$$

The fraction of acoustic power transmitted through the tonehole is then

$$\mathcal{T}_t = \frac{(\rho_0 c/S)R_t}{(\rho_0 c/2S + R_t)^2 + X_t^2}. \quad (2.40)$$

In the low frequency limit the tonehole resistance is negligible in the above equations and  $X_t$  is obtained from equation 2.30. The main tube power transmission coefficient

then becomes

$$\mathcal{T} \simeq \frac{1}{1 + (S_t/2St_e k)^2} = \frac{1}{1 + (S_t c/4\pi St_e f)^2}. \quad (2.41)$$

The open tonehole therefore acts as a high pass filter for the transmission of acoustic waves along the main tube.

## 2.6 Undercutting

The method and purpose of undercutting a tonehole have been described in chapter 1. One of the reasons for undercutting a tonehole is to slightly raise the pitch of the notes played with it as the first open hole. Undercutting increases the volume of a tonehole. Referring to figure 2.1, the tonehole height  $t$  does not change. Undercutting therefore increases the effective cross-sectional area of the tonehole  $S_t$ .

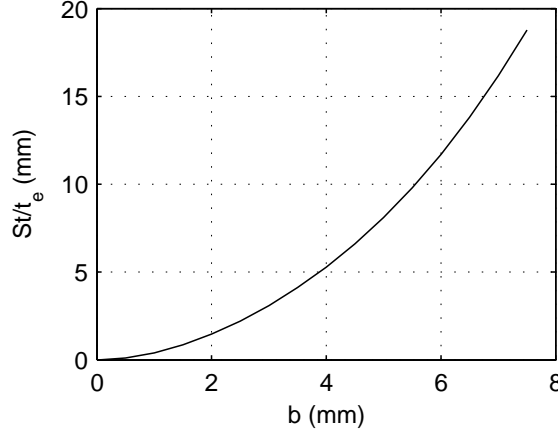


Figure 2.4:  $S_t/t_e$  against  $b$ .  $t + t_r = 7\text{mm}$ ,  $a = 7.5\text{mm}$ . From equations 2.34, 2.35 and 2.42.

Undercutting will also influence the value of the effective tonehole height  $t_e$ . If we approximate the effect of undercutting to be a localised increase in  $b$  at the bottom of the tonehole, then it will change  $t_m$  and  $t_i$  but not  $t$  or  $t_r$ . Analysis of the equations for  $t_m$  and  $t_i$  show that  $t_m + t_i$  increases with increasing  $b$ . To see the overall effect of increasing  $b$  in the region of the bottom of the hole we write

$$\frac{S_t}{t_e} \simeq \frac{\pi b^2}{t + t_r + t_m + t_i}. \quad (2.42)$$

To explore the behaviour of this function with respect to  $b$  we assume that  $t + t_r$  is constant and substitute in the expressions for  $t_m$  and  $t_i$  from equations 2.34 and 2.35. Using typical values for a clarinet of  $t + t_r = 7\text{mm}$  and  $a = 7.5\text{mm}$  [Nederveen 98a]

we obtain the relationship shown in figure 2.4, with  $S_t/t_e$  increasing with  $b$ . Assuming that all the other quantities on the right hand side of equation 2.32 remain constant, an increase in  $S_t/t_e$  will result in a decrease in  $L_x$ , thereby raising the pitch of the note played on the undercut tonehole. A more exact calculation of the effect of undercutting on the pitch of a tonehole can be obtained using the modal decomposition method [Keefe 82b] or the 3-D finite difference method [Nederveen 98b] mentioned above, taking into account the change in geometry.

## 2.7 Non-linearity in woodwind instruments

The term ‘non-linear’ is used in the area of wind instrument acoustics in reference to a range of phenomena [Hirschberg 94]. The reed mechanism responds in a non-linear fashion such that the pressure difference across the reed is proportional to the square of the volume flow rate through it. The restoring force on the reed is also non-linearly related to its displacement. In wind instruments of sufficient length, which are played at high acoustic pressures, non-linear wave propagation can occur in the bore. The non-linear relationship between acoustic pressure and acoustic particle velocity leads to the peaks of the sound wave propagating faster than the lower amplitudes, causing the wave to steepen [Morse 86]. This contributes to the brassy sound produced by certain brass instruments during loud playing. For woodwind instruments non-linear propagation seems to be negligible due to their shorter length and particular reed motion [Campbell 99]. We consider *local non-linear phenomena*, that is, flow conditions confined to the region around an open end or a tonehole that cannot be described using the linear theory outlined in sections 2.2 to 2.6.

### 2.7.1 Boundary layer separation and reattachment in steady flow

The origins of local non-linear flow effects are found in the fluid dynamical idea of boundary layer separation. Consider steady flow of mean velocity  $u$  entering a tube of radius  $a$  and travelling in the  $x$ -direction. If the Reynolds number of the flow (defined as  $Re_a = 2au/\nu$ , where  $\nu$  is the kinematic viscosity of the fluid) is sufficiently high then any viscous effects in the flow are confined to a region close to the wall called the viscous boundary layer. Within this viscous boundary layer the velocity of the fluid varies from zero at the wall ( $y = 0$ ), to  $u$  at a distance  $y = \delta$  from the wall. The velocity gradient inside the boundary layer implies that the flow there must be rotational [Hirschberg 95]. As the flow travels in the  $x$ -direction along the tube,  $\delta$  will increase until viscous forces are significant over the whole flow.

Consider the case where the boundary layer thickness is still small compared to

the radius of the tube. If the flow encounters a sudden expansion in the tube it will experience a deceleration and hence an adverse pressure gradient. The fluid nearest the wall in the boundary layer (which is also experiencing a negative frictional force from the wall) may begin to flow backwards. If this occurs the boundary layer at this point will separate from the wall. Next to the wall there will be an area of slowly backward-moving fluid. To conserve the volume flow the main flow will therefore increase in velocity. The thin region which separates the areas of high and low velocity is known as a free shear layer.

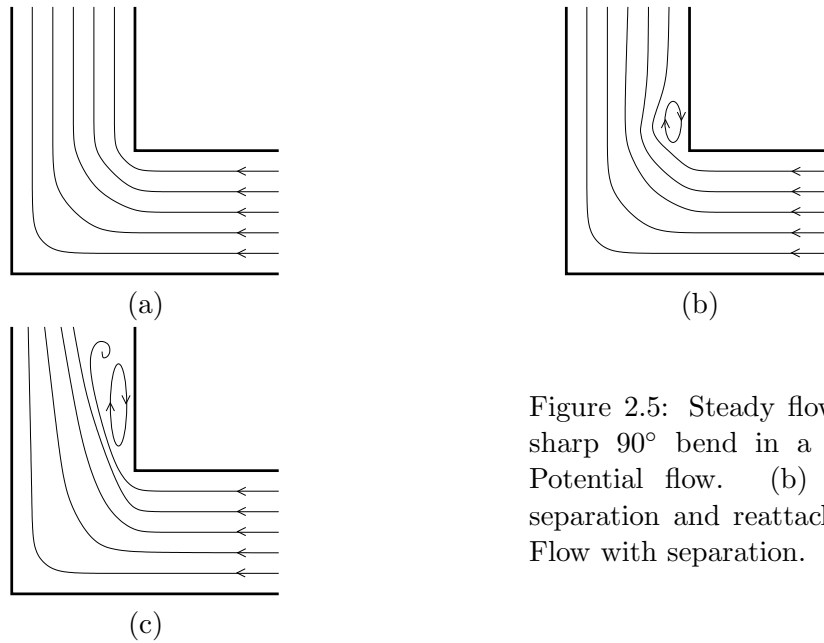


Figure 2.5: Steady flow around a sharp  $90^\circ$  bend in a tube. (a) Potential flow. (b) Flow with separation and reattachment. (c) Flow with separation.

The separated high velocity flow will entrain fluid from the low velocity area and therefore will be drawn back towards the wall [Tritton 99]. This can lead to the reattachment of the boundary layer to the wall of the tube. The result is a salient in the streamlines close to the wall, with the salient enclosing a circulating region. An example of this is shown in figure 2.5 (b).

If the adverse pressure gradient experienced by the flow at the expansion is sufficiently large, reattachment will not occur and the free shear layer will remain. Free shear layers are unstable and will roll up to produce structures of concentrated vorticity called vortices. These vortices are broken down to smaller scale vortices by the action of turbulence. At small enough length scales the viscosity of the fluid causes the dissipation of the vortex kinetic energy as heat.

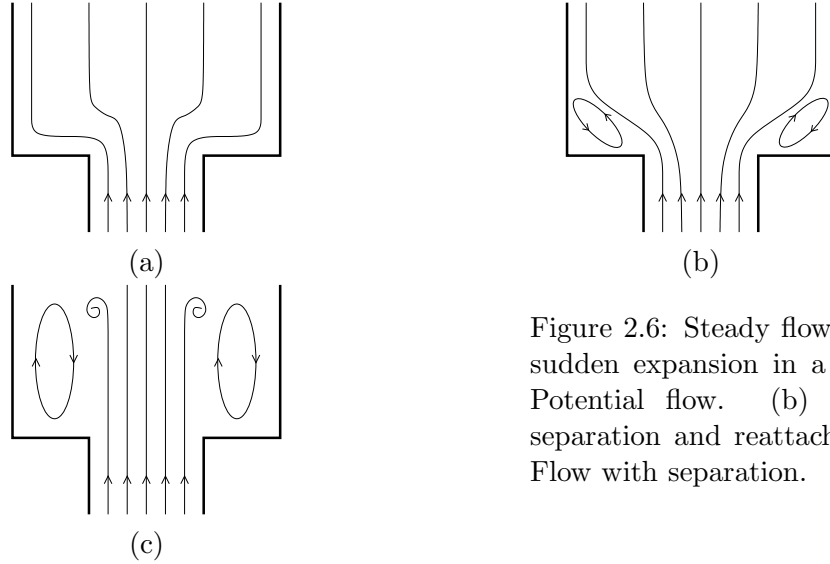


Figure 2.6: Steady flow through a sudden expansion in a tube. (a) Potential flow. (b) Flow with separation and reattachment. (c) Flow with separation.

### 2.7.2 Steady flow at discontinuities in tubes

Certain tube geometries are relevant to the study of woodwind instruments and it is instructive to consider steady flows around these geometries. Figure 2.5 (a) shows potential flow around a sharp  $90^\circ$  bend in a tube. On the inside of the bend, the streamlines are pressed together, indicating a higher velocity in this region. As the Reynolds number increases (due for example to a higher velocity), separation may occur at the inner corner of the bend, as shown in figure 2.5 (b). The fluid at the inner corner experiences a localised sudden expansion, which creates the necessary adverse pressure gradient for separation. The shear layer will reattach some distance downstream of the bend. In the vicinity of the inner corner, just downstream of the separation point, there will be a high velocity region in the main flow, indicated in figure 2.5 (b) by the compression of the streamlines. Between the free shear layer and the inner wall of the tube is a circulating region. As the velocity increases further, vortices are formed at the corner and convected downstream by the separated flow before dissipating their energy by the action of turbulence (figure 2.5 (c)).

The flow through a sudden expansion is shown in figure 2.6. At high enough Reynolds number the sudden widening of the tube causes separation at both sides of the expansion. For the case where no reattachment occurs (figure 2.6 (c)), there are free shear layers on either side of the main flow, resulting in a free jet. This type of flow can also occur at the exit from a tube.

Figure 2.7 shows flow for the case of a sudden contraction under the first two flow conditions. For the separation-reattachment case, the fluid passing the wall at either side of the contraction experiences an adverse pressure gradient. The separation and

reattachment leads to a narrowing of the cross-section of the main flow known as a vena-contracta. The same phenomena can be observed in the flow into the entrance of a tube.

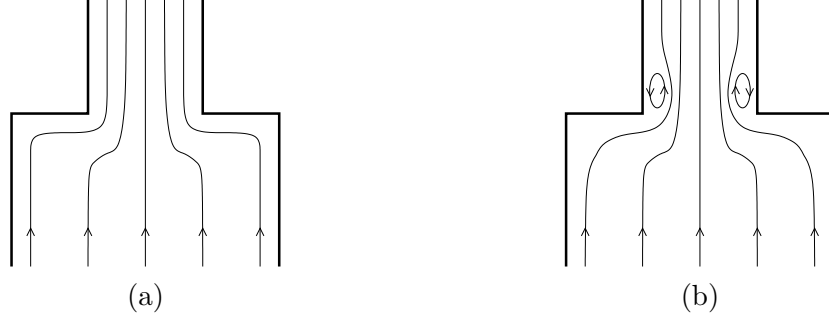


Figure 2.7: Steady flow through a sudden contraction in a tube. (a) Potential flow. (b) Flow with separation and reattachment.

### 2.7.3 Strouhal number

Turning our attention back to oscillating flows, it can be seen from the discussion following equation 2.1 that the equations describing the flow become non-linear when

$$\left| \frac{\partial \vec{u}}{\partial t} \right| \simeq |(\vec{u} \cdot \nabla) \vec{u}|. \quad (2.43)$$

Following Keefe [Keefe 83], consider the case of oscillating flow around a discontinuity in a tube, such as a bend or a sudden expansion, the geometry of which is characterised by some length  $\mathcal{L}$ . If the acoustic velocity amplitude in the region of the discontinuity is  $u_{ac}$  then, using an order of magnitude estimate,

$$|(\vec{u} \cdot \nabla) \vec{u}| \sim \frac{u_{ac}^2}{\mathcal{L}}. \quad (2.44)$$

Using a similar argument

$$\left| \frac{\partial \vec{u}}{\partial t} \right| \sim \frac{u_{ac}}{T} \sim u_{ac} \omega \quad (2.45)$$

and hence the condition for non-linearity becoming significant is given by combining 2.43, 2.44 and 2.45

$$u_{ac} \omega \simeq \frac{u_{ac}^2}{\mathcal{L}} \quad (2.46)$$

or

$$St_{\mathcal{L}} = \frac{\omega \mathcal{L}}{u_{ac}} \simeq 1. \quad (2.47)$$



$St_{\mathcal{L}}$  is the Strouhal number. If the Strouhal number is roughly equal to or less than 1, local non-linear flow effects will become significant. It is clear from equation 2.47 that this will occur for high acoustic velocities, low frequencies or sharp geometries.

The displacement amplitude of the oscillating air particles is defined as

$$d_{ac} = \frac{u_{ac}}{\omega}. \quad (2.48)$$

It is therefore possible to write the Strouhal number as

$$St_{\mathcal{L}} = \frac{\mathcal{L}}{d_{ac}}. \quad (2.49)$$

A Strouhal number of 1 then indicates that the displacement amplitude is equal to the characteristic length.

#### 2.7.4 Acoustic boundary layer

For oscillating flow the thickness of the viscous boundary layer is given by

$$\delta_{ac} = \sqrt{\frac{2\nu}{\omega}} \quad (2.50)$$

where  $\nu$  is the kinematic viscosity of the fluid [Pierce 81]. This relation is true for the regions of the flow where the boundary layer has not separated.

#### 2.7.5 Turbulence

The transition from laminar to turbulent behaviour of the main flow is governed by the Reynolds number. For oscillating flow in a tube the relevant Reynolds number is defined using  $\delta$  as the characteristic length scale:

$$Re_{\delta} = \frac{\delta_{ac} u_{ac}}{\nu} = \frac{\sqrt{2} u_{ac}}{\sqrt{\nu \omega}}. \quad (2.51)$$

Transition to turbulence will occur above a critical Reynolds number  $Re_{\delta}^{crit}$ . From experiment  $Re_{\delta}^{crit}$  has been found to lie between 300 and 500 [Merkli 75, Hino 76]. Again, this analysis is true for the regions of the flow where the boundary layer has not separated.

#### 2.7.6 Quasi-steady approximation

Steady flows with boundary layer separation are better understood than oscillating flows where similar effects are evident. When the Strouhal number is much less than 1,

oscillating flows with local non-linear flow phenomena can be treated using the quasi-steady approximation [Disselhorst 80, Peters *et al* 93]. This assumes that the flow at any point in the acoustic cycle can be approximated by an equivalent steady flow with an appropriate velocity. Simple Bernoulli relations can then be used to calculate the pressure drop across the discontinuity in terms of the velocity through it. Two different Bernoulli relations are used for the parts of the cycle when the flow is flowing into or out of, say, the end of a tube [Disselhorst 80, Peters *et al* 93]. When  $St \sim 1$  then the quasi-static approximation is not valid and there is no simple relationship between pressure and velocity in the vicinity of the discontinuity.

### 2.7.7 Energy losses due to non-linear flow effects

In the case of steady tube flow, energy losses due to local non-linear flow effects are described as *minor losses* to distinguish them from *major losses* which occur within the attached boundary layer [Benedict 80, Ward-Smith 80]. The minor loss coefficient  $K$  gives the ratio of dissipated flow energy per unit mass to flow kinetic energy per unit mass at a discontinuity [Smith 03]. In the quasi-steady approximation minor losses for oscillatory flow can be treated using different minor loss coefficients for the two flow directions.

In oscillatory flow it is common to describe the power lost from the flow to local non-linear effects as a modification to the real part of the impedance in the plane of the discontinuity at which the effects occur [Sivian 35, Ingard 50, Ingard 67, Petculescu 02, Atig 03, Skulina 03]. This is done using equation 2.21 rearranged as:

$$R_{nl} = \frac{2\langle P_{nl} \rangle}{Su_{ac}^2} \quad (2.52)$$

where  $R_{nl}$  is the change to the resistance due to local non-linear flow effects and  $\langle P_{nl} \rangle$  is power lost to local non-linear flow effects averaged over the acoustic cycle.

### 2.7.8 Jet driven streaming

Local non-linear effects caused by oscillating flows can give rise to steady flows [Boluriaan 03]. The mechanism for this is illustrated in figure 2.8, showing the streamlines of flow at the exit from a tube. Figure 2.8 (a) shows inflow to the tube that is diffuse (the same in all directions) occurring during one half of the acoustic cycle. This remains an approximately accurate description of the inflow even at low Strouhal numbers. Figure 2.8 (b) shows the outflow from the tube during the other half of the acoustic cycle at moderately low Strouhal number, characterised by jet formation and vortices forming on either side of the tube exit. If the flow is averaged over the cycle,

the inflow and outflow behaviour is added together and results in a steady flow similar to that shown in figure 2.8 (c). This *jet driven streaming* is dominated in the centre by a strong outward jet. At the sides the mean flow is directed into the tube, and the vortices that were formed during outflow lead to areas of steady rotation. Overall there will be no net mass flux either into or out of the tube. The velocities present in the jet driven streaming can be of the same order of magnitude as the velocity amplitude of the oscillating flow.

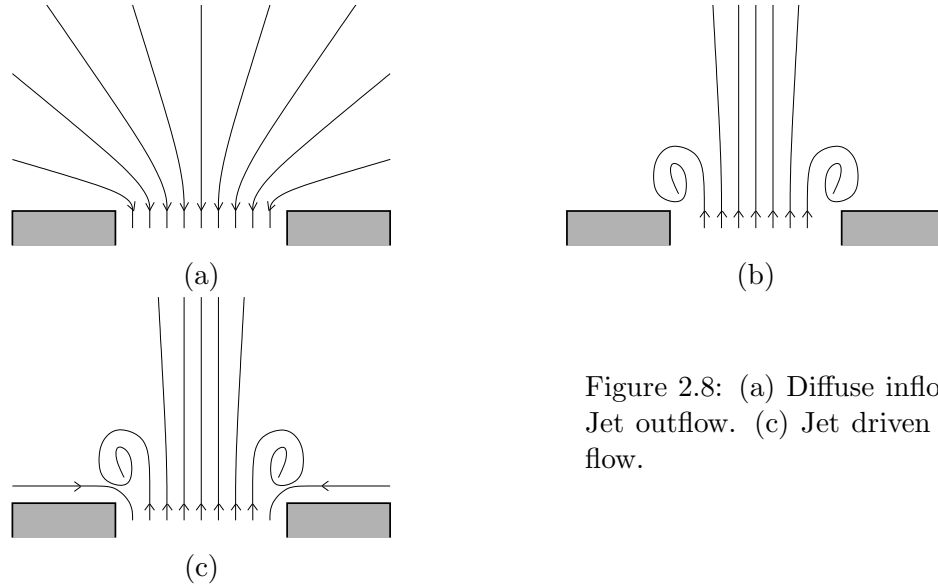


Figure 2.8: (a) Diffuse inflow. (b) Jet outflow. (c) Jet driven steady flow.



## Chapter 3

# Particle Image Velocimetry

### 3.1 Introduction

At its most basic, Particle Image Velocimetry (PIV) can be described as a simultaneous, quantitative measurement of fluid velocity at a large number of points in a flow. It is a development of qualitative measurement of fluid flow (*flow visualisation*) which has been carried out since the 19th century. Using one method of visualisation it is possible to observe the form of the flow by photographing illuminated seeding particles distributed throughout it. An example of this is given in figure 3.1.

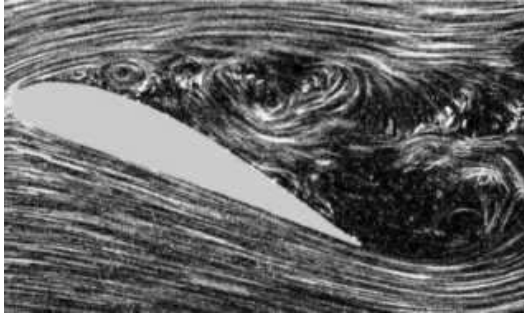


Figure 3.1: Flow visualisation of boundary layer separation on inclined wing using tracer particles. Taken from [Visualisation 08].

PIV advances this type of visualisation by using  $N$  short flashes of light separated by a small amount of time  $\tau$  to capture  $N$  images of the particles in the flow field. The motion of particles between each exposure is then assessed, either using computer analysis if the images are digital or, using various optical methods if they are captured on film [Grant 97]. This provides a map of displacement vectors from each pair of images that can be converted to velocity vectors using  $\tau$ .

PIV is ideally suited to the study of spatially complex flows in a variety of fluid dynamics applications [Grant 97, Raffel 98]. These include time-varying flows. Particle velocities in acoustic flows have been measured with PIV for over 10 years [Hann 97]. Specific acoustics applications have included sound generation in wind instruments and vocal folds [Bamberger 05, Bruecker 04, Neubauer 07], bass loudspeaker ports [Esposito 03], stacks in thermoacoustic refrigerators [Berson 06], standing waves in closed tubes [Tonddast-Navæi 05] and woodwind terminations and toneholes [Rockliff 02b, Skulina 02, Skulina 03, Skulina 05b].

Along with Laser Doppler Anemometry (LDA), PIV has the advantage over other velocity measurement methods that rely on a probe (such as Hot-Wire Anemometry) of being less disruptive to the flow being measured. LDA differs from PIV in that it provides time-varying velocity information from a fixed point in the flow [Adrian (Editor) 93]. It is possible to build up a map of velocity vectors by scanning the LDA probe across a large number of points but this is time-consuming. PIV therefore has the advantage of providing a universal picture of the velocity field, while LDA has a higher precision [Degroot 07].

This chapter describes the PIV principles and system used to obtain the results in chapters 5, 6 and 7. Sections 3.2 and 3.3 go over the fundamentals of the technique. Section 3.4 is a discussion on how to optimise the parameters of the system to obtain the best quality vector maps. The method of synchronising the PIV system to an acoustic signal is the subject of section 3.5.

## 3.2 Basic Principles

While it is possible to carry out PIV in three dimensions [Raffel 98], the PIV system in this study is designed to make 2-D measurements of an area whose size is of the order of centimetres. A digital camera is used for image capture. A basic diagram of the type of experiment described in this section is shown in figure 3.2.

### 3.2.1 Seeding particles

In order to visualise the motion of a flow it is necessary to seed it with particles which reflect light. In order for PIV to provide an accurate description of a flow it is vital that the seeding particles faithfully follow the motion of the fluid particles. Ignoring external forces, Melling [Melling 97] considers the forces acting on spherical particles suspended in a fluid. For an oscillating flow, the following relationship was derived

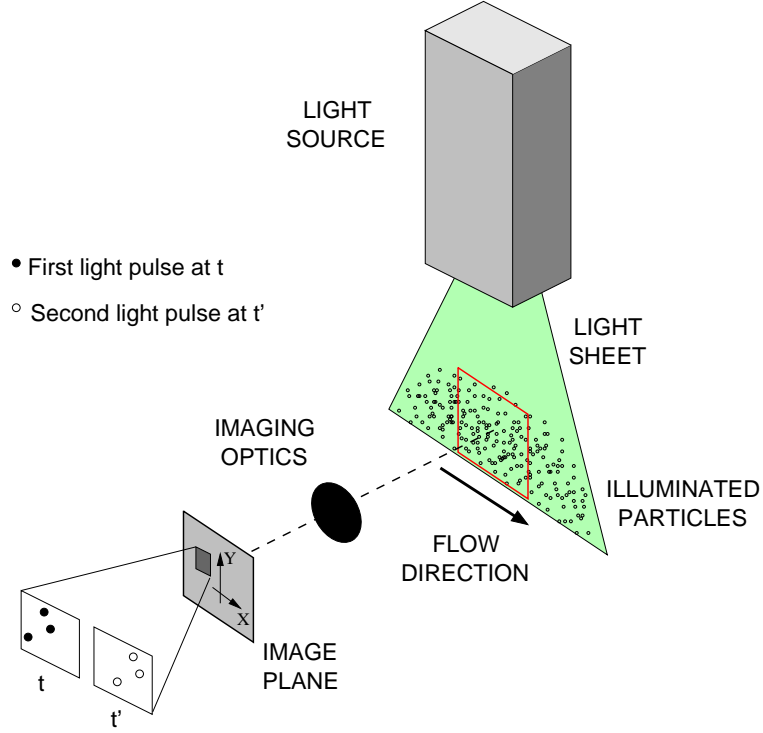


Figure 3.2: Basic PIV setup referred to in section 3.2. Taken from [Skulina 05a].

between the amplitude of the velocity of the fluid  $|u_{fl}|$  and that of the particle  $|u_p|$

$$|u_{fl}| = |u_p| \sqrt{1 + \frac{2\pi f d_p^2 \rho_p}{18\mu}} \quad (3.1)$$

where  $f$  is the frequency of the oscillation,  $d_p$  is the diameter of the particle,  $\rho_p$  is the density of the particle and  $\mu$  is the dynamic viscosity of the fluid. The relationship between the phases is

$$\angle u_{fl} = \angle u_p + \tan^{-1} \left( \frac{2\pi f d_p^2 \rho_p}{18\mu} \right). \quad (3.2)$$

These relationships show that small particles follow the motion of the flow more accurately. However, the intensity of scattered light increases with particle size [Raffel 98], so that for a given intensity of illumination, small particles may not scatter a sufficient amount of light for sharp PIV images. A compromise of particle size is therefore required.

The particles used in this study are provided by a SAFEX 2004 fog generator using SAFEX Normal fog fluid. The particles generated consist of water ( $\rho_p = 1000 \text{ kg m}^{-3}$ ) with a minimal amount of alcohol and have an average radius of  $1 \mu\text{m}$  [Dantec 98]. With

the experiments taking place in air using an excitation frequency of 180Hz, equations 3.1 and 3.2 give a tracer particle velocity amplitude that is 0.17% less than the fluid velocity amplitude, and a phase difference of 0.2 degrees. In comparison with errors derived from other sources, these are negligible (see section 4.5.6).

PIV can be considered non-intrusive to the flow to the extent that the seeding particles do not alter the fluid mechanical properties of the fluid studied. In the case of acoustic flows, the presence of seeding will alter the speed of sound in the fluid by increasing the attenuation due to viscothermal effects [Kinsler 00, Tonddast-Navæi 05]. The density of droplets used in this study ( $\sim 6.7 \times 10^{11}$  per  $\text{m}^3$ ) leads to a reduction of the speed of sound of roughly 0.3%.

### 3.2.2 Illumination

Once the tracer particles have been introduced to the flow it is necessary to illuminate them for photographic capture. For 2-D PIV this is done using a thin light sheet. The light sheet must be adequately bright to provide sufficient contrast in the images but must deliver this high intensity in a short amount of time to prevent the images of particles being blurred. A high energy pulsed laser is therefore ideal for this application.

The light source used in this work is an Oxford Lasers LS20-50 copper vapour laser. It gives a pulsed output at a repetition frequency of 10kHz, with an average power of 20W. Each light pulse lasts for 25-30ns and delivers a light energy of around 0.4mJ. The wavelength of the laser light is 510.6nm (green).

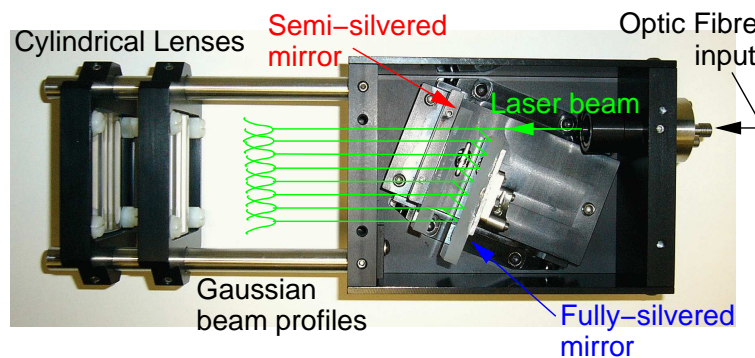


Figure 3.3: Oxford Lasers ‘Fibresheet’ light sheet optics. Taken from [Skulina 05a].

The beam from the laser is collected by an optical fibre cable and delivered to an Oxford Lasers ‘Fibresheet’ optical device which converts the beam into a thin sheet of light. It does this by reflecting the beam between two parallel mirrors, one of which is semi-silvered and the other which is completely reflecting (see figure 3.3). The output sheet then passes through two cylindrical lenses which can be adjusted to ensure a



minimum thickness of sheet in the region in which the images are captured. The resulting section of light sheet is approximately 50mm wide and 1mm thick.

### 3.2.3 Image capture

Each pulse of the light sheet provides one image for capture onto a photographic medium. Image capture can be done using one photographic frame for  $N$  exposures (single frame/multi-exposure PIV) or using  $N$  frames for the  $N$  exposures (multi-frame/single exposure PIV). This study uses a digital camera to perform two-frame/single exposure PIV. This eliminates the directional ambiguity between images of particles which is a feature of single frame methods.

A PCO Sensicam ‘Double Shutter’ camera is used to capture frames. Each frame has a resolution of  $1280 \times 1024$  pixels. Two frames are captured onto the camera with a time between frames of  $1\mu\text{s}$ . The exposure time of each frame is longer than the duration of a laser pulse. Due to the time necessary for the camera to readout the pair of frames to the attached computer, the time required for a pair of frames is around 250ms. The pair of images are saved as 8-bit bitmaps.

## 3.3 Image analysis

In order to extract velocity information from a pair of images they must be broken down into small regions known as interrogation areas (see figure 3.4). The pattern of particles within each interrogation area is then compared between the two images to assess the average displacement within it. The pattern comparison method used here is *cross-correlation*. In this study, each interrogation area has an area of  $32 \times 32$  pixel<sup>2</sup>. In order to obtain a higher resolution of velocity data, the interrogation areas overlap by 50%. The result is a  $79 \times 63$  grid of velocity data points, each 16 pixels apart, describing the whole  $1280 \times 1024$  pixel image.

Depending on the density of particles in an interrogation area, different image analysis techniques can be used. At low densities it is possible to follow the motion of an individual particle using a technique called Particle Tracking Velocimetry. For high particle densities the interference of the scattered light leads to a speckle pattern on the image plane of the camera from which the motion can be determined. This is known as Laser Speckle Velocimetry. The density of particles used in PIV ( $\sim 10$  per interrogation area) lies between these two extremes.

The MatPIV package for Matlab was used to process the PIV images in this work [Sveen 04].

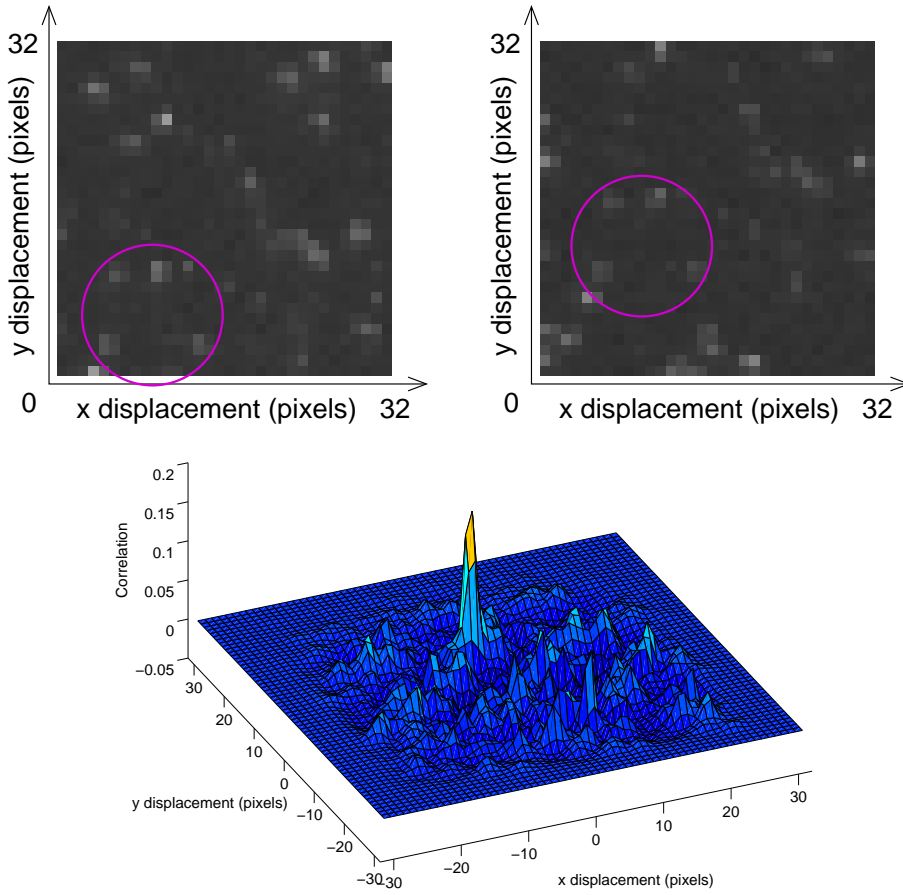


Figure 3.4: Example of the same  $32 \times 32$  pixel interrogation area from a pair of PIV images and the resulting correlation plane. Magenta circle shows same group of particles.

### 3.3.1 Cross-correlation

Consider an interrogation area measuring  $\mathcal{M} \times \mathcal{M}$  pixel. A point in the first interrogation area at position  $(i, j)$  in the  $x, y$  pixel plane has a light intensity described by  $f(i, j)$ . A point in the second interrogation area at position  $(i, j)$  has a light intensity described by  $g(i, j)$ . The cross-correlation function  $R_{fg}(k, l)$  is then given by

$$R_{fg}(k, l) = \sum_{i=0}^{\mathcal{M}} \sum_{j=0}^{\mathcal{M}} f(i, j) g(i + k, j + l). \quad (3.3)$$

$R_{fg}(k, l)$  is evaluated by shifting the first image  $f(i, j)$  around the second image  $g(i, j)$ .  $f(i, j)$  is shifted  $k/l$  pixels in the  $x/y$  direction such that when the two interrogation

areas are directly ‘on top’ of each other  $k$  and  $l = 0$ . For values of  $k$  and  $l$  where particle images in the two interrogation areas coincide  $R_{fg}(k, l)$  will have a high value. By shifting over all values of  $k$  and  $l$  such that  $f(i, j)$  and  $g(i, j)$  ‘overlap’ by a minimum of one pixel, a correlation plane is built up for which  $k, l \in -(\mathcal{M} - 1) : (\mathcal{M} - 1)$ . A correlation plane for a  $32 \times 32$  pixel interrogation area is shown in figure 3.4.

The position of the peak in the correlation plane indicates the optimum shift such that the pattern of particles in the two interrogation areas can be said to coincide. It is therefore the best estimate of the displacement of the flow at that point. The cross-correlation of each interrogation area provides a 2-D displacement vector with units of pixels. This can be converted into a velocity vector, using a calibration image to convert from pixels to metres and dividing by time between laser pulses  $\tau$ . The assumption is made that there are no spatial velocity gradients within the interrogation area or temporal velocity gradients within the time  $\tau$ .

In order to reduce computation time the cross-correlation is evaluated by making use of the Wiener-Kinchin theorem [Raffel 98, Riley 98]

$$\tilde{R}_{fg} = \tilde{f}^* \tilde{g} \quad (3.4)$$

where  $\tilde{f}$  denotes the Fourier transform.

### 3.3.2 Peak detection

To calculate the displacement to sub-pixel accuracy a Gaussian function is fitted to the correlation maximum and its two nearest neighbours in both the  $x$  and  $y$  directions. The displacement is then taken to be from the origin to the peak of the Gaussian.

### 3.3.3 Vector validation and replacement

Looking at figure 3.4, a number of smaller peaks can be observed in the correlation plane which are due to the matching of particle images in the first frame with images of different particles in the second frame. If one of these spurious peaks has a greater magnitude than the true peak the cross-correlation will produce an invalid velocity vector for that interrogation area. The cause of these spurious peaks may be the loss of particles from the interrogation area in the time  $\tau$ , either due to in-plane or out-of-plane motion. This may cause the true correlation peak amplitude to fall below those due to random correlations. A low density of seeding particles in the interrogation area will have a similar effect. Section 3.4 outlines the choices of experimental parameters which minimise the number of spurious vectors.

It is possible to use post-processing to remove spurious vectors from the resulting

velocity vector map of a pair of images. One approach is to assume that correlation peaks of valid vectors will exceed a certain signal-to-noise ratio  $D_0$ . A minimum value for  $D_0$  of 1.2 has been proposed [Keane 90]. In this study, correlation peaks are treated as spurious if their signal-to-noise ratio is below 1.3.

A small number of spurious vectors may not be eliminated using the signal-to-noise filtering. Local filtering can then be used to compare each vector to its nearest neighbours. In this study median filtering is used [Westerweel 94]. The median values of the  $x$  and  $y$  velocities of the 8 nearest neighbours of a particular velocity vector are found. The standard deviations are also calculated. If the difference between the  $x$  or  $y$  velocity of the central vector and the median value are found to be greater than a certain threshold, that vector is treated as spurious. In this study the threshold value is 2.1 times the nearest neighbour standard deviation. This was chosen by trial and error to be the lowest value that eliminates almost all spurious vectors after the signal-to-noise filtering.

Finally, the spurious vectors are replaced by comparing them with their valid neighbours and giving them the mean  $x$  and  $y$  velocities of their nearest neighbours. The replacement begins with those spurious vectors with 8 valid neighbours, then goes on to those with 7, etc.

### 3.4 Optimisation

Various studies have been performed into the properties of the PIV image pair which optimise the results of the cross-correlation, both in terms of the number of valid vectors and their precision [Keane 90, Keane 92, Raffel 98]. These use a Monte Carlo method to simulate a large number of pairs of interrogation areas with certain properties (particle density, particle size, particle displacement). These are then cross-correlated and the resulting percentage of valid vectors and the uncertainty in the velocities are obtained. The properties of the simulated interrogation areas can then be varied.

One important parameter for obtaining valid vectors is the number of particle images which occur in both interrogation areas  $\mathcal{N}$ . It has been found that  $\mathcal{N} > 6$  is required to obtain  $> 95\%$  valid vectors in multi-frame/single exposure PIV, processed using cross-correlation [Keane 92]. It is therefore desirable to have  $> 7$  particle images in the first interrogation area, and to attempt to minimise the loss of pairs between the two interrogation areas, due either to in-plane or out-of-plane motion.

Loss of particle image pairs due to in-plane motion can be reduced by shifting the second interrogation area in the direction of the flow that is being studied. In complex flow fields like those observed in this study, this approach is not feasible. Out-of-plane losses can be reduced by using a thicker light sheet for the second image capture. This

is technically difficult to implement, due to the need to maintain a constant brightness and the correct light sheet alignment between exposures. In this study the flow is assumed to be approximately 2-dimensional and the light sheet is made parallel to the flow to reduce out-of-plane losses (see section 4.5.2).

The main approach which is taken here is to optimise the time between image captures  $\tau$  to minimise the loss of particle image pairs. Keane and Adrian [Keane 90] suggest a maximum mean displacement of particle images between frames of

$$\Delta X = 0.25d_I \quad (3.5)$$

where  $d_I$  is the length of an interrogation area and both lengths are in pixels. If  $\mathbf{u}(x, y)$  describes the velocity field being measured then equation 3.5 gives the condition

$$M \max(|\mathbf{u}|)\tau = 0.25d_I \quad (3.6)$$

where  $M$  is a conversion factor between pixels and metres obtained using a calibration image. Rearranging gives a maximum time between image captures:

$$\tau_{max} = \frac{0.25d_I}{M \max(|\mathbf{u}|)}. \quad (3.7)$$

It would be possible to use smaller values of  $\tau$ . However, reducing  $\tau$  increases the relative uncertainty in the velocity data by amplifying the errors in the displacement data obtained from the cross-correlation [Raffel 98].  $\tau_{max}$  is therefore used in this study as the optimum time between image captures.

The other important parameter for achieving a high percentage of valid vectors is the number of particle images in the first interrogation area. This cannot be controlled precisely in an experiment as it depends on the density of seeding particles. Taking the interrogation areas in figure 3.4 as typical examples from this experiment, it can be seen that there are  $\simeq 15$  particles in each one. This is well above the minimum of 7 prescribed above. The diameter of particle images is also important for the uncertainty in displacements calculated using cross-correlation. An optimum mean particle image diameter of around 2.5 pixels has been found for multi-frame/single exposure PIV [Raffel 98]. Looking at the particles in figure 3.4, we see that a typical particle size for this study is  $\simeq 2$  pixels.

### 3.5 System Timing and Synchronisation

A system has been developed at the University of Edinburgh to synchronise PIV measurements with an acoustic oscillation such that it is possible to take PIV

measurements at a number of evenly spaced times in the acoustic cycle [Skulina 05a]. The components of the system are shown in figure 3.5. National Instruments Labview software is used to generate a sine wave which drives a loudspeaker to provide the acoustic field. The sine wave frequency for this experiment is 180Hz. Labview also generates a 3V square wave with an offset of +3V and a frequency of 2Hz. The sine wave and square wave are initially in phase such that the rising edge of the square wave occurs at the positive-going zero-crossing of the sine wave. The square wave is sent to a Berkley Nucleonics Model 500A pulse generator, arriving at time  $T_{SQ}$ . The rising edge of the square wave triggers four output pulses from the pulse generator: T1, T2, T3 and T4. The delays of these four with respect to  $T_{SQ}$  and their widths can be programmed. T3 is sent to the ‘Force External’ input on the LS20-50 copper vapour laser. This forces the laser to suppress its normal pulsed operation for the duration of T3. T1 and T2 are then sent to the ‘Pulse In’ input of the laser, causing it to provide two flashes of light to the measurement area via the fibre optic cable, as outlined in section 3.2.2. The delay of T1 relative to  $T_{SQ}$  is set as one period of the sine wave. The delay of T2 relative to T1 defines  $\tau$ . When the laser is operated in this way, the minimum value of  $\tau$  obtainable is  $20\mu\text{s}$ . Below this value the two light pulses have an uneven intensity.

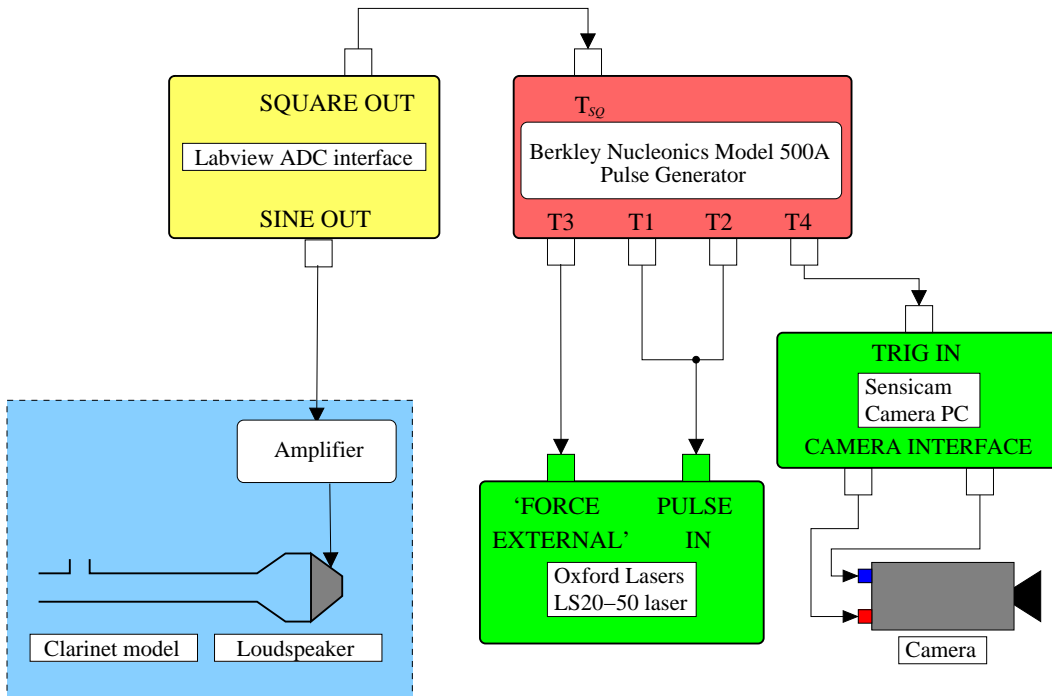


Figure 3.5: Components of PIV synchronisation system.

T4 from the pulse generator is sent to trigger the computer controlling the PCO Sensicam camera in order to synchronise the two frames of the camera with the flashes of laser light. The length of the first frame is dictated by the width of T4. The length of the second frame is dictated by the readout time of the camera, as discussed in section 3.2.3.

Table 3.1: Timings on pulse generator relative to rising edge of triggering square wave for measurement of 180Hz acoustic signal.

	Channel	Delay (ms)	Width (ms)
Laser Pulse 1	T1	5.5556	0.0004
Laser Pulse 2	T2	$5.5556 + \tau$	0.0004
Force External	T3	0	396
PCO Camera	T4	5.4656	0.1

Figure 3.6 shows the timings of the four pulses relative to  $T_{SQ}$  and Table 3.1 lists the timings used in this experiment. T3 must be wide enough to allow the entire image pair capture process to occur within it. T4 is programmed to trigger the first camera frame 0.09ms before the first laser flash to ensure that the flash occurs within the frame. The pulse box can be programmed to run the image pair capture process every time the rising edge of the square wave arrives. That is why the square wave has a frequency of 2Hz: it gives 500ms for the image pair capture process to occur. The pulse box is programmed to perform 30 image pair captures, taking a total time of 15 seconds.

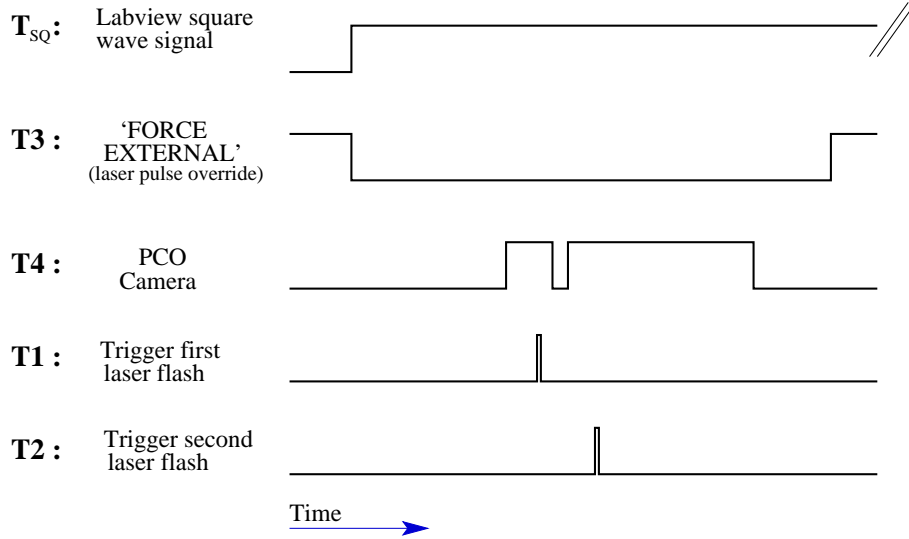


Figure 3.6: PIV timing (not to scale).

The phase of the square wave can be shifted relative to the sine wave so that the image pair capture process occurs at any point in the acoustic cycle. For this experiment image pairs are captured at 20 equally spaced points in one acoustic cycle labelled  $t_i$ ,  $i = 1 \dots 20$ , separated by a time of  $1/(180 \times 20)$ s.

The phase relationship between the sine wave and the square wave can be set accurately. However, the relative phase between the square wave and the acoustic velocity field in the region of the light sheet is not easily determined, due to a fixed phase lag introduced by the loudspeaker. The phase shift between the sine wave and square wave is therefore adjusted in a trial and error fashion, looking at the resultant PIV vector maps to ensure that  $i = 1$  and  $i = 11$  correspond roughly to the zero-crossings of the acoustic velocity field.

For each sound level studied, the flow at the maximum point in the acoustic velocity cycle ( $i = 6$ ) is measured with PIV in the lab to determine  $\max(|\mathbf{u}(x, y, t_i)|)$ , the maximum velocity magnitude present at any time in the cycle. This is used in equation 3.7 to calculate  $\tau_6$ , the optimum time between image captures when  $i = 6$ . The same process is repeated at the zero-crossing point in the acoustic velocity cycle ( $i = 1$ ) to obtain  $\tau_1$ . The optimum value of  $\tau$  for the intervening phase steps is then calculated assuming a sinusoidal variation in the maximum velocity magnitude:

$$\tau_i = \tau_1 - |(\tau_1 - \tau_6) \sin(2\pi f(t_i - t_1))| = \tau_1 - \left| (\tau_1 - \tau_6) \sin\left(\frac{\pi}{10}(i - 1)\right) \right| \quad (3.8)$$

where  $f$  is the frequency of the acoustic oscillation. Velocity magnitude symmetry is assumed on either side of the acoustic velocity maximum and on either side of the acoustic velocity zero-crossing such that:

$$\begin{aligned} \tau_1 &= \tau_{11} \\ \tau_2 &= \tau_{10}, \tau_{12}, \tau_{20} \\ \tau_3 &= \tau_9, \tau_{13}, \tau_{19} \\ \tau_4 &= \tau_8, \tau_{14}, \tau_{18} \\ \tau_5 &= \tau_7, \tau_{15}, \tau_{17} \\ \tau_6 &= \tau_{16}. \end{aligned}$$



## Chapter 4

# Experimental Apparatus and Method

### 4.1 Introduction

A previous study has revealed the difficulties of performing PIV at the side hole of an acoustically excited tube [Skulina 05b]. This chapter describes the model clarinet constructed to perform PIV around an open tonehole as well as the experimental method used to obtain the results described in chapters 5 and 7 (sections 4.2 and 4.5).

### 4.2 Clarinet model

A simplified model of a clarinet with one open tonehole was constructed for the purpose of performing PIV on the flow around the tonehole. The main deviations from a real clarinet are described below.

#### 4.2.1 Main tube

The main section of the model consists of two sections of rectangular cross-section aluminium tube joined together to give a total length of 988mm. The reason for the rectangular shape is explained in section 4.2.3. The length scale of the model has to be twice that of a clarinet (to support frequencies in the chalameau register) because the real instrument is approximately described as a cylindrical tube closed at one end, whereas the model, being driven by a loudspeaker is approximately described as open at both ends.

The internal bore dimensions of the main tube are 17.7mm high and 10mm wide,

with wall thickness of 10mm. This leads to a bore area,  $S$ , of  $177\text{mm}^2$ . Clarinets have a similar bore area in the main section, before flaring begins at the bell [Nederveen 98a].

#### 4.2.2 Excitation mechanism

For the PIV model the reed-mouthpiece-player excitation mechanism of the clarinet is replaced by a loudspeaker to provide the oscillating flow field. The loudspeaker is a Maplin Electronics 150mm diameter cone with  $6\Omega$  DC resistance and rated power of 35W. This is mounted in a wooden box, and the back of the loudspeaker surrounded with foam to damp radiation. The front of the loudspeaker is coupled to the main tube of the model by a wooden adapter in the shape of a square-based pyramid. The base of the adapter is sealed onto the front of the loudspeaker box. The narrow end has an internal bore equal to that of the main tube and has an external structure that uses screws to hold the main tube in place (see figure 4.1). An airtight seal between the adapter and the tube is ensured by the use of vacuum grease.

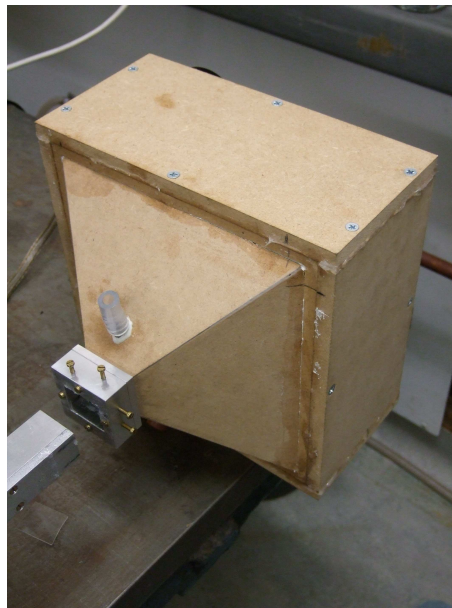


Figure 4.1: Speaker box and pyramid adapter for coupling speaker to main tube.

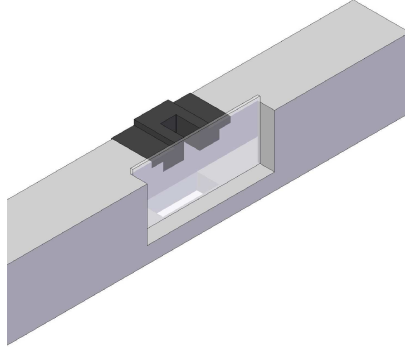
#### 4.2.3 Tonehole section

A section of the main tube is modified to model an open tonehole (see figure 4.2). The shorter wall of the tube is cut away to allow the insertion of a removable tonehole piece. One of the longer walls is removed and replaced by a microscope slide, 56mm long, 26mm high and 1mm thick. This provides a window through which the inside of

the model can be seen. The slide is held in place with clamps and sealed with vacuum grease to prevent air leaks. This allows it to be removed for cleaning.



(a)



(b)

Figure 4.2: (a) Tonehole section with tonehole inserted. (b) CAD drawing showing simplified tonehole section.

The window provides the reason for the rectangular geometry of the model. Performing PIV measurements through curved transparent surfaces leads to areas of glare in the image causing a loss of velocity information from parts of the flow map [Rockliff 02a]. This is exacerbated at the junction between the main bore and the tonehole [Skulina 05b]. The current setup allows clear viewing of this important region. The last feature of the section is a small glass window in the wall of the tube opposite the tonehole. This is to provide access to the inside of the tube for the laser light sheet required for PIV.

The position of the tonehole section was chosen to give the system a fundamental resonance frequency corresponding to a note played on one of the lower open holes of the clarinet in the chalameau register. The tonehole section is therefore positioned

such that the tonehole centre is 90mm from the end of the main tube. This leads to a fundamental resonance frequency for the whole system of  $180 \pm 0.5 \text{ Hz}$ . This roughly corresponds to playing a clarinet with the fourth lowest tonehole closed (F3 sounding pitch).

#### 4.2.4 Tonehole pieces

Tonehole pieces are constructed from aluminium and can be slotted into the tonehole section of the main tube. These are held in place with fixtures that are screwed down (see figure 4.2 (a)) and sealed with vacuum grease. The three sides of each piece describe a hole which is rectangular in cross-section. The missing side is provided by the glass window (see figure 4.2 (b)). The depth of the tonehole in the direction across the main bore is equal to the width of the main bore (10mm) such that two of the walls of the tonehole are flush to two of the walls of the tube.

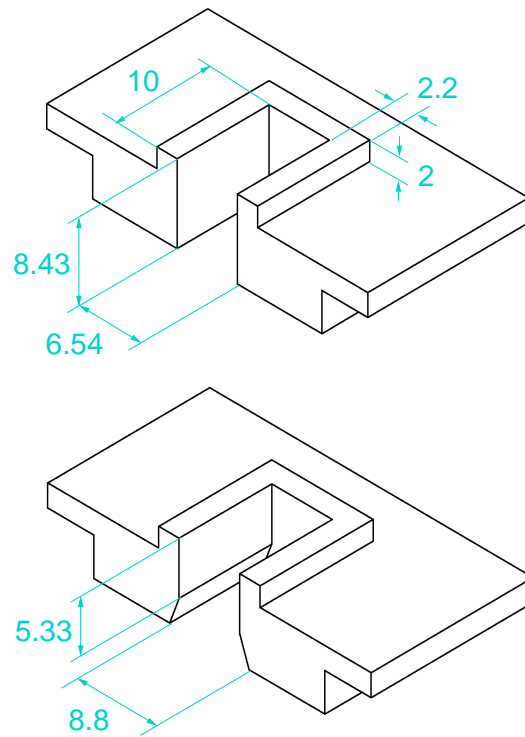


Figure 4.3: Important dimensions of toneholes used in clarinet model. Upper: square tonehole. Lower: undercut tonehole. The undercut tonehole has the same dimensions as the square tonehole, apart from those indicated. All lengths are in millimetres.

The sizes of the tonehole in the other two directions were chosen based on the dimensions of the fifth lowest hole on a real clarinet. This is the lowest hole which is not

covered by a pad. Nederveen [Nederveen 98a] gives the bore and tonehole dimensions of two clarinets, made by Dolnet and SML. The heights of hole 5 for the two instruments are 7.7mm and 9mm. The hole height of the model was chosen to be a compromise between these: 8.43mm. The radii of the holes on the two instruments are 9.1mm and 9.3mm, giving cross-sectional areas of 65mm<sup>2</sup> and 68mm<sup>2</sup>. The ratio of the tonehole cross-sectional area to the bore cross-sectional area is the same for both instruments. This ratio governs the extent of flow splitting that occurs at the hole. It is therefore maintained in the model tonehole, giving a tonehole cross-sectional area of 65.4mm<sup>2</sup>. The size of the tonehole in the longitudinal direction of the bore is therefore 6.54mm. Mimicking the rim of those clarinet toneholes covered by a ring key (such as hole 5), the model toneholes have a 2.2mm wide, 2mm high raised section on the outer surface. Figure 4.3 gives all the dimensions of the tonehole pieces used.

Following Greenham [Greenham 03], two different geometries of tonehole were constructed for use with the PIV model. The first, shown at the top of figure 4.3, has square corners (to within manufacturing accuracy). This corresponds to a non-undercut tonehole and will henceforth be described as the *square tonehole*. The second, shown at the bottom of figure 4.3, is based on the undercut geometry used by Greenham in his playing tests which was based on the most common geometries found in a large survey of clarinet toneholes. It has one third of the tonehole height cut away at an angle from the wall of the tonehole of 20°. It is labelled as the *undercut tonehole*.

Both of the tonehole pieces have approximately the same geometry for the external parts and are spray-painted black to eliminate reflections from the laser light sheet.

### 4.3 PCB transducer placement

A PCB 106B pressure transducer was used to monitor the RMS pressure at the antinode  $\bar{p}_{an}$  in the clarinet model. This required that the position of the pressure antinode for the model be located. As it is approximately a tube open at both ends, the pressure antinode for the fundamental resonance would be roughly halfway along the length of the main tube. There are however end corrections associated with both the tonehole and the loudspeaker/adapter. The sizes of these dictate the position of the pressure antinode in the main tube.

The main tube could be split in two, giving one length of tube terminated by the tonehole section and another section terminated by the loudspeaker/adapter. The input impedance of each of these sections was then measured using the BIAS impedance measurement system [BIAS 08]. The frequency of the first input impedance peak was measured and the wavelength of the standing wave associated with it calculated. As the BIAS head acts as a pressure antinode when attached to the tube, the effective acoustic

length associated with the first input impedance peak frequency is a quarter of the wavelength. The effective acoustic length of the section terminated by the tonehole is labelled  $L_e^{TH}$  and that of the loudspeaker/adaptor  $L_e^{LS}$ . This is the geometrical length of the section plus its end correction.

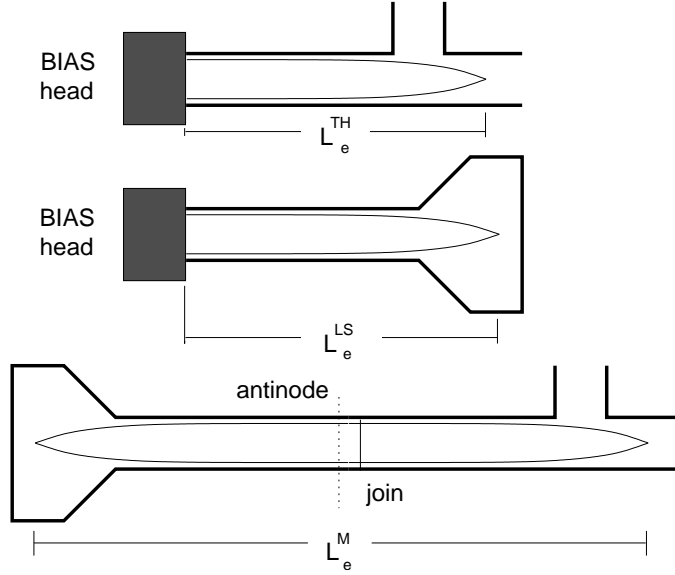


Figure 4.4: Effective acoustic lengths  $L_e^{TH}$ ,  $L_e^{LS}$  and  $L_e^M$ .

When the two sections are reconnected the overall acoustic length of the model is  $L_e^M = L_e^{TH} + L_e^{LS}$ . If the join between the two sections is taken as the origin, with the tonehole being in the positive direction, the pressure antinode for the total model is then located at  $L_e^{TH} - \frac{1}{2}L_e^M$ . The lengths involved are illustrated in figure 4.4.

The measurement surface of the PCB transducer is then mounted flush with the inside wall of the main tube at this position. The PCB transducer centre is a distance of 440mm from the centre of the tonehole.

#### 4.4 PCB transducer pressure calibration

With the loudspeaker exciting the tube at its fundamental resonant frequency (180Hz) and at a low sound level, the voltage from the PCB transducer mounted in the tube was recorded, having passed through the 482A22 signal conditioner. The RMS value of the voltage,  $\bar{v}_1^{PCB}$  was measured. The PCB transducer was then removed and a Brüel and Kjær 4192 half-inch microphone with a 15mm probe of 2mm external diameter was placed in its stead, with the tip of the probe just protruding into the bore. The probe passed through the centre of a bung in order to fill the larger hole left by the

PCB transducer. The signal from the probe was amplified by a Brüel and Kjær Nexus amplifier. The RMS voltage output of the probe microphone was taken, giving  $\bar{v}_1^{probe}$ . The relative value  $\bar{v}_1^{PCB}/\bar{v}_1^{probe}$  was calculated.

The probe microphone was then placed in a Brüel and Kjær probe calibration device which holds the end of the probe in a small sealed chamber, along with a reference microphone (another 4192 with no probe attachment) and a small loudspeaker. The Brüel and Kjær Pulse measurement system was used to give a signal to the loudspeaker and take inputs from the two microphones. The Nexus amplifier was not used with the probe. A swept sine from 100-1100Hz was then fed to the loudspeaker and a frequency response function between the two microphone outputs was performed using the Pulse software. From this could be obtained a ratio between the RMS voltages,  $\bar{v}_2^{probe}/\bar{v}_2^{ref}$  at 180Hz.

Finally, the reference microphone was placed in a Norsonic Nor1253 half-inch microphone calibrator and amplified with the Nexus. The calibrator produces a reference tone at 250Hz and 124dB. If we label this acoustic pressure  $\bar{p}_{124dB}$  and the reference microphone produces an RMS voltage  $\bar{v}_{124dB}^{ref}$  then the two are related by

$$\bar{v}_{124dB}^{ref} = n\bar{p}_{124dB} \quad (4.1)$$

where n is the sensitivity of the reference microphone in V/Pa. If the PCB transducer were in the same sound field it would give a voltage reading

$$\bar{v}_{124dB}^{PCB} = \frac{\bar{v}_1^{PCB}}{\bar{v}_1^{probe}} \frac{\bar{v}_2^{probe}}{\bar{v}_2^{ref}} \bar{v}_{124dB}^{ref}. \quad (4.2)$$

Hence

$$\bar{v}_{124dB}^{PCB} = \frac{\bar{v}_1^{PCB}}{\bar{v}_1^{probe}} \frac{\bar{v}_2^{probe}}{\bar{v}_2^{ref}} n\bar{p}_{124dB} \quad (4.3)$$

and generally

$$\bar{v}^{PCB} = \frac{\bar{v}_1^{PCB}}{\bar{v}_1^{probe}} \frac{\bar{v}_2^{probe}}{\bar{v}_2^{ref}} n\bar{p}. \quad (4.4)$$

For a voltage reading of  $\bar{v}^{PCB}$  from the PCB transducer, the calibrated RMS pressure is then given by

$$\bar{p} = \frac{\bar{v}_1^{probe}}{\bar{v}_1^{PCB}} \frac{\bar{v}_2^{ref}}{\bar{v}_2^{probe}} \frac{\bar{v}^{PCB}}{n} = 82.60 \times 0.916 \times \frac{\bar{v}^{PCB}}{3.16 \times 10^{-3}} = 23941\bar{v}^{PCB}. \quad (4.5)$$

This analysis relies on the reference microphone having a flat frequency response between 180Hz and 250Hz and on using the same gain setting on the Nexus amplifier at all stages in the process.

## 4.5 PIV experiment

The PIV system and its triggering has been described in chapter 3. This section describes how the PIV system was applied to measuring the velocity field around the tonehole in the model clarinet.

### 4.5.1 Enclosure



Figure 4.5: Aluminium enclosure used in experiment. Taken from [Skulina 05a].

The laser light sheet, the digital camera and the tonehole section of the model were all positioned inside a 1.2m-sided cubic aluminium box (see figure 4.5). This enclosure was secured on top of an optical table. Inside the enclosure were rails to which the digital camera and light sheet optics were attached. The main tube of the model passed through a hole in one of the walls so that the loudspeaker rested on a platform on the optical bench outside. The enclosure served as a safety feature, keeping the laser light away from the experimenter's eyes. It kept the tonehole area free from the light of the lab, improving the contrast of the PIV images. It also helped to sustain a sufficient density of seeding particles in the region of the tonehole for the period of time necessary to complete measurements once the fog had been injected into the enclosure.

### 4.5.2 Optical alignment

Once the tonehole section was in place inside the enclosure, the digital camera and light sheet optics had to be correctly positioned. This was facilitated by their being mounted on fixtures that could be adjusted in three translational directions. The camera could also be rotated in two dimensions.

First, the main tube was levelled using a spirit level. Next, the light sheet was correctly aligned. For safety reasons, this process was carried out with the laser beam partially blocked before the optical fibre cable so that 5% of the laser light intensity



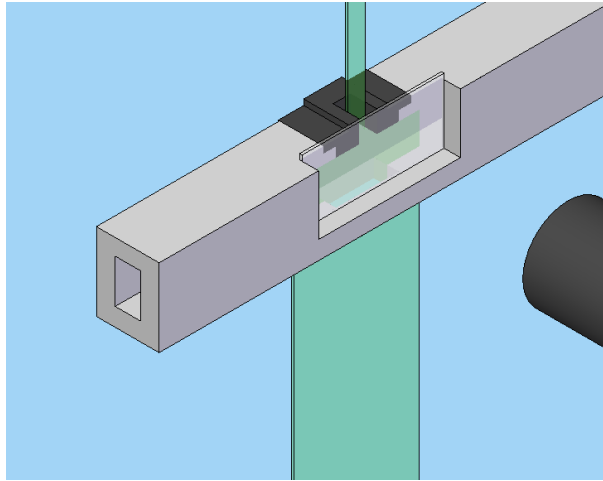


Figure 4.6: Alignment of model, light sheet and camera used for PIV of inside of clarinet model.

was passed to the light sheet. There were two light sheet configurations used, one for viewing the inside of the tonehole and one for the outside. For the internal view the light sheet passes through the window in the lower wall of the tube, as shown in figure 4.6. The height of the light sheet optics was adjusted so that the narrowest part of the light sheet coincided with the region of interest. It was also necessary to align the light sheet so that it ran parallel to the walls of the main tube and through the centre of the bore. This was to minimise any out of plane motion which has an adverse affect on the quality of PIV results [Raffel 98]. The positioning was aided by the use of a specially modified steel rule. This had a rectangular plastic block attached to it, holding it upright. The combined thickness of the block and rule was equal to half of the width of the bore so that, when the rule was inserted into the tube and pressed against the rear wall, it could be used as a guide for positioning the light sheet.

Finally the camera was correctly oriented to be square with the light sheet. This was achieved in the vertical plane by the use of a spirit level and in the horizontal plane by looking at an image of the steel rule and ensuring that all parts of it were equally in focus. For the internal view, the camera was zoomed in such that the image contained all of the tonehole length and enough of the inside of the tube to capture any flow phenomena that may occur there. This was ascertained from preliminary PIV measurements.

For external images the light sheet optics were moved to the other side of the tube and the camera position adjusted. The light sheet was again aligned using the steel rule.

### 4.5.3 Acoustic field

The loudspeaker coupled to the tube was driven by a sine wave signal of 180Hz generated using National Instruments Labview software via a digital-analogue converter. The signal was amplified by a Pioneer A-107 audio amplifier which could be used to vary  $\bar{p}_{an}$  in the tube.  $\bar{p}_{an}$  was monitored by the PCB transducer as described in section 4.3. For setting the level, the output from the signal conditioner was measured using a Hewlett-Packard 54602A oscilloscope. The voltage was also recorded onto Labview at 20 points throughout the course of an experimental run using 5 second, 10kHz samples.

### 4.5.4 Seeding

Seeding for the PIV was generated by a SAFEX 2004 fog generator. The fog was injected into the enclosure and the sound field initiated to draw the fog into the clarinet model. The seeding was then allowed to settle before commencing. The fog would gradually leak out of the enclosure, resulting in a seeding density which was too low. It was found that re-injecting smoke into the enclosure halfway through a set of 20 phase step measurements ( $\sim 5$ mins) provided a sufficient seeding density throughout.

### 4.5.5 Procedure

Two areas were examined; inside and outside the tonehole. PIV measurements were taken at 20 phase steps throughout the acoustic cycle using the technique outlined in chapter 3. At each phase step 30 image pairs were captured for the purpose of averaging, giving a total of 600 image pairs for each measurement set.

Once the correct value of  $\bar{p}_{an}$  had been set, the appropriate time separation between laser pulses for the phase step to be measured was input into the system (see section 3.5). The seeding procedure was performed. The 30 image pairs were then captured and exported from the camera software as 8-bit bitmap images. The next phase step was then programmed into Labview and the correct laser pulse time separation programmed before repeating the process.

For each set of measurements the temperature, atmospheric pressure and relative humidity inside the enclosure were measured with an Oregon Scientific atmospheric analyser. The typical conditions provide a speed of sound in air  $c = 345\text{ms}^{-1}$  and  $\rho_0 c = 405\text{Pa}\cdot\text{s}\cdot\text{m}^{-1}$ .

### 4.5.6 Processing

As described in section 3.3 the PIV data was processed in Matlab. For the four lowest sound levels each image was divided up into a grid of  $32\times 32$  pixel interrogation areas

for cross-correlation. Because the laser used limited the minimum time between images, the data for the highest sound level had to be processed using  $64 \times 64$  pixel interrogation areas to fulfil the requirements of equation 3.7. This results in a lower spatial resolution of velocity vectors in the PIV maps.

For each phase step  $t_i$ ,  $n = 30$  instantaneous vector fields  $\mathbf{u}_n(x, y, t_i)$ ,  $n = 1 \dots 30$  were produced. These were averaged for each phase step to give a phase-averaged vector field  $\mathbf{u}(x, y, t_i)$ . The typical standard error of the mean for the magnitude of  $\mathbf{u}(x, y, t_i)$  ranges from 1% for the lowest sound level studies to 5% for the highest.

Two sets of  $\mathbf{u}(x, y, t_i)$  were obtained for each geometry of tonehole and particular value of  $\bar{p}_{an}$ , one for the inside of the tonehole and one for the outside. These were ‘stitched together’ in Matlab to allow the whole velocity field around the tonehole to be viewed.

The vorticity of the velocity field was calculated in Matlab using a center difference operator to calculate the differentials [Raffel 98].

#### 4.5.7 Timing

The method of controlling the timing of the different phase steps captured using PIV was described in section 3.5. Figure 4.7 shows the resulting distribution of the phase steps  $i$  with respect to the acoustic velocity cycle. These data were obtained by taking the average of the magnitude of  $\mathbf{u}$  over  $x$  and  $y$  at a particular value of  $i$ , for the lowest value of  $\bar{p}_{an}$  for the square tonehole. This shows a slight phase lag compared with the timing scheme outlined in section 3.5.  $i = 1$  does not coincide with the zero-crossing of the acoustic velocity and the velocity minimum now occurs between  $i = 5$  and  $i = 6$ . The cause of this discrepancy is the approximate nature of the phase-shift adjustment procedure outlined in section 3.5.

Figure 4.7 explains the terminology used in chapters 5 and 7. *Suction* describes the period when the oscillating flow is directed into the tonehole, in the direction of the loudspeaker. *Ejection* describes the period when the oscillating flow is directed out of the tonehole.

## 4.6 Reverberation Chamber Measurements

An experiment was carried out in the University of Edinburgh reverberation chamber to obtain quantitative data concerning the power lost from the clarinet model system over the range of  $\bar{p}_{an}$  covered by the PIV experiments. The model’s loudspeaker was driven by a single frequency sine wave of 180Hz generated using the same apparatus as described above. The time-averaged AC power driving the loudspeaker  $P_{ls}$  was obtained

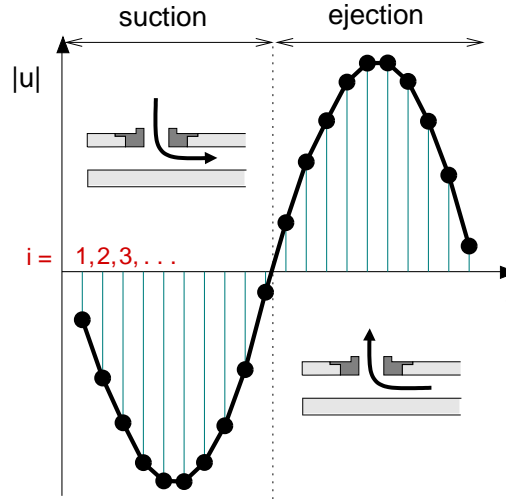


Figure 4.7: Points in acoustic velocity cycle at which PIV measurements are made,  $t_i$ .

by measuring the RMS voltage across the loudspeaker terminals and the RMS current being drawn using Labview for a given input voltage. At the same time,  $\bar{p}_{an}$  was measured using the PCB transducer. The loudspeaker end of the system was situated in a room adjacent to the reverberation chamber. The main tube of the model passed through a hole in the wall, such that the tonehole section of the model was inside the chamber.

Inside the reverberation chamber, a Brüel and Kjær 4133 half-inch free-field microphone was used to record the sound field. This was used with a Brüel and Kjær 2669 pre-amplifier and a Brüel and Kjær Nexus conditioning amplifier. Calibration was performed with a Norsonic Nor1253 half-inch microphone calibrator. The 4133 microphone was used to measure the RMS sound pressure inside the chamber  $\bar{p}_{rad}$ . Making the approximation that the sound field inside the reverberation chamber is completely diffuse, it is possible to calculate the sound power radiated by the model

$$P_{rad} = \frac{\bar{p}_{rad}^2 A_{ch}}{4\rho_0 c} \quad (4.6)$$

where  $A_{ch}$  is the total sound absorption of the chamber in metric sabins [Kinsler 00]. If the assumption is made that air absorption can be neglected (due to the low volume

of the chamber and the low frequency of the sound) then  $A_{ch}$  is given by

$$A_{ch} = \frac{0.161V_{ch}}{T_{ch}} \quad (4.7)$$

where  $V_{ch}$  is the volume of the chamber and  $T_{ch}$  is the reverberation time [Kinsler 00]. Therefore

$$P_{rad} = \frac{0.04\bar{p}_{rad}^2 V_{ch}}{\rho_0 c T_{ch}}. \quad (4.8)$$

Values for  $V_{ch}$  and  $T_{ch}$  at 125Hz were obtained from another study which used the reverberation chamber [Merchant 08].

A power efficiency for the system was constructed using the input electrical power and the output acoustical power:

$$G = \frac{P_{rad}}{P_{ls}}. \quad (4.9)$$

This is expressed as a percentage.

All signals were recorded as 2 second, 40kHz samples into Labview and analysed in Matlab. After being high-pass filtered the RMS value was calculated. The uncertainty in the RMS value was obtained by dividing the sample into 25 sections, taking the RMS value of each and calculating the standard error of the mean.



## Chapter 5

# PIV Applied to Oscillating Flow Around a Model Tonehole

### 5.1 Introduction

This chapter seeks to examine the differences between a clarinet model incorporating a square edged tonehole and one incorporating an undercut tonehole. Two approaches are used. Firstly, the flow around each tonehole has been visualised, and the velocity and vorticity measured, using PIV. The majority of this chapter is given over to describing and comparing the main PIV results. Secondly, the results are given for the experiments conducted on the model in a reverberation chamber, examining the radiated acoustic power and frequency spectra.

### 5.2 Background

#### 5.2.1 Visualisation

The presence and behaviour of local non-linear flow effects at discontinuities in tubes during acoustic oscillation have been observed in several different studies. The main discontinuities which have been studied are orifices (inside or at the end of tubes), tube terminations and nozzles.

Rayleigh [Rayleigh 45] observed air currents generated outside a small hole in a Helmholtz resonator under excitation with the aid of a candle flame. Ingard and Labate [Ingard 50] used smoke particles and a light sheet to visualise the flow around an orifice inside a tube. They found that the strength of jets and vortices could be characterised by four distinct regions, and that these were dependent on the acoustic velocity, the geometry of the orifice and the excitation frequency.

The schlieren method was used by Disselhorst and van Wijngaarden [Disselhorst 80] to image the flow around one edge of a sharp termination of a tube at high acoustic Strouhal number. The termination was made rectangular to allow the flow inside the tube to be viewed. It was found that a vortex was formed on the inside of the termination during the suction phase which was then expelled from the tube during the ejection phase. Smith and Swift [Smith 03] took schlieren images of the flow outside the termination of a tube with round edges at low Strouhal number. These show outward-rotating vortices forming at either side of the termination during ejection, which are then shed from the end of the tube.

PIV has been used to examine non-linear flow phenomena outside the open ends of tubes during acoustic excitation at the resonance frequency [Rockliff 02a, Skulina 05a]. Skulina used a range of different termination geometries, from sharp to having a radius of curvature of 4mm, and a range of acoustic velocities. He found that, apart from for the two extreme geometries, 3 distinct regimes were evident, depending on the radius of curvature and acoustic velocity. First, at low velocities, the flow could be approximately described as potential during both suction and ejection. Then, at higher velocities, during ejection the boundary layer separates from the end of the tube but reattaches to the outside of the tube. The result is a vortex ring forming around the end of the tube. These increase in size and vorticity with increasing acoustic velocity. During suction, the air is at first drawn most strongly into the tube near the walls. The inflow then becomes approximately diffuse. This is called the *vortex formation* regime.

At higher values of acoustic velocity the *vortex shedding* regime is reached. In this regime, during ejection a vortex ring appears around the end of the tube which is subsequently shed. It is also inferred that a vortex ring is formed inside the tube during suction, and this is expelled during ejection, having an opposite vorticity sign to the externally formed vortex ring. During suction, the jet associated with the external vortex shedding persists, so that, a certain distance away from the end of the tube, there is still outward moving flow, at the same time as air is being drawn into the tube. The values of acoustic velocity amplitude at which the vortex formation and vortex shedding regimes began were found to increase with the radius of curvature of the tube termination.

### 5.2.2 Acoustic properties

Rayleigh states that non-linear flow effects must drain energy from the acoustic wave and also affect the pitch of the resonator [Rayleigh 45]. The effects of local non-linear flow phenomena on the acoustic properties of the discontinuity at which they occur have been studied with a variety of experimental techniques. A number of studies using



impedance measurement techniques have found the resistive part of the impedance to increase with acoustic velocity amplitude [Sivian 35, Bolt 49, Ingard 50, Ingard 67, Disselhorst 80, Peters *et al* 93, Petculescu 02, Atig 03, Atig 04a, Skulina 05a]. Ingard and Labate [Ingard 50] found that the increased energy loss from the acoustic field could be accounted for by the energy required to generate and shed vortex rings at an orifice. It is generally found that the gradient of the resistance versus acoustic velocity graph is dependent on the geometry of the discontinuity: sharper geometries result in higher gradients [Disselhorst 80, Petculescu 02, Atig 03, Atig 04a, Skulina 05a]. Energy losses due to non-linear flow effects have been found to influence the loudest note sustainable on an artificially blown clarinet model [Atig 04b].

Some of the impedance studies also investigated the influence of non-linear flow effects on the reactance of the discontinuity [Sivian 35, Bolt 49, Ingard 67, Peters *et al* 93, Petculescu 02, Atig 03, Atig 04a]. The agreement on the behaviour of the reactance with respect to acoustic velocity amplitude is a lot weaker. Some studies find that it slightly decreases [Bolt 49, Ingard 67, Petculescu 02], others that it remains approximately constant [Sivian 35, Peters *et al* 93, Atig 03, Atig 04a].

Other studies have reported the generation of higher harmonics in the radiated spectra of tubes excited at a single frequency, due to non-linear flow effects at the discontinuity at the end of the tube [Ingard 67, Richards 82, Skulina 05a].

### 5.2.3 Toneholes

Local non-linear flow effects at side holes in tubes under acoustic excitation have been little studied. Keefe confirmed that for certain playing parameters, the Strouhal number around the toneholes of woodwind instruments could be less than one [Keefe 83]. In the same study, two clarinet bodies were constructed to be played with the same mouthpiece. One body had narrow, short toneholes such that  $2b = 6\text{mm}$  and  $t = 1.5\text{mm}$  (see figure 2.1). The other had wider, tall toneholes ( $2b = 9.5\text{mm}$ ,  $t = 9\text{mm}$ ). Both provided the same input impedance when measured at low sound levels, but when played, it was found to be very difficult to sustain a note on the body with narrow, short toneholes. The differences were attributed to local non-linear flow effects. As part of his study on clarinet tonehole undercutting, Greenham performed playing tests on three clarinets, one with square, non-undercut toneholes, one with toneholes undercut in the traditional manner with a fraise and one with a minimal amount of rounding on the internal tonehole edges [Greenham 03]. The non-undercut instrument was found to be the least easy to play, although it performed better when played at low sound levels and high frequencies (suggesting a dependence on Strouhal number). The undercut and rounded clarinets were judged to be better instruments.

Rockliff performed PIV measurements on the streaming flow outside the toneholes of a model flute [Rockliff 02a]. She found that the direction of the outward streaming jet was dependent on the acoustic velocity magnitude. A similar phenomenon was observed by Skulina et al, who were also able to view the flow inside the tube to see that jet driven streaming occurs there also [Skulina 05b]. Neither of these studies were able to view the flow inside the tonehole.

Dalmont et al performed impedance measurements using a two microphone technique on a tube with one open tonehole at high sound levels [Dalmont 02]. For the series impedance of the open hole, they found that the real part increased linearly with acoustic velocity amplitude, and that the constant of proportionality was not strongly dependent on the geometry of the tonehole. For the real part of the shunt impedance, they found a similar linear relationship, but with a strong dependence on the radius of curvature of the inner edge of the tonehole. A small radius of curvature resulted in a higher constant of proportionality than a large radius of curvature.

### 5.3 PIV Results

In this section, the PIV results for the square and undercut toneholes are given, obtained from the one open tonehole model described in section 4.2. The driving frequency is the fundamental resonance of the model, 180Hz. PIV measurements were performed at five values of  $\bar{p}_{an}$  (the RMS sound pressure measured at the pressure antinode of the tube) from approximately 200Pa to 1700Pa. The lower limit was imposed by the PCB transducer (see section 4.3). It is designed to measure high amplitude pressure fields and its voltage output becomes quantised at low levels. The upper limit on  $\bar{p}_{an}$  was dictated by the minimum time between pulses for the copper vapour laser, and hence the maximum measurable acoustic velocity using PIV (see section 3.5).

Table 5.1: Values of  $\bar{p}_{an}$ ,  $SPL_{an}$ ,  $\bar{u}_{an}$ ,  $St_b$ ,  $Re_\delta$  and musical dynamic level used in the PIV experiments.

Level	$\bar{p}_{an}$ (Pa)	$SPL_{an}$ (dB)	$\bar{u}_{an}$ (ms <sup>-1</sup> )	$St_b$	$Re_\delta$	Dynamic level
1	214	141	1.4	2.6	15	-
2	457	147	3.1	1.2	33	<i>ppp</i>
3	744	151	5.0	0.7	54	<i>pp</i>
4	1084	155	7.2	0.5	78	<i>p</i>
5	1728	159	11.5	0.3	125	<i>mp</i>

The 5 values of  $\bar{p}_{an}$  used are given in table 5.1.  $\bar{p}_{an}$  was found to vary over the course of one set of PIV measurements, such that the maximum standard deviation was 3%.

The measurements made at nominally the same level measured on the oscilloscope were found to vary in actual value of  $\bar{p}_{an}$  when the recorded signal from the PCB transducer was analysed in Matlab. In the rest of this chapter the value measured for each tonehole is given, while Table 5.1 gives an average between the two. Also given is  $SPL_{an}$ , the sound pressure level derived from  $\bar{p}_{an}$ .

It is possible to approximate the RMS acoustic velocity at the velocity antinode (in the region of the tonehole)  $\bar{u}_{an}$  by assuming that no sound is radiated from the tube and assuming continuity of volume flow:

$$\bar{u}_{an} = \frac{\bar{p}_{an}}{\rho_0 c} \frac{S}{S_t}. \quad (5.1)$$

$\bar{u}_{an}$  for the 5 levels used is shown in Table 5.1. From this it is possible to derive the Strouhal number of the flow  $St_b$  from equation 2.47, using half the width of the tonehole  $b = 3.27\text{mm}$  as the characteristic length and  $\bar{u}_{an}$  as the characteristic velocity. Table 5.1 shows that, for all levels measured,  $St_b$  is of the order of or less than 1, suggesting that local non-linear flow effects will be evident. Equation 2.51 can be used to define the Reynolds number of the flow  $Re_\delta$  using  $\bar{u}_{an}$ . Even at the maximum value of  $\bar{p}_{an}$  Table 5.1 shows that  $Re_\delta$  is below the critical Reynolds number for the onset of turbulence in the bulk of the flow (see section 2.7.5).

Finally, Table 5.1 gives a musical dynamic level corresponding to each of the values of  $\bar{p}_{an}$ . These were approximated from a short experiment in which the PCB transducer was mounted into the mouthpiece of clarinet which was played at a range of dynamic levels. It can be seen that the PIV experiment limits the study to the lower half of the musical dynamic range of the clarinet.

With 5 sound levels for each geometry, 200 PIV maps were generated and it is impractical to include all of these here. Instead, maps from the most informative points in the acoustic cycle for each level and geometry are included in figures 5.1 to 5.10 (starting on page 62). All 200 maps are available on the accompanying CD.

To explain the way the PIV data are presented, take figure 5.1 (c) as an example. The upper, large map shows in detail the flow around the tonehole, which is shown in grey. Below the tonehole is the main bore of the tube, with the loudspeaker situated to the right. Above the tonehole is the outside of the tube. In the  $x$  direction, the origin is defined as halfway across the tonehole's width. In the  $y$  direction, the origin is defined as the bottom of the tonehole. The upper map will be referred to as the *vector map*.

To ascertain the magnitude of the velocity vectors, a reference vector is shown in the top right corner. The point in the acoustic cycle,  $i$ , which the map describes is shown in the inset plot at (-6,4). PIV measurements are made at 20 equally spaced

points in the acoustic cycle.  $i$  has integer values between 1 and 20. The inset graph is obtained by plotting the average  $y$  velocity through a horizontal line exactly halfway up the tonehole for each of the 20 phase steps. By looking at figures 5.1 to 5.10 it can be seen that there are slight phase shifts in the acoustic cycle plots for each PIV data set. The exact cause of this is unknown, but is probably related to the complexity of the flow halfway up the tonehole due to local non-linear flow effects. It means that, for instance, the maximum of the ejection cycle occurs at  $i = 16$  for  $\bar{p}_{an} = 207\text{Pa}$  for the square tonehole (figure 5.1 (f)) and at  $i = 17$  for  $\bar{p}_{an} = 222\text{Pa}$  for the undercut tonehole (figure 5.6 (c)). Therefore, in comparisons between different sets of PIV data equivalent points in the acoustic cycle may have different values of  $i$ . The terms *suction* and *ejection* were explained in figure 4.7.

In the bottom left of the figure is the *vorticity map* corresponding to the vector map, along with a colour bar. A positive vorticity describes an anti-clockwise rotation. The *velocity magnitude map* is shown in the bottom right of the figure. The velocity magnitude map also shows streamlines of the flow in black and magenta. These are generated at the positions of the major discontinuities in the flow using the Matlab streamline function. These streamlines must be interpreted cautiously because a particle in the flow will not travel the distance indicated by them. A particle in the flow will only travel roughly the acoustic particle displacement along the streamline. This will be dictated by the acoustic velocity at the origin of the streamline. The streamlines shown are still useful however for giving a sense of the localised path of particles at a particular location in the flow. Ideally each streamline would be given the length of its acoustic particle displacement, but there was insufficient time to implement this in Matlab.

In all three maps the scaling (reference vector, vorticity and velocity magnitude colour range) is dictated by the point in the cycle of maximum velocity for the particular value of  $\bar{p}_{an}$  (usually  $i = 16$ ). The scaling is chosen to make the maps clear for the point in the acoustic cycle of maximum velocity, and this scaling is maintained for all of the other points in the cycle.

The PIV measurements of the external and internal flow data were made at different times, and the two sets of data ‘stitched together’ in Matlab. For some of the measurements, this resulted in a discontinuity at the point where the two sets of data are joined. An example of this is figure 5.2 (a) where the discontinuity can be seen at around  $y = 8\text{mm}$ . It is most clearly visible in the velocity magnitude map. Three possible causes of the discontinuity are proposed:

- Different values of  $\bar{p}_{an}$  being used in the two sets of data. This was monitored with an oscilloscope and caution was taken to ensure consistent values of  $\bar{p}_{an}$  were

used. However, as noted above, there was a considerable standard deviation in  $\bar{p}_{an}$  for a set of measurements.

- Different atmospheric conditions. These would lead to different values  $\rho_0 c$  and hence different values of  $\bar{u}_{an}$  for the same value of  $\bar{p}_{an}$ .
- Air currents inside the PIV enclosure.

While the presence of the discontinuity is not ideal, this way of presenting the data is more concise and informative than presenting the internal and external data separately.

Firstly, the PIV data for the square tonehole are examined, observing how the flow changes with increasing  $\bar{p}_{an}$ . The undercut tonehole data at corresponding values of  $\bar{p}_{an}$  are then compared.

### 5.3.1 Square tonehole - level 1

Figure 5.1 consists of PIV maps which show the development of the flow over the acoustic cycle for  $\bar{p}_{an} = 207\text{Pa}$ . Figure 5.1 (a) is taken at  $i = 20$ , the zero-crossing before the suction phase begins. As expected, there is very little motion evident in any of the three maps. The flow approximately halfway through the acceleration part of the suction phase ( $i = 3$ ) is shown in figure 5.1 (b) (the terms *suction* and *ejection* have been defined in section 3.4). The vector map shows that the flow is drawn into the tonehole in an approximately diffuse, sink-like manner, and that inside the tonehole it is parallel with the walls. At the bottom of the tonehole the flow is drawn to the right, in the direction of the loudspeaker, as it enters the main tube.

Inside the main tube there are large magnitude velocity vectors on the loudspeaker side of the tonehole. To the left of the tonehole the velocity magnitude of the flow is approximately zero. This is a consequence of the high pass filter behaviour of the tonehole. At this excitation frequency the power transmission coefficient for the main tube is  $\mathcal{T} \simeq 0.02$  (from equation 2.41). The majority of the flow energy is therefore reflected back along the main tube or transmitted into the tonehole. At higher excitation frequencies it is expected that greater velocity magnitudes would be evident in the main bore flow to the left of the tonehole.

At this excitation frequency, the geometry that the tonehole presents during the suction phase can be described as a sudden contraction, followed by a sudden expansion which is combined with a bend. The exact flow conditions would be impossible to recreate with a steady flow. The Strouhal number of the flow at this level is of the order of 1 so the quasi-steady flow approximation is not applicable. A comparison with steady flow is valid only at localised areas in the flow, over the distance of the acoustic

displacement at that point in the cycle. For example, in figure 5.1 (b), at the lower-right corner of the tonehole (4,0) there is a region of higher velocity. This is expected at the inside corner of a sharp bend in a pipe for steady flow even at low flow velocities (see section 2.7.2).

The vorticity map for figure 5.1 (b) shows regions of vorticity confined to just beside the walls. Using equation 2.50, the boundary layer thickness should be  $\sim 0.1\text{mm}$ . The region of vorticity on the left wall of the tonehole is  $\sim 0.6\text{mm}$  thick. This artificially thick boundary layer is caused by the finite resolution of the PIV data. Also, poor PIV data caused by glare close to the wall can lead the PIV processing to produce false zero-velocity vectors. These result in false areas of vorticity separated from the wall. An example of this can be seen close to (5,9) in the vorticity map for 5.1 (b). Vorticity data near the walls must therefore be interpreted cautiously.

Figure 5.1 (c) shows the flow for  $\bar{p}_{an} = 207\text{Pa}$  at the maximum of suction,  $i = 6$ . Again there is the high velocity region at the inside corner (4,0). There are now also two high velocity regions at  $(\pm 3, 7)$ , although not of the same magnitude or extent as that at (4,0). The streamlines do not show clear evidence that boundary layer separation has taken place, such as a vena-contracta.

Figure 5.1 (d) is taken from the deceleration part of the suction phase ( $i = 9$ ). It is interesting to notice that, even though the overall velocity of the main flow is lower than in (b), boundary layer separation is clearly occurring at (4,0), indicated by the bulge in the streamlines and the enlarged area of vorticity at this point. The explanation for this is that during the accelerating part of the cycle the acceleration of the flow counteracts the adverse pressure gradient caused by the sudden expansion of the main tube. As the flow slows down, the deceleration imposed by the loudspeaker and that caused by the geometry are combined, leading to boundary layer separation.

The accelerating part of the ejection phase ( $i = 13$ ) is shown in figure 5.1 (e). The sign of the vorticity has reversed. Again the corner at (4,0) is the site of a high velocity area. Overall, the form of the streamlines is similar to figure 5.1 (b). This suggests that, for this  $\bar{p}_{an}$ , during the accelerating part of both suction and ejection the flow is close to potential. Figure 5.1 (f) shows the maximum of the ejection phase,  $i = 16$ . The high velocity area at (4,0) has grown in magnitude and extent, but has not clearly separated. In figure 5.1 (g) ( $i = 18$ ) there is a slight vena-contracta at the location of the high velocity region, caused by the decelerating flow.

For  $\bar{p}_{an} = 207\text{Pa}$ , the flow is approximately potential for the majority of the acoustic cycle, with limited boundary layer separation and reattachment during the times when the flow is decelerating.

### 5.3.2 Square tonehole - level 2

The next highest value of  $\bar{p}_{an}$  studied is 452Pa. The significant developments from the  $\bar{p}_{an} = 207$ Pa flow are shown in figure 5.2. Figure 5.2 (a) shows how slight separation and reattachment now occurs at (4,0) during the accelerating part of the suction phase, as evidenced by the salient in the streamline as it travels around the corner. The maximum of suction (figure 5.2 (b)) shows a larger high velocity region at (4,0) than for  $\bar{p}_{an} = 207$ Pa. There is also now what appears to be a slight amount of boundary layer separation at (-4,0) although this is not clear from the streamlines. In the decelerating part of the suction phase (figure 5.2 (c)), the boundary layer separation is stronger at (-4,0). The streamline here is diverted to the left at this point as the separated shear layer attempts to reattach to the wall, as described in section 2.7.1. (4,0) shows a large separation but then a rapid reattachment, leading to an enclosed, circulating low velocity area. At the zero-crossing from suction to ejection (figure 5.2 (d)) some residual rotational motion is left at ( $\pm 4,0$ ), when the rest of the flow field is almost stagnant.

As the ejection phase begins, we see a slight vena-contracta effect as the flow enters the tonehole, as shown in figure 5.2 (e). By the time of maximum ejection, shown in (f), the separation and reattachment on the left side has disappeared, the flow being forced to the left by the larger separation occurring at (4,0). In (g), as the flow decelerates, there is, like in the suction phase, an area of slowly moving air between the jet and the wall at the bottom-right corner. A change from the  $\bar{p}_{an} = 207$ Pa case is that the flow at the top of the tonehole, at ( $\pm 4,8$ ), seems to have separated and reattached, as indicated by the enlarged areas of vorticity.

At  $\bar{p}_{an} = 452$ Pa the flow has departed from potential flow for most of the acoustic cycle, with clear boundary layer separation occurring at all corners of the tonehole at some point in the acoustic cycle.

### 5.3.3 Square tonehole - level 3

A selection of maps from  $\bar{p}_{an} = 760$ Pa are shown in figure 5.3. Figure 5.3 (a) is for  $i = 4$ . The most noteworthy feature is the uneven inflow at the top of the tonehole, with the flow being stronger near the walls than in the centre. This is also evident for certain geometries and flow velocities at the termination of a tube [Skulina 05a]. Figure 5.3 (b) ( $i = 6$ ) shows the formation of free shear layers at ( $\pm 4,0$ ). There is now also a slight vena-contracta forming around ( $\pm 4,7$ ). This remains visible as the flow decelerates (figure 5.3 (c)). Vortices develop at ( $\pm 4,0$ ), with the vortex at (-4,0) being more concentrated.

The ejection phase shows similar behaviour to that for  $\bar{p}_{an} = 452$ Pa (see figure 5.3

(d) and (e)). At  $i = 14$ , it is now the case that the vortices which developed at  $(\pm 4, 0)$  during the end of the suction phase have remained, and have been convected slightly into the tonehole.

Looking at the flow for  $i = 16$  in figure 5.3 (e), it is interesting to compare the length of the high velocity region formed at the bottom-right corner of the tonehole to the acoustic displacement amplitude  $\bar{d}_{an}$  calculated using equation 2.48 and  $\bar{u}_{an}$  from Table 5.1. For this level  $\bar{d}_{an} = 4.4\text{mm}$ . This roughly corresponds to the length of the high velocity region, and hence the free shear layer, formed at the bottom right corner, which stretches approximately halfway up the tonehole. This correlation can be observed at the other values of  $\bar{p}_{an}$  (see for instance figures 5.2 (f) and 5.5 (c)).

The main development during deceleration (see figure 5.3 (f)) is the appearance of coherent vortex structures at  $(\pm 4, 8)$ . These attached vortices have also been seen at the same part of the acoustic cycle for a tube termination [Skulina 05a].

The flow at  $\bar{p}_{an} = 760\text{Pa}$  contains many of the same features as the flow at  $\bar{p}_{an} = 452\text{Pa}$ , but with the addition of more coherent vortex structures. The flow behaviour at the top of the tonehole is similar to that observed at the end of tubes in the vortex formation regime.

### 5.3.4 Square tonehole - level 4

Figure 5.4 shows the flow for  $\bar{p}_{an} = 1067\text{Pa}$ . In figure 5.4 (a) we again see a non-diffuse inflow to the tonehole during suction ( $i = 4$ ). Above the tonehole there is an outward current centred around  $(-1, 14)$ . In comparison with  $\bar{p}_{an} = 760\text{Pa}$ , the inflow at  $i = 4$  has developed a distinct asymmetry around  $x = 0\text{mm}$ . At the upper-left corner of the tonehole, a much higher velocity is evident than at the upper-right corner. At  $i = 9$  a large vortex centred at  $(6, -2)$  has developed, while the small vortex formed at the bottom-left corner has been shed (see figure 5.4 (b)).

During ejection (figure 5.4 (c)), similar flow is visible at the bottom of the tonehole to that seen at the top of the tonehole during suction (figure 5.4(a)). We again see the asymmetry around the centre of the tonehole, with a large jet developing at the upper-left corner, but not at the upper-right (figure 5.4 (d)). This results in a larger vortex forming at  $(-5, 10)$  than at  $(5, 10)$  (figure 5.4 (e)). Looking again at figure 5.4 (a) for  $i = 4$ , we see that the vortex formed at  $(-5, 10)$  is shed, and it remains visible in proximity to the top of the tonehole in the early part of the suction phase.

The new developments at  $\bar{p}_{an} = 1067\text{Pa}$  are the asymmetry of the flow at the upper-left and upper-right corners of the tonehole leading to asymmetrical vortex shedding at the top of the tonehole which in turn causes the appearance of an outward flow above the tonehole when the main flow is being drawn into the tube. This outward flow is



typical of the vortex shedding regime for tube terminations [Skulina 05a].

### 5.3.5 Square tonehole - level 5

The highest value of  $\bar{p}_{an}$  measured using PIV for the square geometry was 1703Pa. The suction phase is broadly similar to that for  $\bar{p}_{an} = 1067\text{Pa}$ , with higher velocity magnitudes. As the cycle approaches the zero-crossing between suction and ejection, a very large vortex is visible centred at (6,-5) (figure 5.5 (a)). As the ejection phase begins (figure 5.5 (b)), this vortex remains.

The most significant development at  $\bar{p}_{an} = 1703\text{Pa}$  is that, during part of the ejection cycle, the shear layer generated at the lower-right corner of the tonehole no longer reattaches to the right-hand wall of the tonehole. This is shown in figure 5.5 (c). The result of this is that the vortex formed at the upper-left corner is much more significant than that formed at the upper-right (figure 5.5 (d)). This figure also shows that, late in the cycle, the upper-left vortex is shed and it forces the flow emerging from the tonehole to the right.

The flow for  $\bar{p}_{an} = 1703\text{Pa}$  for the square tonehole is similar to the flow for  $\bar{p}_{an} = 1067\text{Pa}$ , but with external vortex shedding occurring earlier in the acoustic cycle. It is also marked by the clear lack of reattachment of the jet within the tonehole during ejection.

### 5.3.6 Undercut tonehole - level 1

Figure 5.6 shows the flow over the acoustic cycle at the undercut tonehole for the lowest level of  $\bar{p}_{an}$ . This value of  $\bar{p}_{an}$  (222Pa) is slightly larger than that of the lowest level used for the square tonehole. This is due to the inaccuracy of setting  $\bar{p}_{an}$  during each measurement. From steady flow considerations, the undercut geometry should reduce the strength of non-linear flow effects at the bottom of the tonehole during suction and ejection by graduating the deceleration of the flow.

At this lowest sound level, the differences between the flow for the square and undercut toneholes are minimal. Figure 5.6 (a) shows that the flow for the undercut hole at the maximum of suction is very similar to that for the square case (figure 5.1 (c)). The high velocity flow around (4,0) has a slightly lower velocity magnitude. The decelerating part of the suction phase is also similar (see figures 5.6 (b) and 5.1 (d)), with a smaller, separation-reattachment bubble for the undercut geometry. The differences during the ejection part are likewise negligible, as shown in figures 5.6 (c) and (d), and 5.1 (f) and (g).

### 5.3.7 Undercut tonehole - level 2

The second level for the undercut tonehole is  $\bar{p}_{an} = 463\text{Pa}$ . Here, the differences from the square geometry become more apparent. Figure 5.7 (b), from the maximum of suction, shows a high velocity region which closely follows the geometry of the wall at (4,0), in contrast to the same point in the cycle for the square case (figure 5.2 (b)). The result is that, in figure 5.7 (c), during the decelerating part of the suction phase, the separation-reattachment salient at (4,0) is much smaller. The ejection phase for the undercut tonehole also shows no clear separation of the flow entering the tonehole at (4,0) (figure 5.7 (d) and (e), cf figure 5.2 (e) and (g)). There does appear to be a slight difference at the top of the tonehole when comparing the two geometries during the decelerating part of the ejection phase. There are larger areas of vorticity above the outside edges of the undercut tonehole. This could be explained by the slight difference in  $\bar{p}_{an}$  between the two sets of measurements. The vortex formation results in the non-diffuse inflow at the top of the tonehole during the start of the suction phase that is associated with the vortex formation regime (figure 5.7 (a)).

### 5.3.8 Undercut tonehole - level 3

For  $\bar{p}_{an} = 729\text{Pa}$  there is still no strong boundary layer separation at (4,0) throughout the whole acoustic cycle, as shown in figure 5.8, in contrast to the square geometry (figure 5.3). A small vortex appears at (-4,0) as the flow decelerates during suction (figure 5.8 (b)). The flow around the top of the tonehole is very similar to that for the square geometry throughout the acoustic cycle. It should be noted however that for level 3, the value of  $\bar{p}_{an}$  used in the undercut experiments is slightly less than that used for the square experiments.

### 5.3.9 Undercut tonehole - level 4

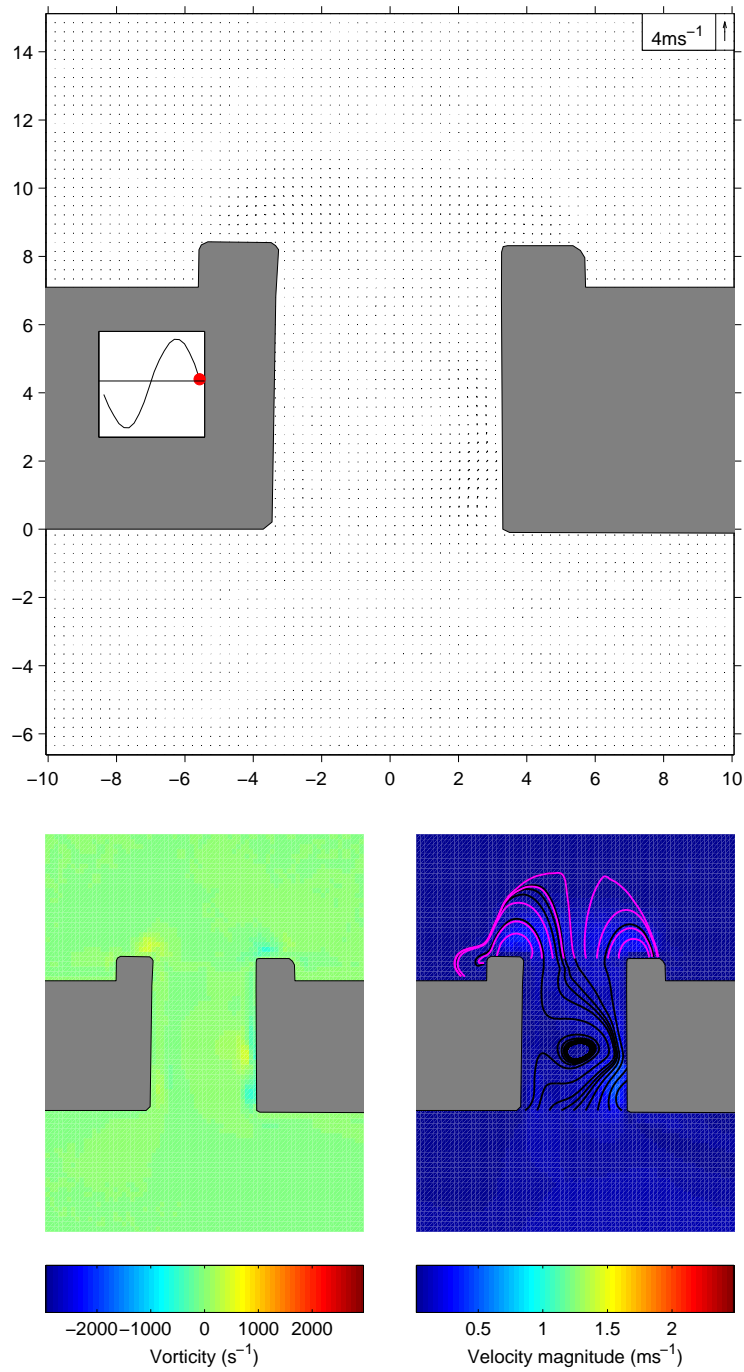
The flow at  $\bar{p}_{an} = 1101\text{Pa}$  for the undercut tonehole lacks the asymmetry between the top-left and top-right edges that was evident at the equivalent level for the square geometry (compare figure 5.9 to figure 5.4). Figure 5.9 (b) shows that significant boundary layer separation and reattachment occurs at the bottom-right corner when  $\bar{p}_{an} = 1101\text{Pa}$  for the undercut tonehole. Boundary layer separation and reattachment also occurs at this location during the ejection phase (figure 5.9 (c), (d) and (e)).

Like for the square geometry, a compact vortex is formed at (-4,0) during the suction phase, although, unlike for the square geometry it is not shed at this sound level (compare figures 5.9 (b) and 5.4 (b)). Figures 5.9 (c) and 5.4 (c) show very different flow behaviours around (-4,0) for the accelerating part of the ejection cycle.

The square corner shows a large high velocity region that is not evident in the undercut case. This can be explained by the shed vortex from the end of the suction cycle that is forcing the flow into a narrow stream around the square corner.

### 5.3.10 Undercut tonehole - level 5

The flow behaviour at  $\bar{p}_{an} = 1753\text{Pa}$  for the undercut tonehole is quite similar to that for the square tonehole at the equivalent sound level, but it still does not display the asymmetry across the line  $x = 0\text{mm}$ . During the decelerating part of the suction phase a vortex forms at  $(-4,0)$  which is shed at around  $i = 11$ , as shown in figure 5.10 (a). At the same phase step, the vortex formed at the square tonehole has been convected considerably further (see figure 5.5 (a)). The main feature at this sound level for the square geometry is that the free shear layer formed during ejection at  $(4,0)$  does not reattach to the right-hand wall inside the tonehole. At the maximum of ejection here, figure 5.10 (b), we seem to have a similar phenomenon, although the high velocity regions at  $(-4,9)$  and  $(4,9)$  are much more even than in the square tonehole case. This is borne out by the flow later in the cycle. Figure 5.10 (c), for  $i = 19$  shows two vortices being formed at the top of the tonehole. For the square geometry at this point in the cycle (figure 5.5 (d)) the left-hand vortex is far more dominant and it has been convected a greater distance from the tonehole.



(a) Square tonehole,  $\bar{p}_{an} = 207\text{Pa}$ ,  $i = 20$

Figure 5.1: PIV data for the square tonehole at  $\bar{p}_{an} = 207\text{Pa}$ .

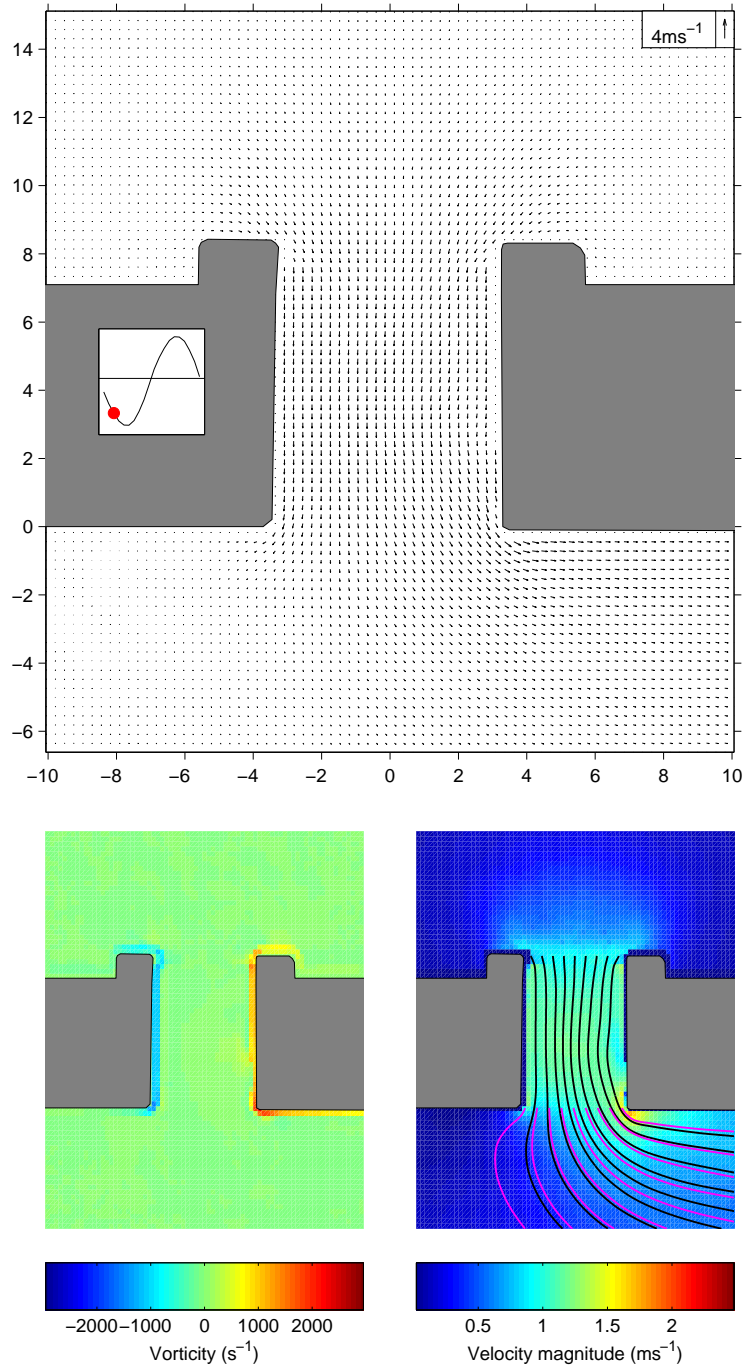
(b) Square tonehole,  $\bar{p}_{an} = 207\text{Pa}$ ,  $i = 3$ 

Figure 5.1 continued.

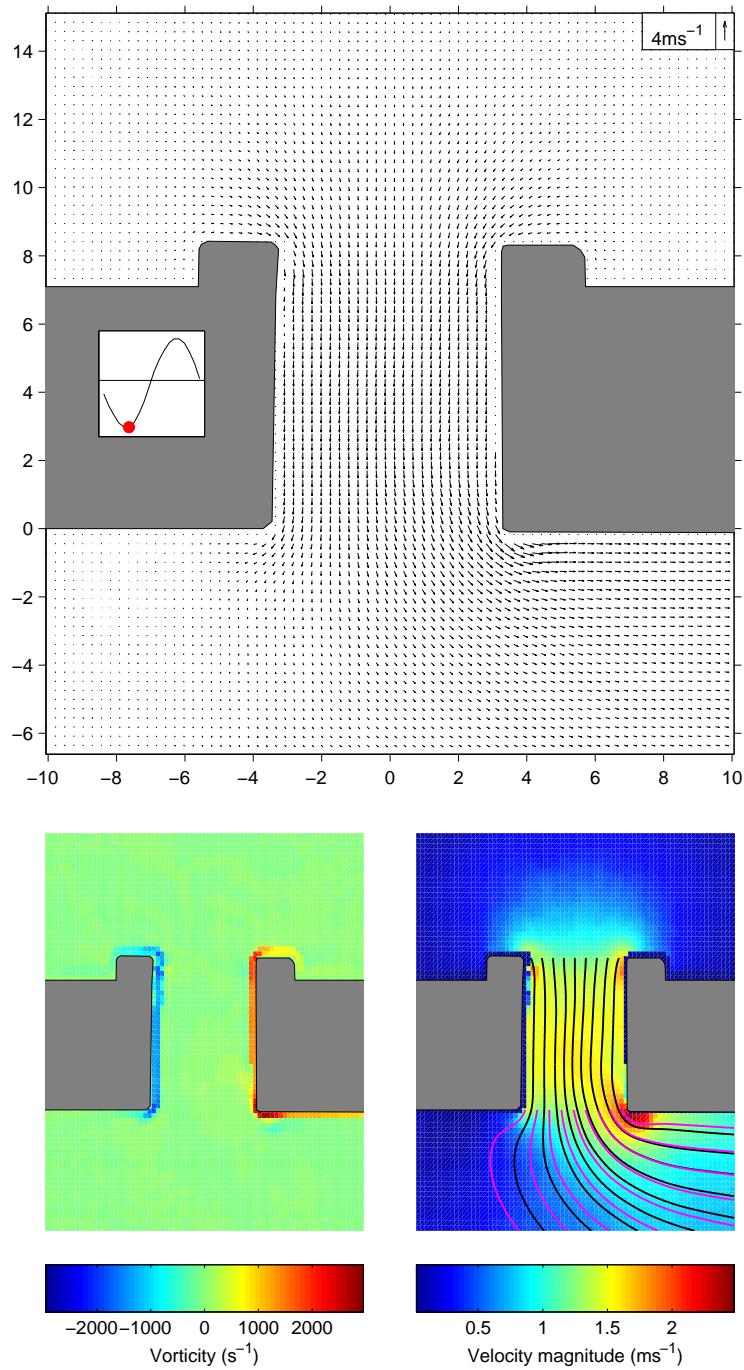


Figure 5.1 continued.

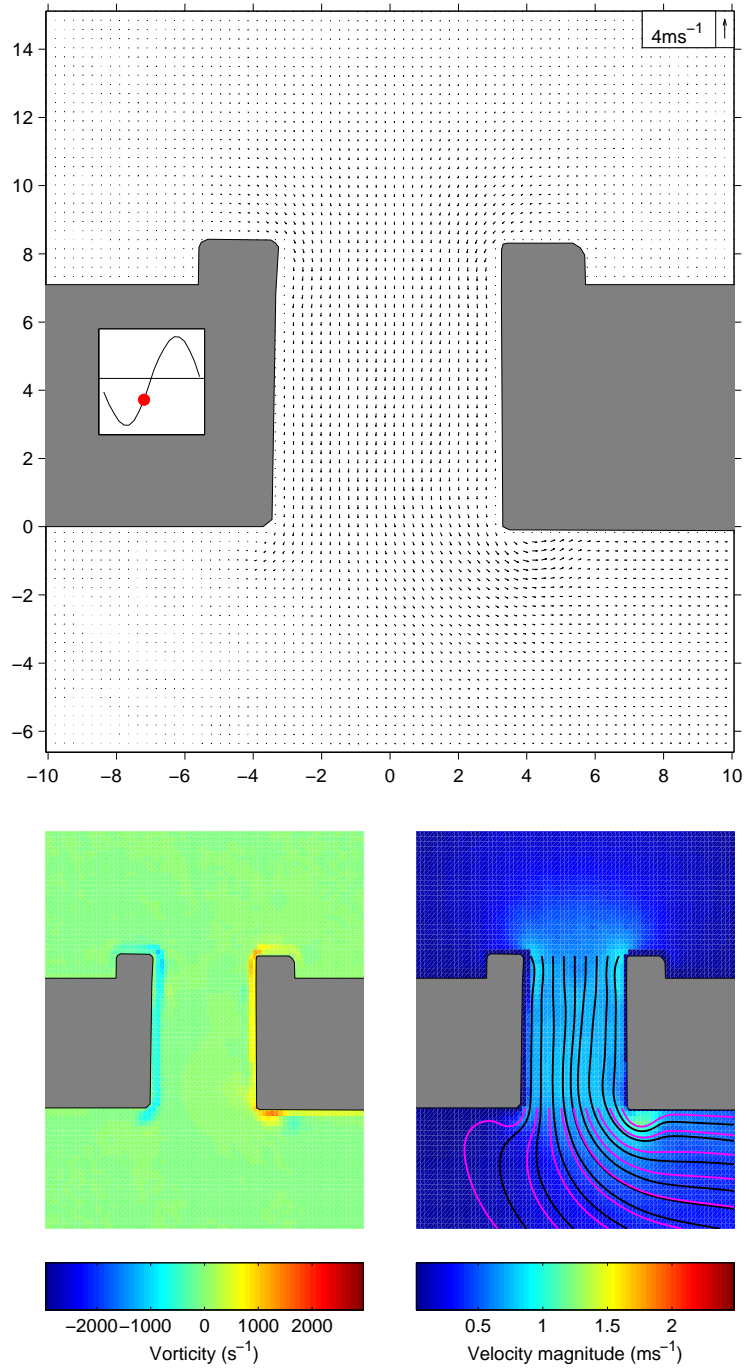
(d) Square tonehole,  $\bar{p}_{an} = 207\text{Pa}$ ,  $i = 9$ 

Figure 5.1 continued.

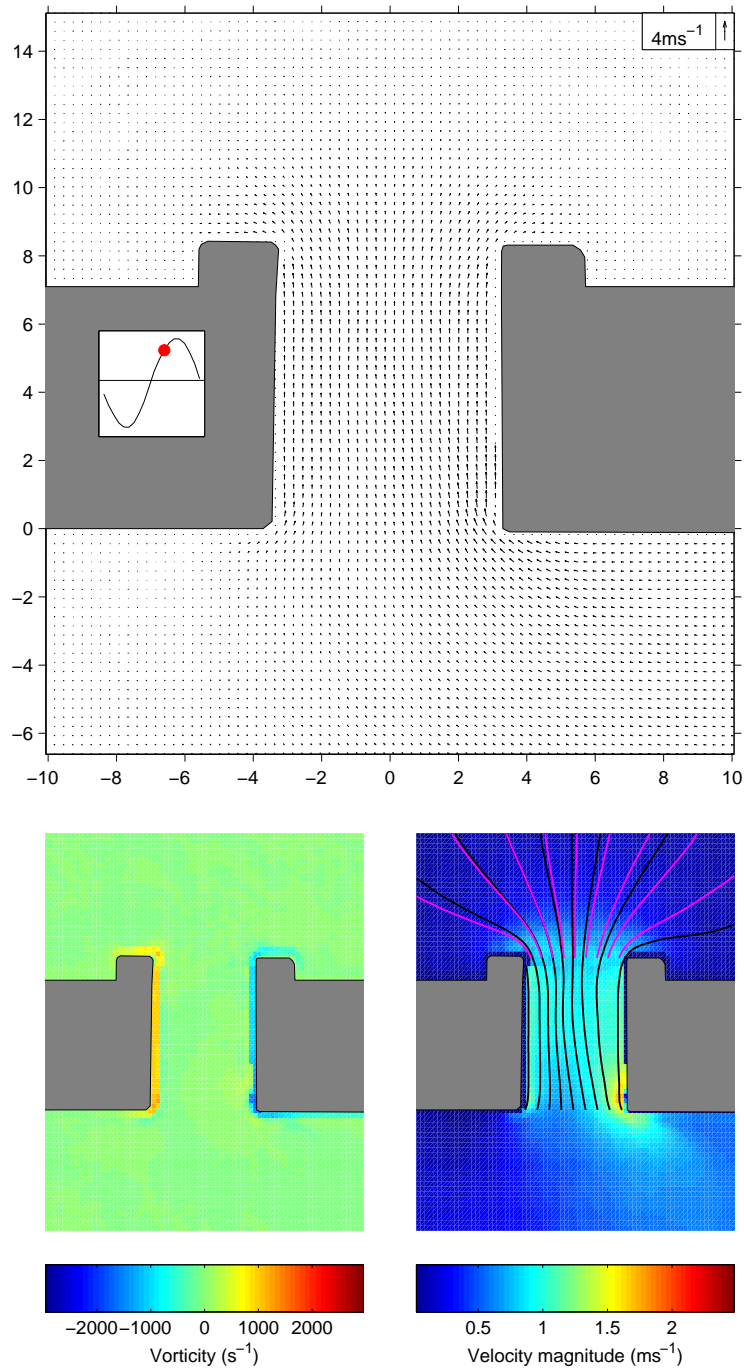
(e) Square tonehole,  $\bar{p}_{an} = 207\text{Pa}$ ,  $i = 13$ 

Figure 5.1 continued.



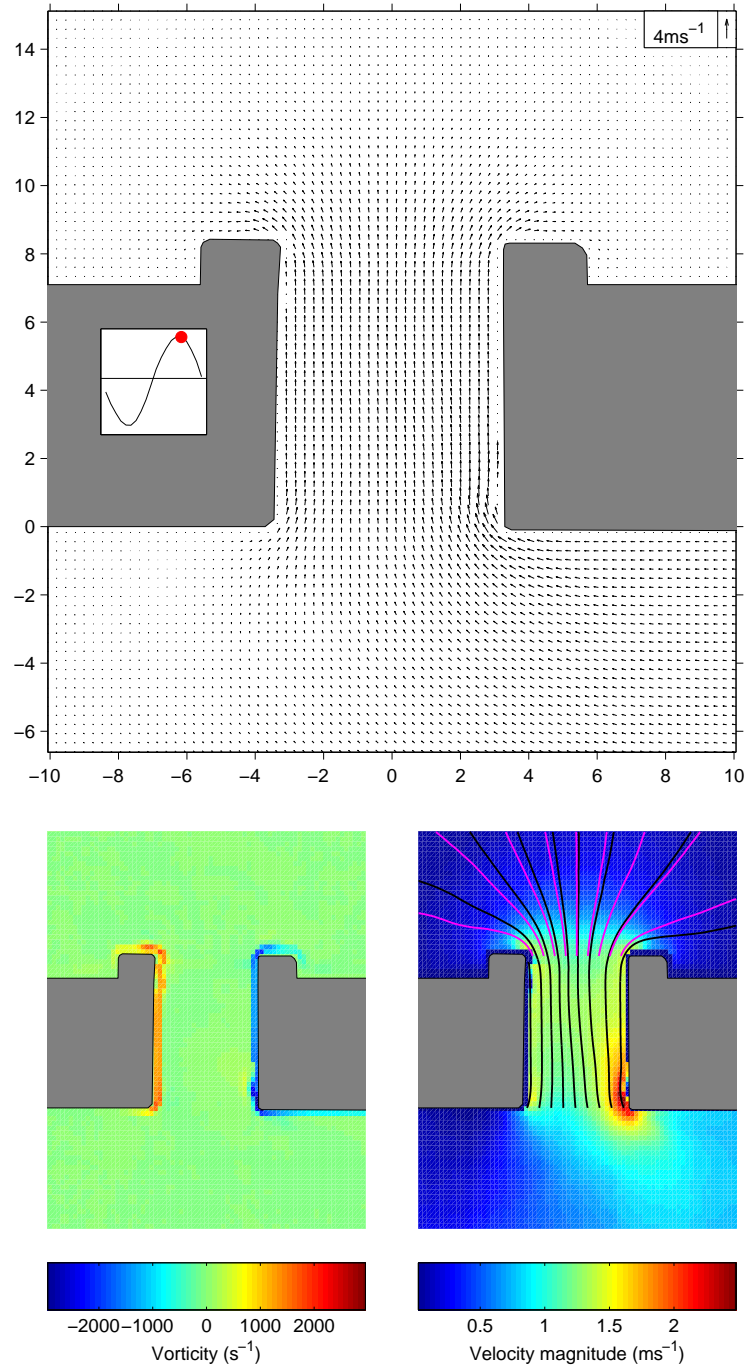
(f) Square tonehole,  $\bar{p}_{an} = 207\text{Pa}$ ,  $i = 16$ 

Figure 5.1 continued.

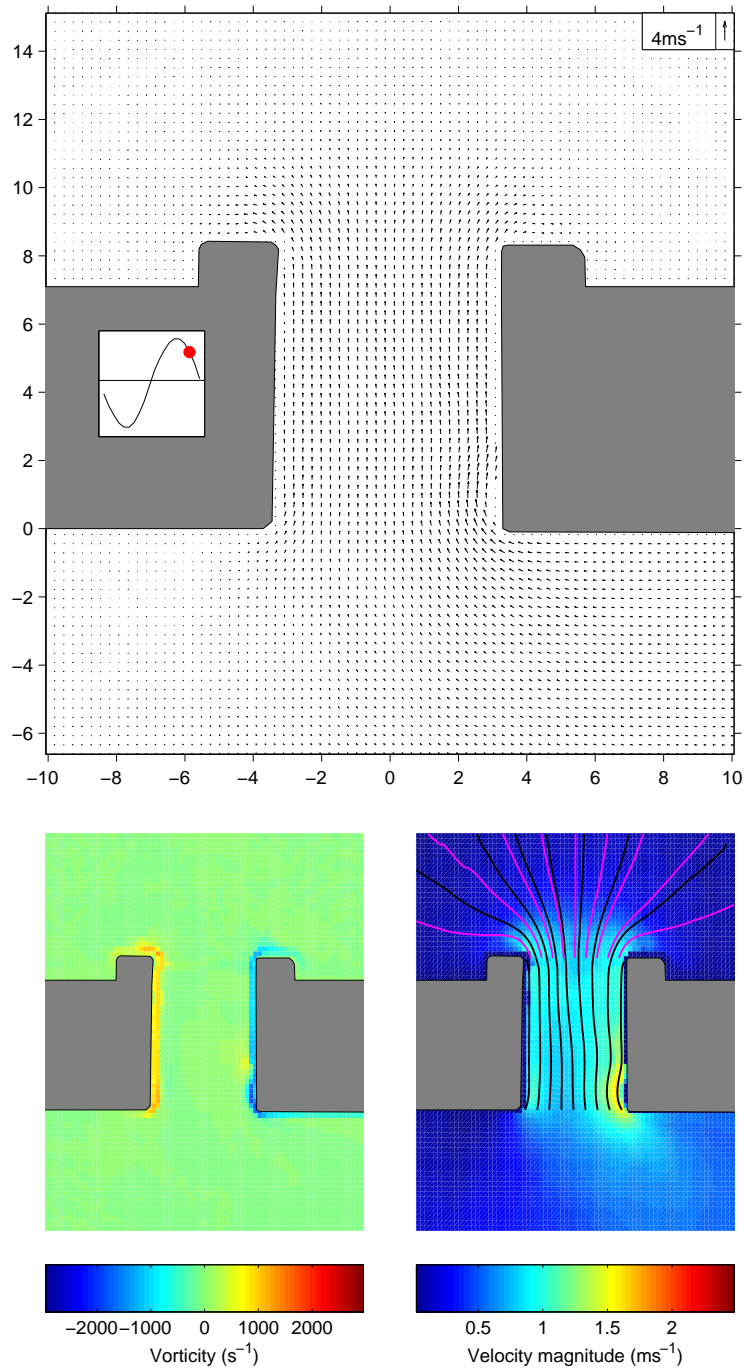
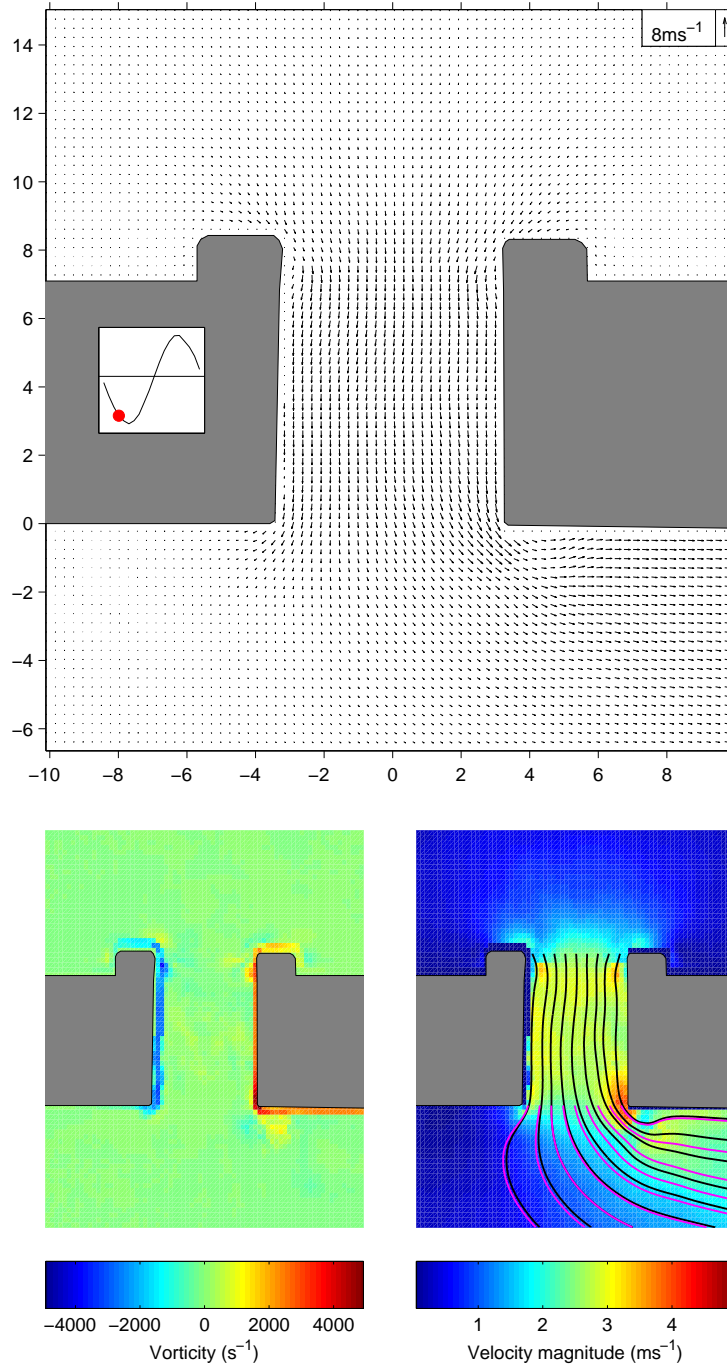
(g) Square tonehole,  $\bar{p}_{an} = 207\text{Pa}$ ,  $i = 18$ 

Figure 5.1 continued.

(a) Square tonehole,  $\bar{p}_{an} = 452\text{Pa}$ ,  $i = 4$ Figure 5.2: PIV data for the square tonehole at  $\bar{p}_{an} = 452\text{Pa}$ .

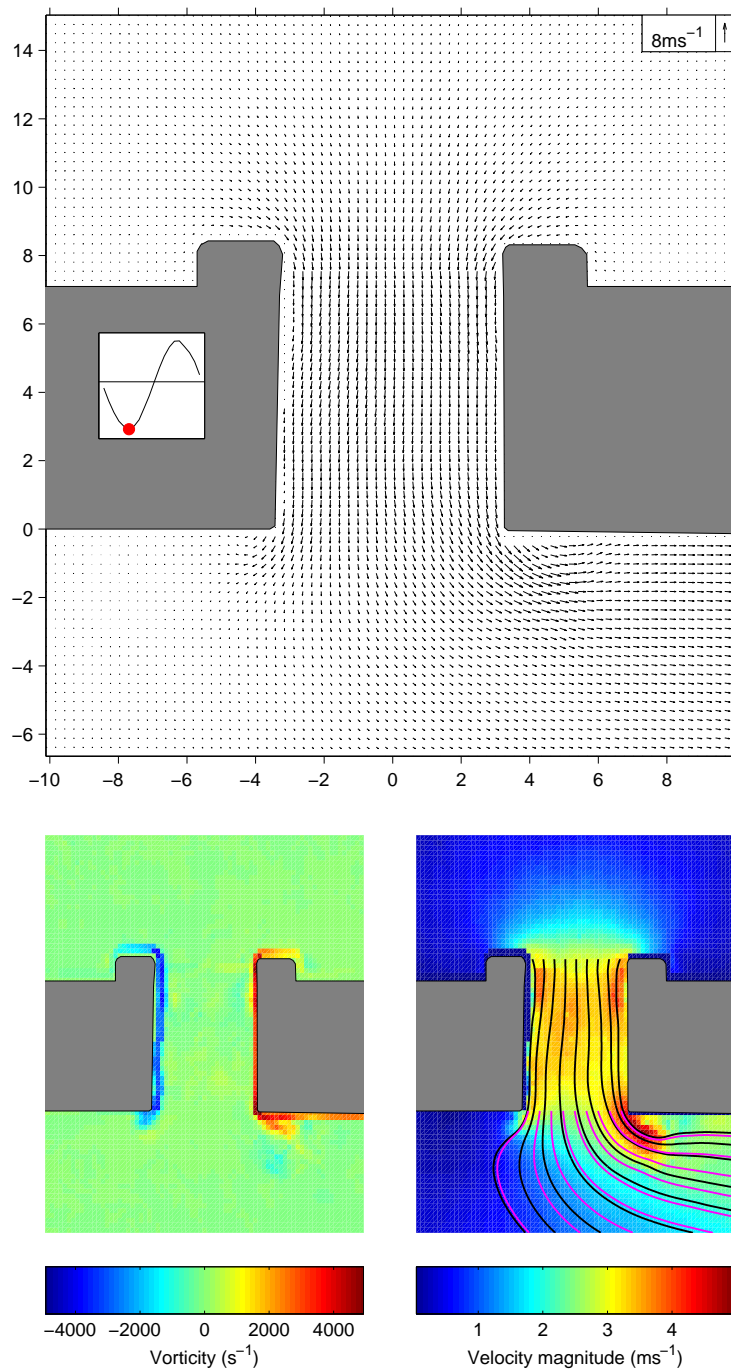


Figure 5.2 continued.

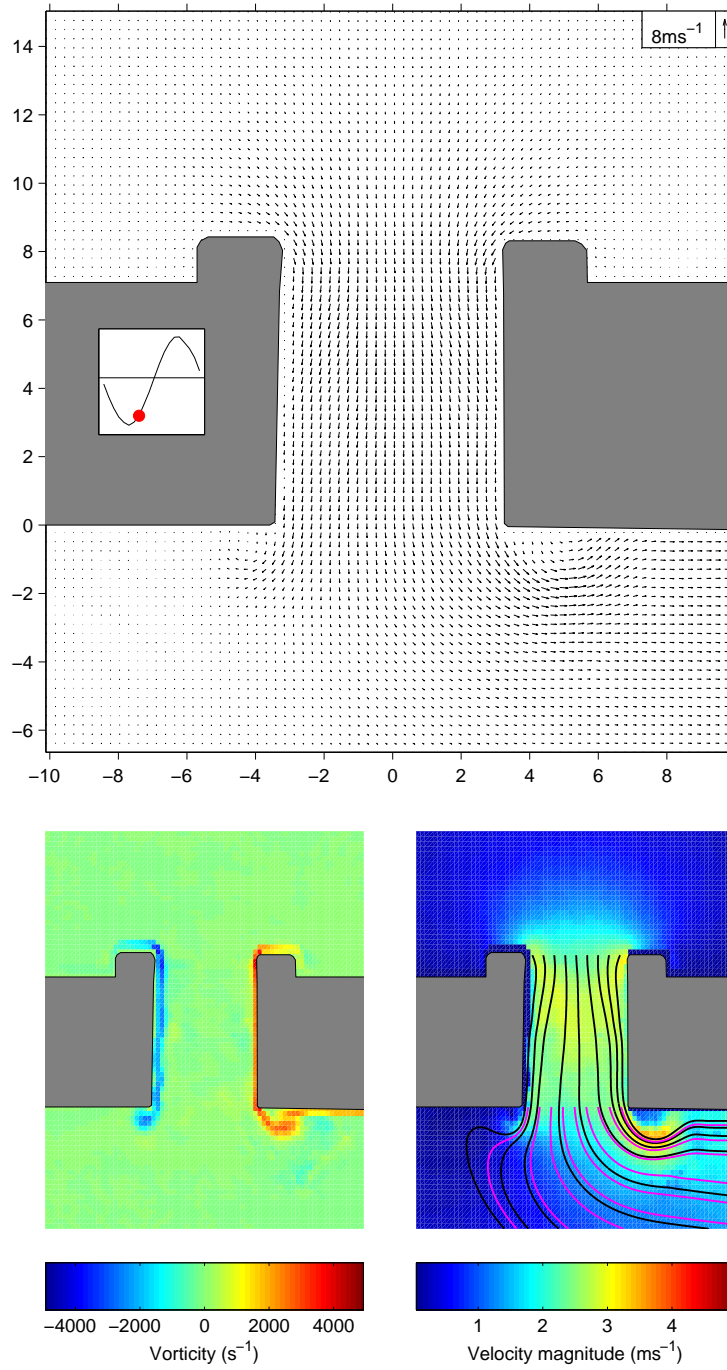
(c) Square tonehole,  $\bar{p}_{an} = 452\text{Pa}$ ,  $i = 8$ 

Figure 5.2 continued.

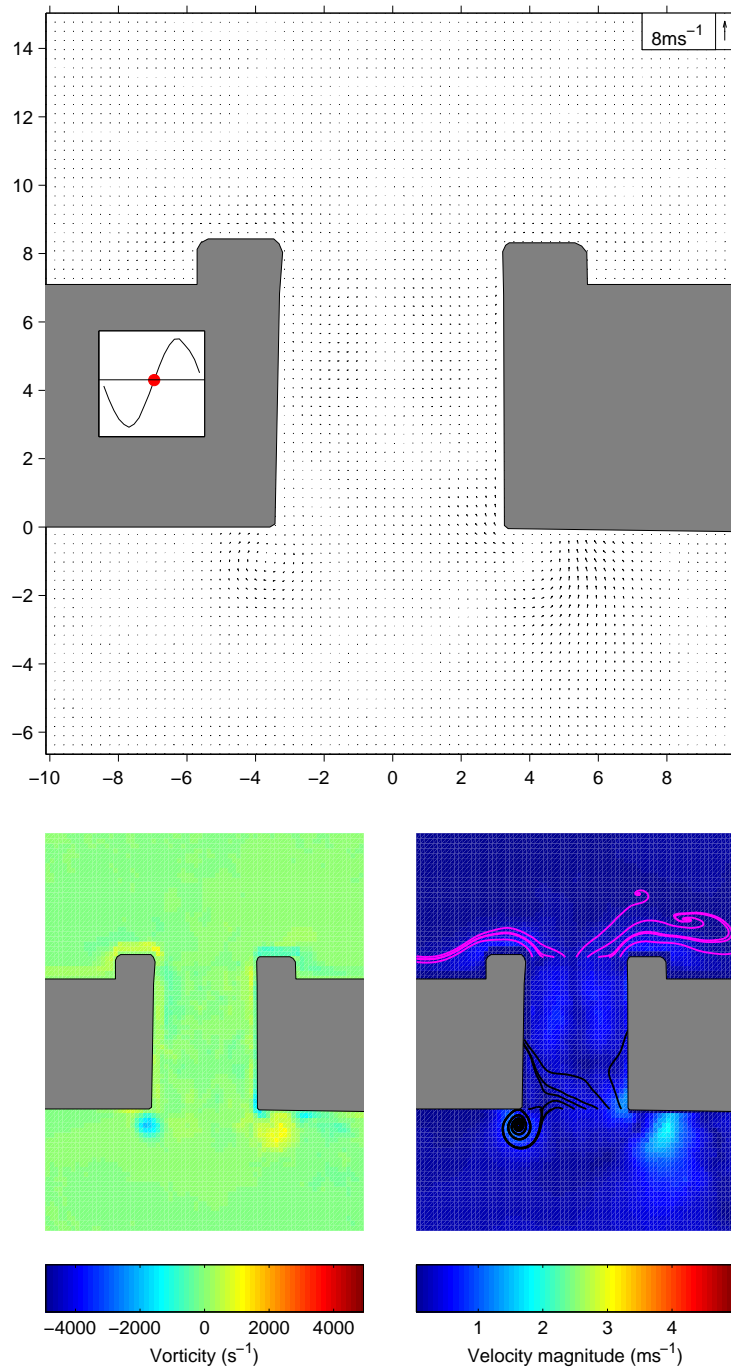
(d) Square tonehole,  $\bar{p}_{an} = 452\text{Pa}$ ,  $i = 11$ 

Figure 5.2 continued.

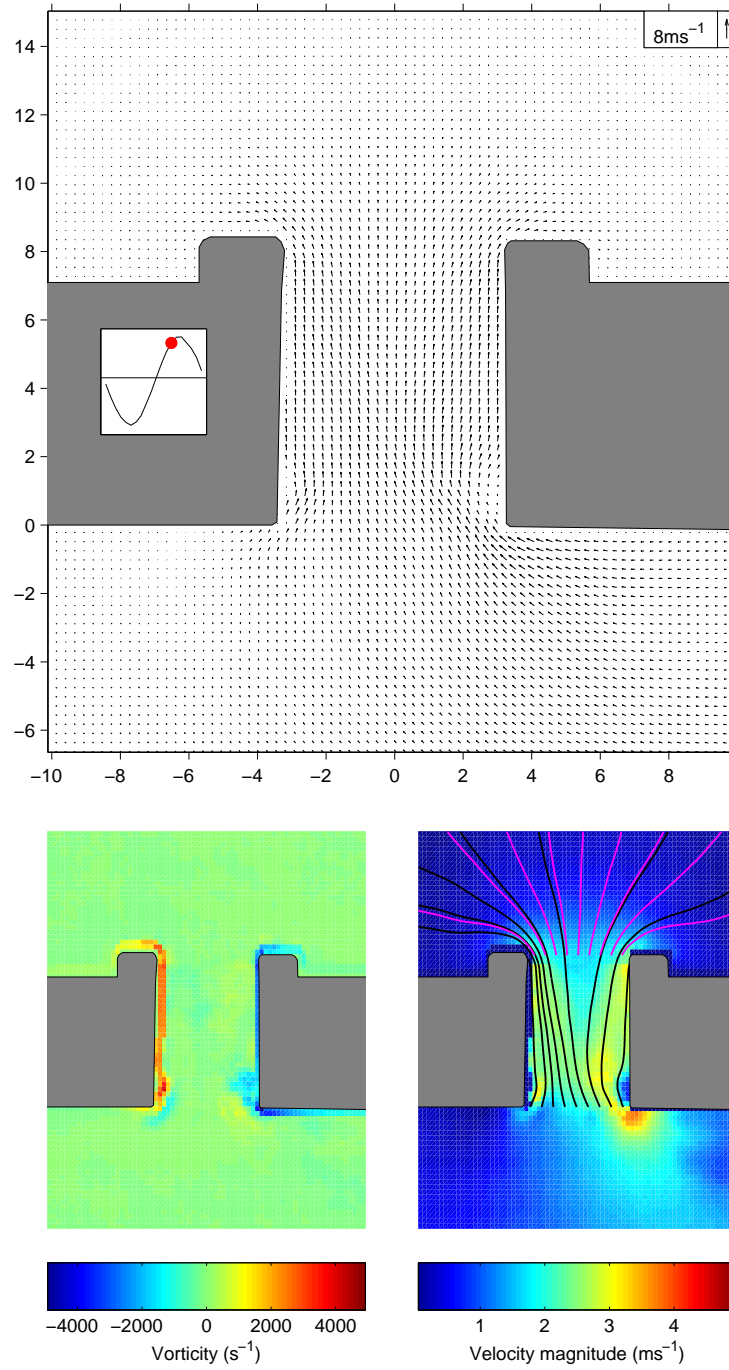
(e) Square tonehole,  $\bar{p}_{an} = 452\text{Pa}$ ,  $i = 14$ 

Figure 5.2 continued.

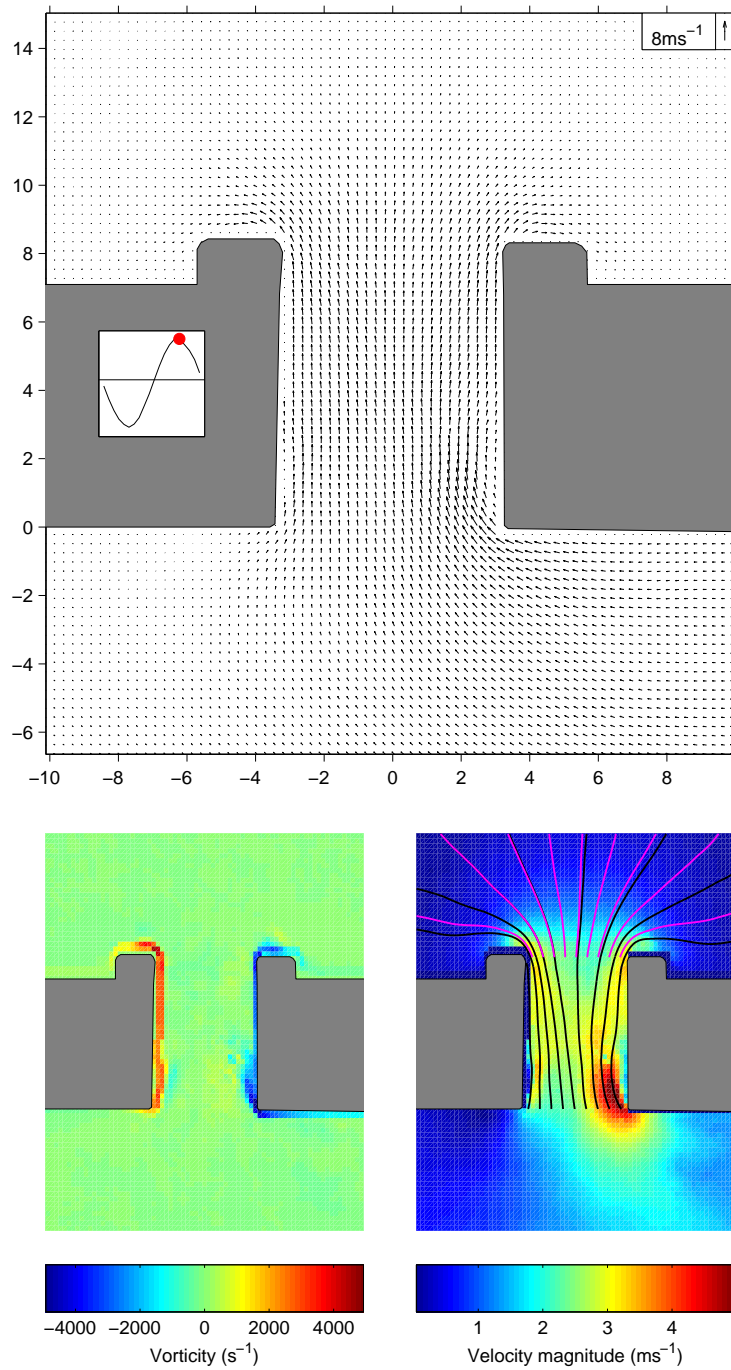
(f) Square tonehole,  $\bar{p}_{an} = 452\text{Pa}$ ,  $i = 16$ 

Figure 5.2 continued.



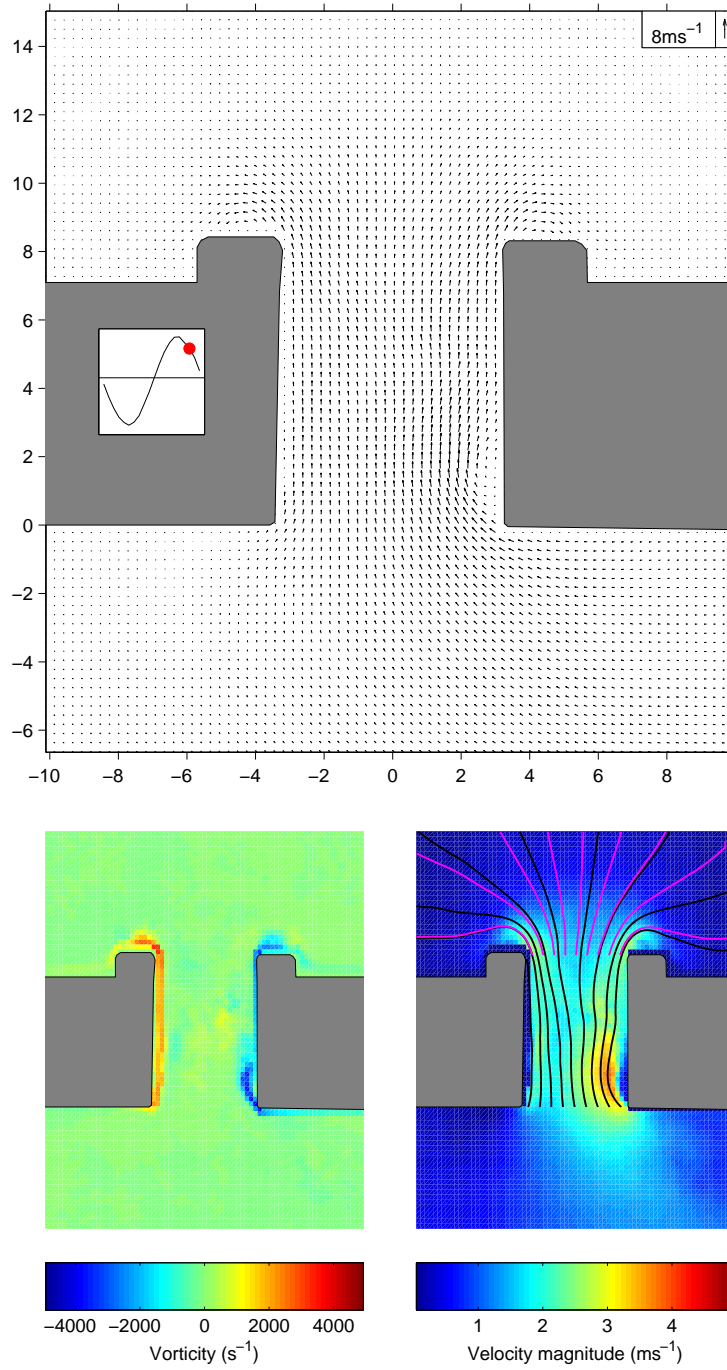
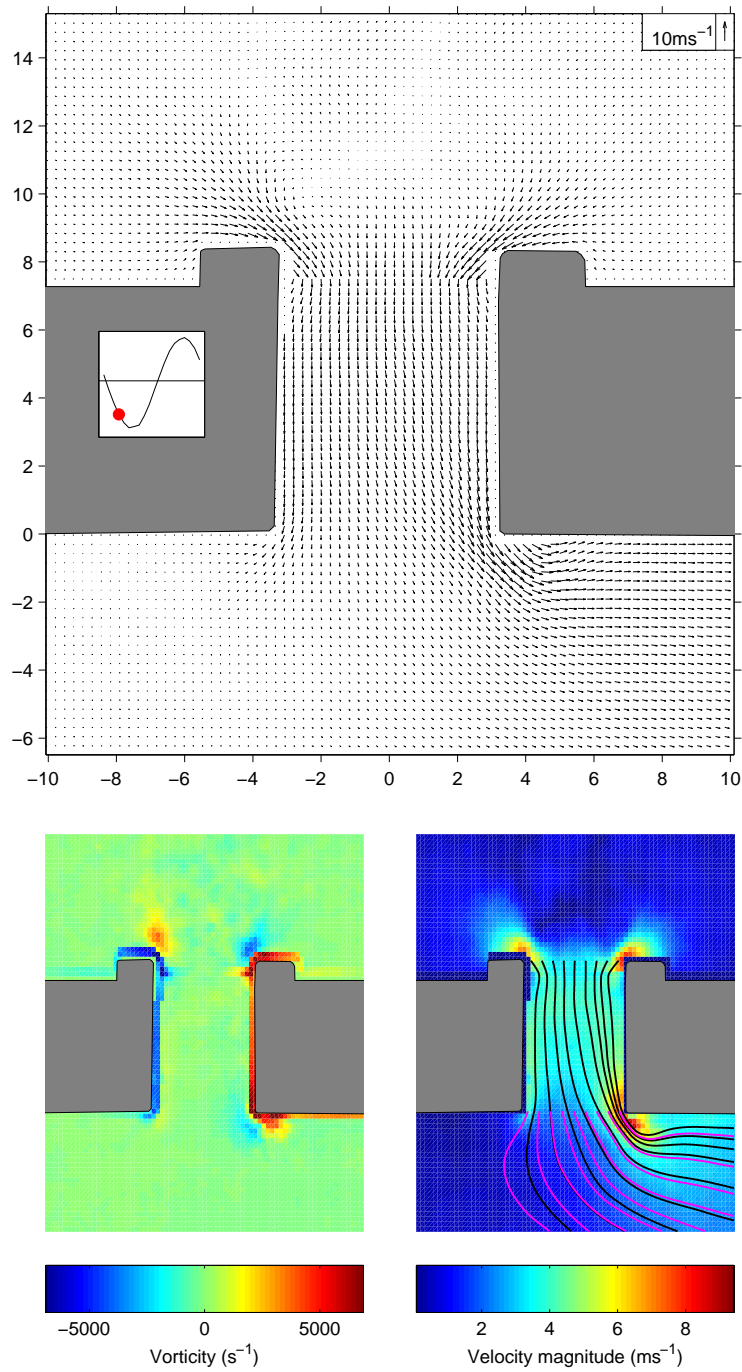
(g) Square tonehole,  $\bar{p}_{an} = 452\text{Pa}$ ,  $i = 18$ 

Figure 5.2 continued.

Figure 5.3: PIV data for the square tonehole at  $\bar{p}_{an} = 760\text{Pa}$ .

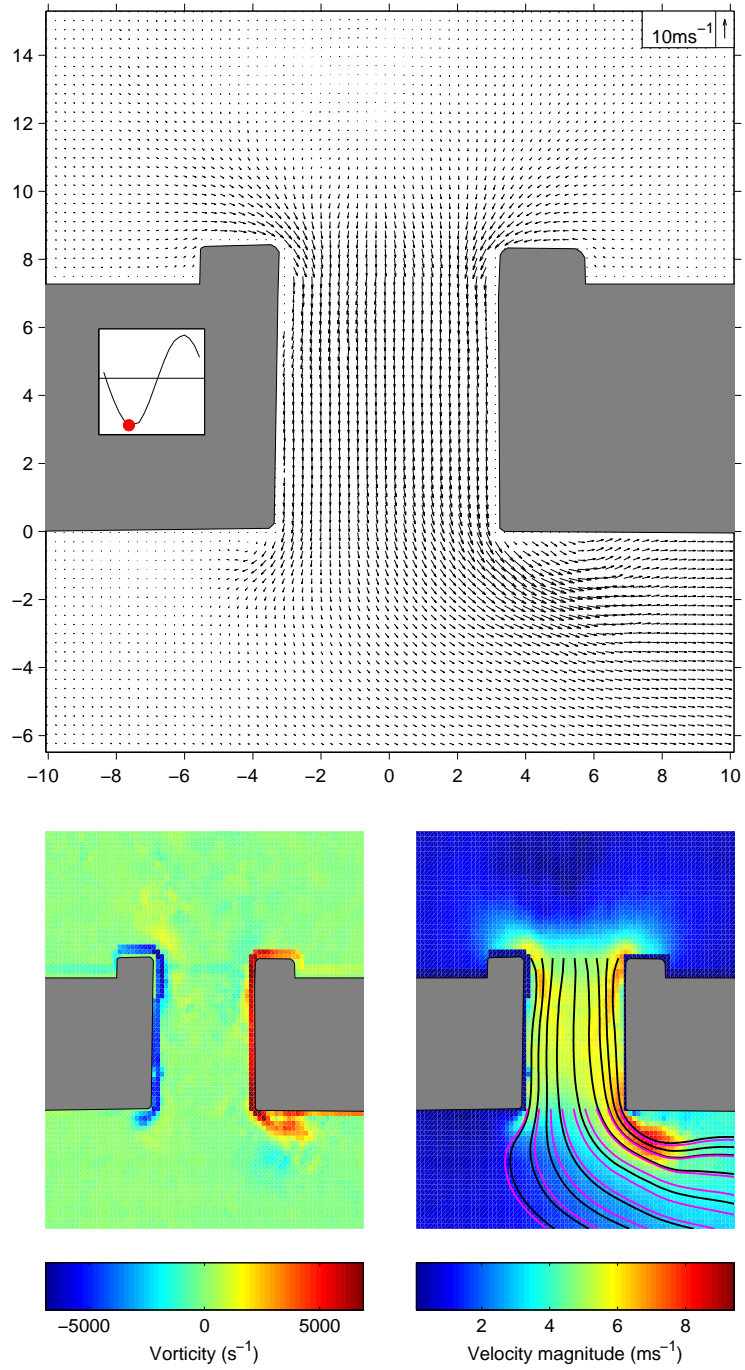


Figure 5.3 continued.

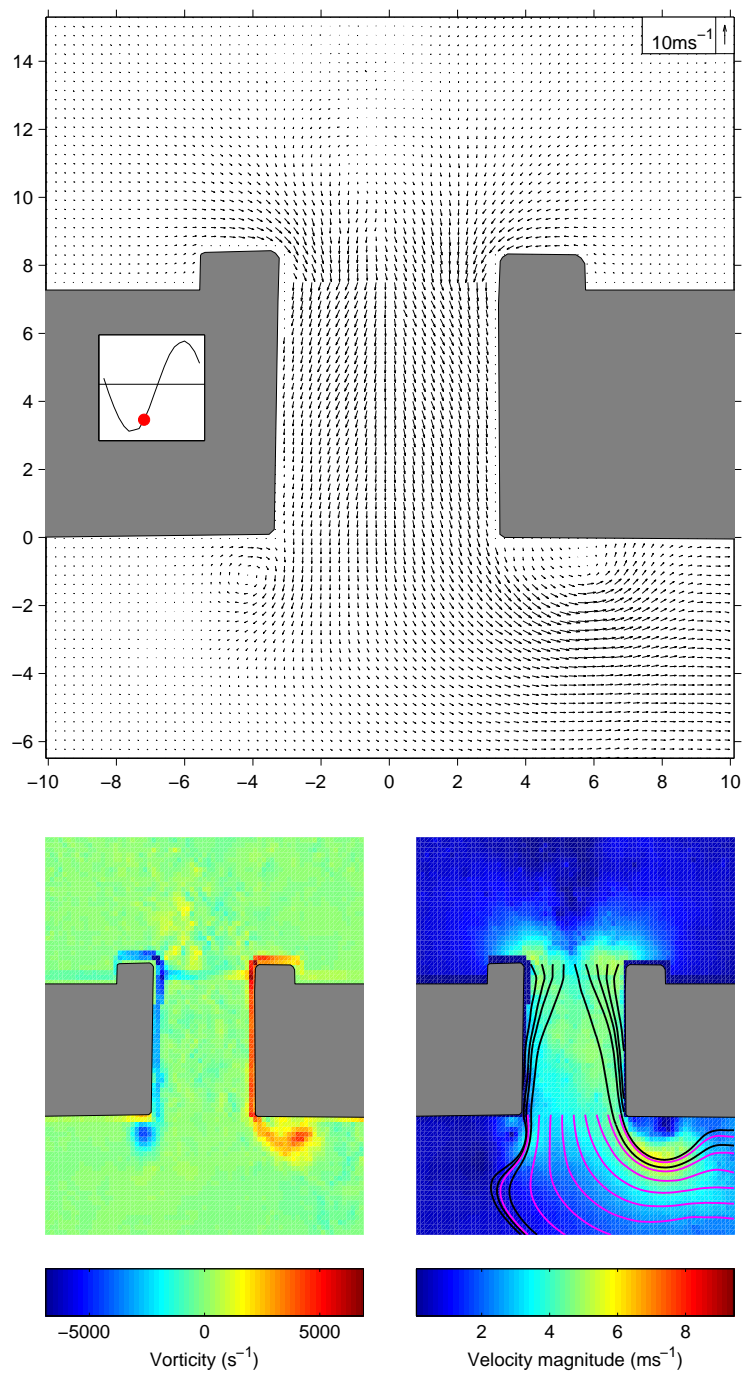


Figure 5.3 continued.

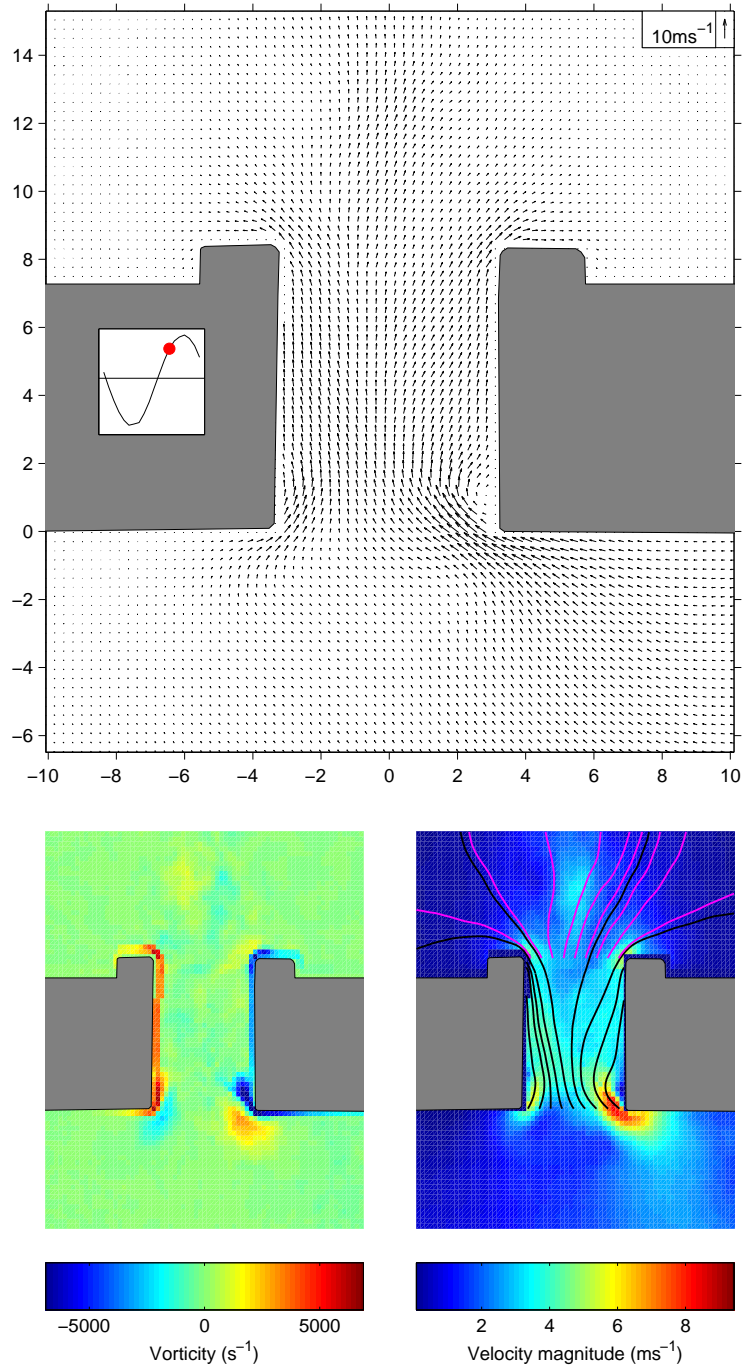
(d) Square tonehole,  $\bar{p}_{an} = 760\text{Pa}$ ,  $i = 14$ 

Figure 5.3 continued.

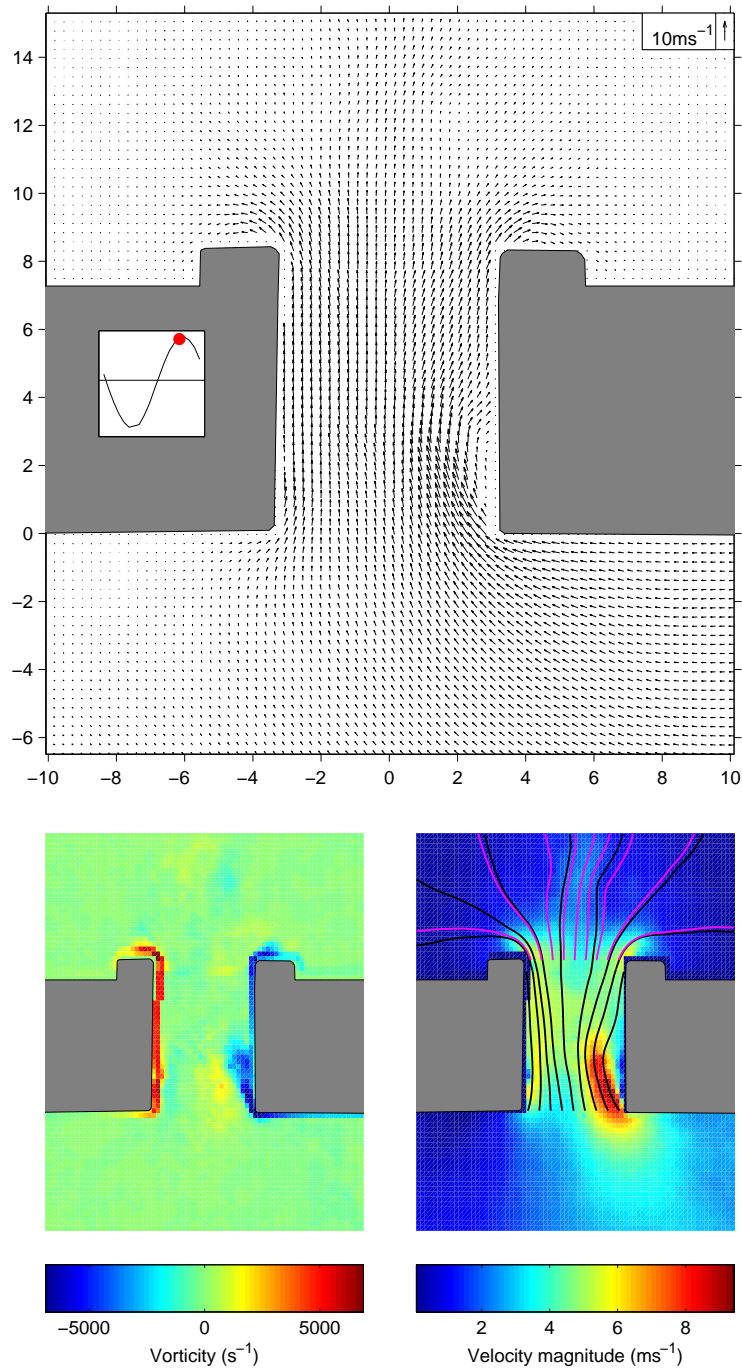
(e) Square tonehole,  $\bar{p}_{an} = 760\text{Pa}$ ,  $i = 16$ 

Figure 5.3 continued.

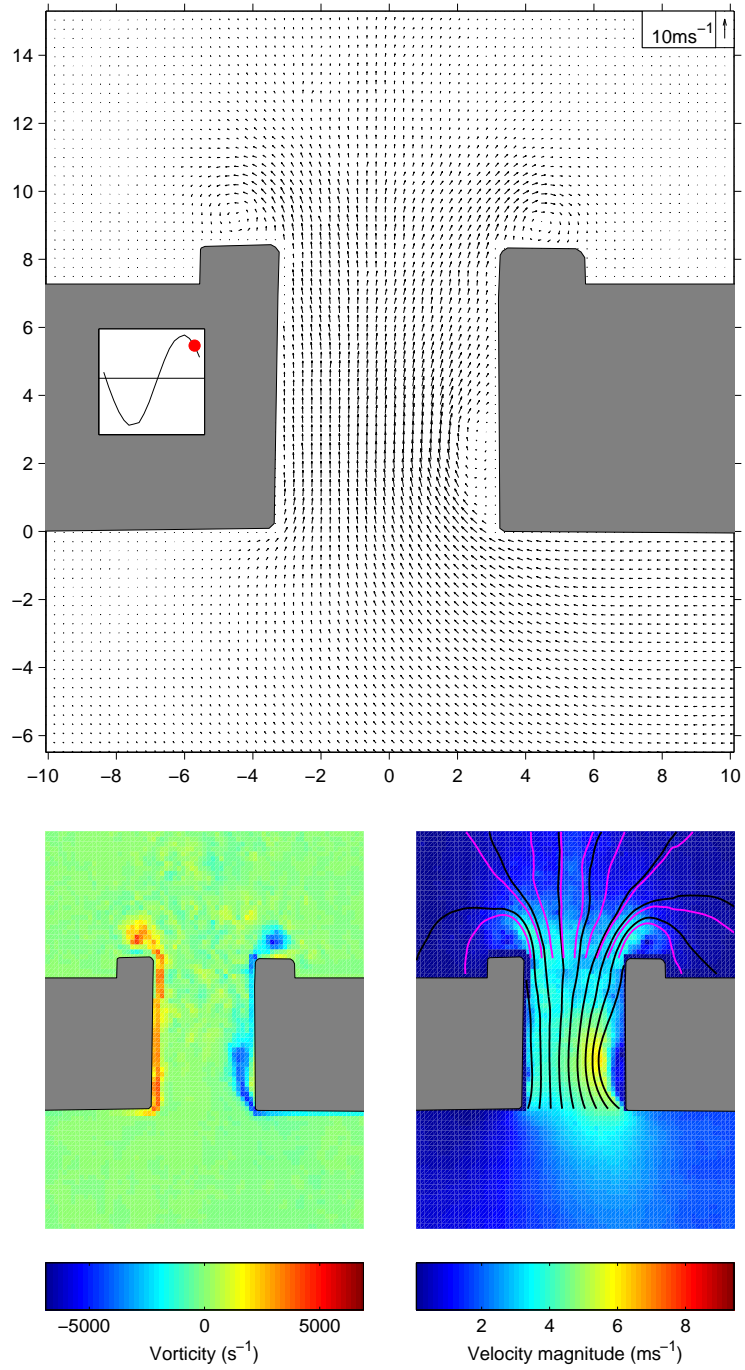


Figure 5.3 continued.



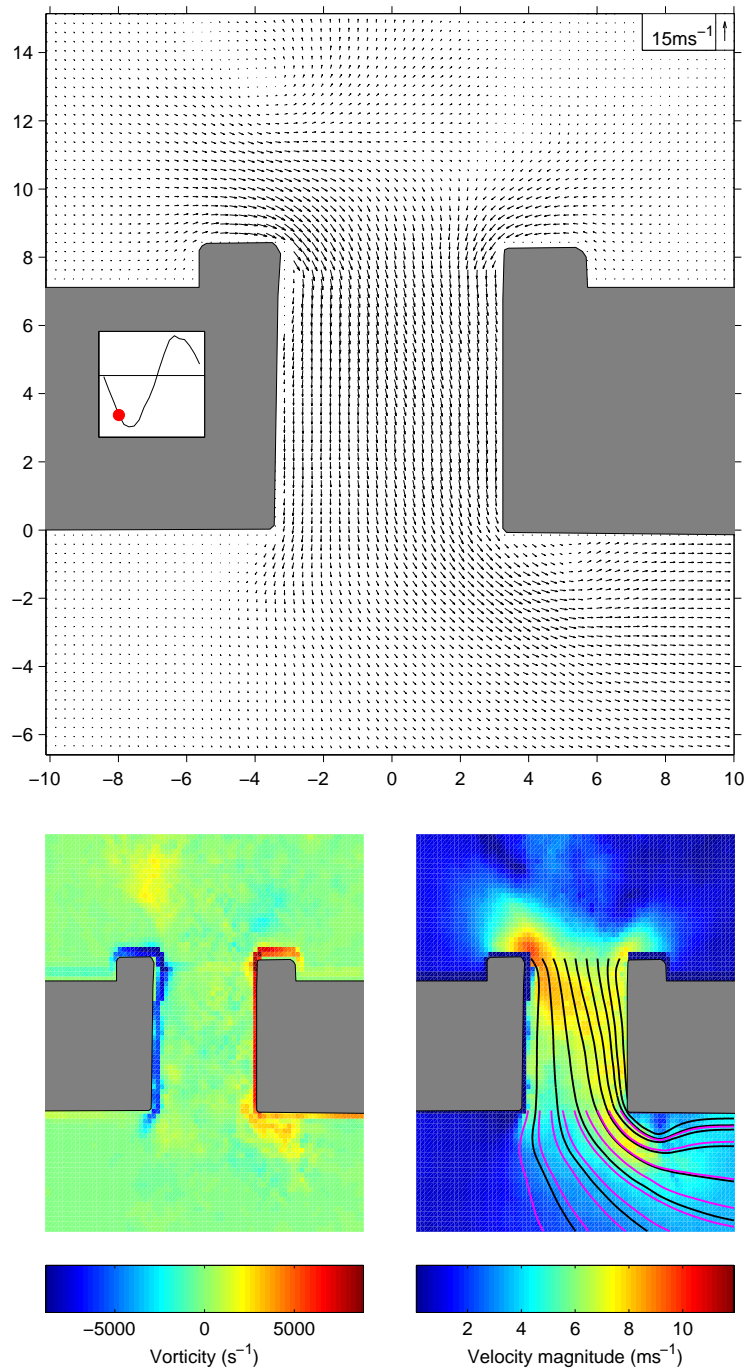


Figure 5.4: PIV data for the square tonehole at  $\bar{p}_{an} = 1067\text{Pa}$ .



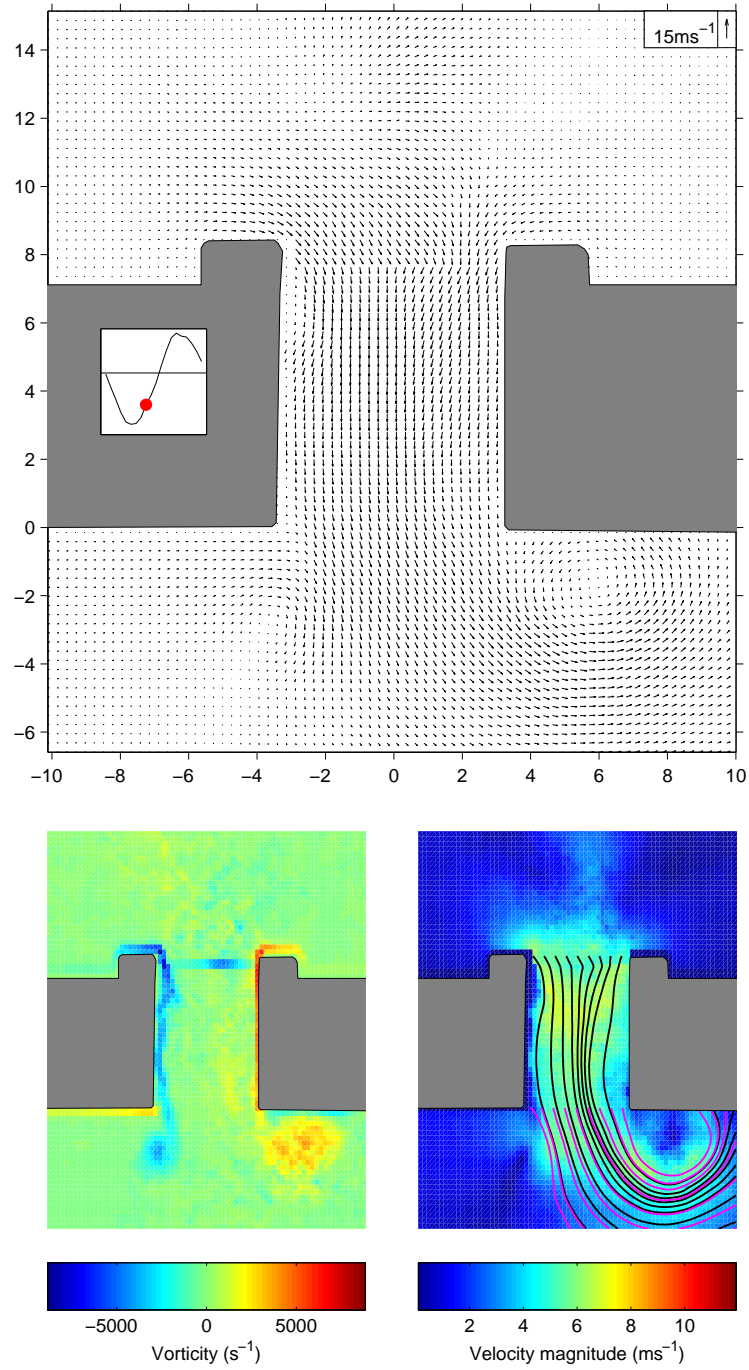
(b) Square tonehole,  $\bar{p}_{an} = 1067 \text{ Pa}$ ,  $i = 9$ 

Figure 5.4 continued.

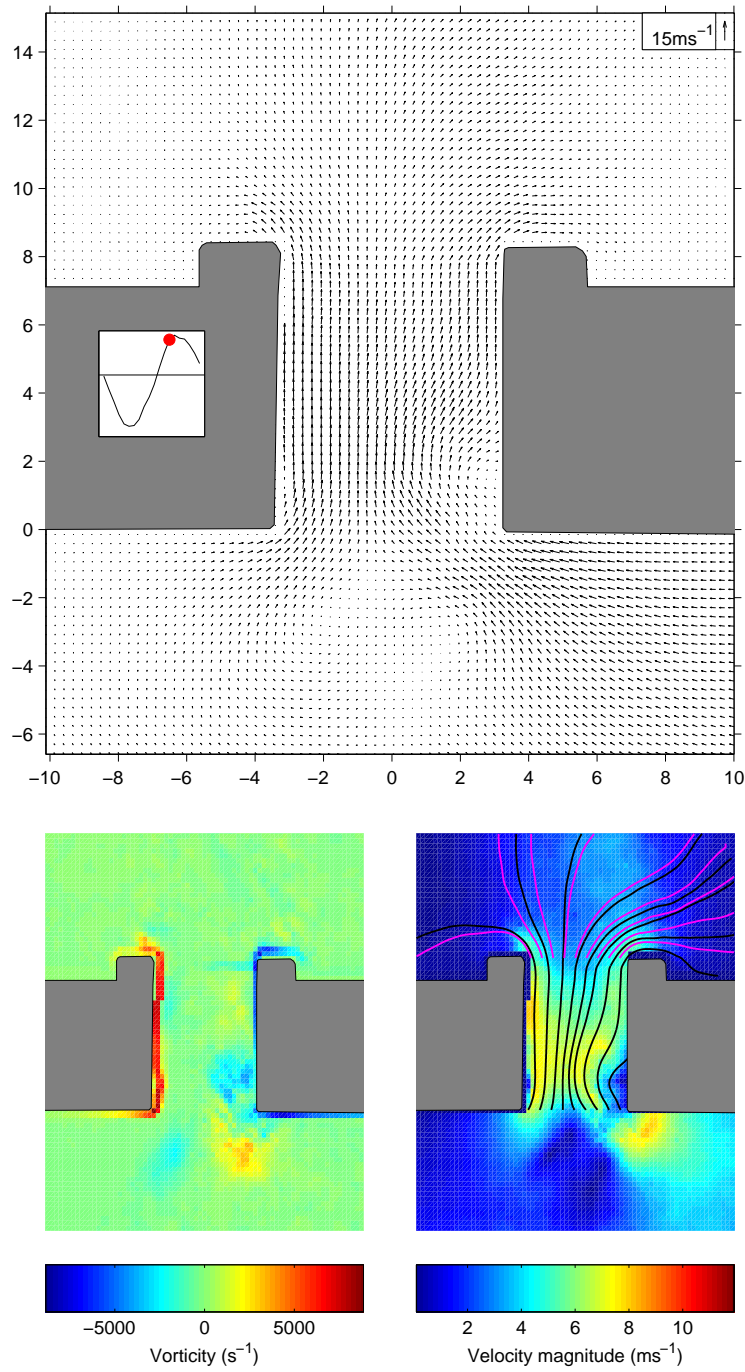


Figure 5.4 continued.

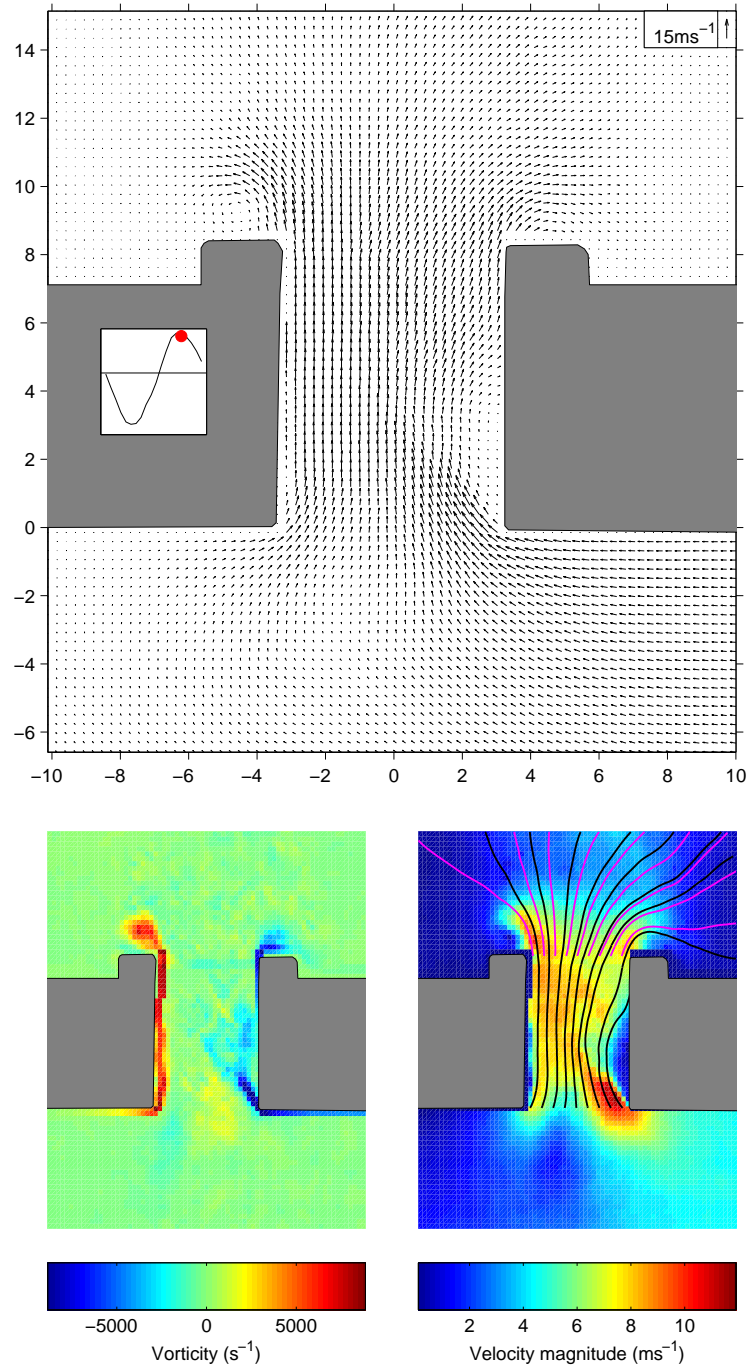


Figure 5.4 continued.

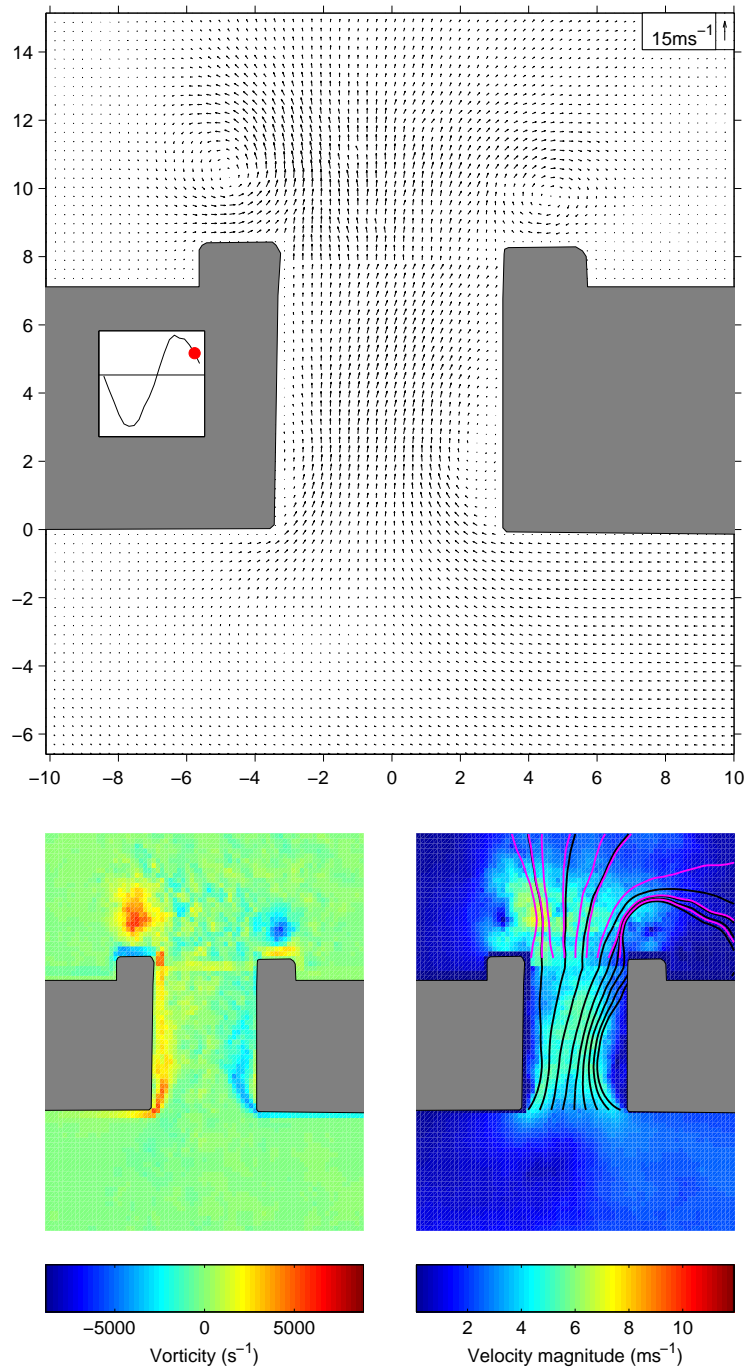
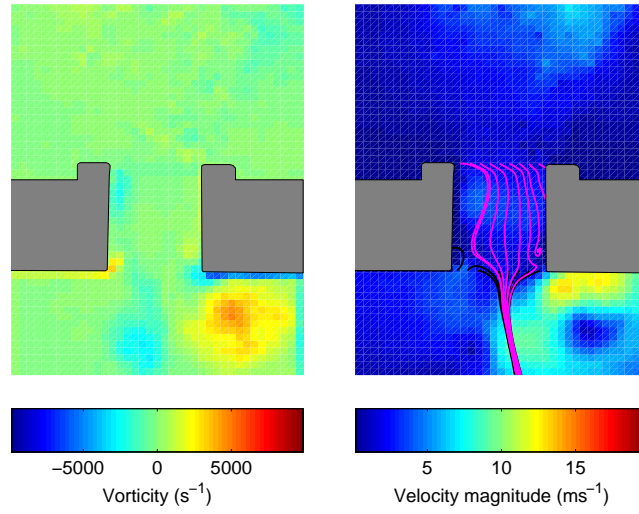
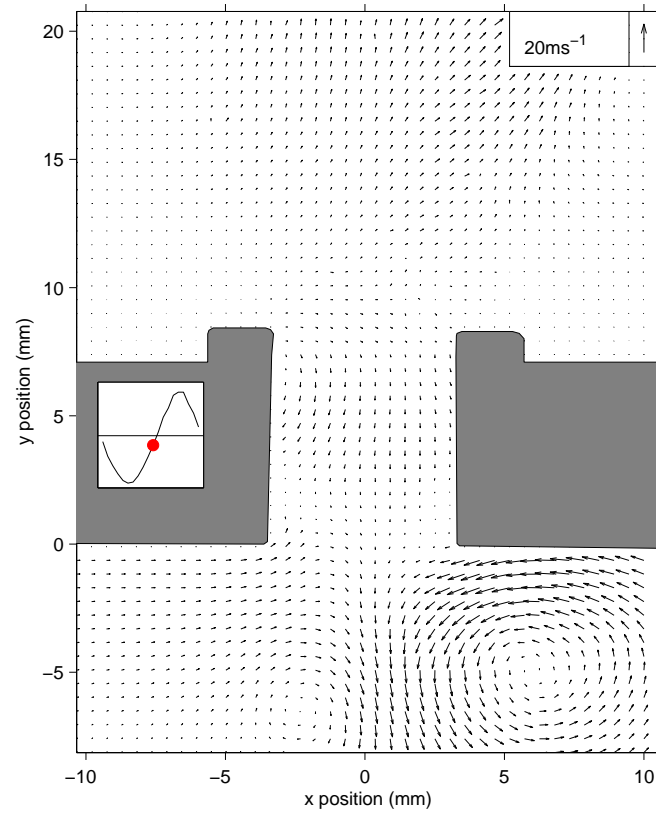


Figure 5.4 continued.



(a) Square tonehole,  $\bar{p}_{an} = 1703\text{Pa}$ ,  $i = 11$

Figure 5.5: PIV data for the square tonehole at  $\bar{p}_{an} = 1703\text{Pa}$ .

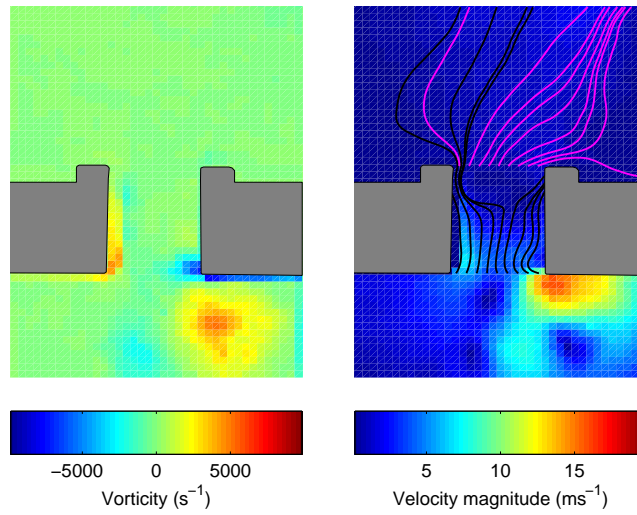
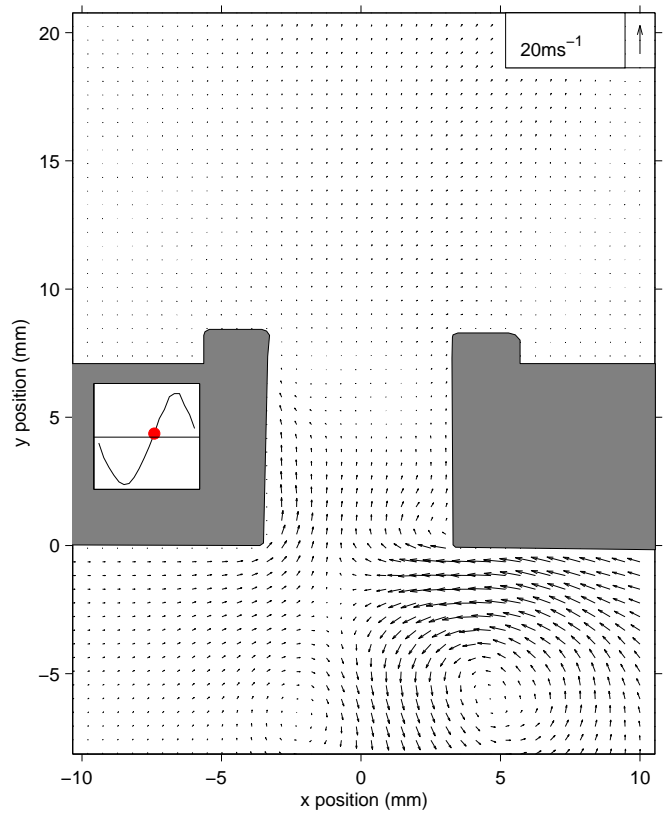
(b) Square tonehole,  $\bar{p}_{an} = 1703\text{Pa}$ ,  $i = 12$ 

Figure 5.5 continued.

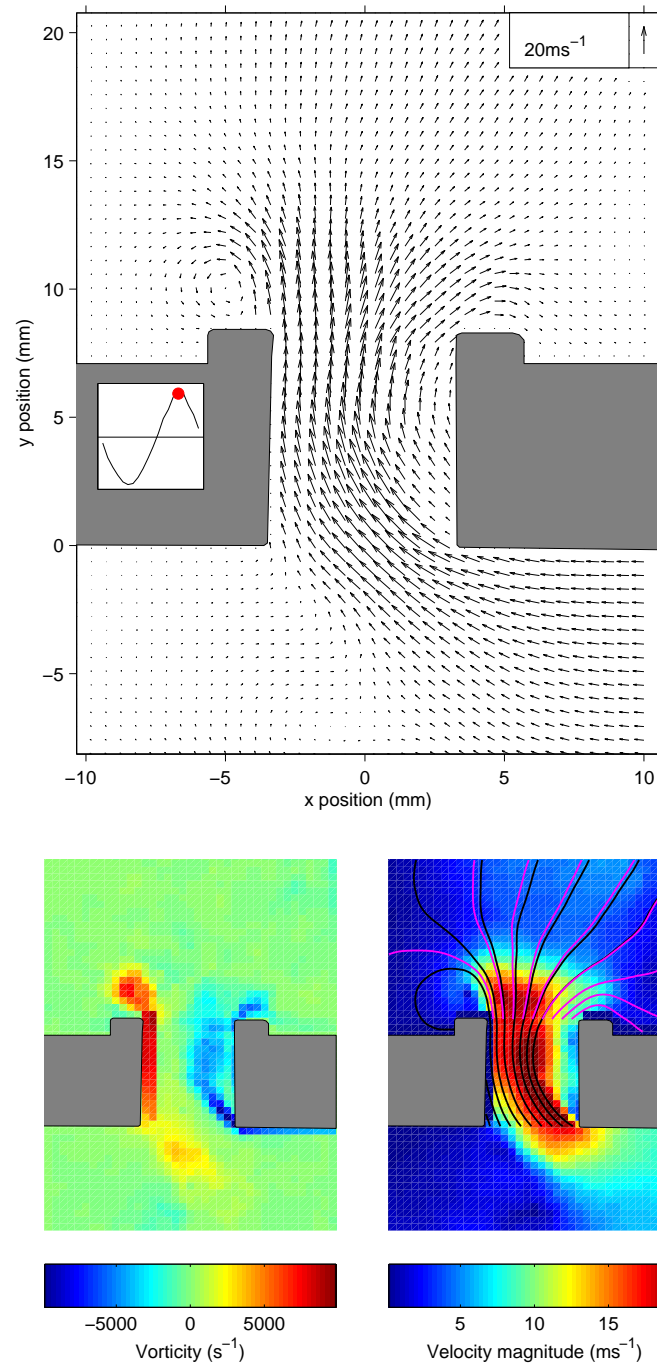
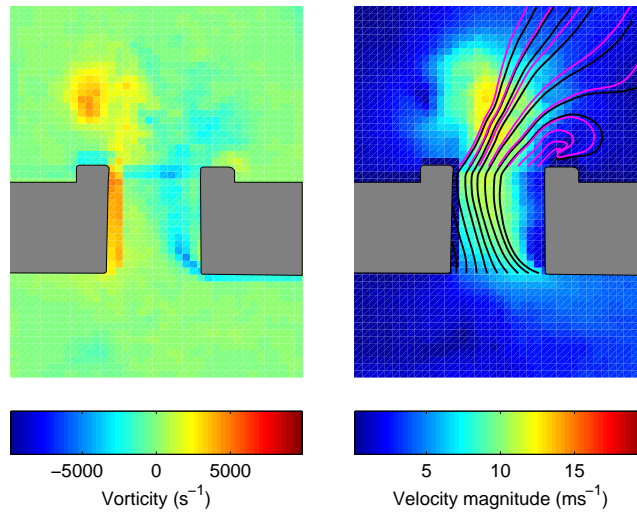
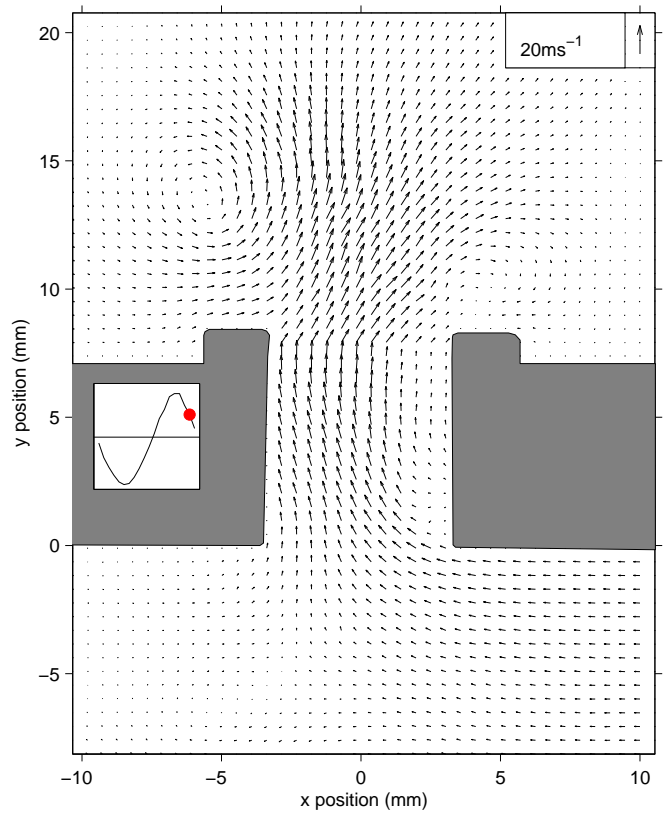
(c) Square tonehole,  $\bar{p}_{an} = 1703\text{Pa}$ ,  $i = 16$ 

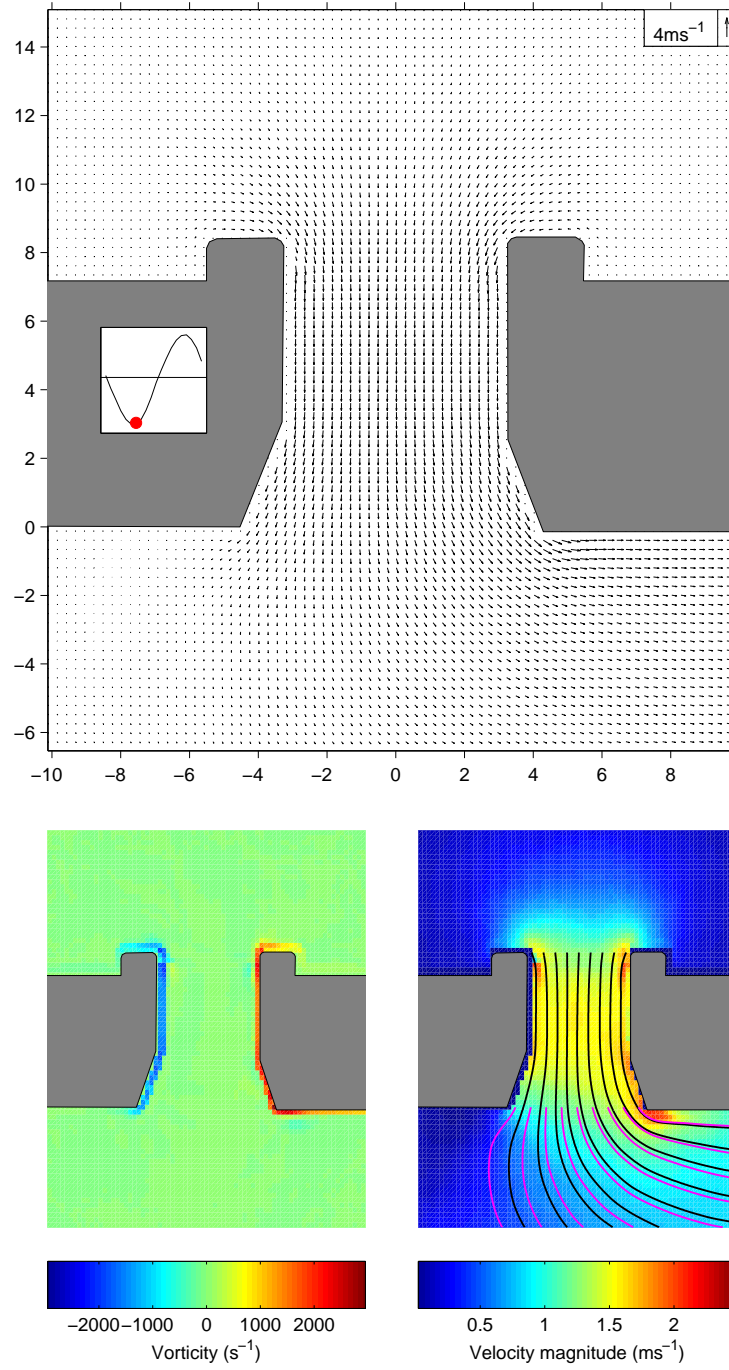
Figure 5.5 continued.



(d) Square tonehole,  $\bar{p}_{an} = 1703\text{Pa}$ ,  $i = 19$

Figure 5.5 continued.



(a) Undercut tonehole,  $\bar{p}_{an} = 222\text{Pa}$ ,  $i = 7$ Figure 5.6: PIV data for the undercut tonehole at  $\bar{p}_{an} = 222\text{Pa}$ .

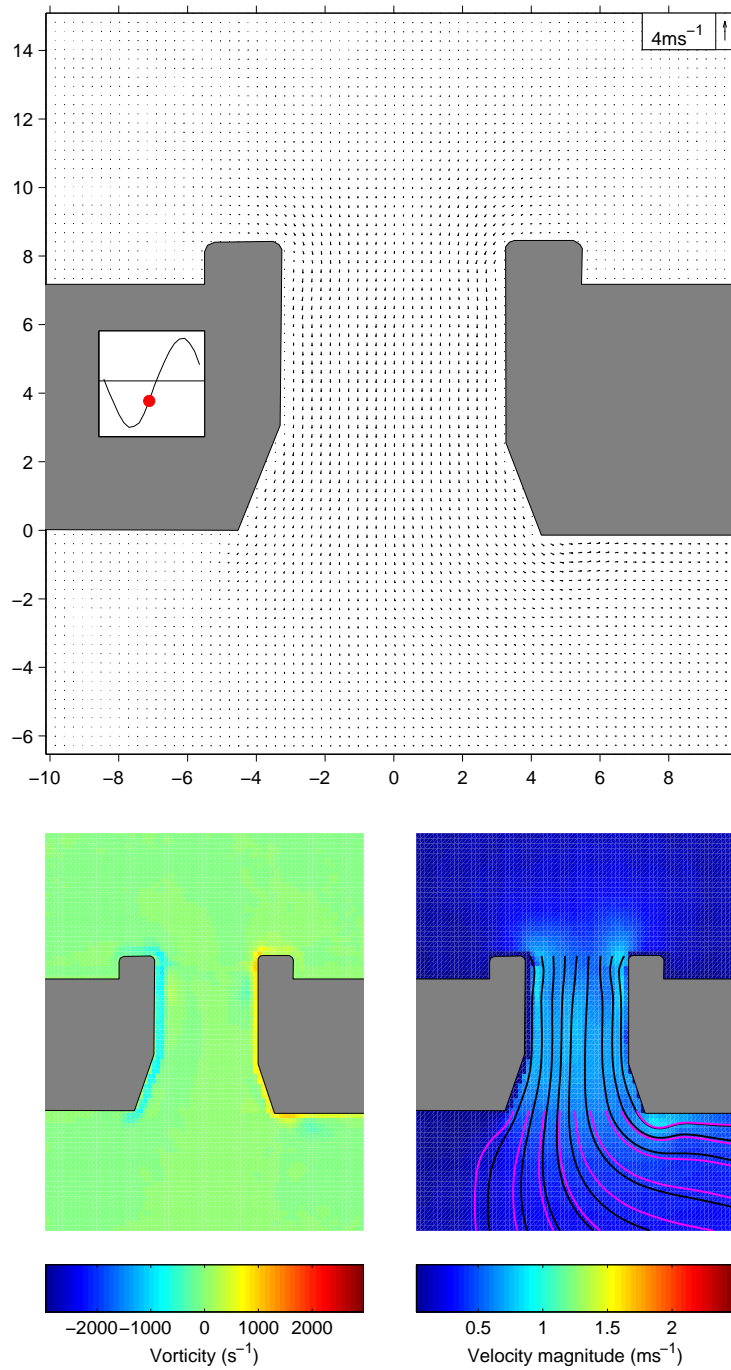
(b) Undercut tonehole,  $\bar{p}_{an} = 222\text{Pa}$ ,  $i = 10$ 

Figure 5.6 continued.

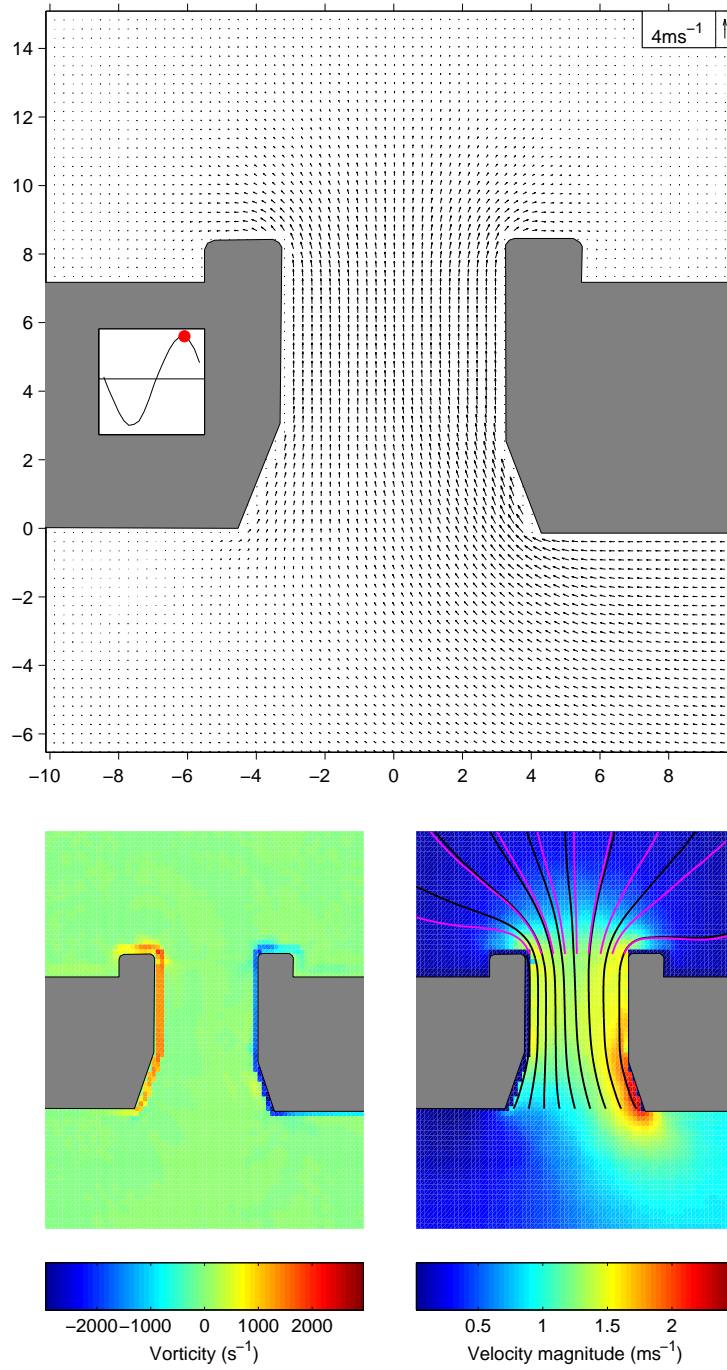
(c) Undercut tonehole,  $\bar{p}_{an} = 222\text{Pa}$ ,  $i = 17$ 

Figure 5.6 continued.

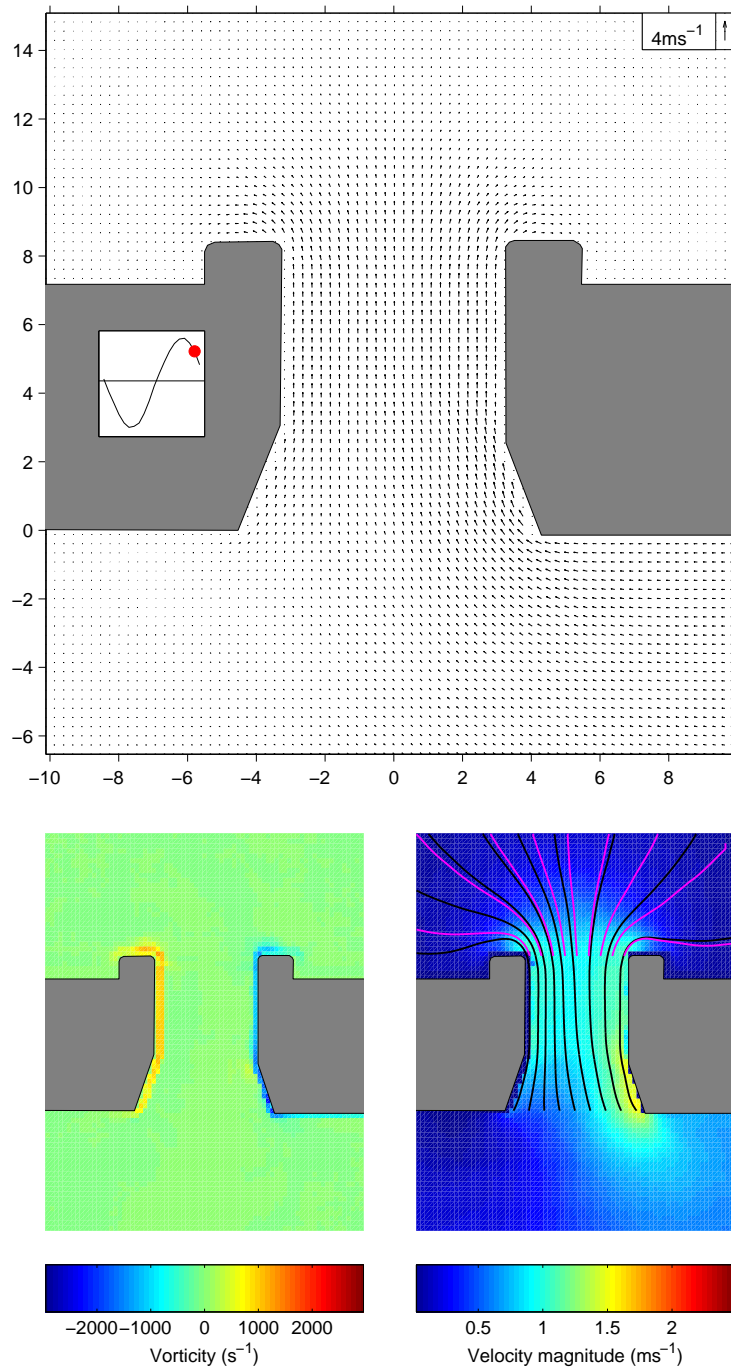
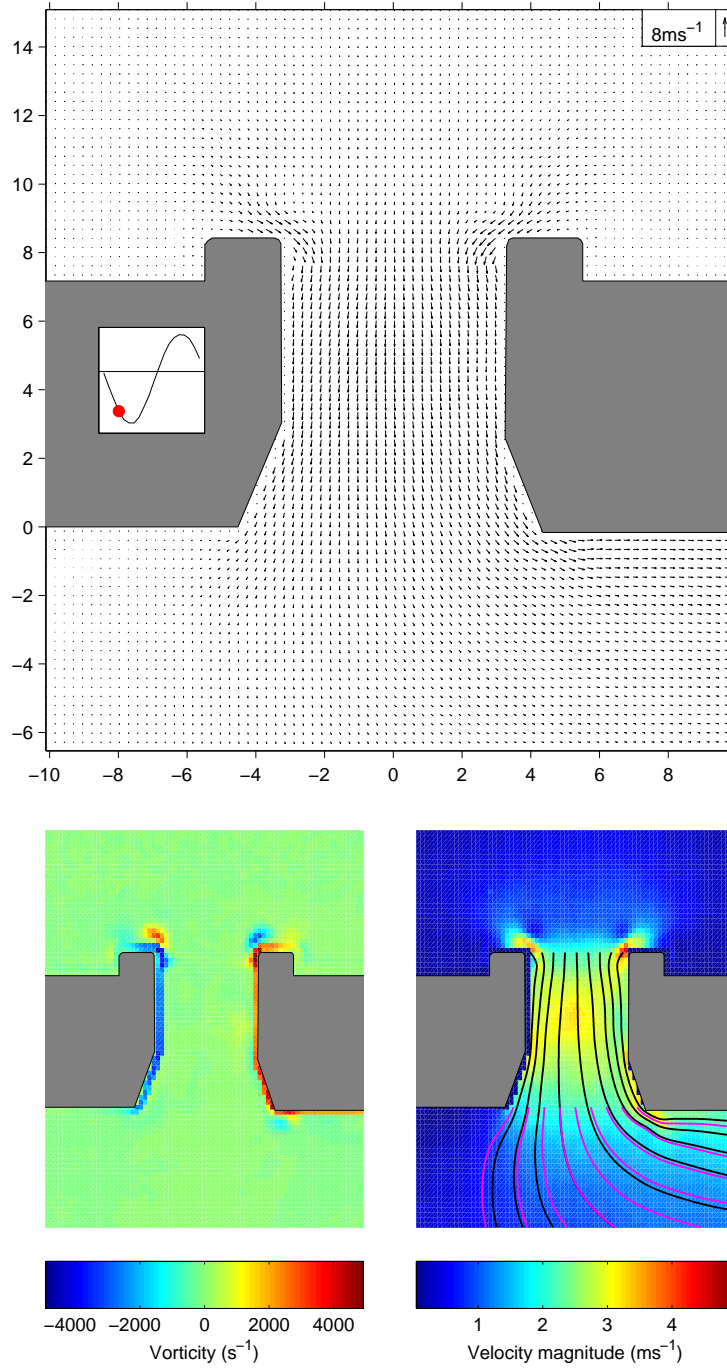
(d) Undercut tonehole,  $\bar{p}_{an} = 222\text{Pa}$ ,  $i = 19$ 

Figure 5.6 continued.

(a) Undercut tonehole,  $\bar{p}_{an} = 463\text{Pa}$ ,  $i = 4$ Figure 5.7: PIV data for the undercut tonehole at  $\bar{p}_{an} = 463\text{Pa}$ .

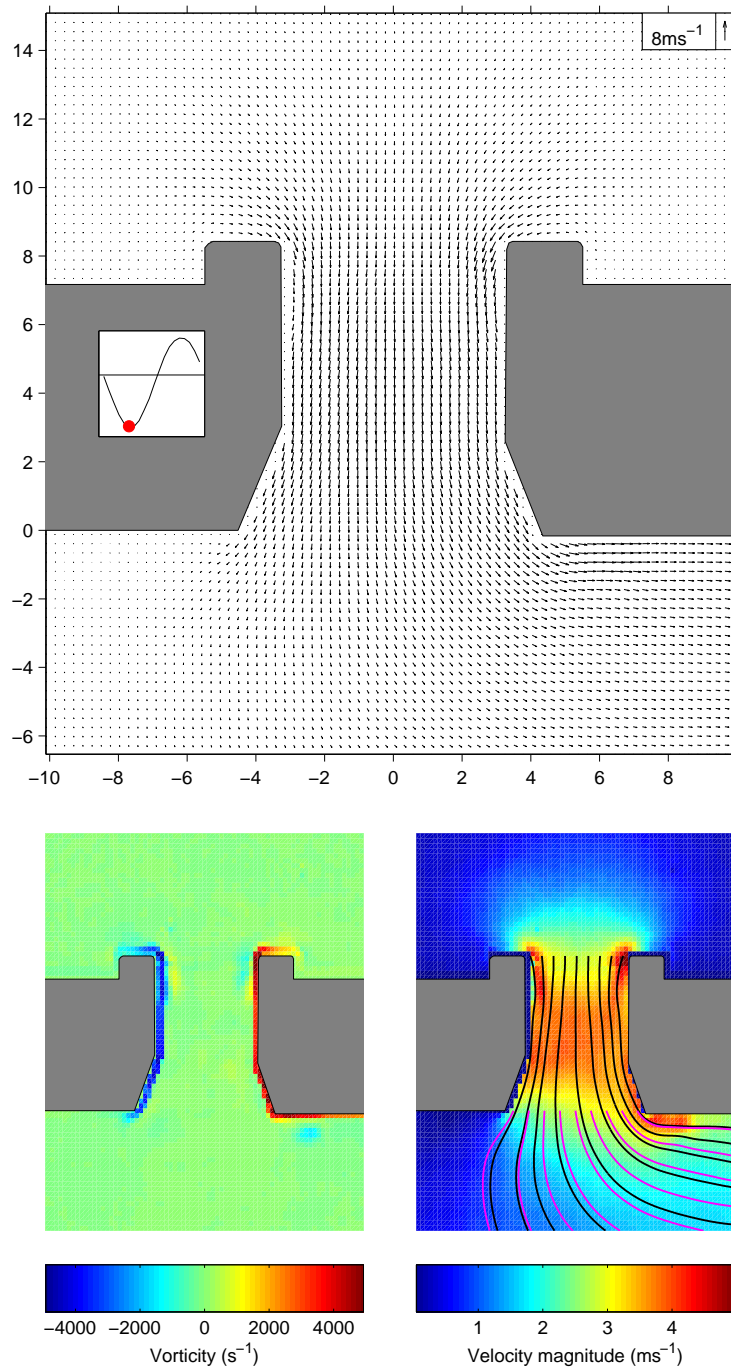


Figure 5.7 continued.

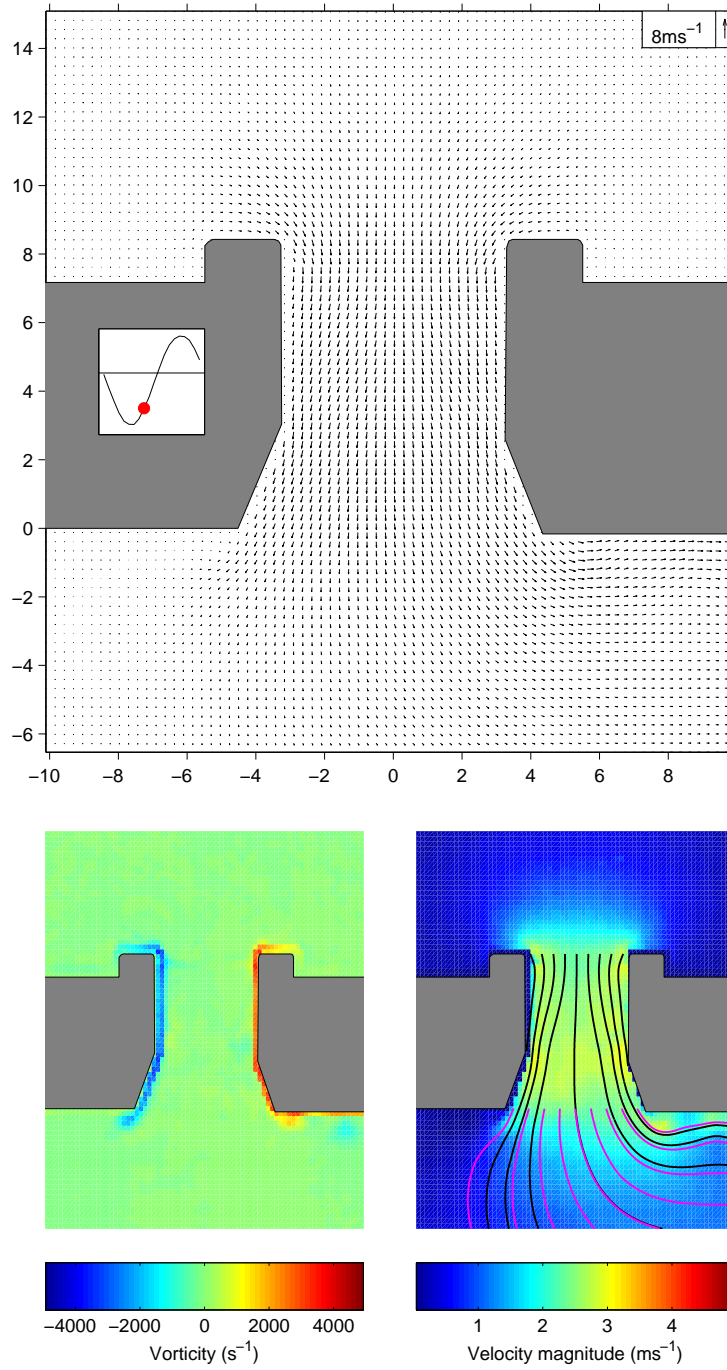
(c) Undercut tonehole,  $\bar{p}_{an} = 463 \text{ Pa}$ ,  $i = 9$ 

Figure 5.7 continued.



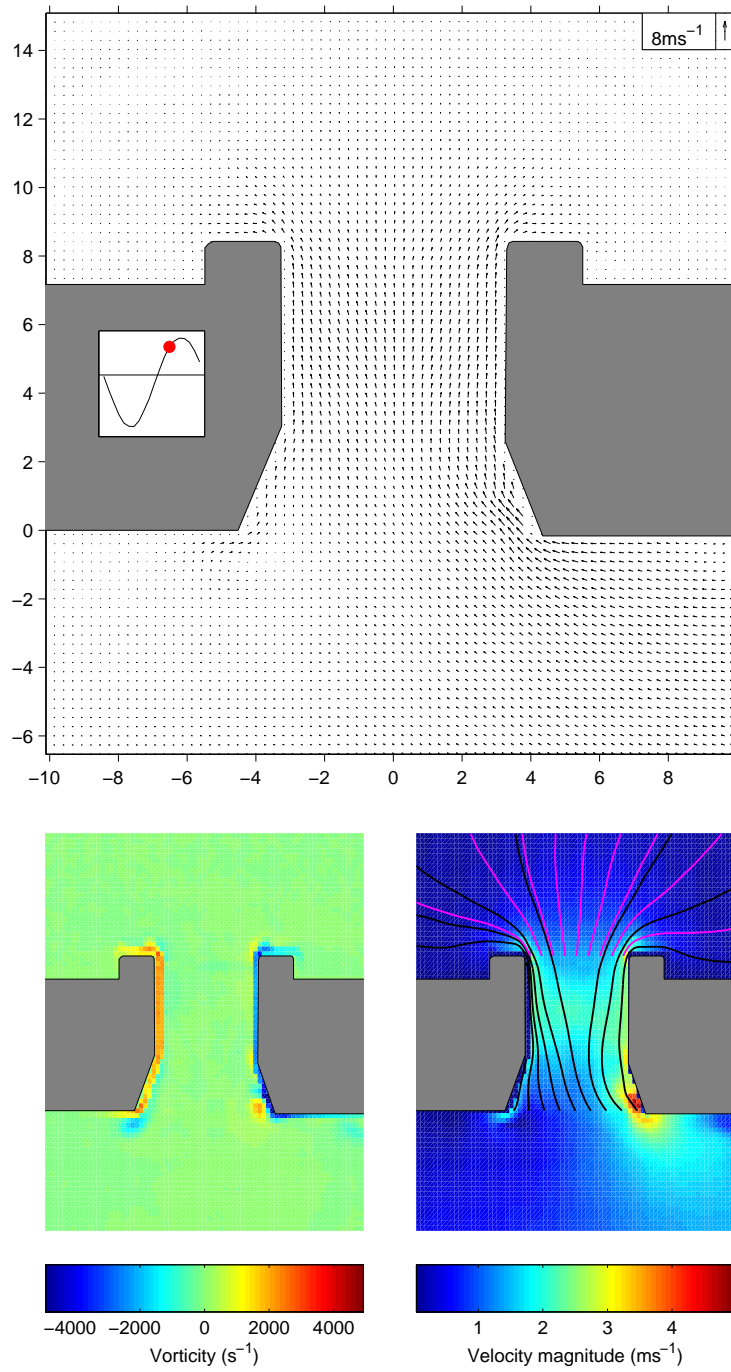
(d) Undercut tonehole,  $\bar{p}_{an} = 463 \text{ Pa}$ ,  $i = 14$ 

Figure 5.7 continued.



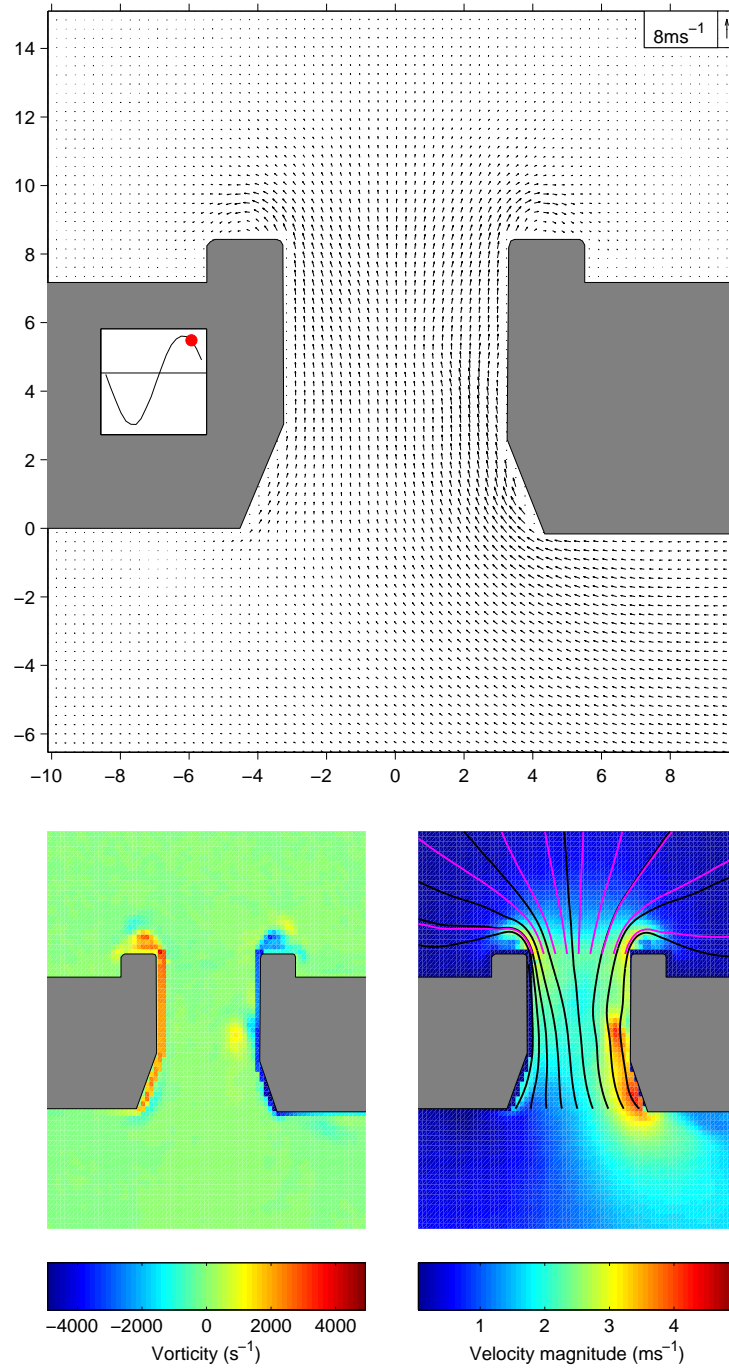
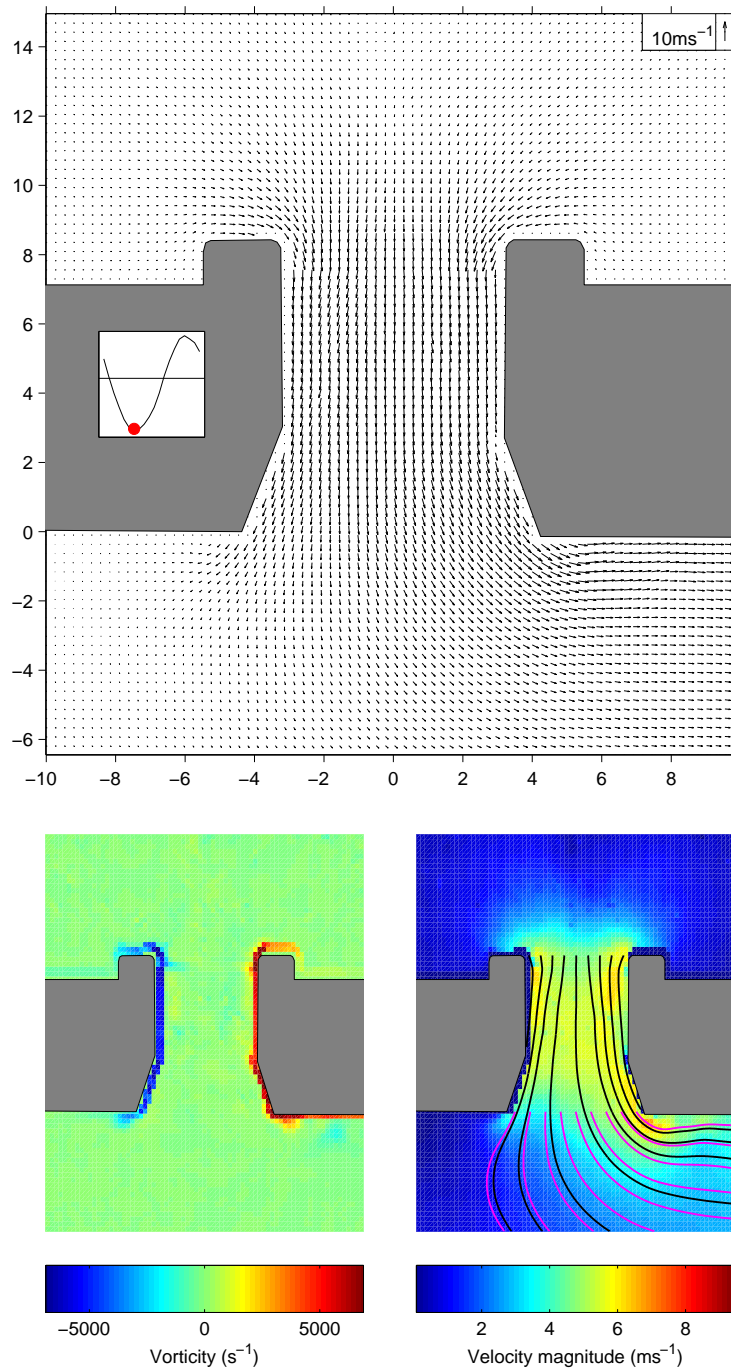
(e) Undercut tonehole,  $\bar{p}_{an} = 463 \text{ Pa}$ ,  $i = 18$ 

Figure 5.7 continued.

Figure 5.8: PIV data for the undercut tonehole at  $\bar{p}_{an} = 729\text{Pa}$ .

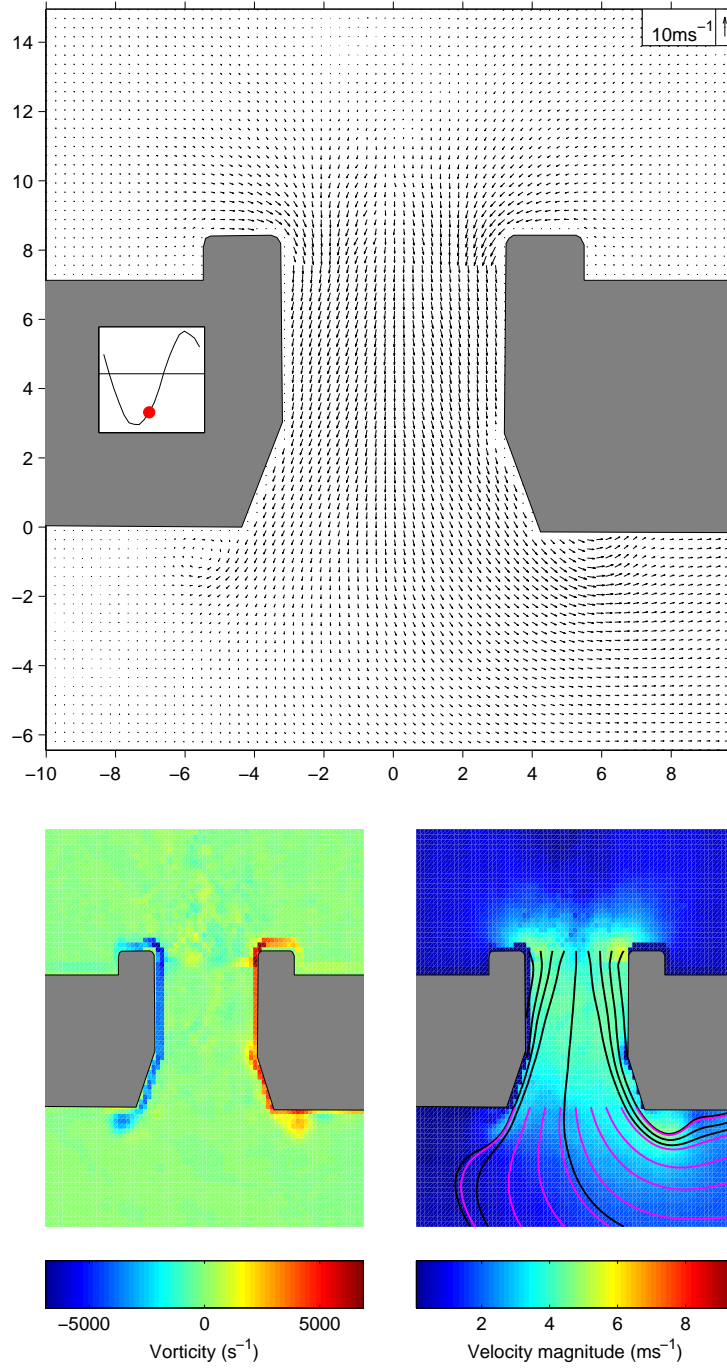
(b) Undercut tonehole,  $\bar{p}_{an} = 729\text{Pa}$ ,  $i = 10$ 

Figure 5.8 continued.

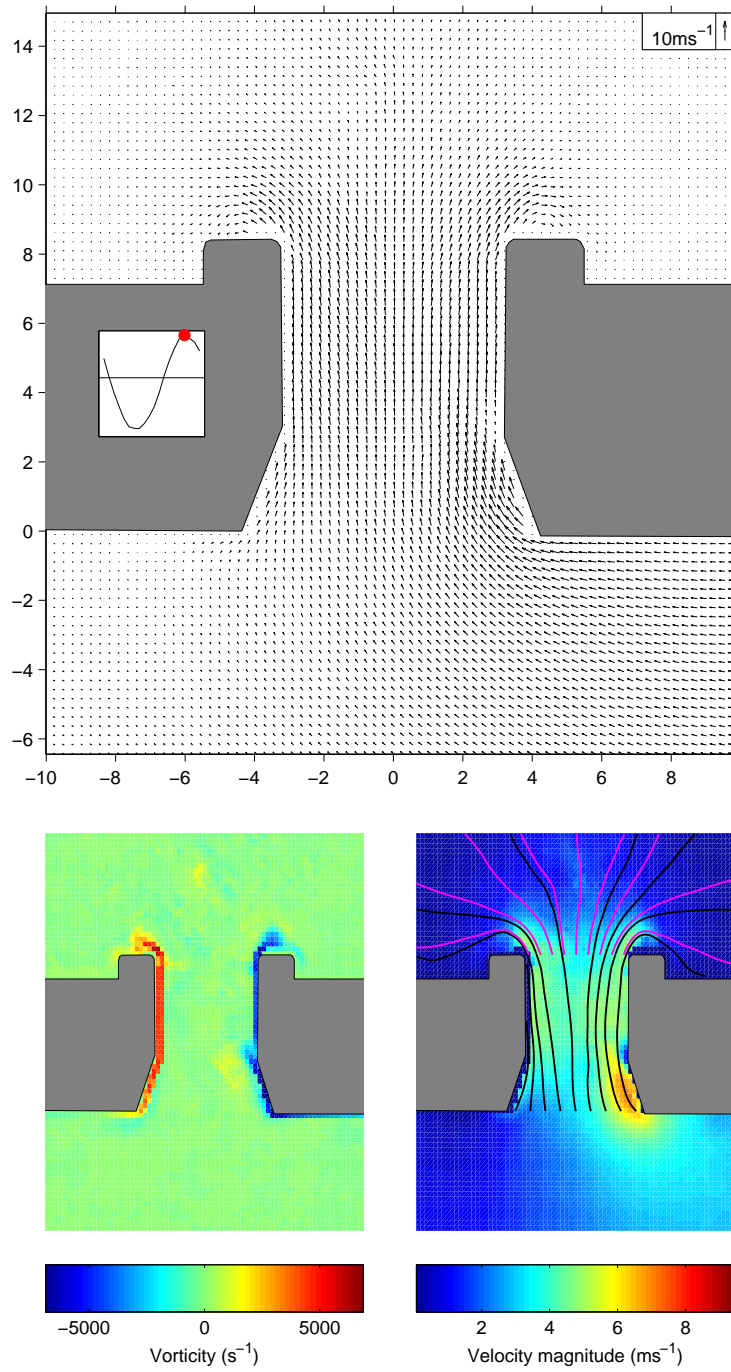


Figure 5.8 continued.

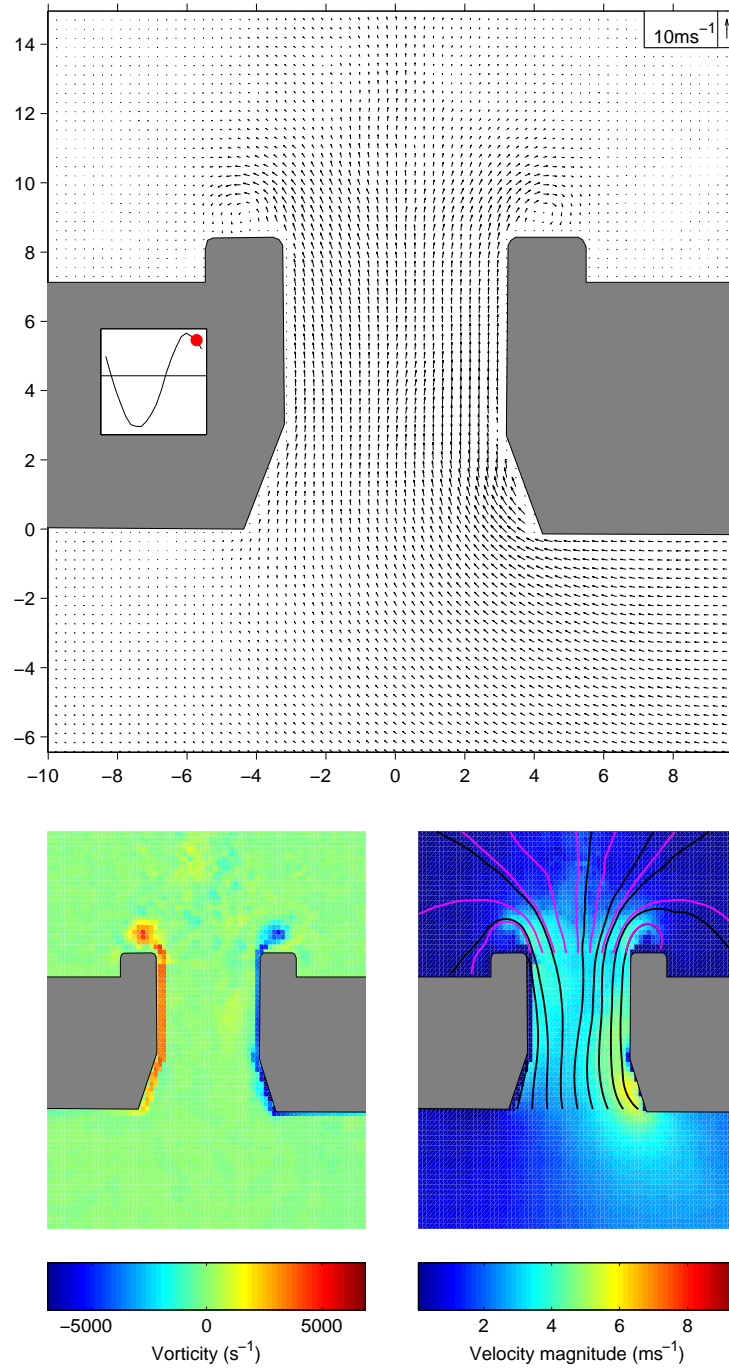
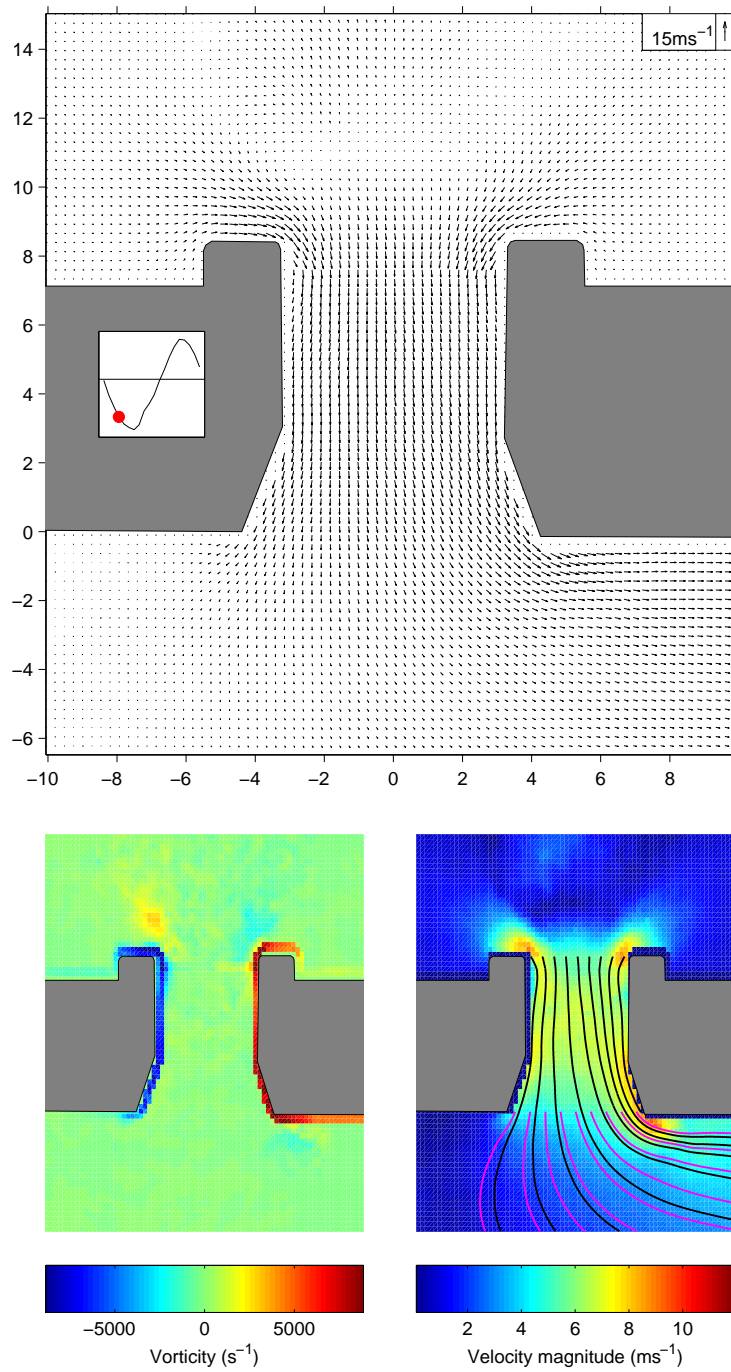
(d) Undercut tonehole,  $\bar{p}_{an} = 729\text{Pa}$ ,  $i = 19$ 

Figure 5.8 continued.



(a) Undercut tonehole,  $\bar{p}_{an} = 1101 \text{ Pa}$ ,  $i = 4$

Figure 5.9: PIV data for the undercut tonehole at  $\bar{p}_{an} = 1101 \text{ Pa}$ .

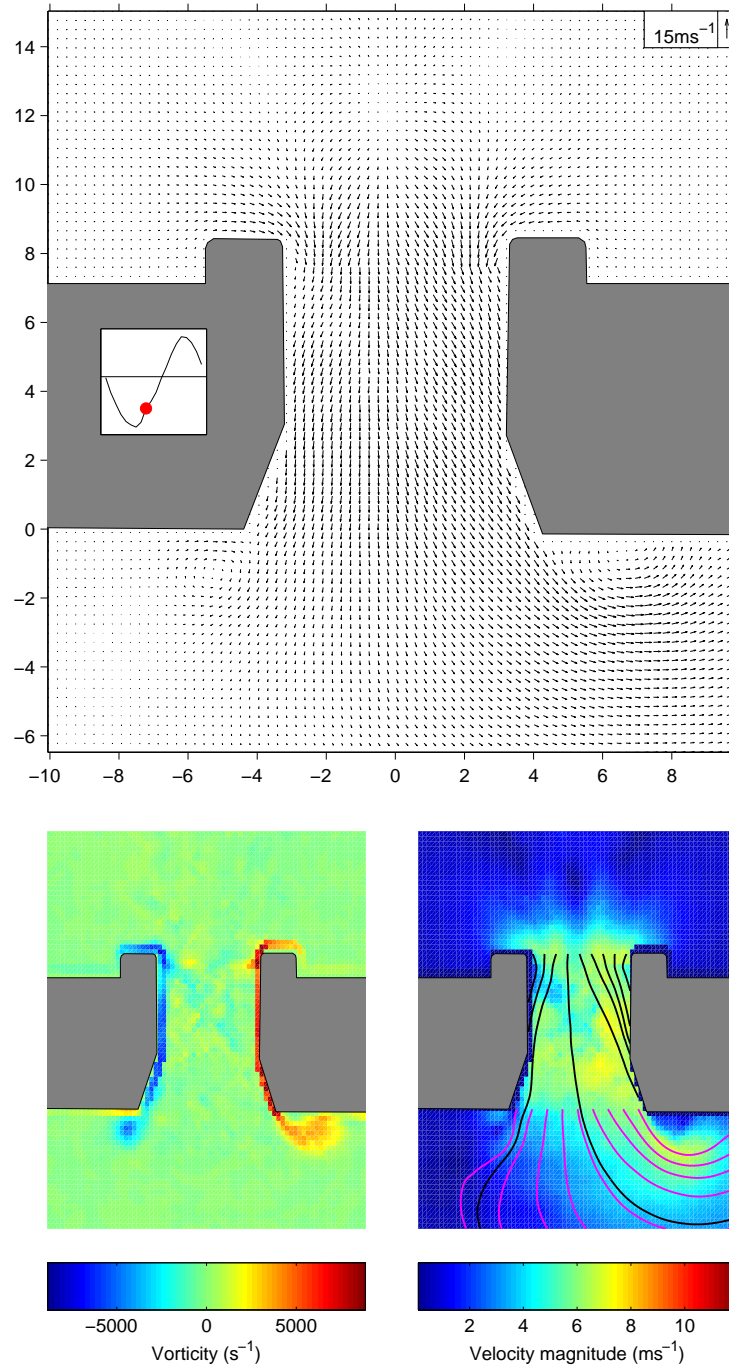
(b) Undercut tonehole,  $\bar{p}_{an} = 1101 \text{ Pa}$ ,  $i = 9$ 

Figure 5.9 continued.



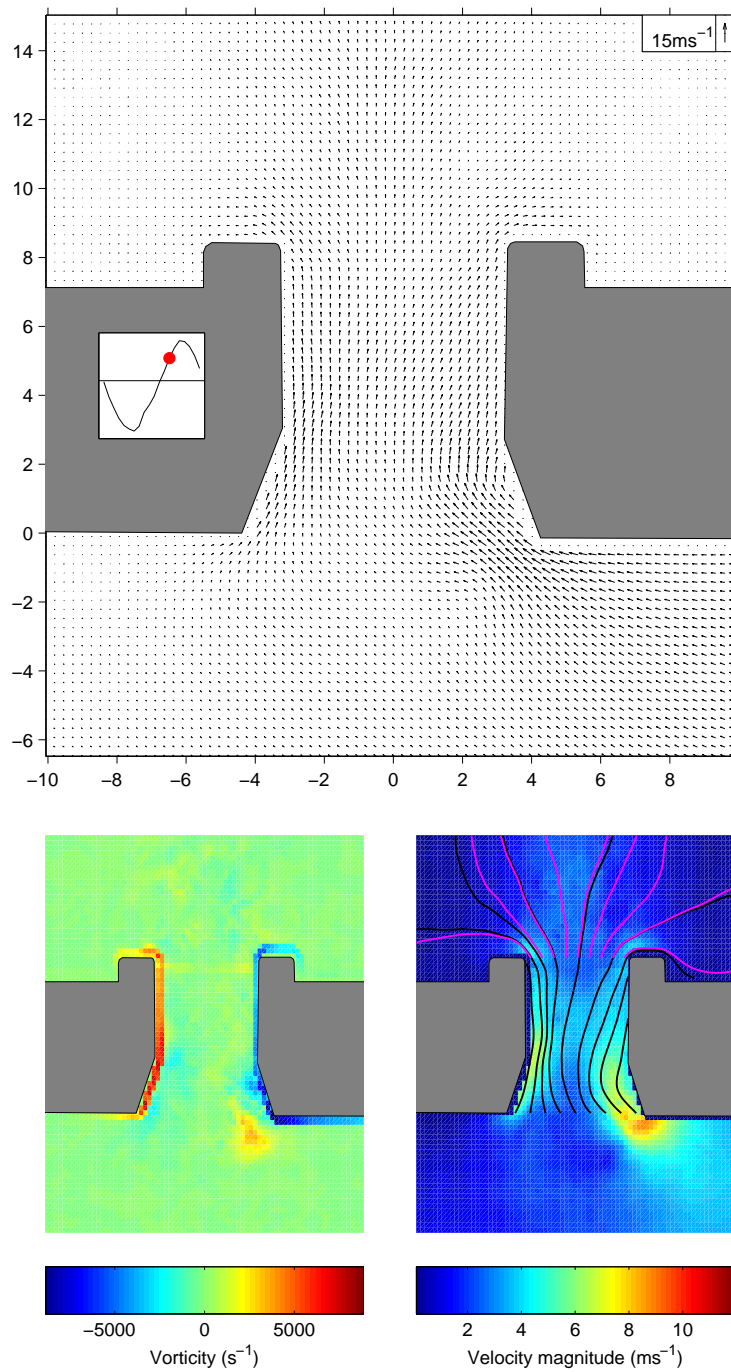


Figure 5.9 continued.



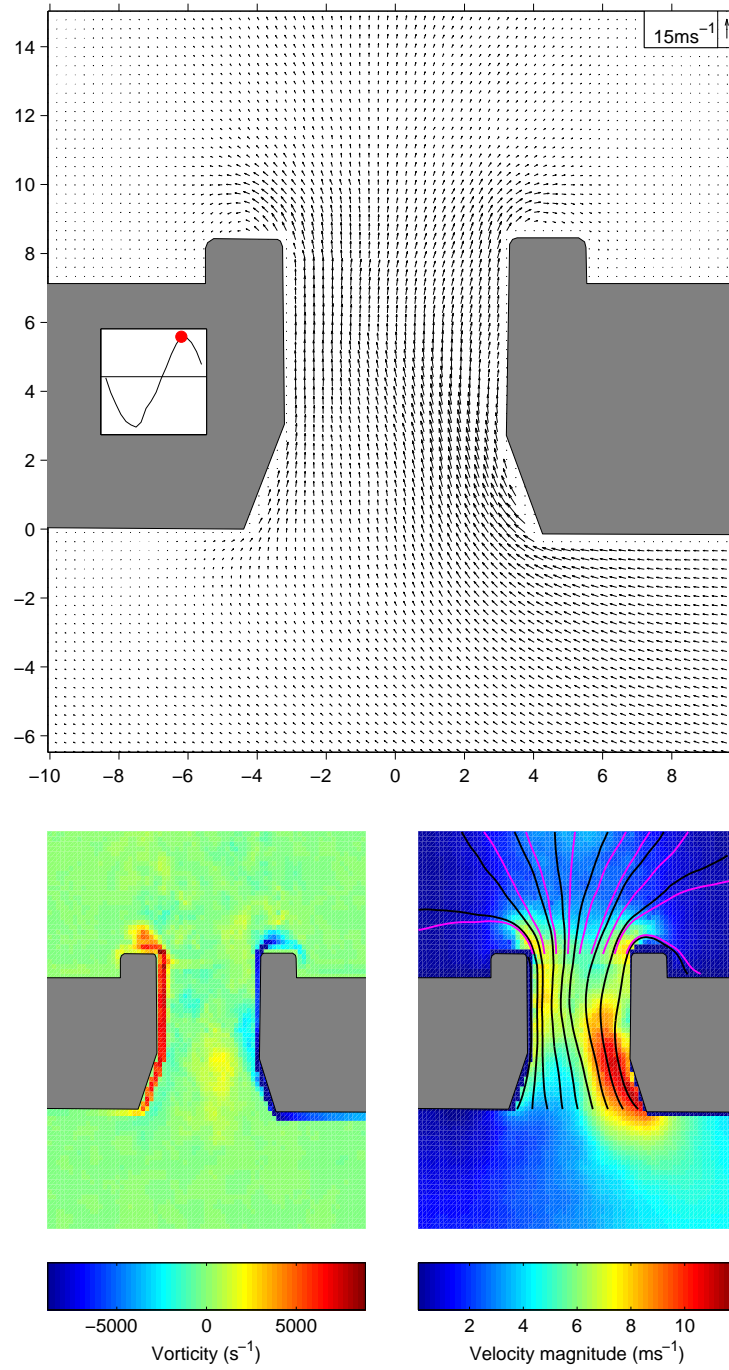
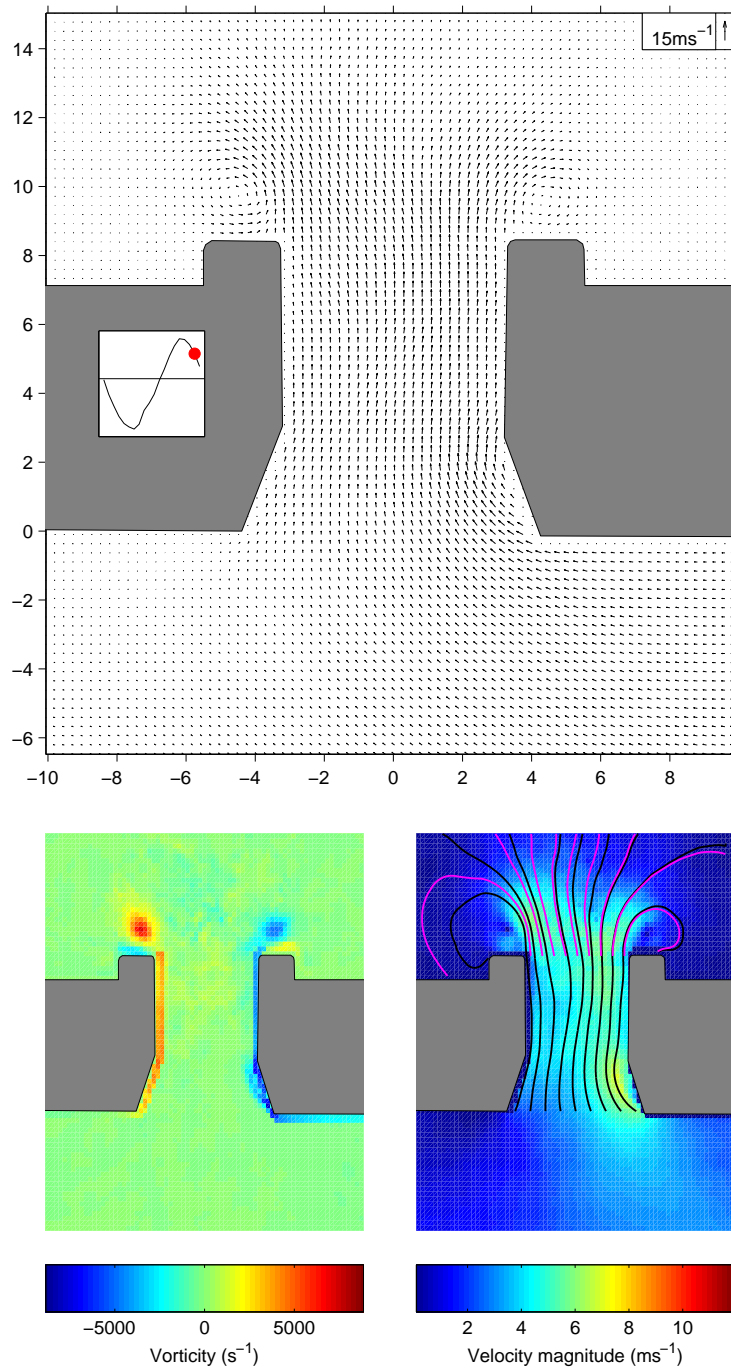
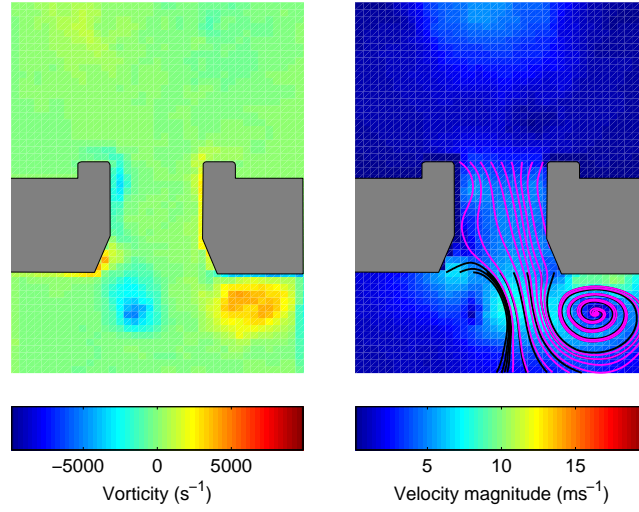
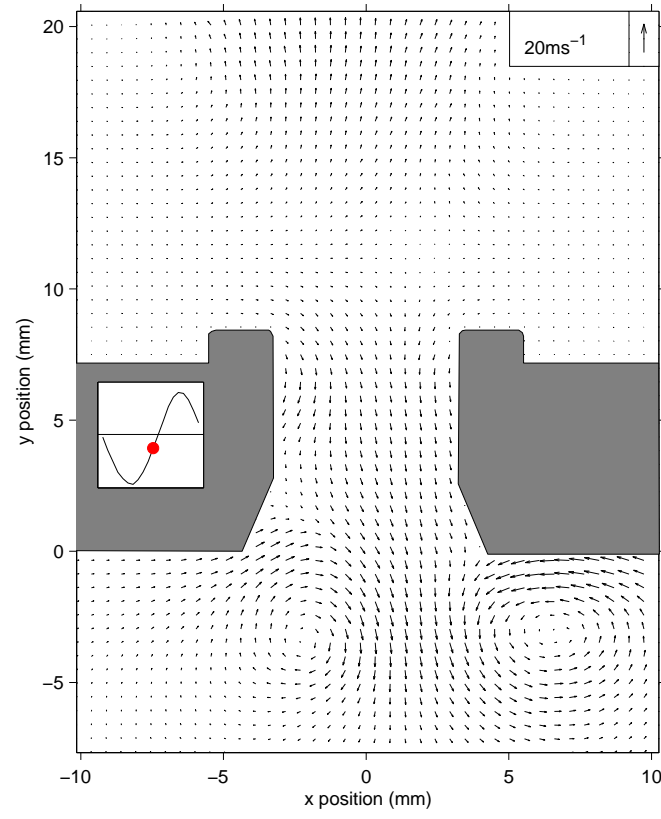
(d) Undercut tonehole,  $\bar{p}_{an} = 1101 \text{ Pa}$ ,  $i = 16$ 

Figure 5.9 continued.



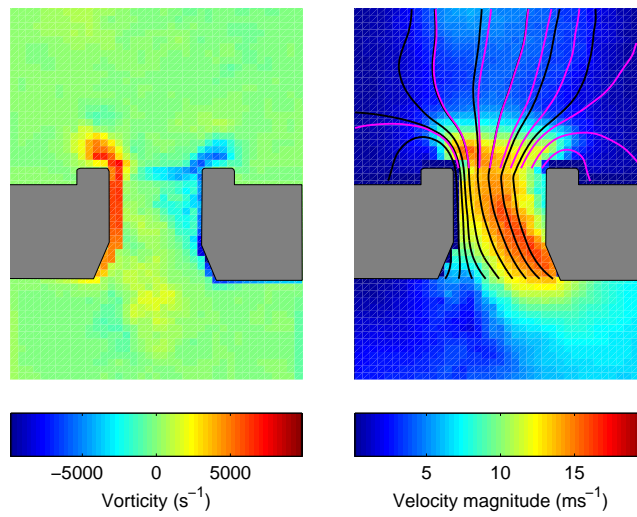
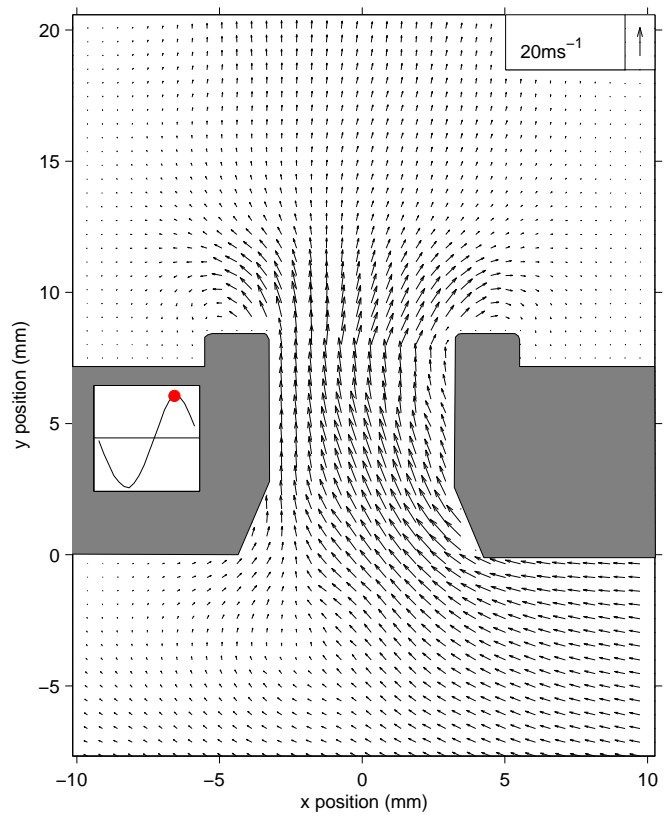
(e) Undercut tonehole,  $\bar{p}_{an} = 1101 \text{ Pa}$ ,  $i = 19$

Figure 5.9 continued.



(a) Undercut tonehole,  $\bar{p}_{an} = 1753 \text{ Pa}$ ,  $i = 11$

Figure 5.10: PIV data for the undercut tonehole at  $\bar{p}_{an} = 1753 \text{ Pa}$ .



(b) Undercut tonehole,  $\bar{p}_{an} = 1753\text{Pa}$ ,  $i = 16$

Figure 5.10 continued.

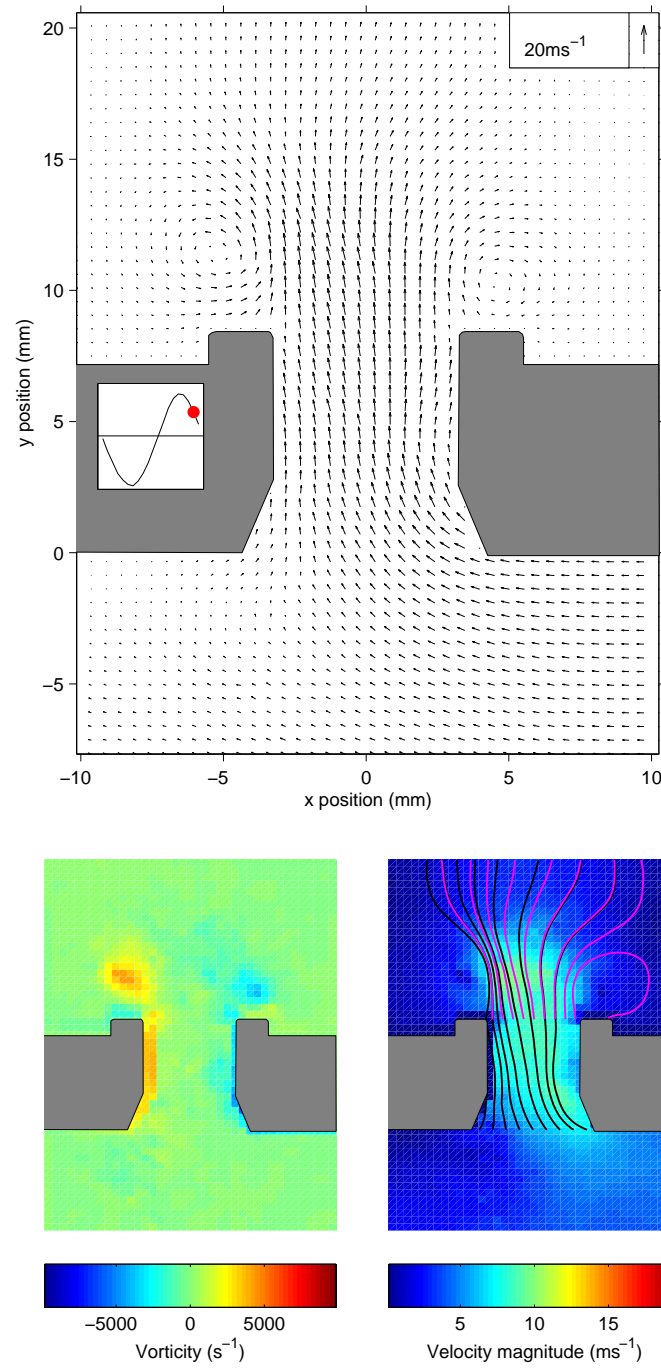
(c) Undercut tonehole,  $\bar{p}_{an} = 1753\text{Pa}$ ,  $i = 19$ 

Figure 5.10 continued.

### 5.3.11 PIV results - summary

For both toneholes it is the case that the lower-right edge is the site of the strongest non-linear flow effects, due to constraints imposed by the overall geometry of the flow. Both geometries of tonehole display a progression in the flow behaviour as the excitation level increases:

- At the lowest level, the flow can be described as approximately potential over most of the acoustic cycle.
- As the level increases, boundary separation and reattachment occurs at various locations in the tonehole at different points in the acoustic cycle leading to the formation of attached vortices. The site of the strongest separation is the lower-right edge. The flow displays characteristics of the vortex formation regime identified in the study of tube terminations.
- At the highest levels, the formed vortices are shed at a certain point in the acoustic cycle and convected by the flow. The free shear layer formed at the lower-right edge during ejection no longer reattaches to the wall of the tonehole for part of the cycle. The flow displays characteristics of the vortex shedding regime identified in the study of tube terminations.

The flow around the undercut tonehole is different to that around the square tonehole in the following ways:

- For the same value of  $\bar{p}_{an}$  the extent and magnitude of high velocity regions is reduced.
- Separation does not occur until higher values of  $\bar{p}_{an}$  have been reached.
- The flow displays much less asymmetry across the line  $x = 0$  at high values of  $\bar{p}_{an}$ .
- When vortices are shed, they are not convected as quickly.

It is clear that the overall influence of undercutting is to reduce the strength of local non-linear flow effects around a tonehole.

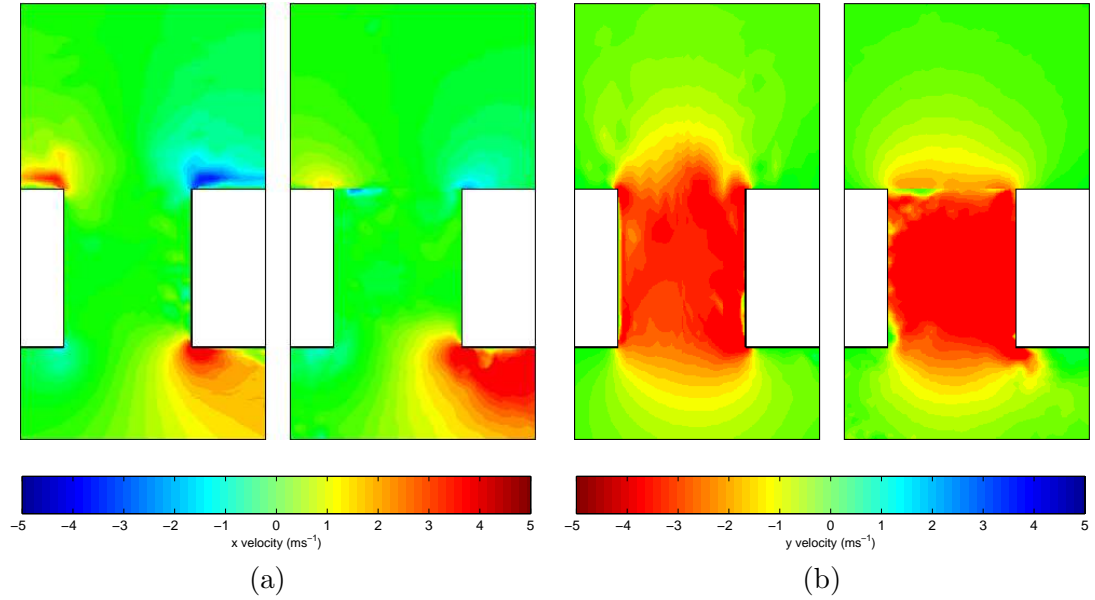


Figure 5.11: Comparison between simulated and PIV data for  $i = 6$ . White areas mark location of tonehole walls. (a)  $x$  velocity. Left: simulation. Right: PIV. (b)  $y$  velocity. Left: simulation. Right: PIV.

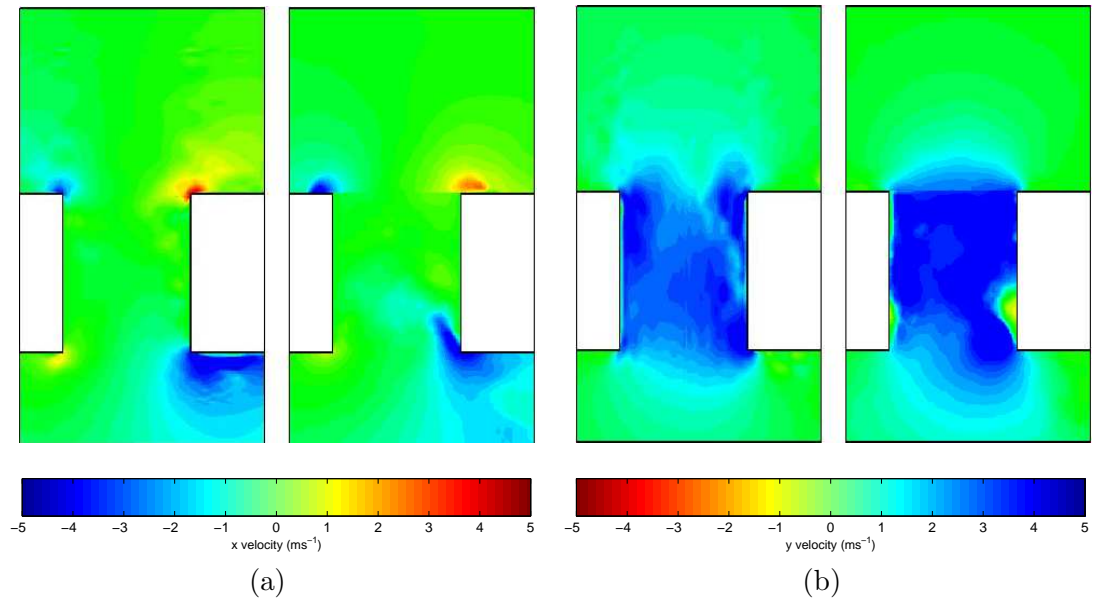


Figure 5.12: Comparison between simulated and PIV data for  $i = 16$ . White areas mark location of tonehole walls. (a)  $x$  velocity. Left: simulation. Right: PIV. (b)  $y$  velocity. Left: simulation. Right: PIV.

### 5.3.12 2D finite element model

Computational fluid dynamics simulation of the flow around a tonehole has been carried out by colleagues at the Technische Universität Dresden [Richter 07]. They solved the compressible, unsteady Navier-Stokes equation with a 2D finite element method, using the same geometry as the square experimental tonehole model. The PIV data used to compare the computational and experimental results come from an earlier set of measurements not described in the preceding sections. The main difference is that the PIV and simulation results were obtained at a higher frequency, 400Hz. Also, the value of  $\bar{p}_{an}$  was not known for the PIV measurements, so the pressure boundary conditions of the simulation were varied until a similar velocity was observed in the bulk of the flow around the tonehole.

A comparison of the simulation and PIV results at  $i = 6$  is shown in figure 5.11. Positive  $x$  velocity is defined as travelling to the right. Positive  $y$  velocity is defined as travelling upwards. It can be seen that the  $y$  velocity is similar inside the tonehole, although the magnitude is slightly higher for the PIV result. At the bottom-right corner the simulation recreates the high  $x$  velocity region visible in the PIV data. At the upper corners the simulated data shows higher magnitude  $x$  velocities of the flow entering the tonehole.

Figure 5.12 compares the simulation and PIV results at  $i = 16$ . The flow around the bottom-right corner again shows a high magnitude  $x$  velocity region in both the experimental and numerical data. The PIV data show clear boundary layer separation at the bottom-right corner which is not reproduced in the simulation. The  $x$  velocities at the top of the tonehole are similar for both, although the  $y$  velocity distribution is slightly different.

The differences between the two sets of results are possibly due to a variation in acoustic velocity amplitude. Figures 5.11 and 5.12 show that the simulation is capable of reproducing non-linear flow effects. Further work is required using more accurate experimental conditions (such as  $\bar{p}_{an}$ , tube geometry, atmospheric temperature, pressure and humidity) in the simulation.

## 5.4 Reverberation Chamber Results

This section uses data obtained from the experiments described in section 4.6 which were performed in a reverberation chamber. Firstly, the power radiated by the clarinet model with each of the two toneholes inserted is assessed, and secondly, the generation of higher harmonics is considered.



## 5.4.1 Power

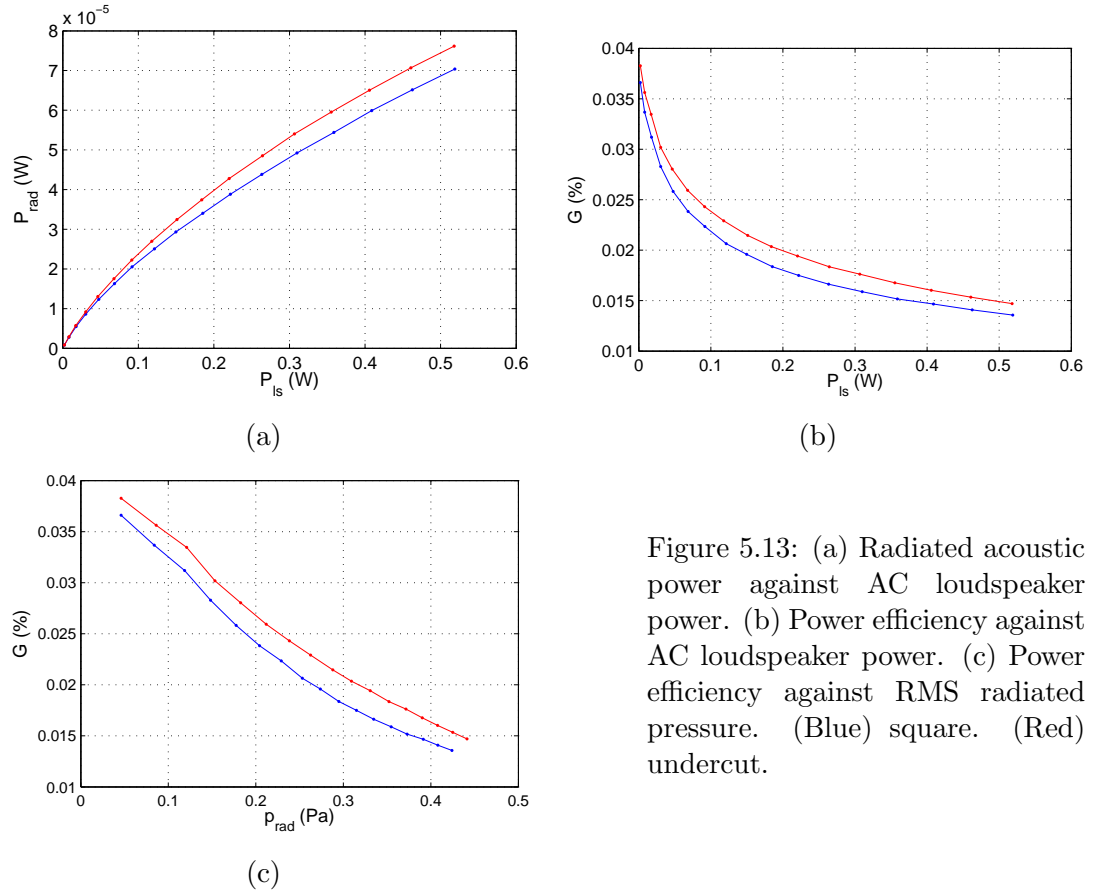


Figure 5.13: (a) Radiated acoustic power against AC loudspeaker power. (b) Power efficiency against AC loudspeaker power. (c) Power efficiency against RMS radiated pressure. (Blue) square. (Red) undercut.

Figure 5.13 shows the power efficiency of the system over the range of AC loudspeaker power used in the PIV experiments. In all of this section and the next, the blue line gives the square tonehole data and the red line is for the undercut geometry. For all measurements, the error bars were found to be smaller than the markers used for plotting. The radiated acoustic power for a given input AC power to the loudspeaker is shown in figure 5.13 (a). The range of values of radiated acoustic power are similar to those obtained by Fuks for real clarinet playing [Fuks 99]. At low values of  $P_{ls}$  the radiated power for both toneholes is approximately equal. This suggests that differences between the toneholes due to linear acoustical effects, such as differences in effective length, are negligible. Overall, the relationship between  $P_{ls}$  and  $P_{rad}$  is clearly non-linear for both toneholes. The non-linearity cannot be simply attributed to the local non-linear flow at the tonehole. The power dissipated by viscosity and heat conduction at the walls of the tube is proportional to  $\bar{p}_{an}^2$  [Disselhorst 80]. The loudspeaker is rated at 35W so in this range of input power its mechanical resistance should be constant with respect to voltage. The deviation from linearity of the undercut tonehole is less

than that for the square tonehole, and the difference between the two sets of data increases with increasing  $P_{ls}$ .

At the highest values of  $P_{ls}$ ,  $P_{rad}$  is approximately 10% higher for the undercut tonehole. This is also expressed in the undercut tonehole giving a higher efficiency than the square one, as shown in figure 5.13 (b), where the efficiency  $G$  is obtained from equation 4.9. The efficiency drops rapidly in the region of  $P_{ls}$  corresponding to levels 1 to 4 in the PIV experiments, before levelling off. When considering the system efficiency against radiated pressure (figure 5.13 (c)) the efficiency drops off at a constant rate:  $G \propto 1/\bar{p}_{rad}$ . This suggests that  $P_{ls} \propto \bar{p}_{rad}^3$ , because we know that  $P_{rad} \propto \bar{p}_{rad}^2$  and  $G \propto P_{rad}/P_{ls}$ .

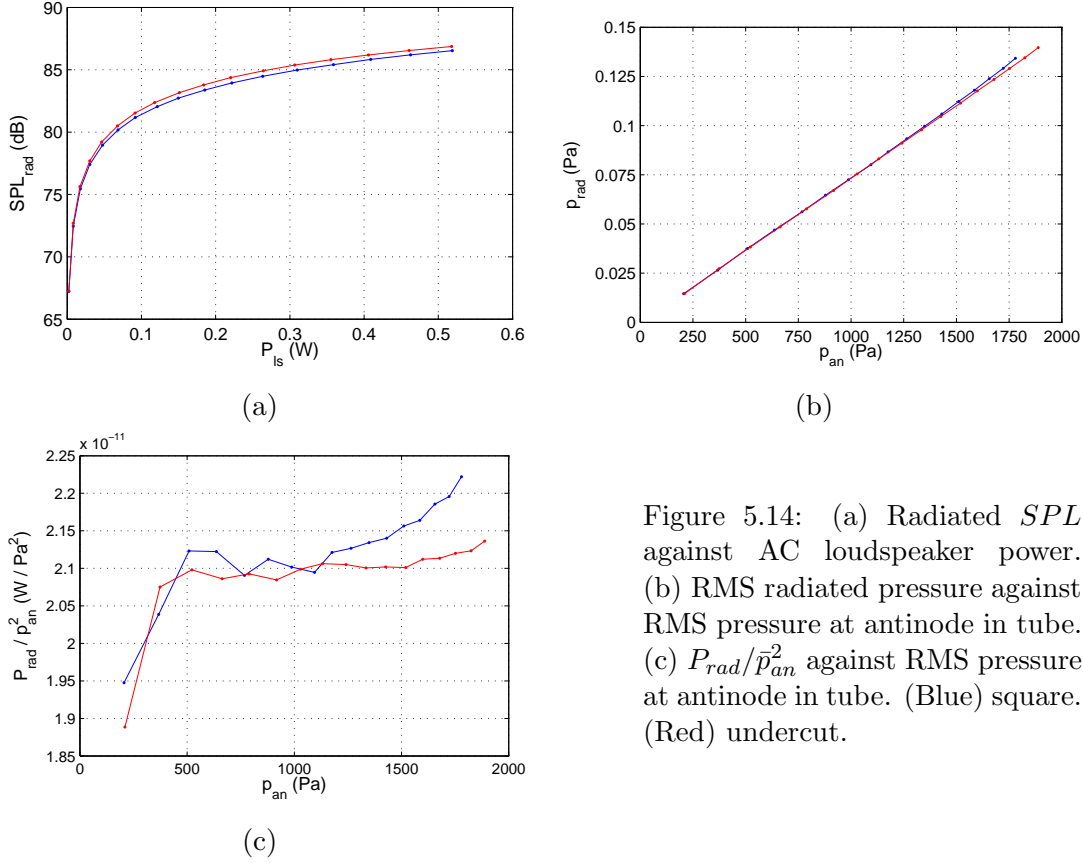


Figure 5.14: (a) Radiated  $SPL$  against AC loudspeaker power. (b) RMS radiated pressure against RMS pressure at antinode in tube. (c)  $P_{rad}/\bar{p}_{an}^2$  against RMS pressure at antinode in tube. (Blue) square. (Red) undercut.

It is not clear how the power-related behaviour described above would affect the relative musical characteristics of the two toneholes. Figure 5.14 (a) shows the radiated  $SPL$  measured in the reverberation room as a function of input power. At higher levels of  $P_{ls}$  there is a difference of  $\simeq 0.5$  dB between the radiated  $SPL$ s of the two toneholes. To obtain equal output  $SPL$ s the input power for the square tonehole would need to be increased. In playing terms this would correspond to an increase in blowing pressure

[Fuks 99]. However, the difference between the *SPLs* of 0.5dB would probably not be discernable at these sound levels under normal listening conditions [Campbell 87].

Figure 5.14 (b) shows that the relationship between the pressure inside the tube and outside the tube is linear. The lines for the two toneholes coincide, apart from at the highest levels of  $\bar{p}_{an}$  where the radiated pressure is higher for the square geometry.

Equations 2.21 and 5.1 tell us that  $P_{rad}/\bar{p}_{an}^2$  should be approximately proportional to the real part of the radiation impedance of the tube.  $P_{rad}$  measured here does not include any energy which is converted into the kinetic energy of the non-linear flow effects, just that which is radiated from the tube as acoustic motion. Therefore, it is expected that  $P_{rad}/\bar{p}_{an}^2$  (and hence the radiation resistance) should be constant with respect to  $\bar{p}_{an}$ , as predicted by linear theory. Figure 5.14 (c) gives this data for the two toneholes. The low level behaviour for each tonehole is difficult to interpret but from  $\bar{p}_{an} \simeq 500\text{Pa}$  to  $\bar{p}_{an} \simeq 1000\text{Pa}$  the lines of both toneholes are approximately constant. Then, at around 1000Pa the value of  $P_{rad}/\bar{p}_{an}^2$  for the square tonehole begins to increase in a roughly linear fashion. The same transition then occurs for the undercut tonehole at around 1500Pa. This result is unexpected and is explained in the following section.

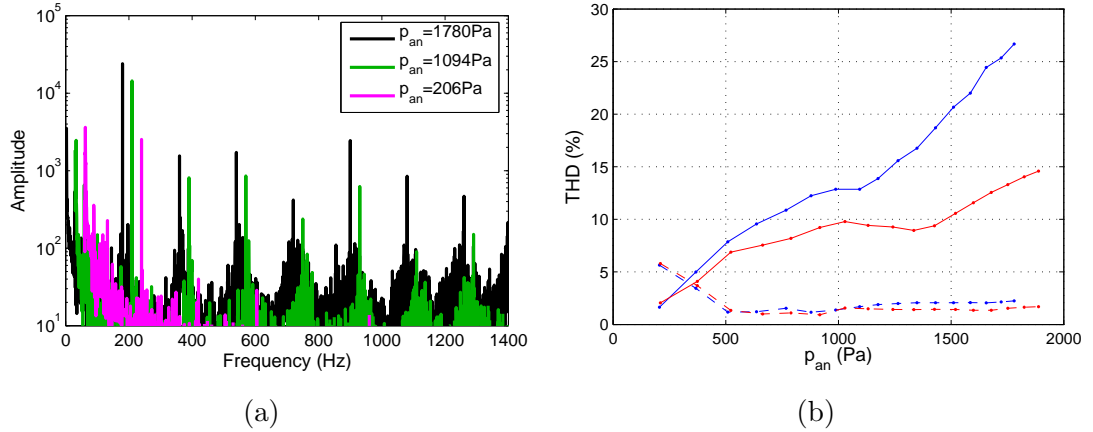


Figure 5.15: (a) Frequency spectra of radiated pressure for square tonehole at three values of  $\bar{p}_{an}$ . Frequencies have been offset for the two lower values of  $\bar{p}_{an}$  to allow comparison of amplitudes. (b) Total harmonic distortion of radiated pressure against RMS pressure at antinode in tube. (Blue) square. (Red) undercut. Dashed line is total harmonic distortion of pressure at antinode in tube.

#### 5.4.2 Harmonic generation

The frequency spectrum of the radiated pressure from the clarinet model into the reverberation chamber was also analysed. Figure 5.15 (a) shows frequency spectra for three increasing sound levels with the square tonehole. Frequencies have been offset

for the two lower values of  $\bar{p}_{an}$  to allow a clearer comparison of amplitudes. At  $\bar{p}_{an} = 206\text{Pa}$  the spectrum is dominated by the peak at 180Hz, the frequency of excitation by the loudspeaker. The relative heights of the higher harmonics can then be seen to increase as  $\bar{p}_{an}$  increases.

The amount of harmonic distortion introduced to the radiated pressure signal at different levels of  $\bar{p}_{an}$  can be seen in figure 5.15 (b) for both toneholes. Here the total harmonic distortion has been calculated in terms of amplitude using the five harmonics above the fundamental:

$$THD = 100 \frac{\sqrt{H_2^2 + H_3^2 + H_4^2 + H_5^2 + H_6^2}}{H_1^2} \quad (5.2)$$

where  $H_n$  is the RMS amplitude of the  $n$ th harmonic measured in frequency space. There are three possible causes for the generation of higher harmonics in the radiated signal: loudspeaker distortion, non-linear propagation of the sound wave in the tube and distortion due to the local non-linear effects at the tonehole. Figure 5.15 (b) also shows the  $THD$  for the pressure measured roughly halfway along the inside of the tube using the PCB transducer. At low levels of  $\bar{p}_{an}$  this has unusually high values due to the quantisation of the voltage output from the PCB transducer, but over most of the measured range the antinode  $THD$  is constant at around 2%. This rules out loudspeaker distortion as a significant contributor to the  $THD$  of the radiated pressure. It also shows that, halfway along the tube, non-linear propagation is not a major factor either. The conclusion is that the main cause of higher harmonic generation is the observed local non-linear flow effects.

The overall behaviour of the radiated  $THD$  curves for the two toneholes is quite similar.  $THD$  increases, before a dip and then a further increase. The gradient for the square tonehole is consistently greater than that for the undercut tonehole. The discontinuity occurs at a lower value of  $\bar{p}_{an}$  for the square tonehole. The start of the second increase in  $THD$  for both geometries appears to correspond to the start of the increase in  $P_{rad}/\bar{p}_{an}^2$  observed in figure 5.14 (c):  $\bar{p}_{an} = 1200\text{Pa}$  for the square tonehole and  $\bar{p}_{an} = 1500\text{Pa}$  for the undercut tonehole. This suggests that the deviation of  $P_{rad}/\bar{p}_{an}^2$  from the constant value predicted by linear theory is associated with the generation of higher harmonics.

To test this hypothesis, the analysis of section 5.4 will be repeated, but with the higher harmonics of the pressure signals ( $p_{an}$  and  $p_{rad}$ ) removed, so that the calculation of  $P_{rad}/\bar{p}_{an}^2$  is done using only the fundamental component of each signal. The results of this analysis are shown in figure 5.16.

Figure 5.16 (a) suggests that the deviation of the  $\bar{p}_{rad}$  data for the square hole

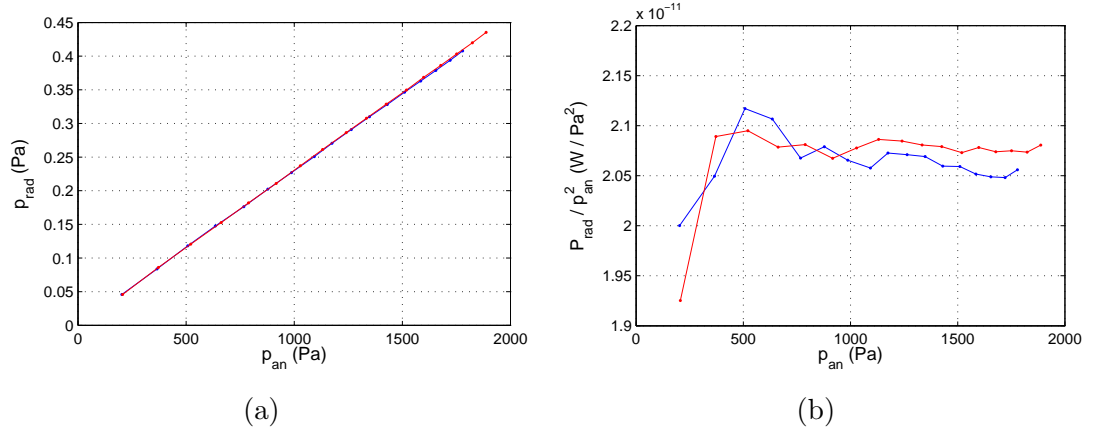


Figure 5.16: (a) RMS radiated pressure against RMS pressure at antinode in tube using only fundamental component of signal. (b)  $P_{rad}/\bar{p}_{an}^2$  against RMS pressure at antinode in tube using only fundamental component of signal. (Blue) square. (Red) undercut.

observed in figure 5.14 (b) is the result of the greater strength of the higher harmonics generated in the radiated pressure for that geometry. Apart from at the lowest values of  $\bar{p}_{an}$ , figure 5.16 (b) now shows  $P_{rad}/\bar{p}_{an}^2$  to be approximately constant over the measured range. This again implies that the non-linear behaviour observed in 5.14 (c) is caused by the generation of higher harmonics in the radiated pressure.

## 5.5 Conclusions

The PIV results presented in this chapter have provided new insights into the flow around woodwind instrument toneholes. Non-linear flow effects are apparent at all sound levels for this excitation frequency, even at the lowest measured sound level, which is probably unplayable on a real instrument. The part of the tonehole which experiences the longest free shear layers, highest velocities and largest vorticities is the internal edge, on the loudspeaker side of the tonehole. This is true for both geometries. While this upstream edge of a tonehole is often selectively undercut for tuning purposes [Nederveen 98a, Greenham 03], these results suggest that smoothing this edge will also have a strong effect on the energy lost to non-linear effects.

The PIV results also demonstrate that undercutting reduces the strength of local non-linear flow effects around a tonehole, by reducing the extent of boundary layer separation at a given sound level.

The difference between the two toneholes has also been shown in terms of radiated sound power and higher harmonic generation. The results show that the generation of higher harmonics contributes to the so-called ‘non-linear radiation resistance’ that has been observed in previous studies [Atig 03, Skulina 05a, Dalmont 02]. The energy

which goes into generating the higher harmonics, as well as the energy required to form the observed non-linear flow effects, causes the radiation resistance of the clarinet model to depart from its linear theoretical value.

## Chapter 6

# POD Applied to PIV Data of Oscillating Flow at a Tube Termination

### 6.1 Introduction

When a sound wave of a sufficiently large amplitude travels past a sufficiently sharp discontinuity, local non-linear flow effects are generated which are superimposed onto the acoustic flow. Proper Orthogonal Decomposition (POD) is a flow analysis technique used, most commonly in the study of turbulent flows, to identify distinct flow structures. Marx et al [Marx 08] have recently suggested that it is possible to separate a purely acoustic flow from the non-linear flow induced by it using POD. They applied the technique to PIV data of oscillating flow around a step inside a closed waveguide. In this chapter the use of POD to study local non-linear effects created by an acoustic flow is extended to the case of a tube open at one end under resonance.

This configuration has been examined by a number of authors. In particular, the power lost from the standing wave to local non-linear flow effects at the end of the tube has been measured [Peters *et al* 93, Atig 03, Atig 04a]. Skulina has also performed PIV measurements of the oscillating flow field outside the end of the tube [Skulina 05a]. POD is here applied to those PIV data. The experimental apparatus and procedure is briefly described in section 6.3. The principles of POD are then outlined in 6.4.1. Marx et al define a parameter  $e_1$  to quantify the transfer of kinetic energy from the acoustic motion to the non-linear flow effects. One of the aims of this chapter is to assess the usefulness of  $e_1$ , which is defined in section 6.4.2.

The results of the POD are presented in section 6.5. Section 6.5.1 considers how accurately POD can pick out the purely acoustic motion. Section 6.5.2 looks at how

POD describes the non-linear flow effects. The energy transferred to local non-linear flow effects is analysed using  $e_1$  in section 6.5.3, which concludes with a discussion on the governing Strouhal number of the flow.

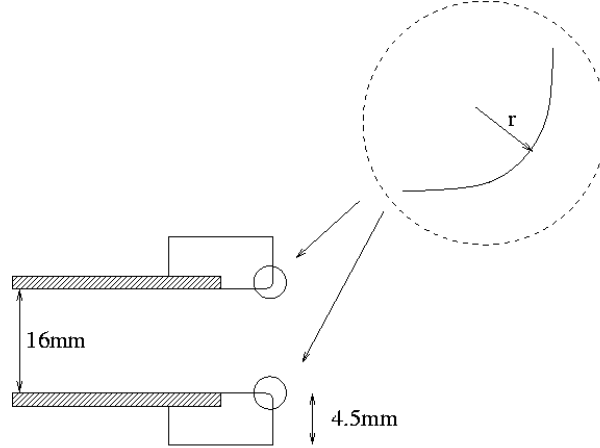


Figure 6.1: Geometry of tube termination used in this study, showing  $r$ , the radius of curvature of the inside corner.

## 6.2 Background

Recent work by Atig [Atig 03, Atig 04a] applied a two microphone impedance measurement technique to a system consisting of a loudspeaker coupled to an open-ended tube. The rate of energy loss due to local non-linear flow effects at the end of the tube was expressed as a modification to the real part of the radiation impedance. It was shown that the radius of curvature of the inner edge of the tube termination ( $r$ , see figure 6.1) has a significant effect on the behaviour of the real part of the termination impedance at high acoustic amplitudes.

The real part of the non-dimensionalised radiation impedance plotted against the RMS acoustic velocity measured at the velocity anti-node at the end of the tube ( $\bar{u}_{an}$ ) is shown in figure 6.2 for a number of values of  $r$ . These are  $r = 0\text{mm}$  (a square corner),  $r = 0.3\text{mm}$  and  $r = 1\text{mm}$ . At low velocities the curves are consistent with linear theoretical predictions, lying somewhere between the flanged and unflanged cases. The linear values are for the case when the only energy lost from the standing wave in the tube is that belonging to the radiated sound. Any deviation from the linear value therefore corresponds to energy which is not radiated as sound from the open end. This is assumed to be the power contained in the local non-linear flow phenomena.

Two points may be made about figure 6.2. The rate of increase of  $Re(Z_r/Z_c)$  with



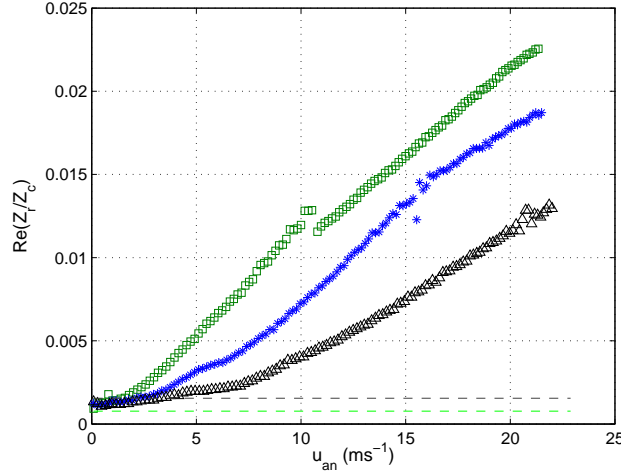


Figure 6.2: Real part of the radiation impedance as a function of the RMS acoustic velocity at the open end for the two different terminations. ( $\square$ )  $r = 0\text{mm}$ . ( $*$ )  $r = 0.3\text{mm}$ . ( $\triangle$ )  $r = 1\text{mm}$ . (—) linear theory, flanged. (---) linear theory, unflanged. From Atig [Atig 04a].

$\bar{u}_{an}$  is greater for smaller values of  $r$ . Also, for each termination geometry there is discontinuity in the data, occurring at a smaller value of  $\bar{u}_{an}$  for a smaller value of  $r$ .

Skulina performed PIV measurements outside the end of a tube driven by a loudspeaker. It was attempted to make the apparatus as similar as possible to that used by Atig [Skulina 05a]. Some of the results of these measurements were described in section 5.2. From observations of the PIV maps at different values of  $\bar{u}_{an}$  and  $r$ , it was concluded that the discontinuities in the radiation resistance data coincided with the transition from attached vortex formation to vortex shedding from the end of the tube. Skulina also measured the radiation resistance of the tube using PIV velocity data and pressure data from a probe microphone. The radiation resistance measured this way also contained discontinuities which corresponded with the transition to vortex shedding.

Marx et al [Marx 08] performed PIV on the flow around a step in a closed waveguide excited at resonance. It was found that POD could be used to pick out a motion that spatially resembled potential flow and varied as a sine wave in time, with the frequency of the loudspeaker excitation. This was identified with the purely acoustic motion. Other modes of the POD described the formation and development of vortices over the acoustic cycle. It was found that the amount of energy in the vortex formation modes relative to the acoustic mode was largely dictated by the Strouhal number of the flow.

### 6.3 Experimental apparatus

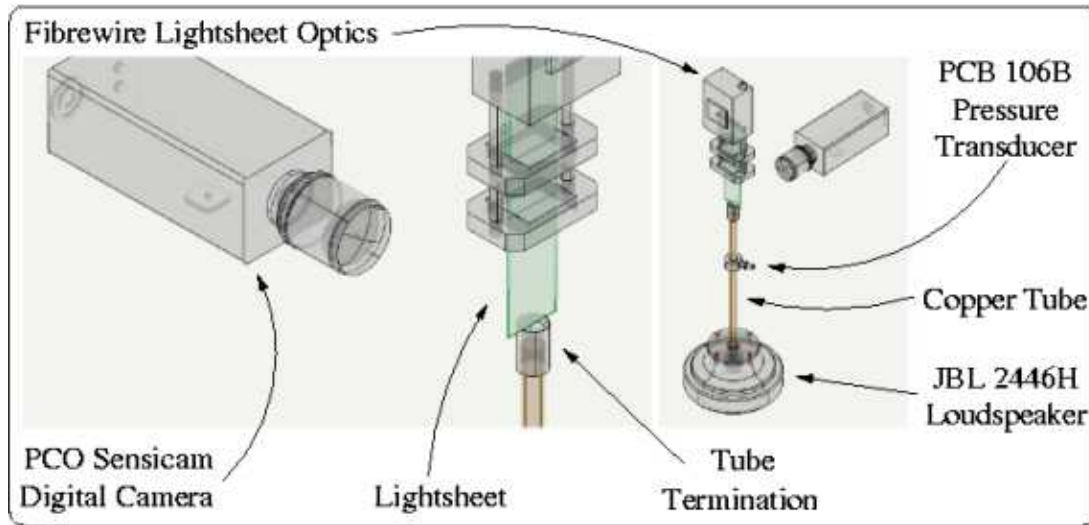


Figure 6.3: Experimental apparatus for tube termination PIV experiments. Taken from [Skulina 05a].

A diagram showing the main experimental apparatus used in the PIV experiments is given in figure 6.3. A copper tube of internal radius 8mm and wall thickness 1mm was coupled to a JBL 2446H  $8\Omega$  compression driver. A termination with a particular value of  $r$  was fitted to the open end. The values of  $r$  examined here are  $r = 0\text{mm}$ ,  $r = 0.3\text{mm}$  and  $r = 1\text{mm}$ . All terminations had a wall thickness of 4.5mm. The terminations were constructed in aluminium and then anodised black to minimise reflective surfaces for use in PIV experiments. The length of the tube from the loudspeaker cavity to the open end of the termination was 460mm. A frequency response analysis of the tube/termination/loudspeaker system indicated a fundamental resonant frequency of 380Hz. The system was excited at this frequency for the PIV measurements.

A PCB Piezotronics model 106B pressure transducer was mounted into the copper tube 160mm from the open end and was used to measure the sound pressure within the tube. From this, the RMS pressure at the pressure anti-node  $\bar{p}_{an}$  (located roughly halfway along the tube) could be calculated.

#### 6.3.1 PIV measurement procedure

Seeding particles with a mean diameter of  $1\mu\text{m}$  were generated using a Safex Nebelgerät F2004 fog generator using standard fog fluid and injected into the measurement area. The sound pressure within the tube was monitored by viewing the output signal from

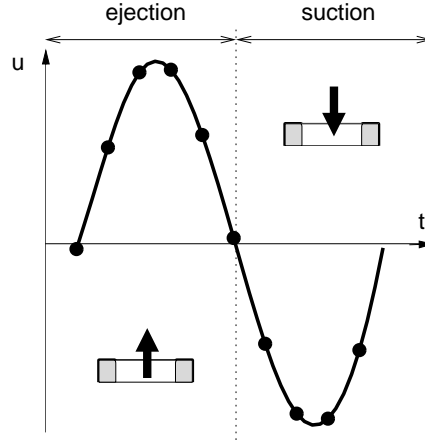


Figure 6.4: Points in cycle at which PIV measurements are made,  $t_i$ .

the PCB transducer, after passing through a PCB Piezotronics ICP sensor signal conditioner type 482A22, on an oscilloscope. The value of  $\bar{p}_{an}$  was adjusted by varying the volume control on the amplifier. The synchronised PIV measurement sequence described in section 3.5 was then initiated and repeated for each of 10 phase steps through the acoustic cycle, labelled  $t_i$ ,  $i = 1 \dots 10$ . These are shown in figure 6.4. The part of the cycle when the flow is coming out of the tube is labelled *ejection*, and the inward motion *suction*. 30 PIV image pairs were recorded at each phase step. Measurements were made at a number of values of  $\bar{p}_{an}$  ranging between 200Pa and 8000Pa for each of the tube terminations.

## 6.4 Analysis

For a particular  $\bar{p}_{an}$  and termination geometry, 300 image pairs are cross-correlated and filtered with a  $32 \times 32$  pixel interrogation window and a 50% overlap resulting in a grid of  $79 \times 63$  velocity vectors per image pair. For each phase step  $t_i$ , there are  $n = 30$  instantaneous vector fields  $\mathbf{u}_n(x, y, t_i)$ ,  $n = 1 \dots 30$ . These are averaged for each phase step to give a phase-averaged vector field  $\mathbf{u}(x, y, t_i)$ .

### 6.4.1 POD

POD is a form of statistical analysis that has been used to identify large-scale structures in complex flows by decomposing a set of descriptive velocity fields into a basis of eigenfunctions [Berkooz 93, Graftieaux 01, Webber 02]. Any stage in the flow can then be reconstructed using a linear combination of basis modes  $\Phi(x, y)$  which are ordered according to kinetic energy. POD can be described as searching in the set of  $\mathbf{u}(x, y, t_i)$  for the  $\Phi(x, y)$  which is closest on average in terms of energy to all the members in the set, then finding the  $\Phi(x, y)$  which is next closest, etc. Mathematically this is equivalent to solving the Fredholm equation

$$\int \int \langle \mathbf{u}(x, y, t_i) \mathbf{u}(x', y', t_i) \rangle \Phi_m(x', y') dx' dy' = \lambda_m \Phi_m(x, y) \quad (6.1)$$

where  $\lambda_m$  is the eigenvalue corresponding to eigenfunction  $\Phi_m$ .  $\langle \dots \rangle$  represents an average over time and the integrals are taken over  $x$  and  $y$ .

The experimental data obtained using PIV, having more spatial than temporal information, lends itself to the snapshot method of POD [Sirovich 87]. Consider a set of  $N_t$  velocity vector maps, with  $N_x \times N_y$  velocity vectors in each map and distances  $\delta x$  and  $\delta y$  between vectors in the  $x$  and  $y$  directions. The first step is to construct the correlation matrix

$$K_{ij} = \frac{1}{N_t} \sum_{x=1}^{N_x} \sum_{y=1}^{N_y} \mathbf{u}(x, y, t_i) \cdot \mathbf{u}(x, y, t_j) \delta x \delta y. \quad (6.2)$$

The eigenvectors of this matrix  $V_m(t_i)$  are then found and ordered according to their eigenvalues  $\lambda_m$ .  $V_m(t_i)$  gives the temporal evolution of each mode.  $\lambda_m$  is descriptive of the kinetic energy associated with each mode because the correlation matrix  $K_{ij}$  consists of terms in  $u^2$ . The corresponding spatial mode  $\Psi_m(x, y)$  is then calculated:

$$\Psi_m(x, y) = \sum_{i=1}^{N_t} \mathbf{u}(x, y, t_i) \cdot V_m(t_i) \delta t. \quad (6.3)$$

Any velocity map can then be described as a superposition of modes using:

$$\mathbf{u}(x, y, t_i) = \sum_{m=1}^{N_t} V_m(t_i) \Psi_m(x, y). \quad (6.4)$$

However,  $\Psi_m(x, y)$  is usually normalised to  $\Phi_m(x, y)$  via

$$\Phi_m = \frac{\Psi_m}{\left( \sum_{x=1}^{N_x} \sum_{y=1}^{N_y} \Psi_m \cdot \Psi_m \delta x \delta y \right)^{1/2}} \quad (6.5)$$

and the corresponding time coefficients  $a_m(t_i)$  are calculated as

$$a_m(t_i) = \sum_{x=1}^{N_x} \sum_{y=1}^{N_y} \mathbf{u}(x, y, t_i) \cdot \Phi_m(x, y) \delta x \delta y. \quad (6.6)$$

Any of the original velocity maps can then be written

$$\mathbf{u}(x, y, t_i) = \sum_{m=1}^{N_t} a_m(t_i) \Phi_m(x, y). \quad (6.7)$$

In order to ensure that the most energetic POD mode obtained is likely to be oscillatory, the cycle-averaged flow is first subtracted from the velocity vector field at each phase step so that

$$\hat{\mathbf{u}}(x, y, t_i) = \mathbf{u}(x, y, t_i) - \tilde{\mathbf{u}}(x, y) \quad (6.8)$$

is analysed using POD. In the above equation

$$\tilde{\mathbf{u}}(x, y) = \frac{1}{N_t} \sum_{i=1}^{N_t} \mathbf{u}(x, y, t_i). \quad (6.9)$$

This is the cycle-averaged flow and describes the jet-driven acoustic streaming resulting from boundary layer separation at the termination (see section 2.7.8). It is common practice to remove the mean from flow velocity data before performing POD [Kostas 05].

#### 6.4.2 Energy transfer

$\lambda_m$  (as defined in equation 6.1) can be used to measure the relative strength of each POD mode. Due to the way that  $K_{ij}$  is constructed (see equation 6.2),  $\lambda_m$  can be defined as

$$\lambda_m = \frac{1}{N_t} \sum_{i=1}^{N_t} \sum_{x=1}^{N_x} \sum_{y=1}^{N_y} |a_m(t_i) \Phi_m(x, y)|^2 = \frac{1}{N_t} \sum_{i=1}^{N_t} \sum_{x=1}^{N_x} \sum_{y=1}^{N_y} |\mathbf{u}_m(x, y, t_i)|^2 \quad (6.10)$$

where

$$\mathbf{u}_m(x, y, t_i) = a_m(t_i) \Phi_m(x, y) \quad (6.11)$$

is the velocity map described by POD mode  $m$  at time  $t_i$ . It can be seen therefore that  $\lambda_m$  is proportional to the kinetic energy per unit mass in POD mode  $m$ , averaged over the number of time steps.

Marx et al [Marx 08] found that the first POD mode ( $m = 1$ ) approximately

described the acoustic motion in oscillating flow around a step. In order to characterise the relative amount of energy transferred into non-linear flow effects, they defined the parameter

$$e_1 = \frac{\sum_{m=2}^{m=N_t} \lambda_m}{\sum_{m=1}^{m=N_t} \lambda_m} \quad (6.12)$$

which is expressed as a percentage. The difference in this study is that the cycle-averaged flow has been removed before carrying out the POD, so  $e_1$  contains no information about the energy of the streaming.

## 6.5 Results

Figures 6.5 (a) to (h) show the decomposition of the flow obtained by taking the cycle average and then performing POD. These results are for the  $r = 0.3\text{mm}$  termination at 8 different values of  $\bar{p}_{an}$ . The upper-left vector map shows the cycle-averaged flow. The upper-right graph shows the temporal coefficients of POD modes 1 and 2,  $a_1(t_i)$  and  $a_2(t_i)$ . The corresponding spatial fields are then given below:  $\Phi_1(x, y)$  on the bottom-left and  $\Phi_2(x, y)$  on the bottom-right.

For clarity, the vector maps show the left-hand side of the termination, with the zero of the x axis corresponding to the central axis of the tube. The vector maps have been scaled to allow comparison of the velocity magnitudes between cycle-averaged flow and the first two POD modes. Therefore, the vector map for  $\Phi_1(x, y)$  consists of velocity data obtained by multiplying  $\Phi_1(x, y)$  by the maximum value of  $a_1(t_i)$ . A similar process is carried out for  $\Phi_2(x, y)$ . A reference vector is given in the top-left of each vector map.

The form of a particular POD mode at a certain time in the cycle  $t_i$  can be obtained by multiplying the vectors of the relevant vector field  $\Phi_m(x, y)$  by the appropriate temporal coefficient  $a_m(t_i)$ . We begin by examining mode 1 of the POD.

### 6.5.1 POD mode 1

In the case of high-amplitude oscillating flow around a step, Marx et al [Marx 08] identify the first mode of the POD with the purely acoustic motion. Three criteria are proposed here to explore the validity of this identification:

1. The coefficients  $a_1(t_i)$  vary sinusoidally with time.
2. The velocity vector field  $\Phi_1(x, y)$  is similar in form to the  $\Phi_1(x, y)$  seen at low  $\bar{p}_{an}$ , when non-linear flow phenomena are negligible.
3. It is possible to fully describe the non-linear flow phenomena without mode 1.

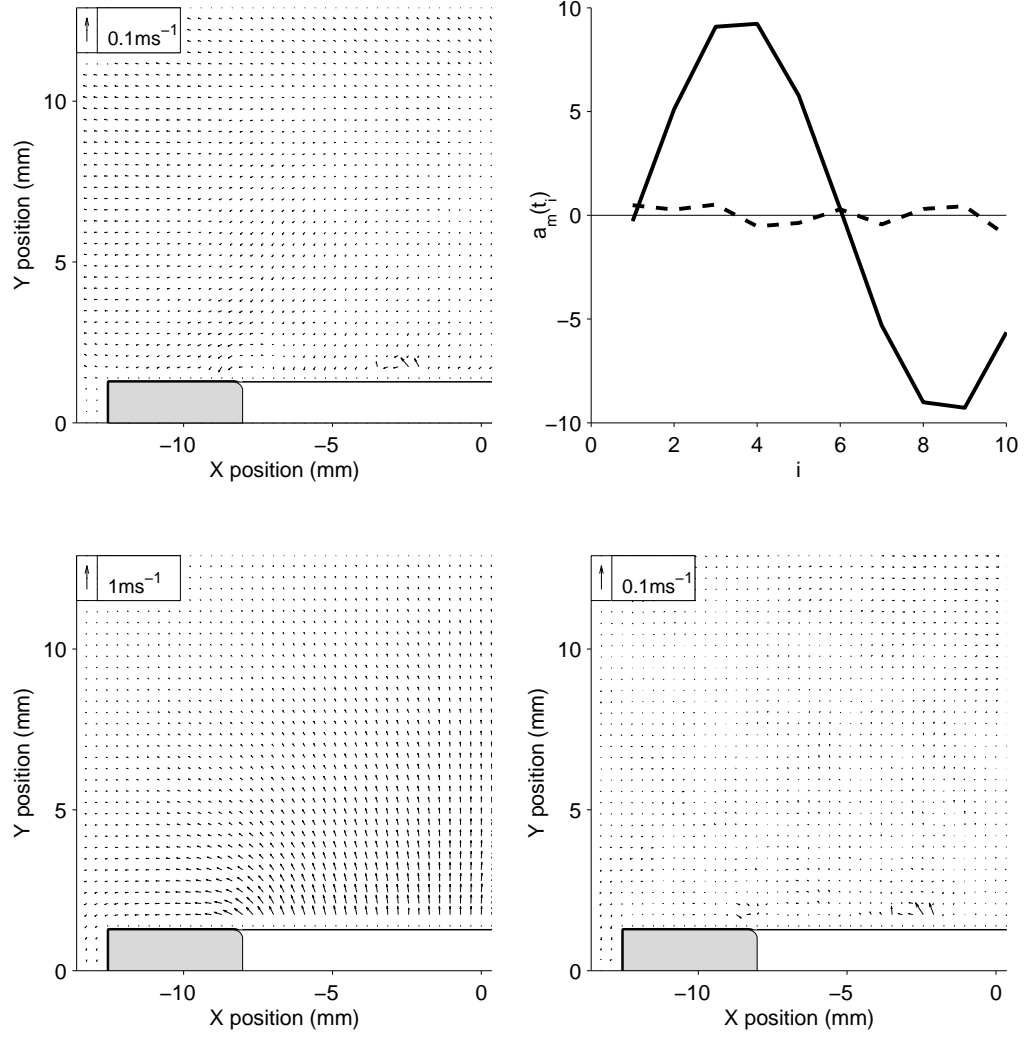
(a)  $\bar{p}_{an} = 203\text{Pa}$ .

Figure 6.5: Flow decomposition for  $r = 0.3\text{mm}$  termination. Top left: Streaming flow  $\tilde{\mathbf{u}}(x, y)$ . Top right:  $a_m(t_i)$  of first 2 POD modes ( $-$ )  $a_1$ , ( $- - -$ )  $a_2$ . Bottom left:  $\Phi_1(x, y)$ . Bottom right:  $\Phi_2(x, y)$ . Spatial maps show left half of termination, with grey areas representing termination wall.

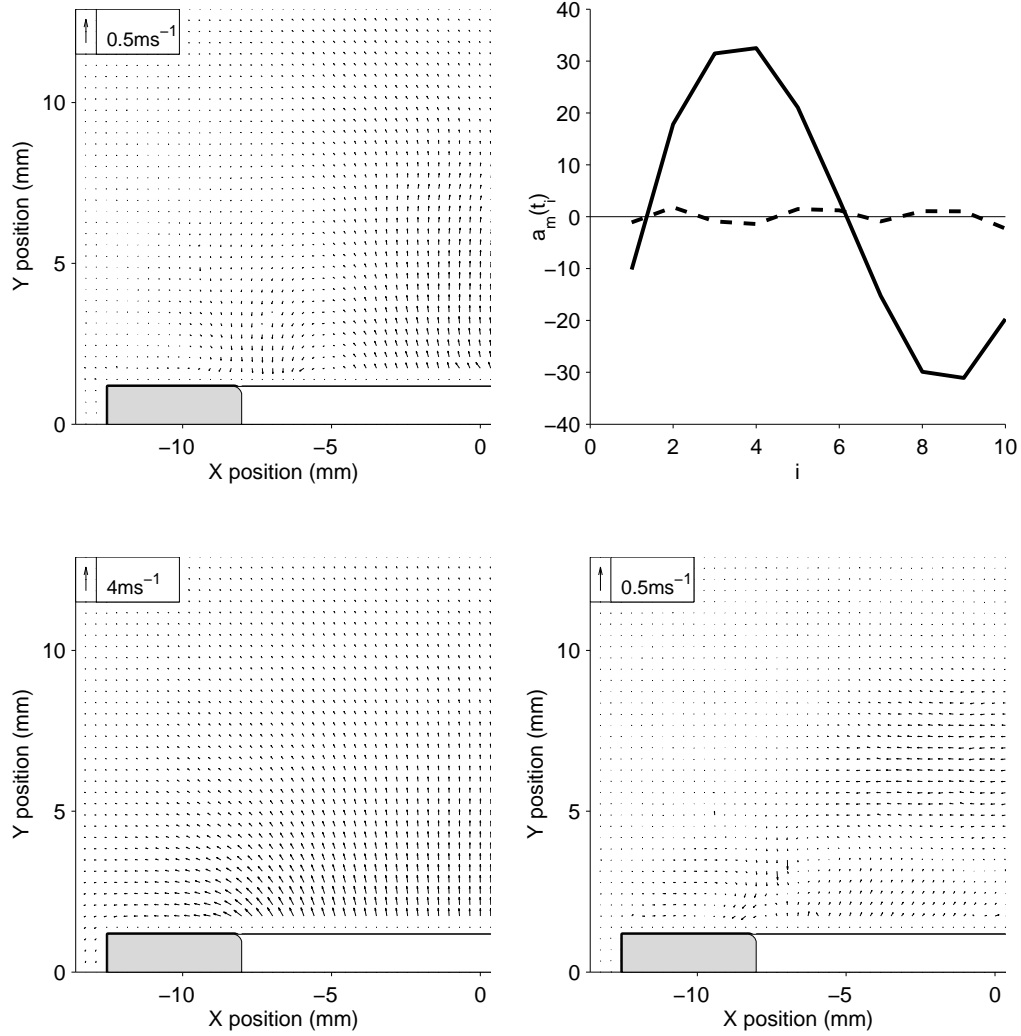
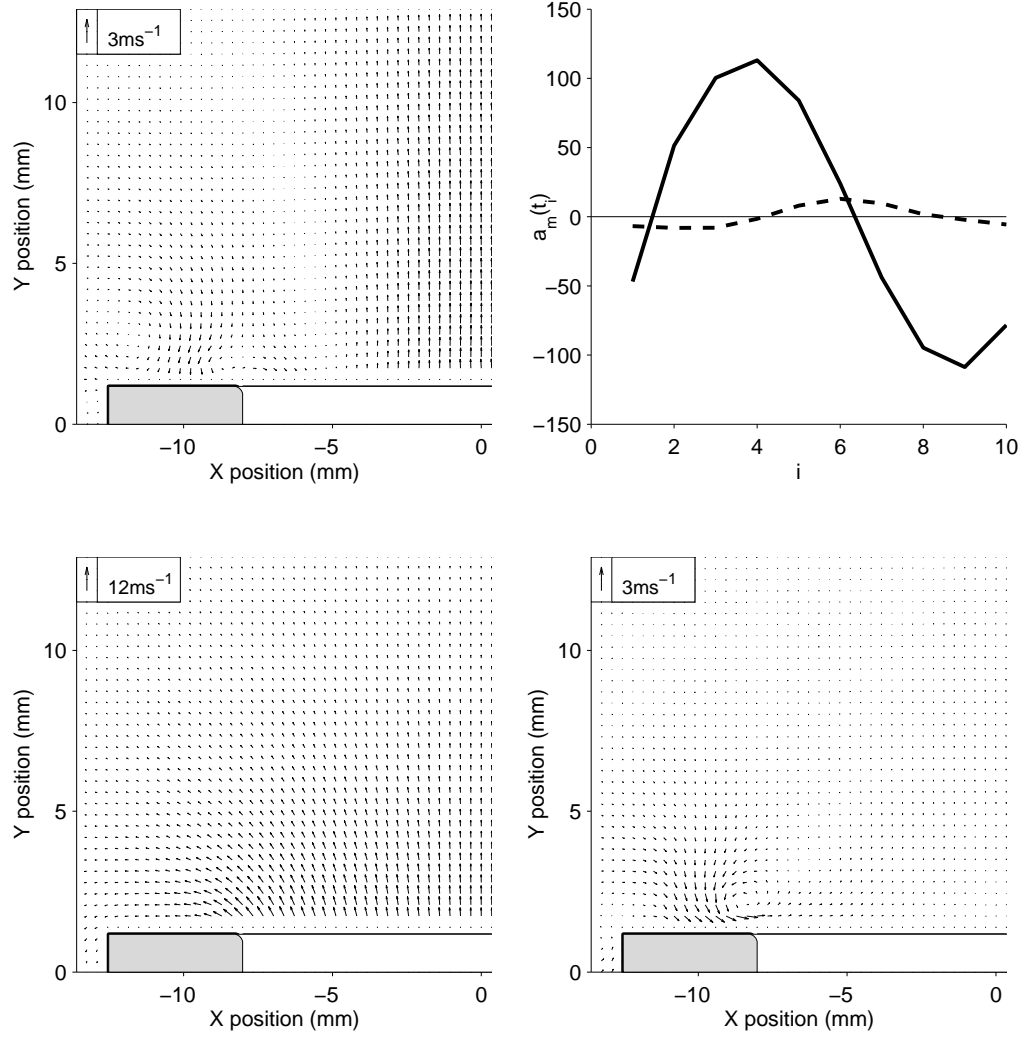
(b)  $\bar{p}_{an} = 685\text{Pa}$ .

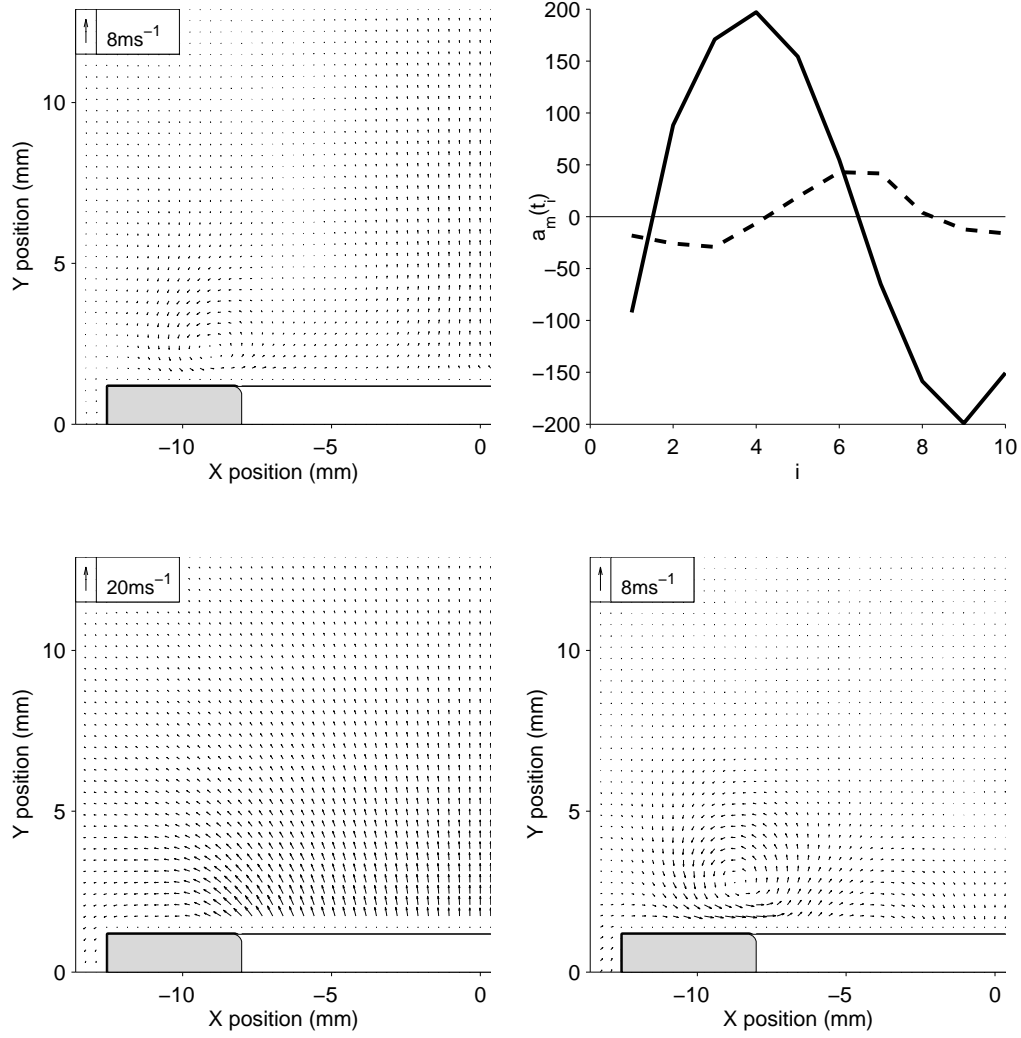
Figure 6.5 continued. Flow decomposition for  $r = 0.3\text{mm}$  termination. Top left: Streaming flow  $\tilde{\mathbf{u}}(x, y)$ . Top right:  $a_m(t_i)$  of first 2 POD modes (—)  $a_1$ , (---)  $a_2$ . Bottom left:  $\Phi_1(x, y)$ . Bottom right:  $\Phi_2(x, y)$ .





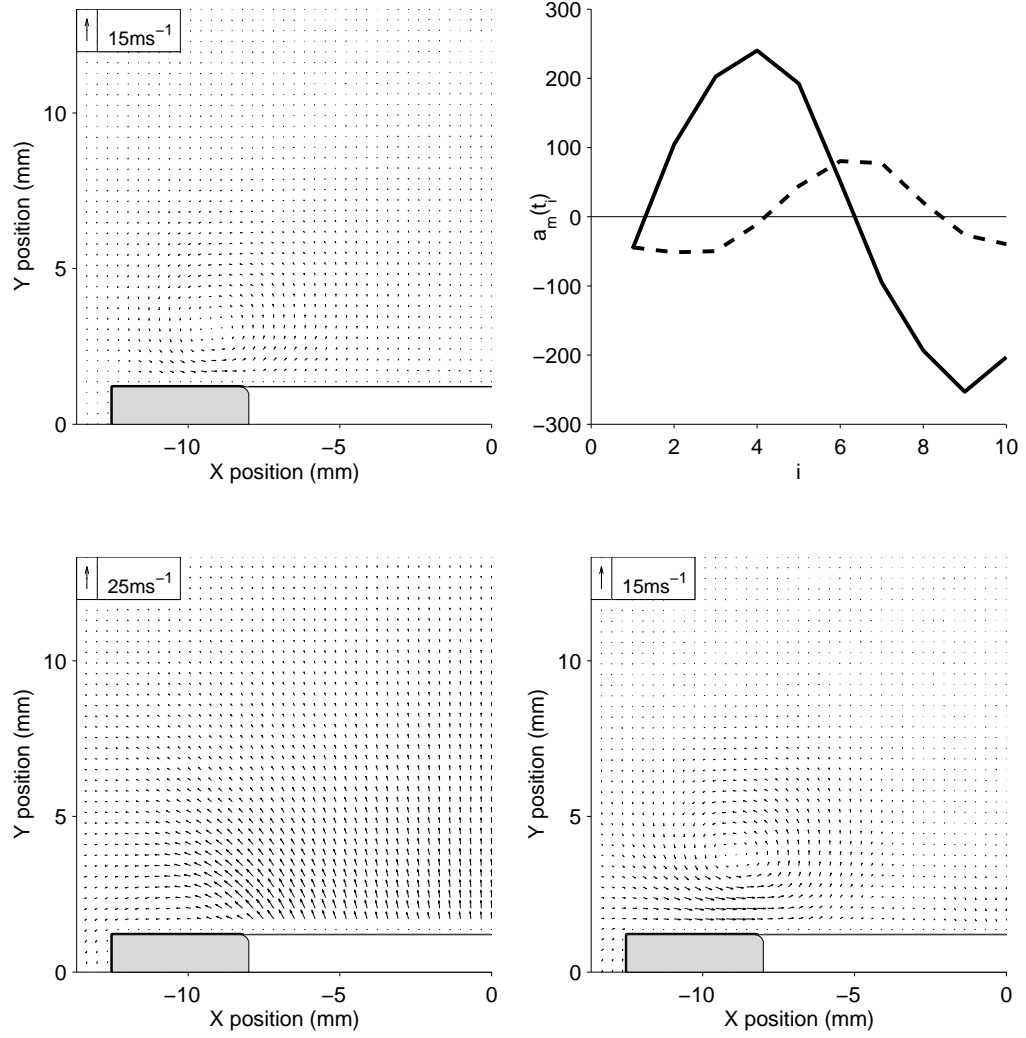
(c)  $\bar{p}_{an} = 2224\text{Pa}$ .

Figure 6.5 continued. Flow decomposition for  $r = 0.3\text{mm}$  termination. Top left: Streaming flow  $\tilde{\mathbf{u}}(x, y)$ . Top right:  $a_m(t_i)$  of first 2 POD modes (—)  $a_1$ , (---)  $a_2$ . Bottom left:  $\Phi_1(x, y)$ . Bottom right:  $\Phi_2(x, y)$ .



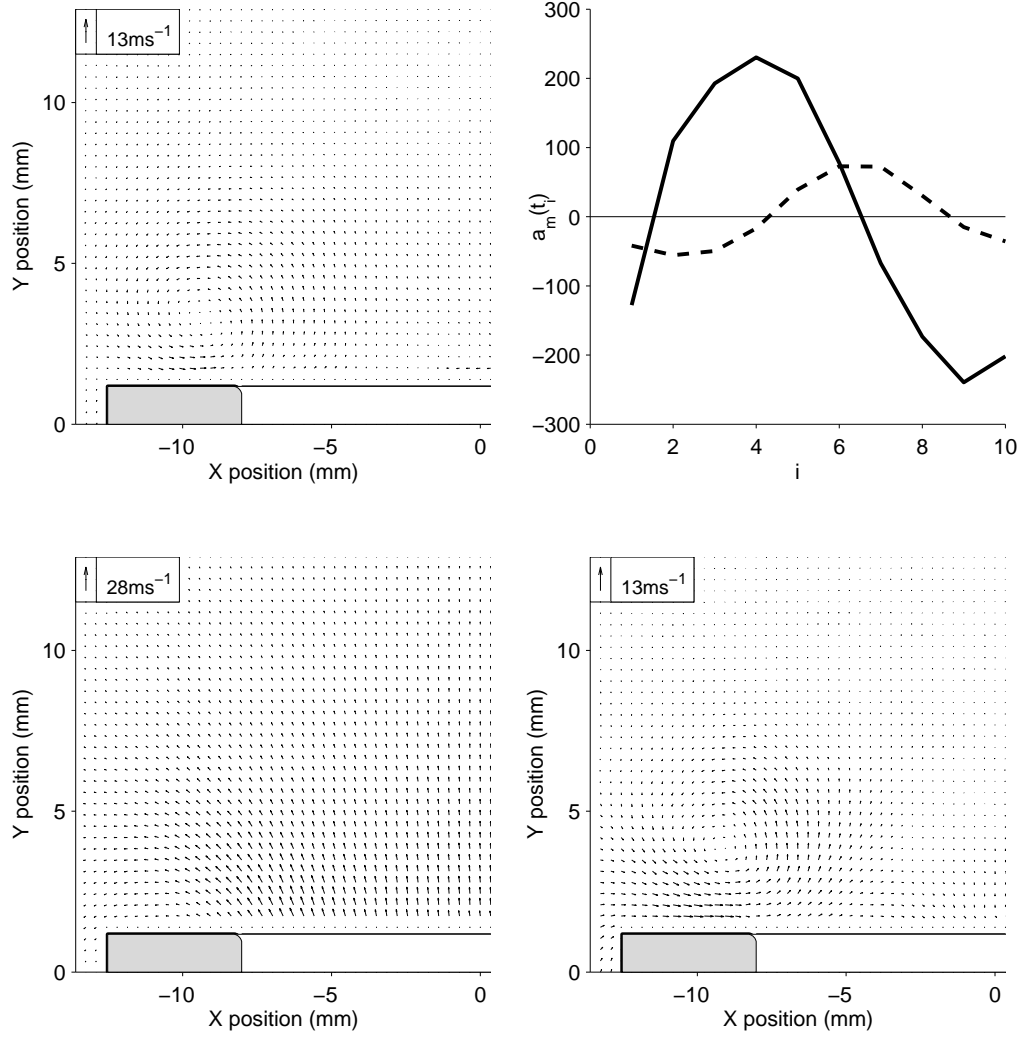
(d)  $\bar{p}_{an} = 4030\text{Pa}$ .

Figure 6.5 continued. Flow decomposition for  $r = 0.3\text{mm}$  termination. Top left: Streaming flow  $\tilde{\mathbf{u}}(x, y)$ . Top right:  $a_m(t_i)$  of first 2 POD modes (—)  $a_1$ , (---)  $a_2$ . Bottom left:  $\Phi_1(x, y)$ . Bottom right:  $\Phi_2(x, y)$ .



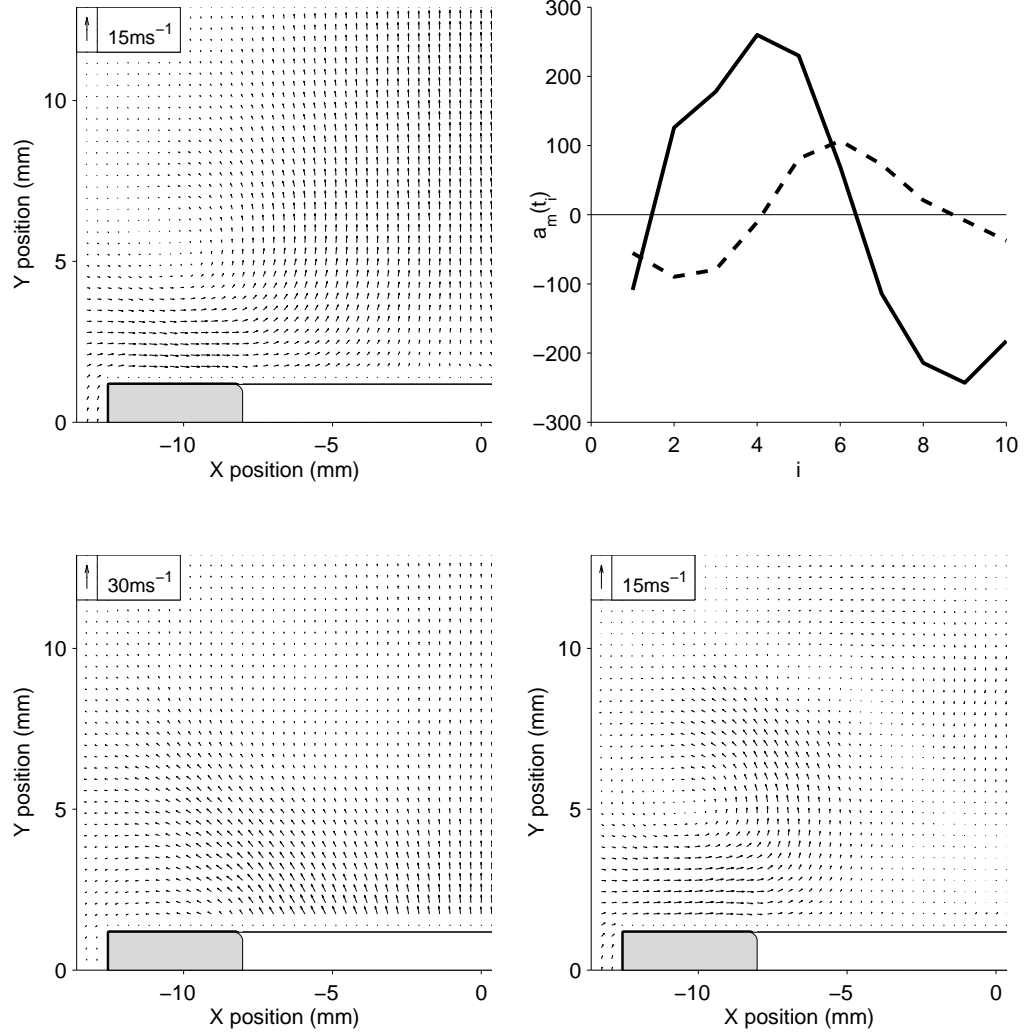
(e)  $\bar{p}_{an} = 5212\text{Pa}$ .

Figure 6.5 continued. Flow decomposition for  $r = 0.3\text{mm}$  termination. Top left: Streaming flow  $\tilde{\mathbf{u}}(x, y)$ . Top right:  $a_m(t_i)$  of first 2 POD modes (—)  $a_1$ , (---)  $a_2$ . Bottom left:  $\Phi_1(x, y)$ . Bottom right:  $\Phi_2(x, y)$ .



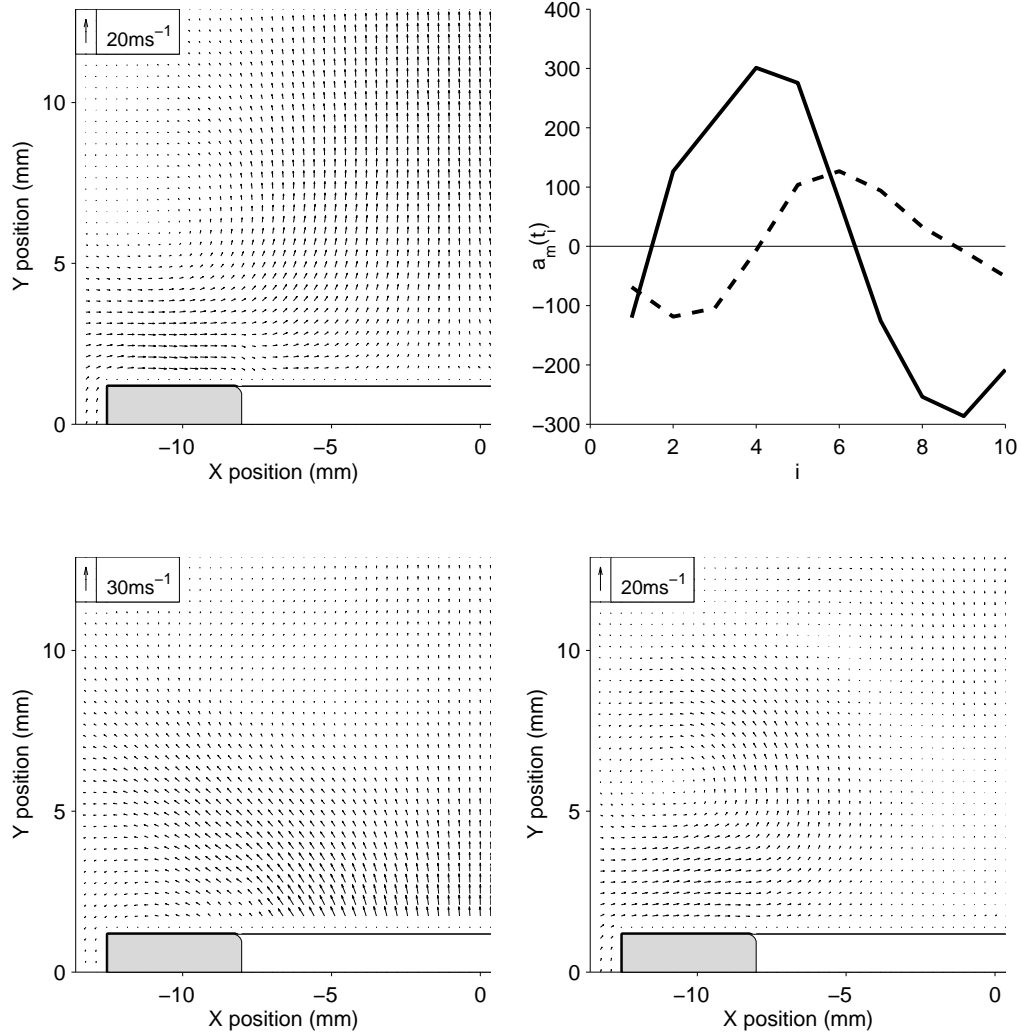
(f)  $\bar{p}_{an} = 5914\text{Pa}$ .

Figure 6.5 continued. Flow decomposition for  $r = 0.3\text{mm}$  termination. Top left: Streaming flow  $\tilde{\mathbf{u}}(x, y)$ . Top right:  $a_m(t_i)$  of first 2 POD modes (—)  $a_1$ , (---)  $a_2$ . Bottom left:  $\Phi_1(x, y)$ . Bottom right:  $\Phi_2(x, y)$ .



$$(g) \bar{p}_{an} = 6723\text{Pa}.$$

Figure 6.5 continued. Flow decomposition for  $r = 0.3\text{mm}$  termination. Top left: Streaming flow  $\tilde{\mathbf{u}}(x, y)$ . Top right:  $a_m(t_i)$  of first 2 POD modes (—)  $a_1$ , (---)  $a_2$ . Bottom left:  $\Phi_1(x, y)$ . Bottom right:  $\Phi_2(x, y)$ .



(h)  $\bar{p}_{an} = 7748\text{Pa}$ .

Figure 6.5 continued. Flow decomposition for  $r = 0.3\text{mm}$  termination. Top left: Streaming flow  $\tilde{\mathbf{u}}(x, y)$ . Top right:  $a_m(t_i)$  of first 2 POD modes (—)  $a_1$ , (---)  $a_2$ . Bottom left:  $\Phi_1(x, y)$ . Bottom right:  $\Phi_2(x, y)$ .

The top-right graph in figure 6.5 (a) to (h) shows the time evolution of mode 1 for each of the different values of  $\bar{p}_{an}$ . These appear approximately sinusoidal. For  $\bar{p}_{an} = 203\text{Pa}$  (figure 6.5 (a))  $a_1(t_i)$  has a total harmonic distortion of 2%, calculated using the first four harmonics. The higher pressure levels have total harmonic distortion in a range between 5% and 12% with no particular correspondence to increasing sound level. The pressure signal measured by the PCB transducer inside the tube typically has a total harmonic distortion of  $\sim 1\%$ , caused by the loudspeaker and any non-linear propagation.

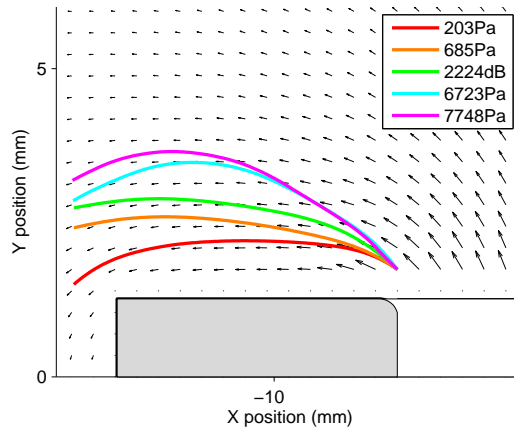


Figure 6.6: Streamlines from the left inside edge of the  $r = 0.3\text{mm}$  termination at a range of  $\bar{p}_{an}$ . The displayed velocity field is  $\Phi_1(x, y)$  for  $\bar{p}_{an} = 203\text{Pa}$ .

At all values of  $\bar{p}_{an}$ , the spatial form of the first mode of the POD ( $\Phi_1(x, y)$ ) appears roughly similar. The second criterion can be investigated in more detail by comparing the streamlines of  $\Phi_1(x, y)$  at low pressure level ( $\bar{p}_{an} = 203\text{Pa}$ ) with those of  $\Phi_1(x, y)$  for higher levels. Figure 6.6 shows the streamline from the inside left edge of the  $r = 0.3\text{mm}$  termination at a range of  $\bar{p}_{an}$ . For  $203\text{Pa}$  the streamline follows the geometry of the solid wall, being almost immediately parallel to the horizontal surface. As  $\bar{p}_{an}$  increases the streamline increasingly deviates from the  $203\text{Pa}$  case. This indicates that  $\Phi_1(x, y)$  increasingly contains separated (non-linear) flow. A similar conclusion was made by Marx et al [Marx 08].

To explore the third criterion we first construct

$$\mathbf{u}_{nl}(x, y, t_i) = \mathbf{u}(x, y, t_i) - a_1(t_i)\Phi_1(x, y) \quad (6.13)$$

which should describe the non-linear flow without the acoustic flow. We can then compare vorticity plots of  $\mathbf{u}(x, y, t_i)$  and  $\mathbf{u}_{nl}(x, y, t_i)$  at different values of  $\bar{p}_{an}$  and at various points in the cycle. Figure 6.7 shows  $\mathbf{u}(x, y, t_4)$  and  $\mathbf{u}_{nl}(x, y, t_4)$ , the flow at

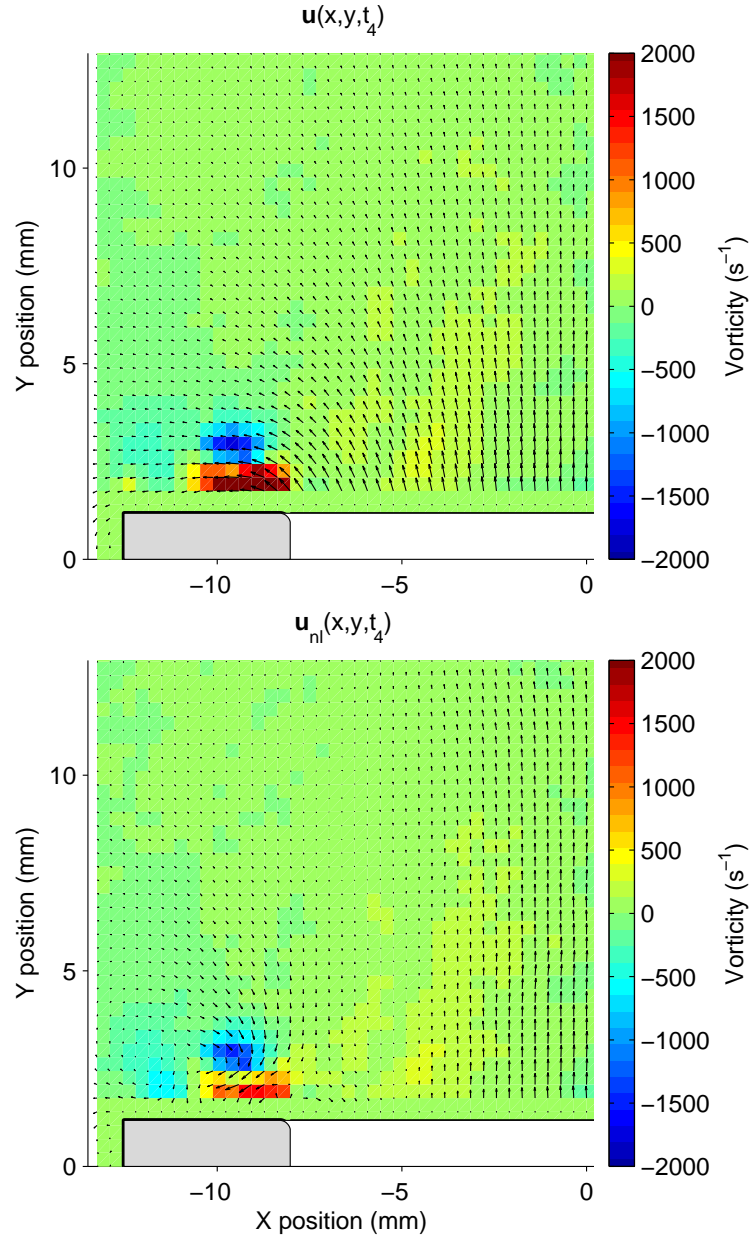


Figure 6.7: Comparison of  $\mathbf{u}(x, y, t_4)$  with  $\mathbf{u}_{nl}(x, y, t_4)$  at 2224 Pa for  $r = 0.3$  mm termination.



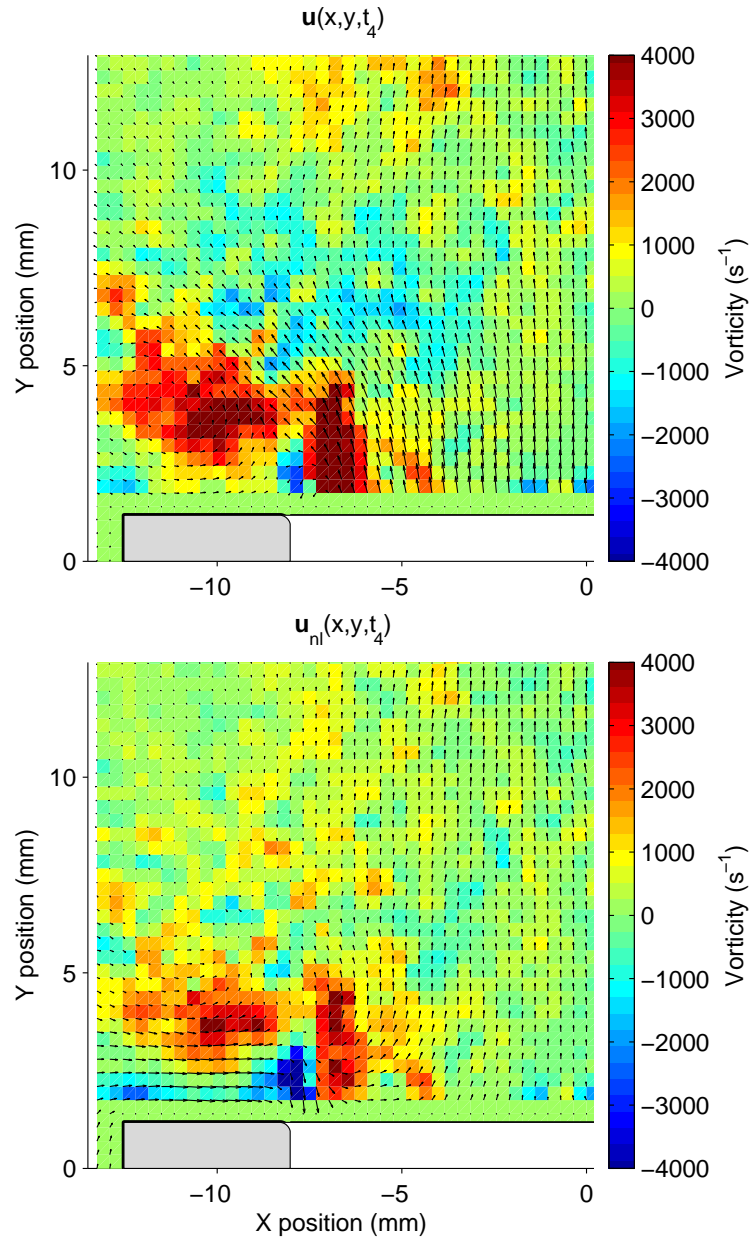


Figure 6.8: Comparison of  $\mathbf{u}(x, y, t_4)$  with  $\mathbf{u}_{nl}(x, y, t_4)$  at 7748Pa for  $r = 0.3\text{mm}$  termination.

maximum ejection, for 2224Pa. Looking at the underlying vorticity map, the regions of large positive and negative vorticity are of similar size, shape, position and magnitude for  $\mathbf{u}$  and  $\mathbf{u}_{nl}$ . As  $\bar{p}_{an}$  increases, this similarity reduces. Figure 6.8 compares  $\mathbf{u}(x, y, t_4)$  with  $\mathbf{u}_{nl}(x, y, t_4)$  for  $\bar{p}_{an} = 7748\text{Pa}$ .  $\mathbf{u}$  shows a significantly larger area of strong positive vorticity around position  $(-11, 5)$  as well as a stronger area of negative vorticity around  $(-9, 6)$ . This again supports the finding that the POD increasingly appropriates non-linear aspects of the flow into mode 1 at higher  $\bar{p}_{an}$ . It can be seen however that  $\mathbf{u}_{nl}$  approximately describes the non-linear behaviour.

### 6.5.2 Decomposition

Table 6.1: Description of non-linear flow constituents for  $r = 0.3\text{mm}$  termination.

$\bar{p}_{an}$ (Pa)	$\tilde{\mathbf{u}}$	$a_2$	$\Phi_2$
203	Unclear	Unclear	Unclear
685	Out at centre In at sides	Unclear	Unclear
2224	Out at centre In at sides	Oscillating 90° out of phase with $a_1$	Weak outward vortex
4030	Out at centre In at sides Outward vortex	Oscillating 90° out of phase with $a_1$	Outward vortex
5212	Strong outward vortex	Oscillating 90° out of phase with $a_1$	Outward vortex
5914	Strong outward vortex	Oscillating 90° out of phase with $a_1$	Outward vortex
6723	Strong central jet Strong side flow	Oscillating 90° out of phase with $a_1$	Outward vortex Weak inward vortex
7748	Strong central jet Strong side flow	Oscillating 90° out of phase with $a_1$	Outward vortex Weak inward vortex

Table 6.1 summarises the main features of  $\tilde{\mathbf{u}}$ ,  $a_2$  and  $\Phi_2$  at the different values of  $\bar{p}_{an}$ , as shown in figure 6.5. These are considered to contain the main features of the

non-linear flow produced at the tube termination.  $\tilde{\mathbf{u}}$  shows three distinct regimes. From 685Pa to 2224Pa the streaming flow is dominated by a strong outward jet in the centre of the termination with air drawn in at the sides. 4030Pa is a transitional level between two regimes. It features the same inward and outward flow but also the appearance of an outward rotating vortex (anti-clockwise on the left side of the termination and clockwise on the right) on the outer edge. At 5212Pa and 5914Pa the streaming flow becomes dominated by a strong outward vortex. A third regime is evident at 6723Pa and 7748Pa, where a strong central jet is evident as well as horizontal flow at the edges of the termination, flowing into the base of the jet.

The POD time coefficient of mode 2 ( $a_2$ ) has a similar form at all levels, apart from the two lowest where it is indistinct. The general form is roughly sinusoidal with the positive amplitude greater than the negative. The phase is also approximately  $90^\circ$  behind  $a_1$ , with the maximum of  $a_2$  occurring at the negative-going zero crossing of  $a_1$ . From 2224Pa to 7748Pa  $a_2$  steadily grows in amplitude. This behaviour of  $a_2$  is similar to that found by Marx et al. The major difference is that, in their study,  $a_2$  never became negative. The cause of this difference is that Marx et al did not remove the cycle-averaged flow before performing POD. Therefore in their case mode 2 of the POD does not have to cancel out the cycle-averaged flow during the suction part of the cycle (see below).

The forms of  $\Phi_2$  at different values of  $\bar{p}_{an}$  also fall into three regimes. At the two lowest pressures the flow pattern exhibits no distinguishable behaviour. From 2224Pa onwards an outward rotating vortex at the outer edge of the tonehole is clearly visible, growing in size with increasing  $\bar{p}_{an}$ . A third regime is evident at the two highest levels, where the outward rotating vortex is joined by a weaker vortex, rotating in the opposite sense and centred around position (-5,10).

To understand the evolution of the flow throughout the acoustic cycle,  $\tilde{\mathbf{u}}$ ,  $a_2$  and  $\Phi_2$  must be considered together. Taking 5212Pa as an example (figure 6.5 (e)), consider phase step  $i = 3$ , when the acoustic flow is approaching the ejection maximum.  $a_2(t_3)$  is then at a maximum negative value. Multiplying  $\Phi_2$  by  $a_2(t_3)$  reverses the direction of all of the vectors. The result is an inward rotating vortex which cancels out the vortex in  $\tilde{\mathbf{u}}$ . The value of  $a_2$  then increases. When  $a_2$  becomes positive, mode 2 combines constructively with  $\tilde{\mathbf{u}}$ , reaching a maximum vortex strength between  $i = 6$  and  $i = 7$ . This process describes the formation of an ejection vortex which stays attached to the end of the tube. A similar process can be applied to the flow at 6723Pa and 7748Pa (figure 6.5 (g) and (h)). Here the combination of  $\tilde{\mathbf{u}}$  and mode 2 describes the formation of a strong outward jet at  $i = 2$  and  $i = 3$ . Phase steps  $i = 4$  to  $i = 8$  mark the appearance of a vortex which is separated from the end of the tube and accompanied by a counter-rotating vortex. The progression through these two regimes,

vortex formation (2224Pa to 5914Pa) and then vortex shedding (6723Pa and 7748Pa), has been observed in PIV maps of the phase averaged flow  $\mathbf{u}(x, y, t_i)$  [Skulina 05a].

### 6.5.3 Energy

It has been proposed that  $e_1$  (defined in equation 6.12) can be used to measure the relative energy transferred to non-linear flow effects. In order to compare the data obtained here with that obtained by Atig and to calculate a Strouhal number, the RMS acoustic velocity at the end of the tube is approximated from the RMS pressure at the pressure anti-node in the tube  $\bar{p}_{an}$  via

$$\bar{u}_{an} = \frac{\bar{p}_{an}}{\rho_0 c} \quad (6.14)$$

where  $\rho_0$  is atmospheric density and  $c$  is the speed of sound in air (this is similar to equation 5.1 for the tonehole).

Figure 6.9 (a) shows  $e_1$  as a function of  $\bar{u}_{an}$  for the  $r = 0\text{mm}$ ,  $r = 0.3\text{mm}$  and  $r = 1\text{mm}$  terminations. At low values of  $\bar{u}_{an}$  all three data sets have a small value of  $e_1$ , meaning that nearly 100% of the kinetic energy of the flow is contained in mode 1 of the POD. As for the radiation resistance data (see figure 6.2), the rate of increase of  $e_1$  with  $\bar{u}_{an}$  is higher for a smaller value of  $r$ . The discontinuities which mark the transition to vortex shedding are also evident for the  $r = 0\text{mm}$  and  $r = 0.3\text{mm}$  terminations. They occur at slightly smaller values of  $\bar{u}_{an}$  than Atig found for the radiation resistance. However, Skulina's resistance data displayed discontinuities at the same values of  $\bar{u}_{an}$  as found here. The disparity between the two-microphone and PIV data may be due to differences in the calibration of the PCB transducers used in the two experiments. The data for  $r = 1\text{mm}$  exhibit no discontinuity because the transition to vortex shedding occurs around the last data point ( $\bar{u}_{an} = 21\text{ms}^{-1}$ ) and there are insufficient data points in that region to define a discontinuity.

Energy is also transferred from the acoustic oscillation to the streaming flow. To estimate this we define

$$e_2 = \frac{\frac{1}{N_t} \sum_{x=1}^{N_x} \sum_{y=1}^{N_y} |\tilde{\mathbf{u}}(x, y)|^2}{\frac{1}{N_t} \sum_{i=1}^{N_t} \sum_{x=1}^{N_x} \sum_{y=1}^{N_y} |\mathbf{u}(x, y, t_i)|^2}. \quad (6.15)$$

This gives the relative kinetic energy per unit mass of the streaming flow to the total flow, averaged over one acoustic cycle. Figure 6.9 (b) gives a plot of  $e_2$  against  $\bar{u}_{an}$  for the three terminations. For all three geometries  $e_2$  fluctuates around a roughly constant level until a certain value of  $\bar{u}_{an}$  when it rapidly increases. This value of  $\bar{u}_{an}$  approximately corresponds to the position of the discontinuity in  $e_1$ , and hence

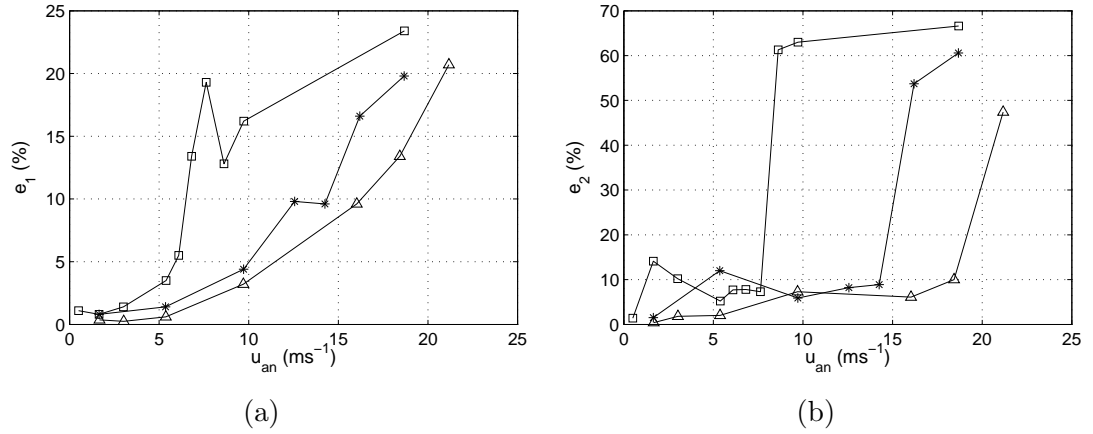


Figure 6.9: (a)  $e_1$  against  $\bar{u}_{an}$  for  $r = 0$ mm,  $r = 0.3$ mm and  $r = 1$ mm terminations. (b)  $e_2$  against  $\bar{u}_{an}$  for  $r = 0$ mm,  $r = 0.3$ mm and  $r = 1$ mm terminations. (□)  $r = 0$ mm. (\*)  $r = 0.3$ mm. (△)  $r = 1$ mm.

to the onset of vortex shedding. Taking the  $r = 0.3$ mm case,  $e_2$  increases rapidly at  $\bar{u}_{an} = 16$ ms<sup>-1</sup> ( $\bar{p}_{an} = 6723$ Pa). Looking at table 6.1, this sound pressure marks the appearance of the strong central jet in  $\tilde{\mathbf{u}}$  which is a sign of vortex shedding. It can be seen from figure 6.5 (g) that the velocities in  $\tilde{\mathbf{u}}$  have become greater than those in POD mode 2.

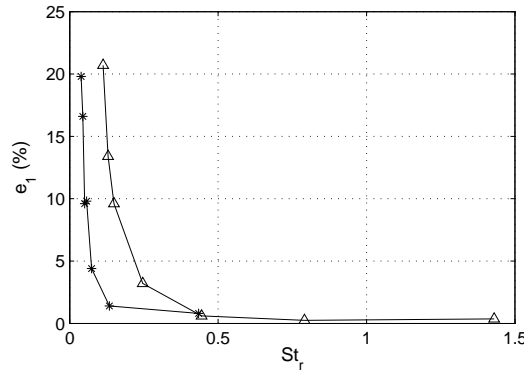


Figure 6.10:  $e_1$  against  $St_r$  for  $r = 0.3$ mm and  $r = 1$ mm terminations. (\*)  $r = 0.3$ mm. (△)  $r = 1$ mm.

As discussed in section 2.7.3, the strength of local non-linear flow effects is governed by the Strouhal number of the flow  $St$ , defined in equation 2.47. Marx et al [Marx 08] found that  $e_1$  was dependent on a Strouhal number defined by the acoustic velocity and the radius of curvature of the corner of the step in the waveguide. Figure 6.10 shows  $e_1$  as a function of  $St_r$  for the  $r = 0.3$ mm and  $r = 1$ mm terminations.  $St_r$  is the Strouhal

number calculated using  $\bar{u}_{an}$  and  $r$  as the characteristic length. It is expected that the plot of  $e_1$  versus  $St_r$  should be independent of  $r$ . The curves for the two geometries are not close to each other and  $e_1$  does not become significant until below  $St_r \sim 0.2$ . This suggests that the wrong definition of Strouhal number has been used.

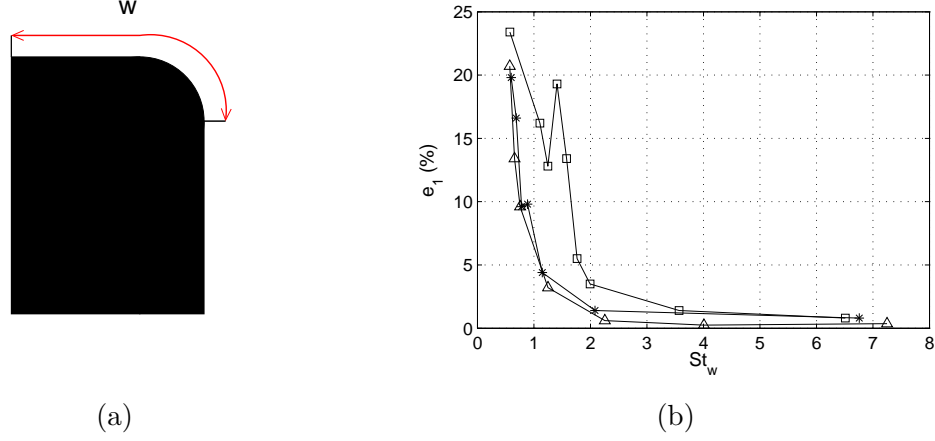


Figure 6.11: (a) Definition of  $w$ , the distance from the start of the inside corner of the termination to the outside corner. (b)  $e_1$  against  $St_w$  for  $r = 0\text{mm}$ ,  $r = 0.3\text{mm}$  and  $r = 1\text{mm}$  terminations. ( $\square$ )  $r = 0\text{mm}$ . ( $*$ )  $r = 0.3\text{mm}$ . ( $\triangle$ )  $r = 1\text{mm}$ .

Figure 6.11 (a) defines a characteristic length  $w$  that is of the same order of magnitude as the wall thickness (4.5mm) but also takes into account the radius of curvature. For the  $r = 0\text{mm}$  termination  $w = 4.5\text{mm}$ . For the  $r = 0.3\text{mm}$  termination  $w = 4.7\text{mm}$ . For the  $r = 1\text{mm}$  termination  $w = 5.1\text{mm}$ . Figure 6.11 (b) shows  $e_1$  against  $St_w$ . For the  $r = 0.3\text{mm}$  and  $r = 1\text{mm}$  terminations the lines of data are very close and  $e_1$  starts to become large at  $St_w \simeq 1$ . The curves for these two terminations are similar in form to the plot of  $e_1$  versus  $St$  given by Marx et al [Marx 08]. Also as found by Marx et al, one of the sets of data does not coincide with the other two; in this case the  $r = 0\text{mm}$  data. In the case of the flow around a step this disparity led the authors to suggest that the Strouhal number may not be the only scaling factor. Here, it is also the case that the value of  $e_1$  may be influenced by the cycle-averaged flow at that particular Strouhal number.

Figure 6.12 shows  $e_2$  against  $St_w$  for the three geometries. Again, the two curves for  $r = 0.3\text{mm}$  and  $r = 1\text{mm}$  coincide. Overall the form of these two curves differ to those of the  $e_1$  graph. At  $St_w = 1$   $e_1$  and  $e_2$  are both approximately equal to 7%, but  $e_2$  climbs more rapidly at the lowest values of  $St_w$ . Again, the curve for  $r = 0\text{mm}$  does not coincide with the other two, but displays a similar shape.

To confirm whether  $w$  is the governing length scale for the strength of local non-linear flow effects at a tube termination would require PIV and POD analysis of

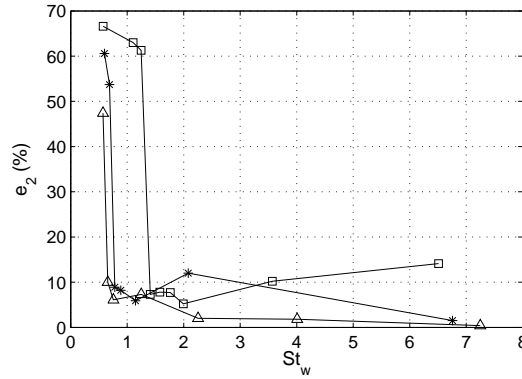


Figure 6.12:  $e_2$  against  $St_w$  for  $r = 0\text{mm}$ ,  $r = 0.3\text{mm}$  and  $r = 1\text{mm}$  terminations. ( $\square$ )  $r = 0\text{mm}$ . ( $*$ )  $r = 0.3\text{mm}$ . ( $\triangle$ )  $r = 1\text{mm}$ .

geometries with more values of  $w$ . Particularly, maintaining a constant value of  $r$  but varying  $w$  (equivalent to varying the wall thickness) would be informative. Studies have shown that, at a given value of  $\bar{u}_{an}$ , a termination with a vanishingly thin wall thickness results in more energy loss to local non-linear flow effects than an  $r = 0\text{mm}$  termination with a finite wall thickness [Peters *et al* 93, Atig 03, Atig 04a, Skulina 05a].

## 6.6 Conclusion

PIV and POD have been applied to high amplitude oscillating flow outside the end of a tube. It has been found that, when the cycle-averaged flow is first removed, mode 1 of the POD approximately describes the acoustic flow. As the sound pressure in the tube increases, more aspects of the induced non-linear flow are appropriated into mode 1. Mode 2 of the POD describes the formation and motion of vortices outside the tube over the course of the acoustic cycle, but must be understood together with the cycle-averaged flow to reconstruct the non-linear flow behaviour.

Once the POD analysis has been shown to approximately split the flow into acoustic and non-linear constituents, it is possible to meaningfully construct the parameters  $e_1$  and  $e_2$ . These have been proved to be useful quantitative indicators of the energy transferred from the acoustic flow to local non-linear flow effects.  $e_1$  and  $e_2$  are strongly dependent on the Strouhal number of the flow and also reproduce the discontinuities in the radiation resistance data which signal the transition to vortex shedding.

The  $e_1$  and  $e_2$  data for the terminations do not take into account all of the non-linear flow effects generated: some vortex formation and streaming will occur inside the tube [Skulina 05a]. It would be of interest to calculate  $e_1$  and  $e_2$  over a region that

enclosed all of the non-linear flow effects. This may resolve the inconsistencies in the results for  $e_1$  and  $e_2$  against  $St_w$  due to the  $r = 0\text{mm}$  data.



## Chapter 7

# POD Applied to PIV Data of Oscillating Flow at a Tonehole

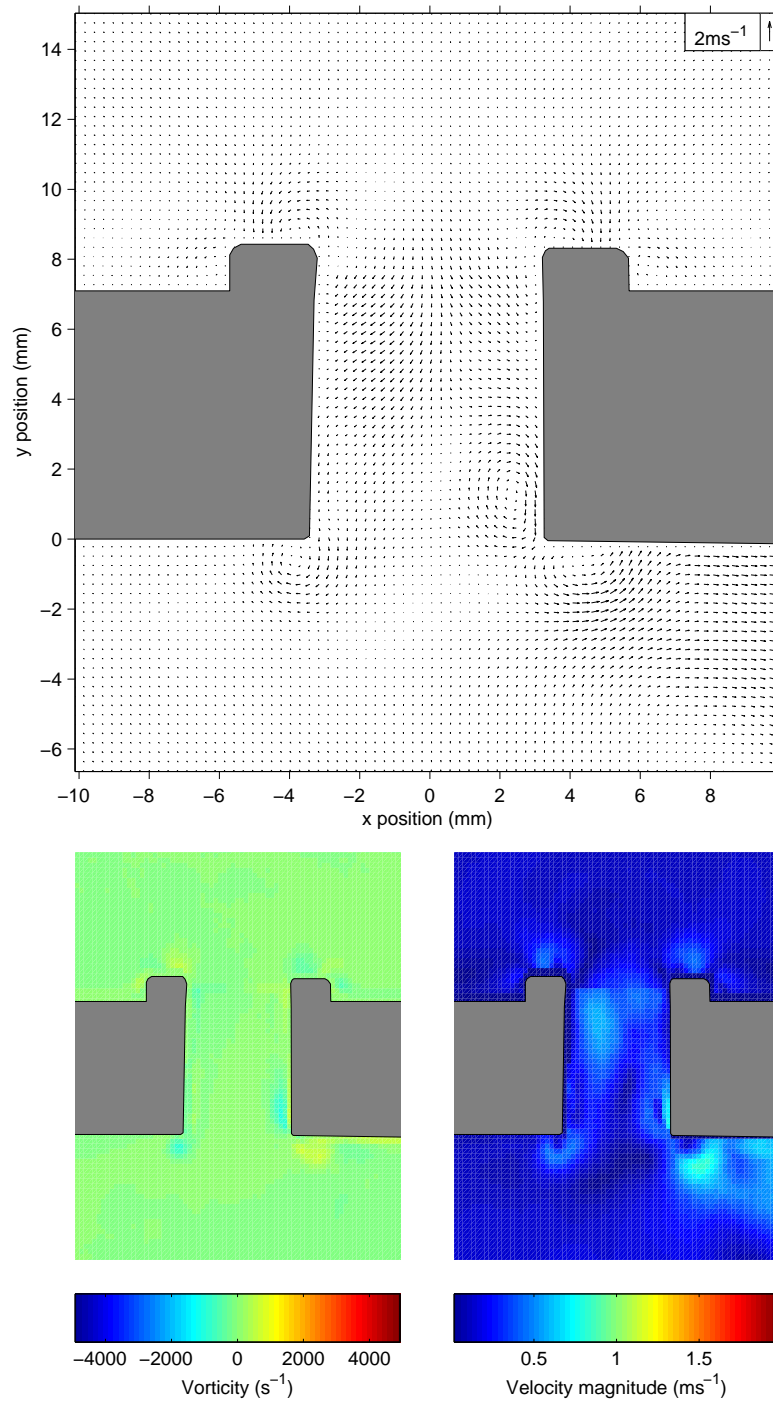
### 7.1 Introduction

In chapter 6 Proper Orthogonal Decomposition (POD) was applied to oscillating flow at the end of a tube. It was found that the flow could be decomposed into a part which approximately described the acoustic motion and other components which described the behaviour of the induced local non-linear flow effects. The parameters  $e_1$  and  $e_2$  were found to be useful for describing the strength of local non-linear flow phenomena.

In this chapter the POD techniques developed in chapter 6 are applied to the PIV data for the model toneholes. Firstly, the presentation of the graphical data is explained. Then in section 7.3 the cycle-averaged flow is described. Sections 7.4 and 7.5 deal with POD modes 1 and 2. Lastly, the transfer of energy to non-acoustic modes is considered, as well as the relevant Strouhal number.

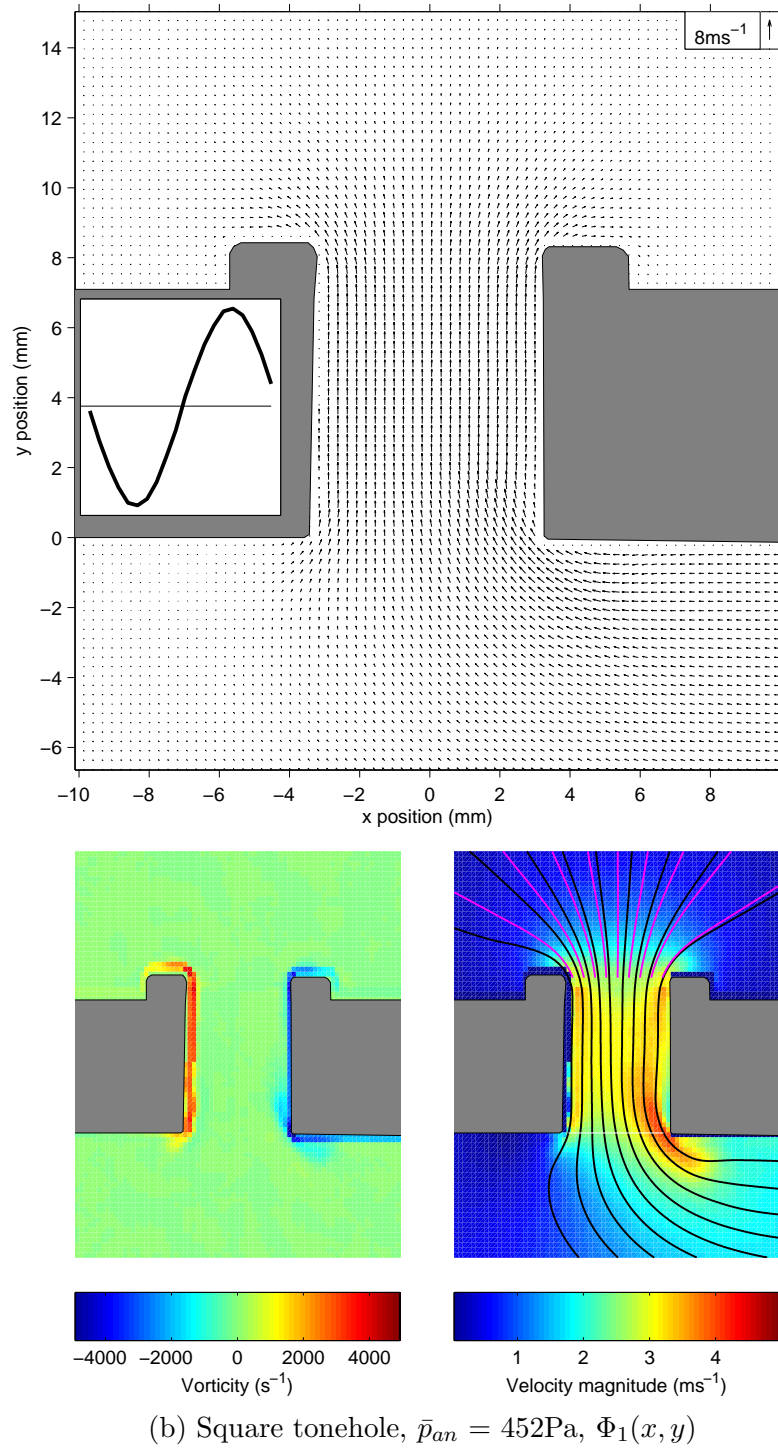
### 7.2 Data Presentation

The POD analysis described in section 6.4.1 was applied to the PIV data for the model toneholes. Again, the cycle-averaged flow was subtracted from the total flow at each phase step before the POD was performed. The only difference in the analysis is that, for the tonehole data, the number of phase steps  $N_t$  is 20 (instead of 10 for the terminations). This means that the POD decomposes the flow into 20 modes instead of 10.



(a) Square tonehole,  $\bar{p}_{an} = 452\text{Pa}$ ,  $\tilde{\mathbf{u}}(x, y)$

Figure 7.1: Flow decomposition for the square tonehole at  $\bar{p}_{an} = 452\text{Pa}$ .

Figure 7.1 continued.  $a_1(t_i)$  is plotted inset into the vector map.

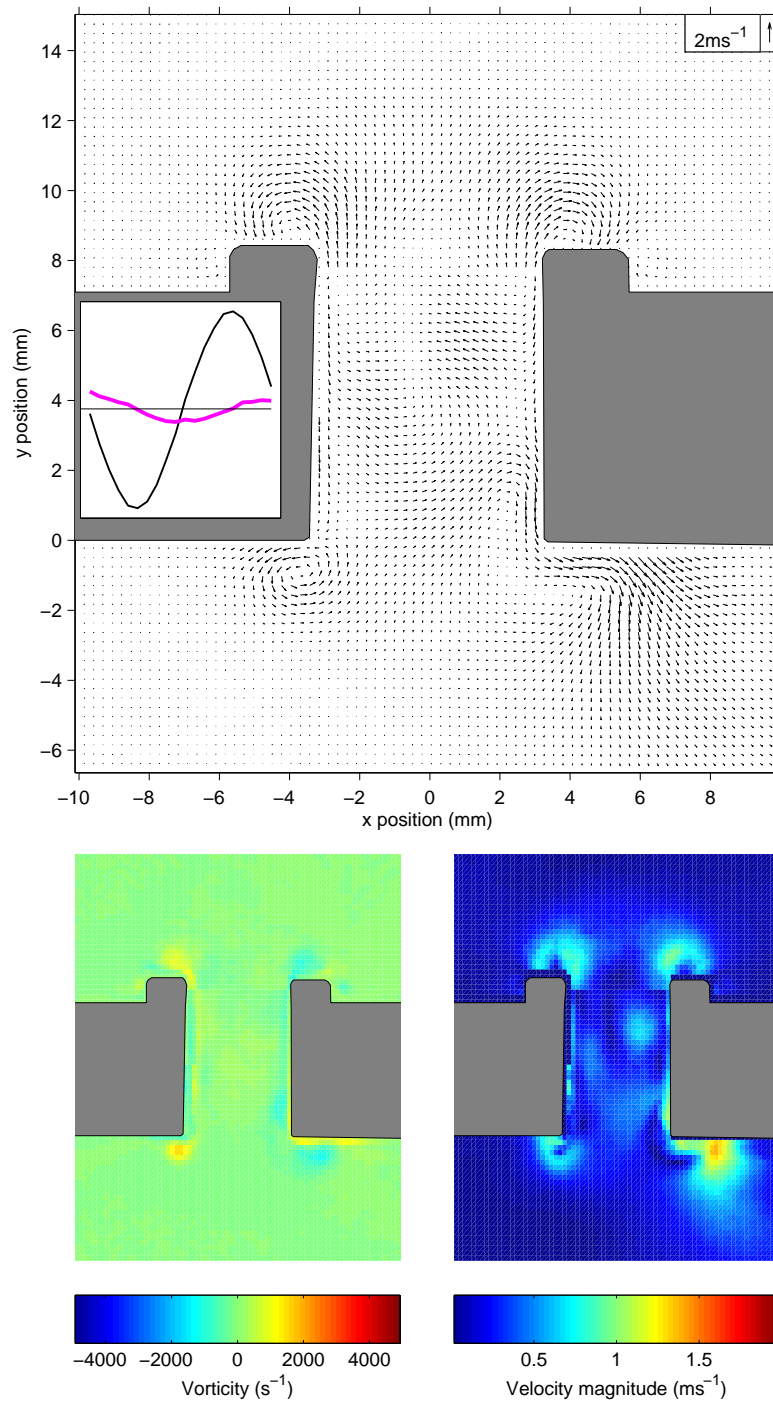
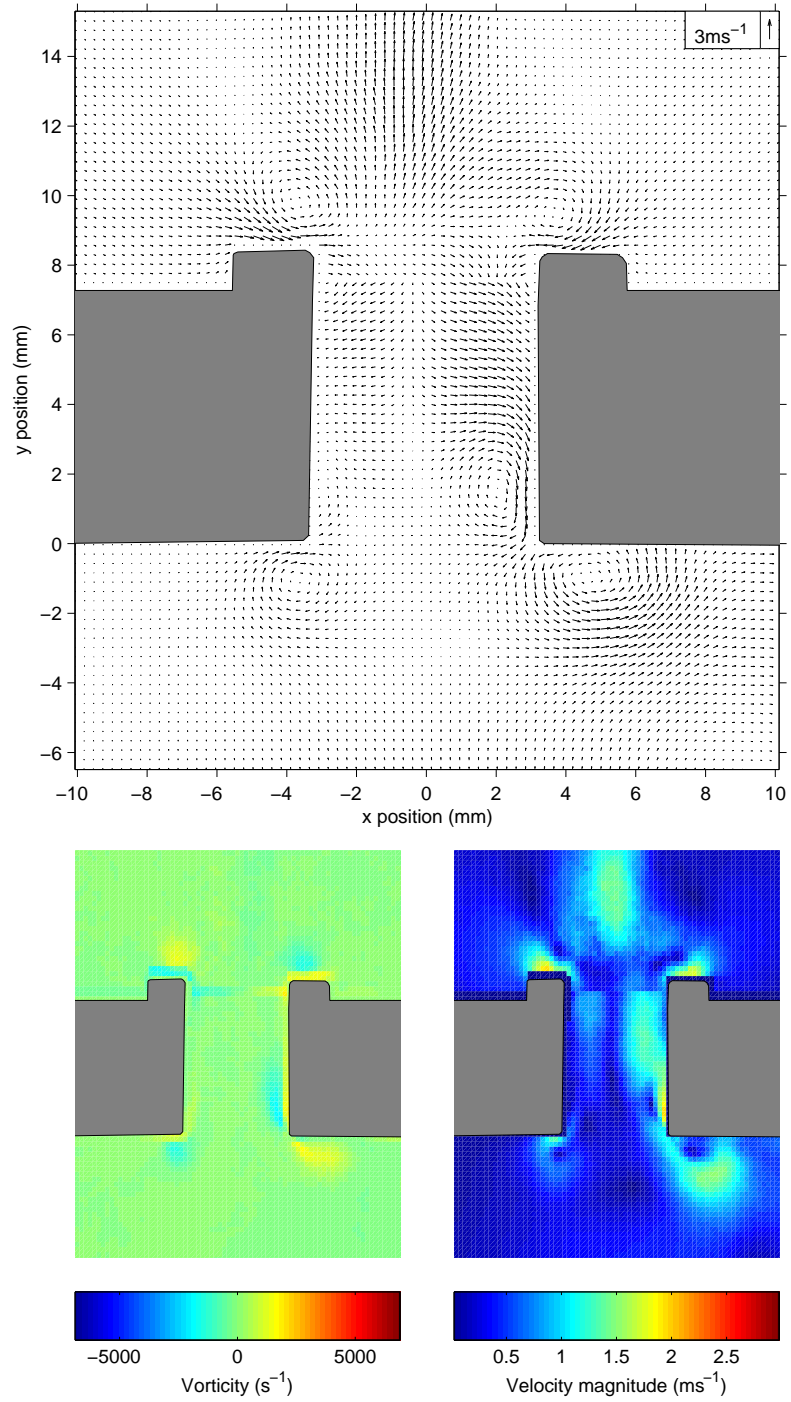
(c) Square tonehole,  $\bar{p}_{an} = 452\text{Pa}$ ,  $\Phi_2(x, y)$ 

Figure 7.1 continued.  $a_1(t_i)$  and  $a_2(t_i)$  are plotted inset into the vector map.  
 (Black)  $a_1(t_i)$ . (Magenta)  $a_2(t_i)$ .



(a) Square tonehole,  $\bar{p}_{an} = 760\text{Pa}$ ,  $\tilde{\mathbf{u}}(x, y)$

Figure 7.2: Flow decomposition for the square tonehole at  $\bar{p}_{an} = 760\text{Pa}$ .

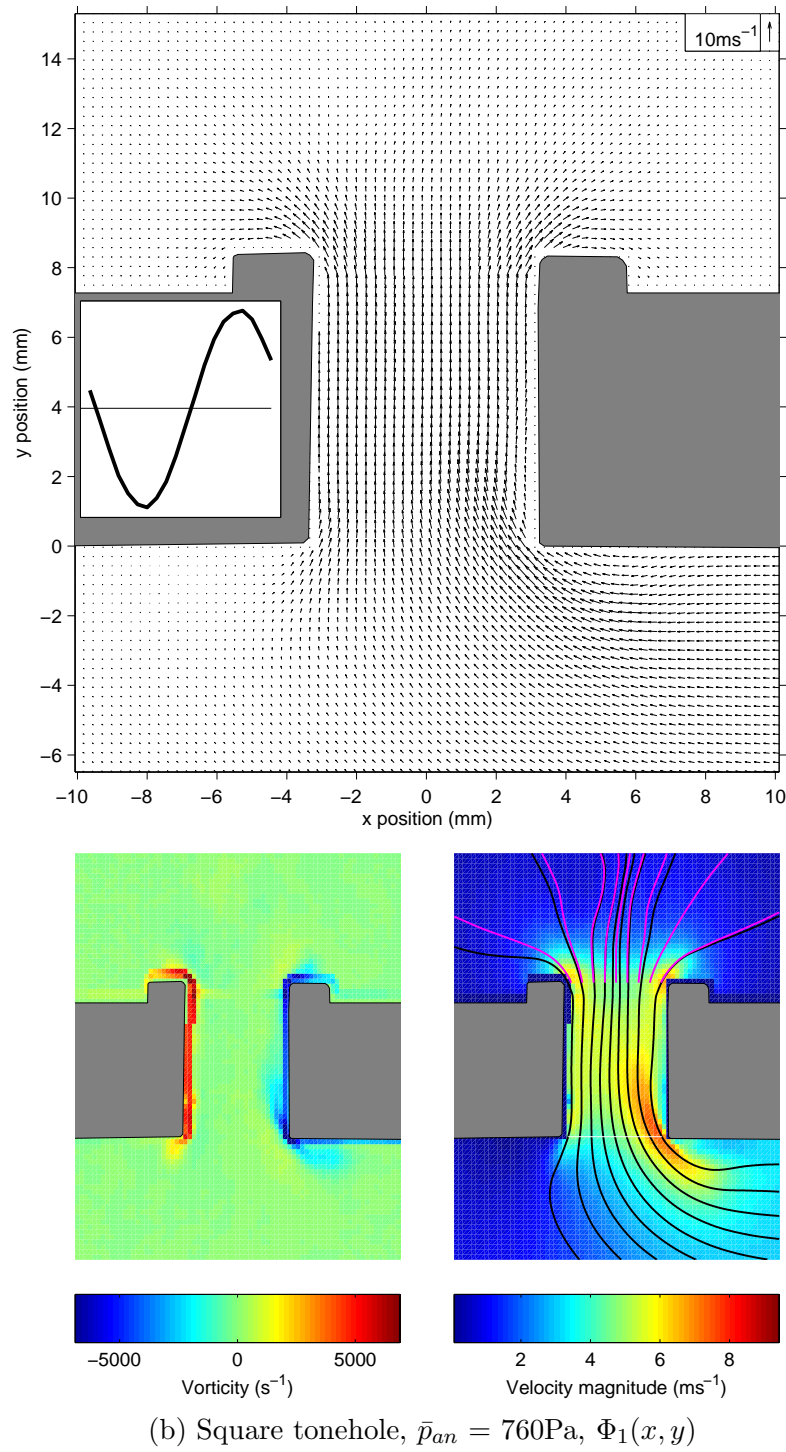


Figure 7.2 continued.  $a_1(t_i)$  is plotted inset into the vector map.

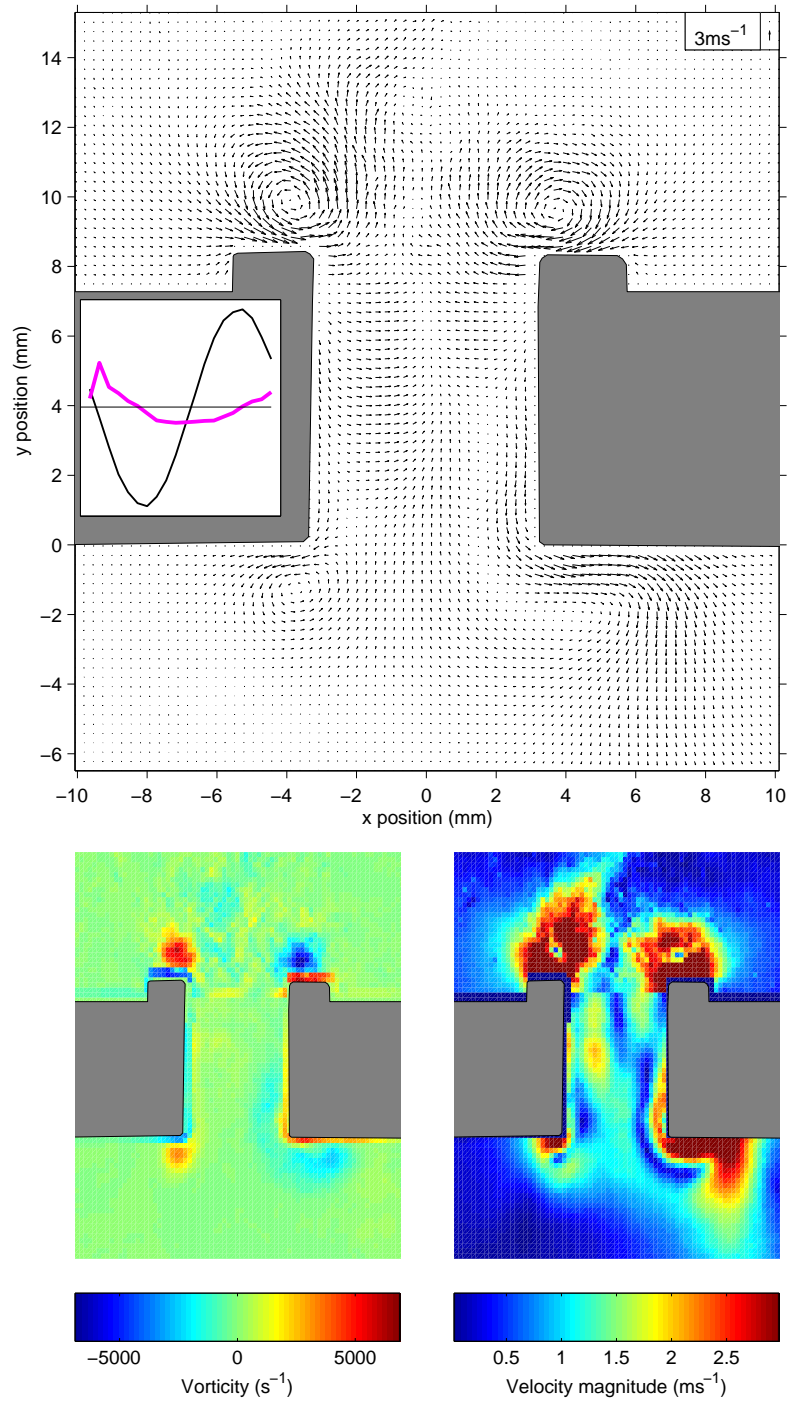
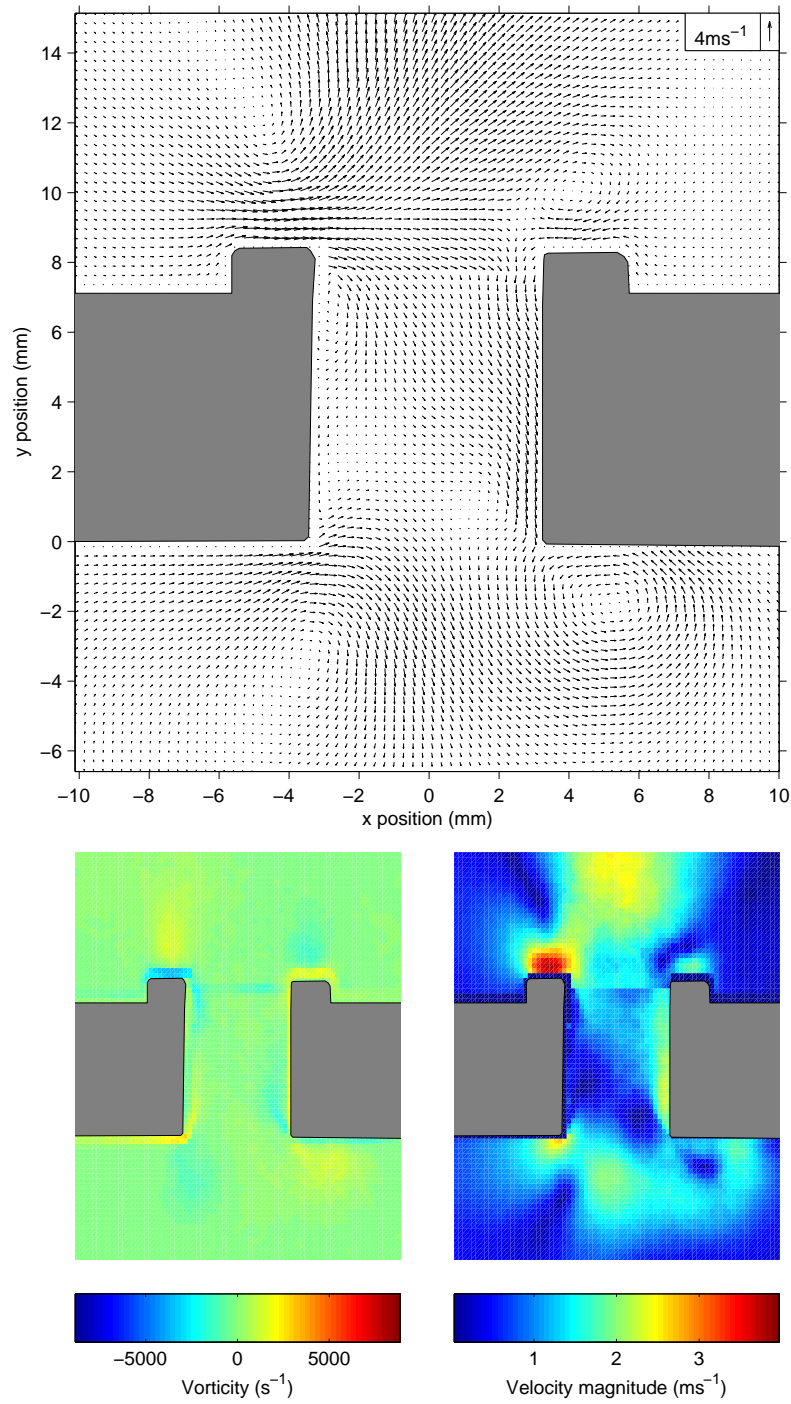
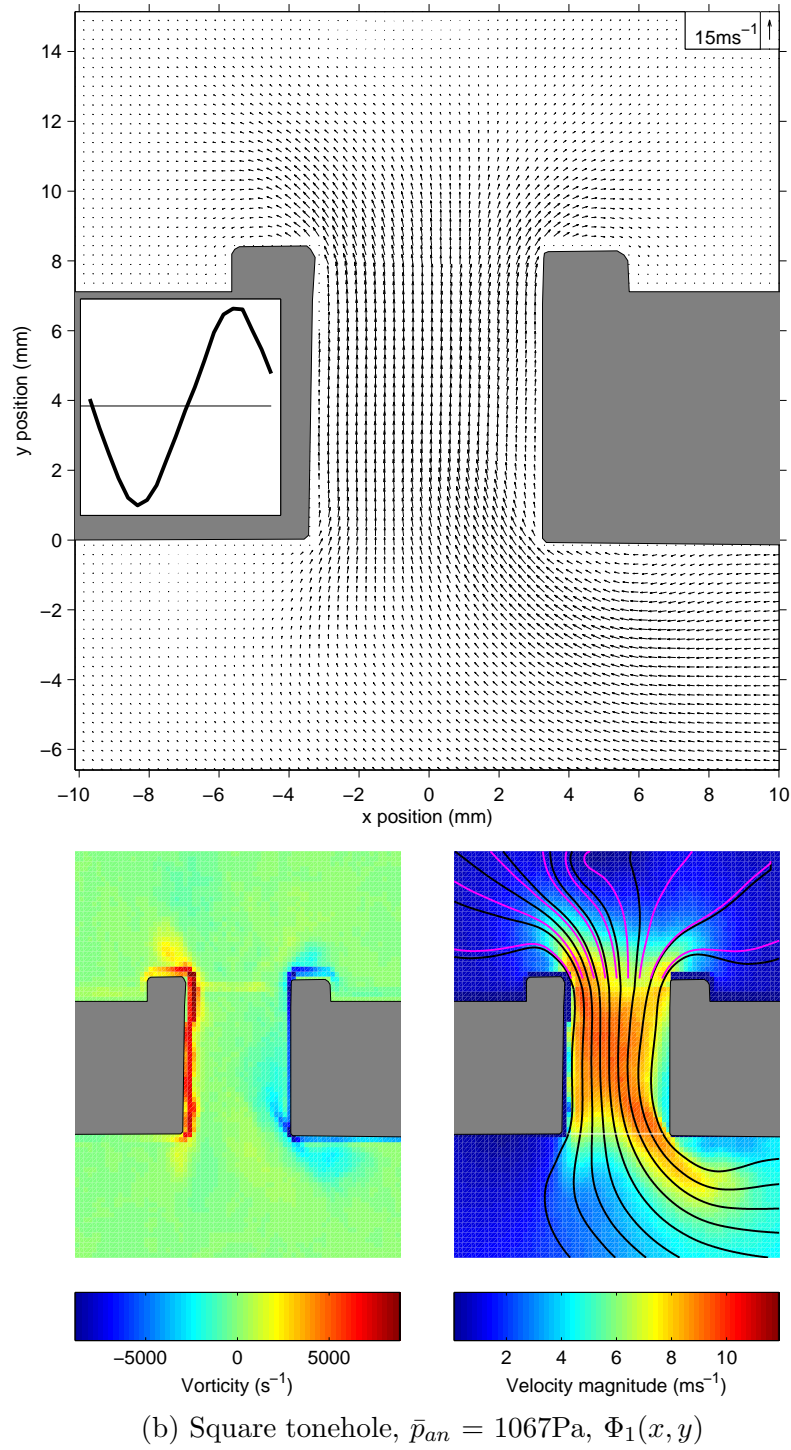
(c) Square tonehole,  $\bar{p}_{an} = 760\text{Pa}$ ,  $\Phi_2(x, y)$ 

Figure 7.2 continued.  $a_1(t_i)$  and  $a_2(t_i)$  are plotted inset into the vector map.  
 (Black)  $a_1(t_i)$ . (Magenta)  $a_2(t_i)$ .



Figure 7.3: Flow decomposition for the square tonehole at  $\bar{p}_{an} = 1067\text{Pa}$ .



Figure 7.3 continued.  $a_1(t_i)$  is plotted inset into the vector map.

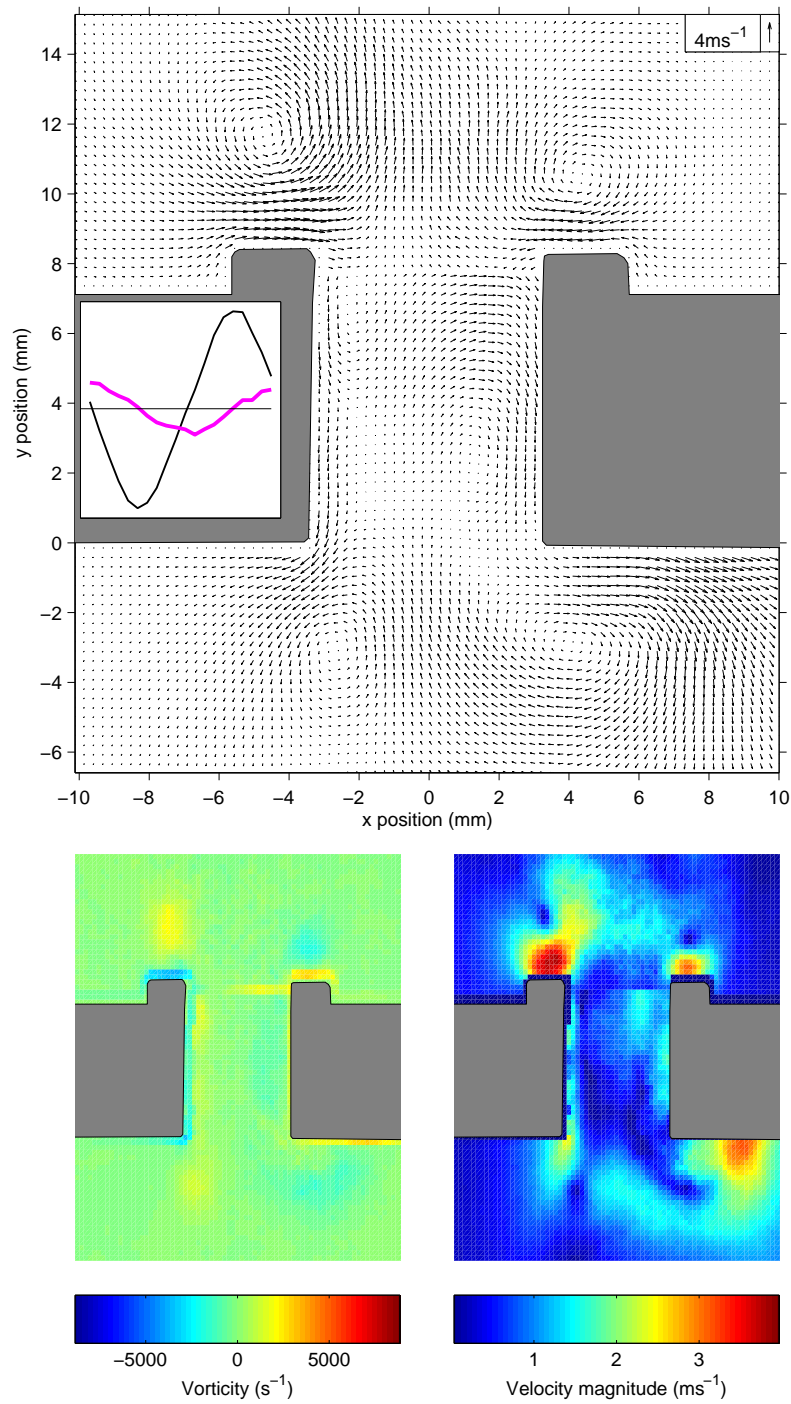
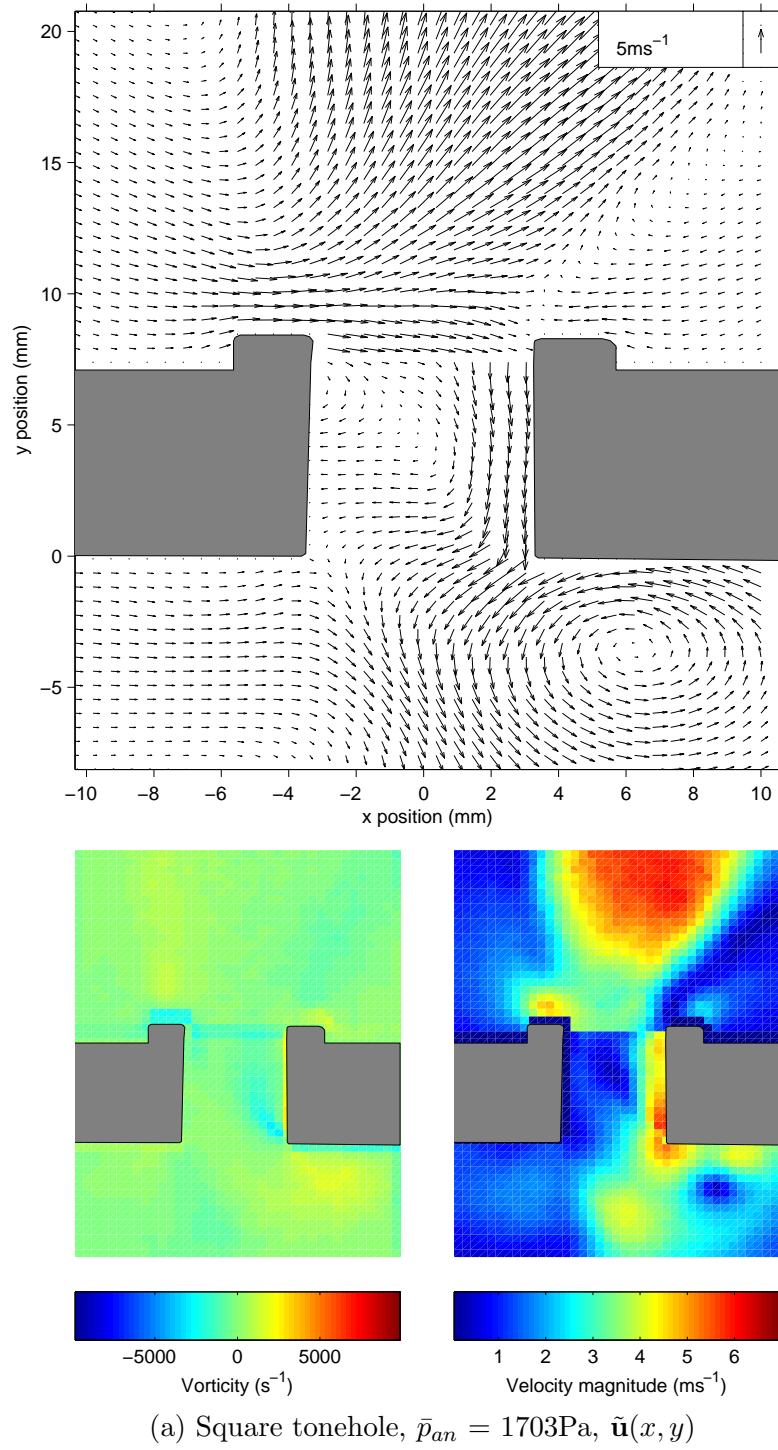


Figure 7.3 continued.  $a_1(t_i)$  and  $a_2(t_i)$  are plotted inset into the vector map.  
(Black)  $a_1(t_i)$ . (Magenta)  $a_2(t_i)$ .

Figure 7.4: Flow decomposition for the square tonehole at  $\bar{p}_{an} = 1703\text{Pa}$ .

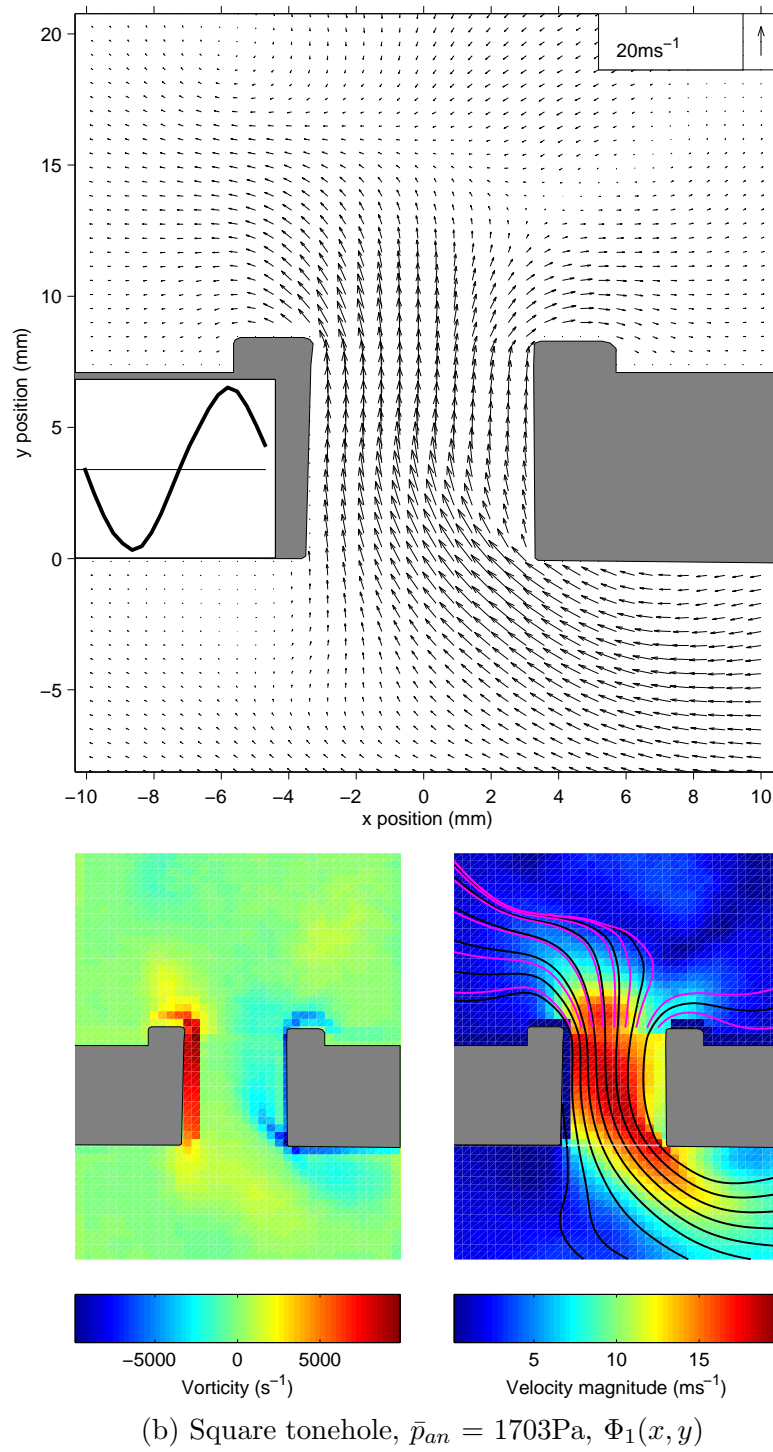


Figure 7.4 continued.  $a_1(t_i)$  is plotted inset into the vector map.

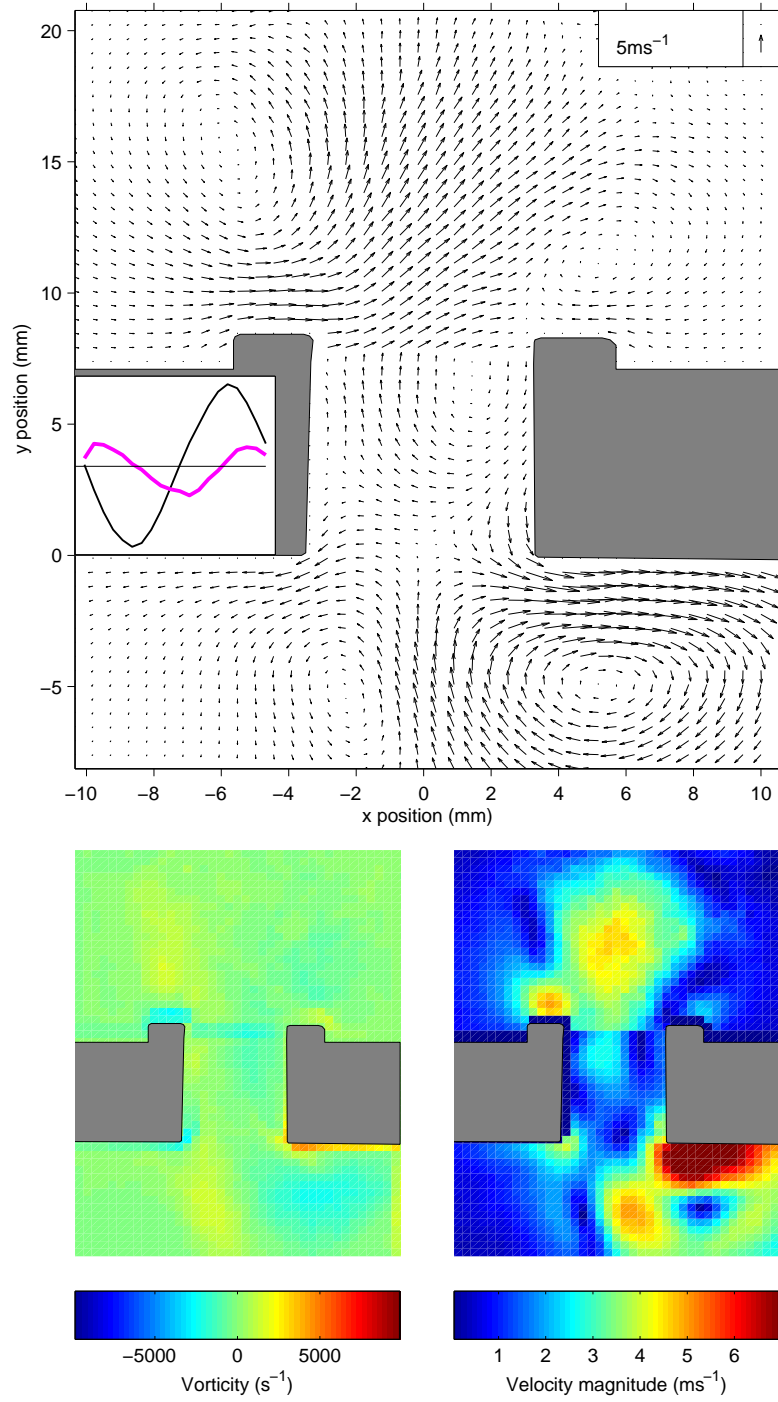
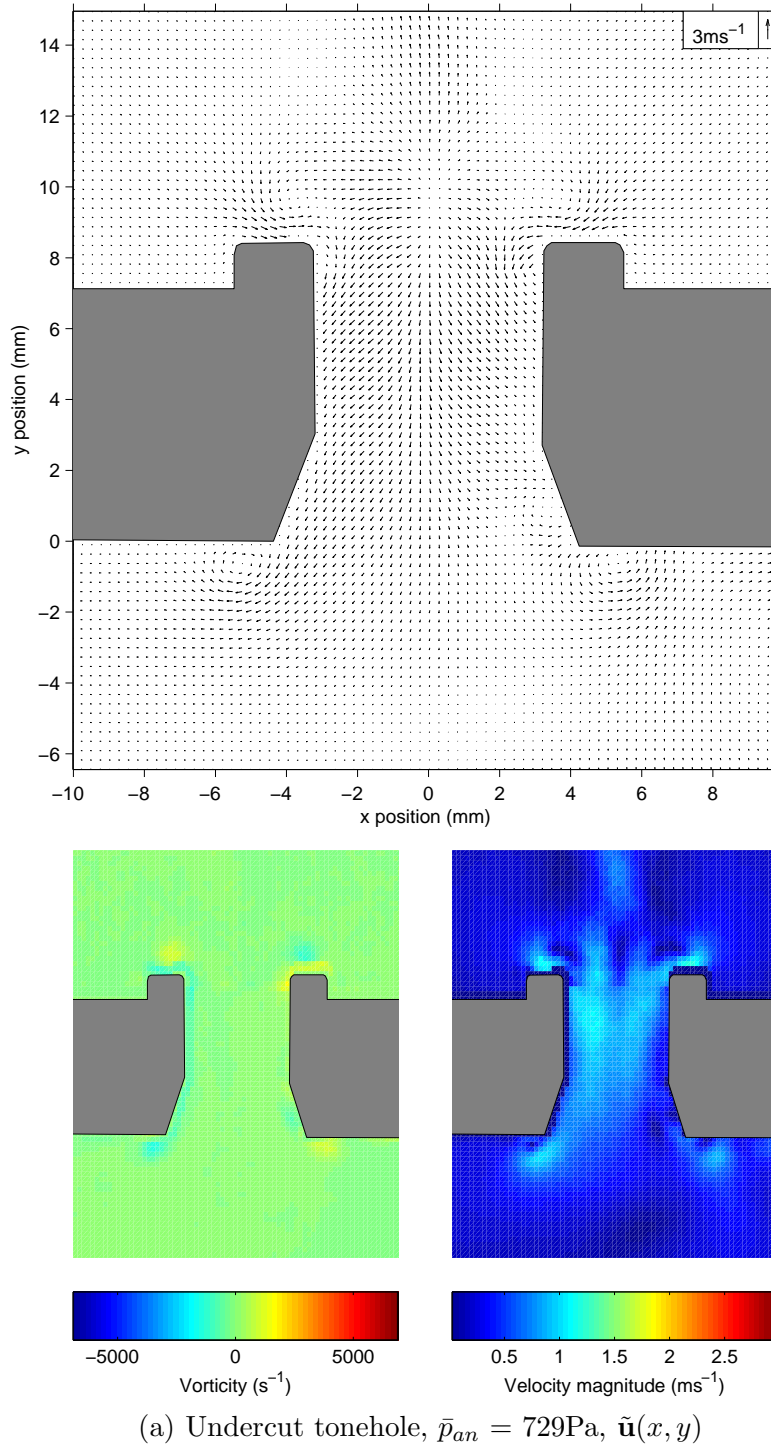


Figure 7.4 continued.  $a_1(t_i)$  and  $a_2(t_i)$  are plotted inset into the vector map. (Black)  $a_1(t_i)$ . (Magenta)  $a_2(t_i)$ .

Figure 7.5: Flow decomposition for the undercut tonehole at  $\bar{p}_{an} = 729\text{Pa}$ .

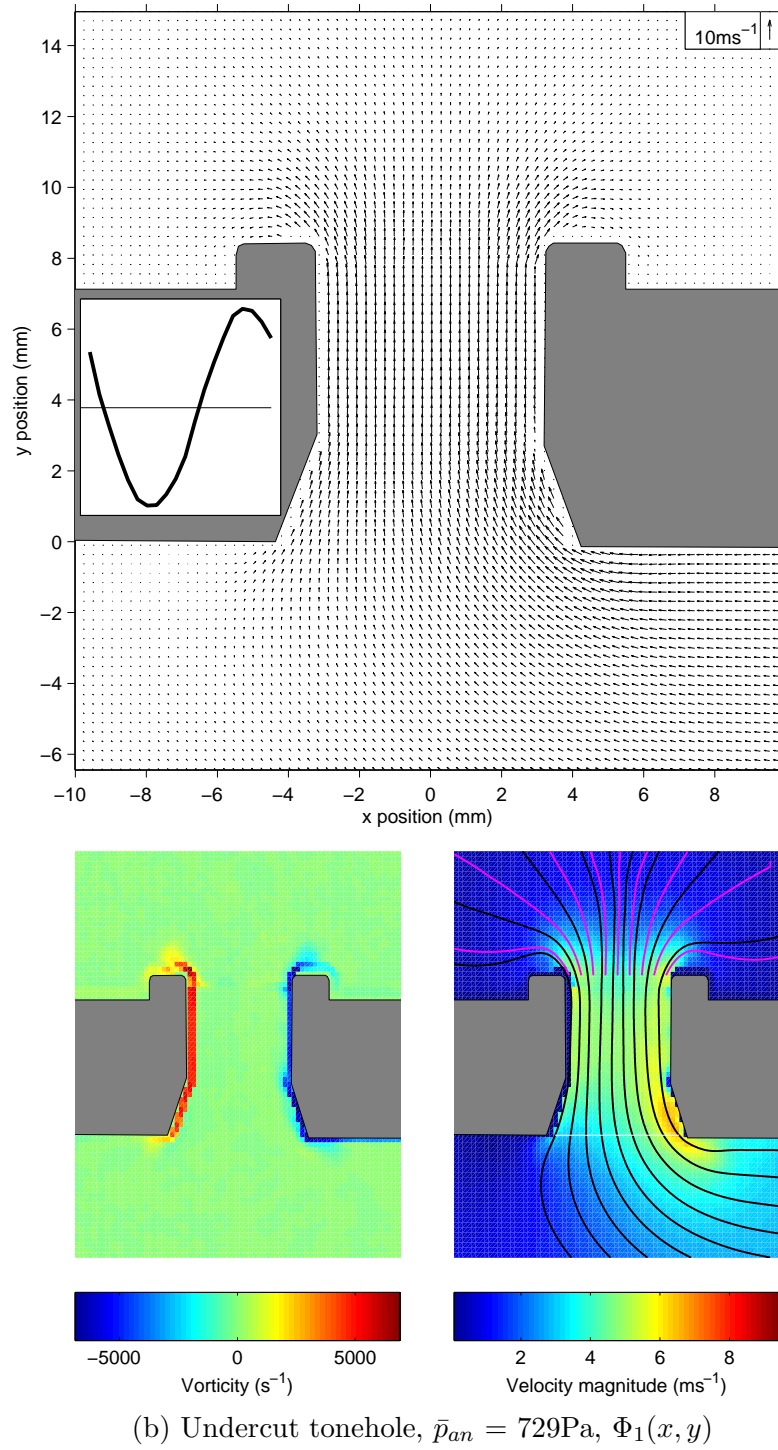
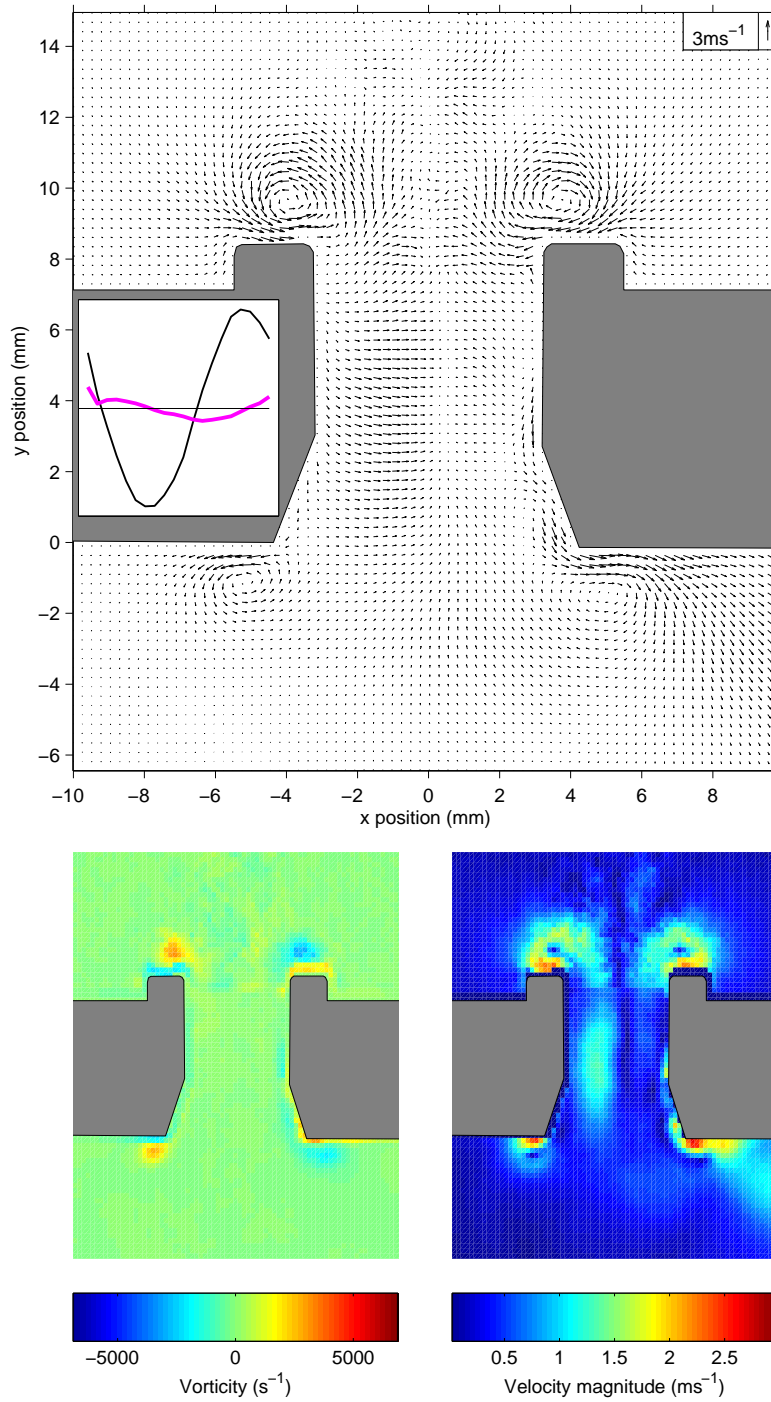


Figure 7.5 continued.  $a_1(t_i)$  is plotted inset into the vector map.

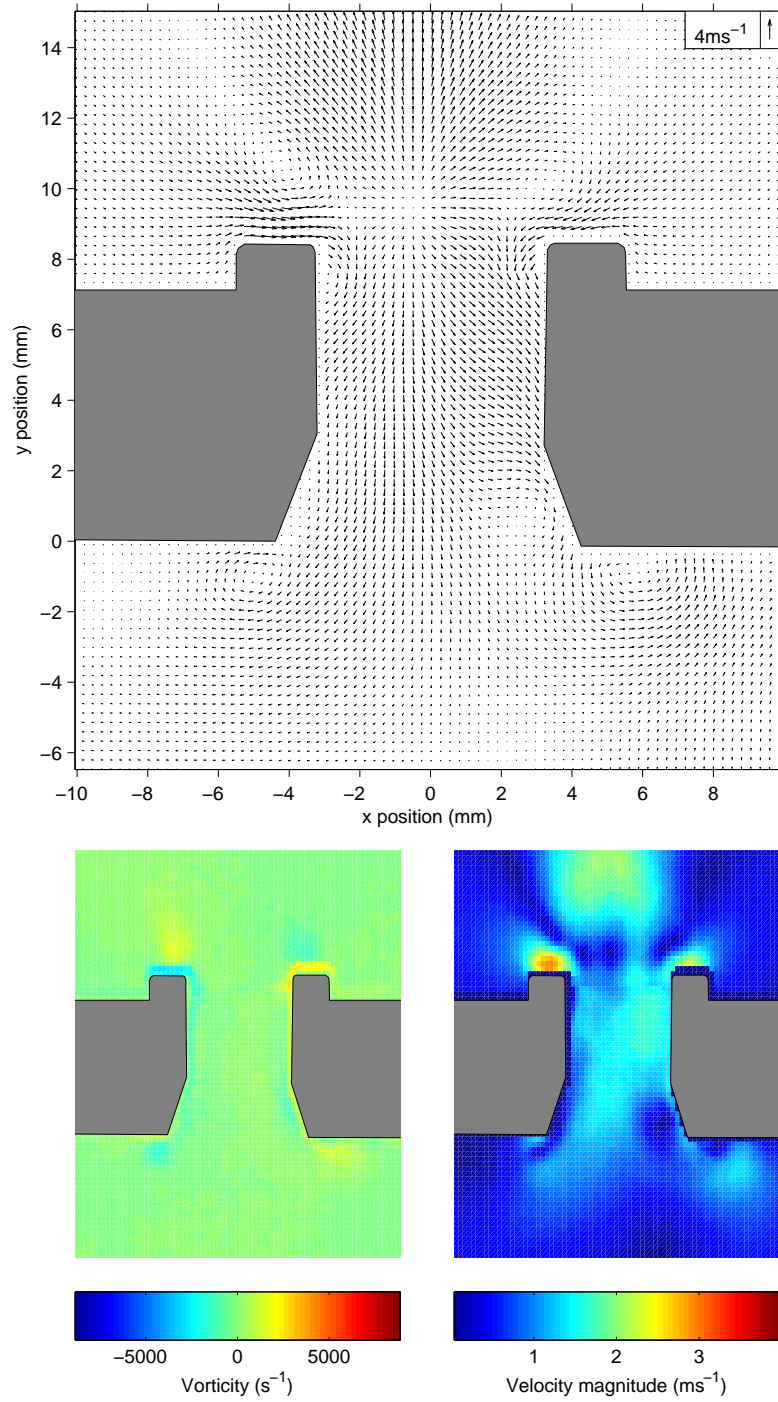




(c) Undercut tonehole,  $\bar{p}_{an} = 729\text{Pa}$ ,  $\Phi_2(x, y)$

Figure 7.5 continued.  $a_1(t_i)$  and  $a_2(t_i)$  are plotted inset into the vector map.  
(Black)  $a_1(t_i)$ . (Magenta)  $a_2(t_i)$ .



Figure 7.6: Flow decomposition for the undercut tonehole at  $\bar{p}_{an} = 1101\text{Pa}$ .

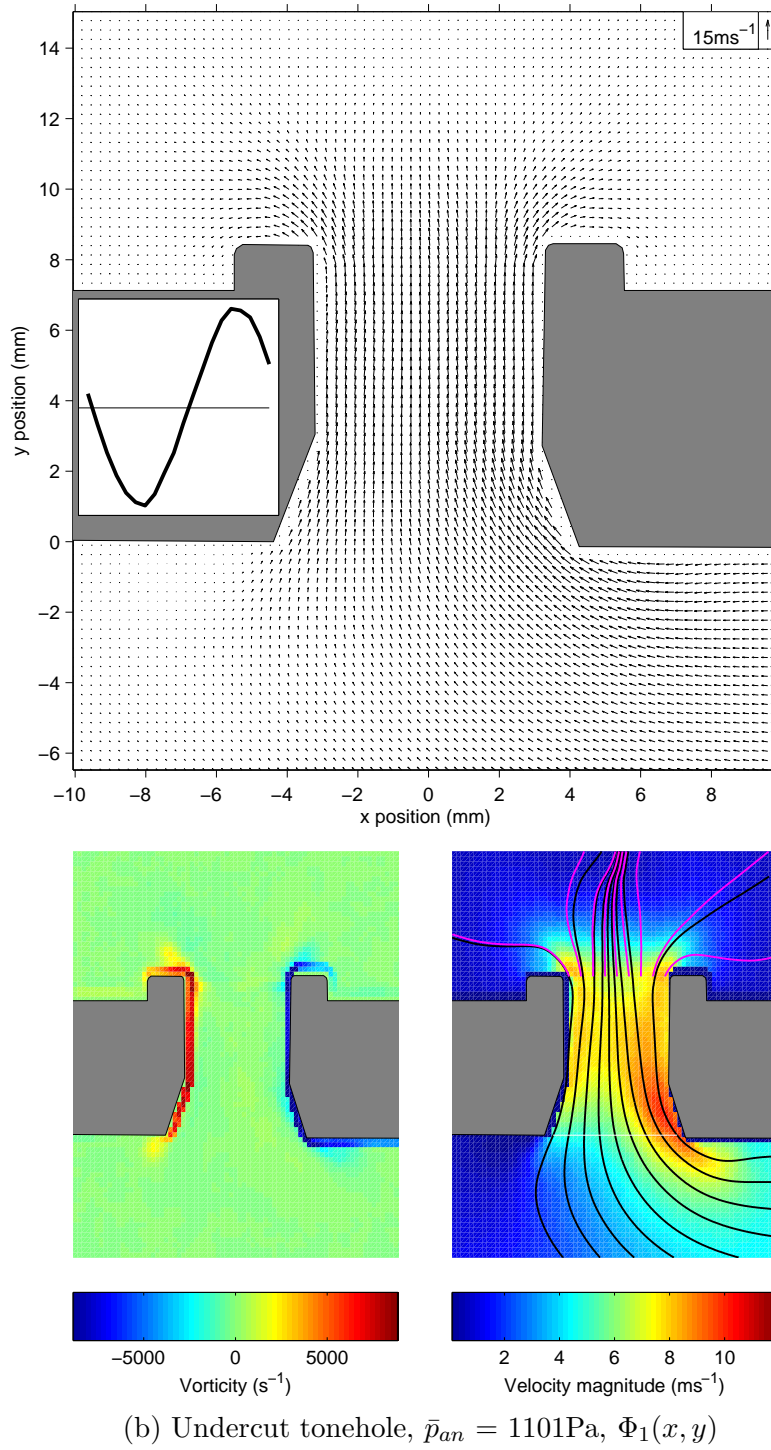
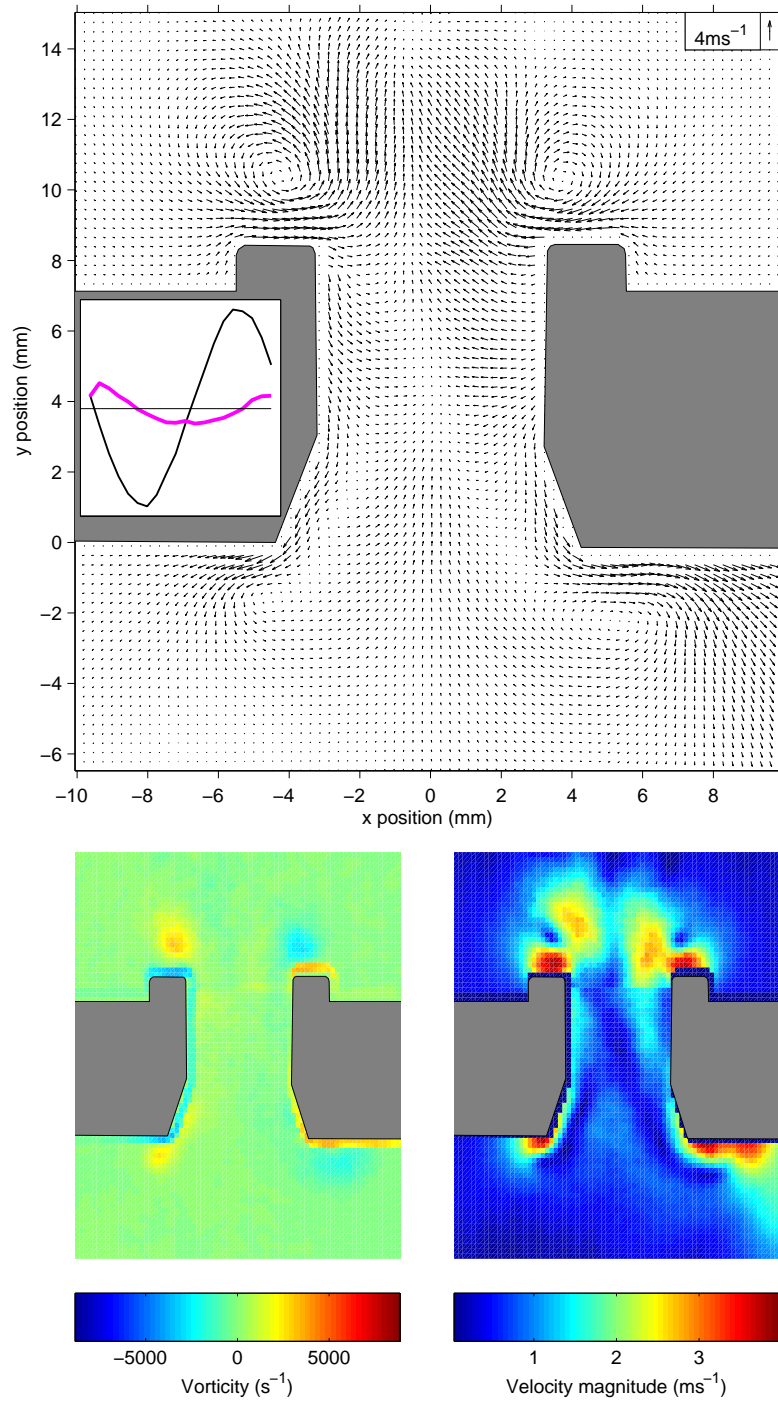


Figure 7.6 continued.  $a_1(t_i)$  is plotted inset into the vector map.



(c) Undercut tonehole,  $\bar{p}_{an} = 1101\text{Pa}$ ,  $\Phi_2(x, y)$

Figure 7.6 continued.  $a_1(t_i)$  and  $a_2(t_i)$  are plotted inset into the vector map.  
 (Black)  $a_1(t_i)$ . (Magenta)  $a_2(t_i)$ .

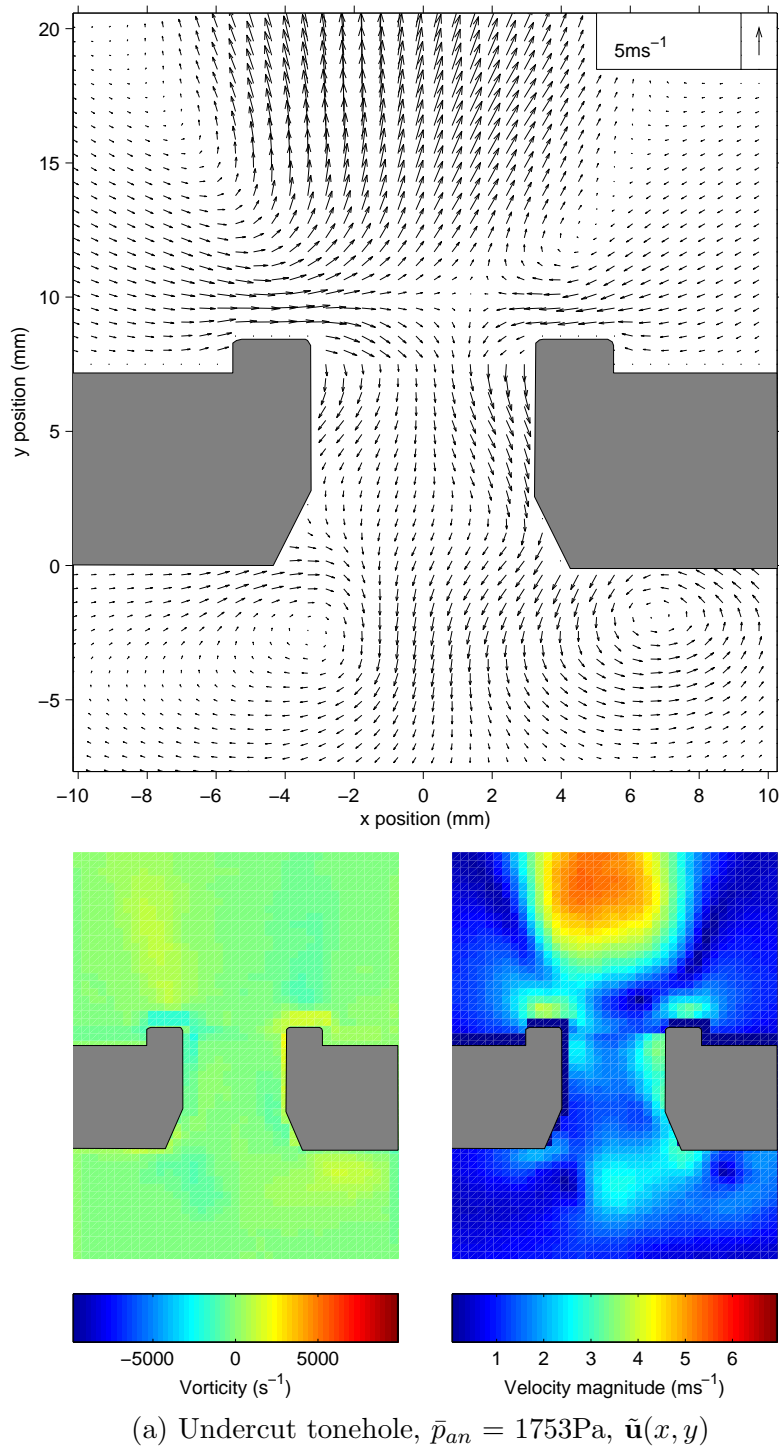
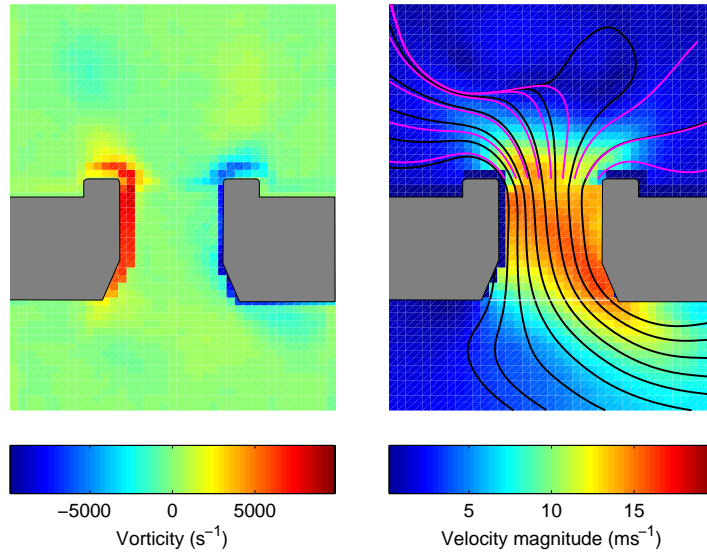
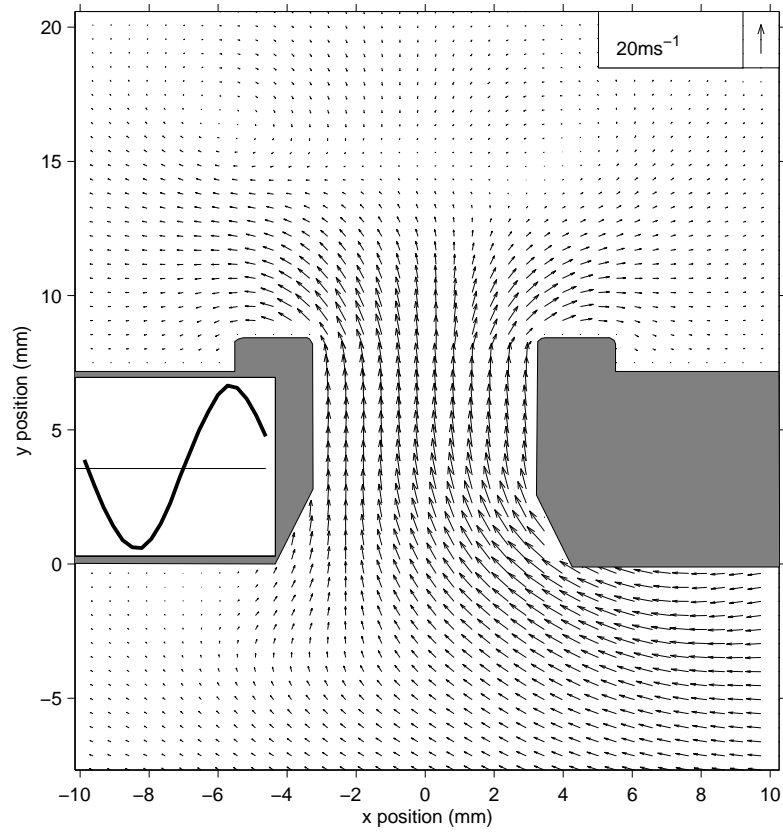
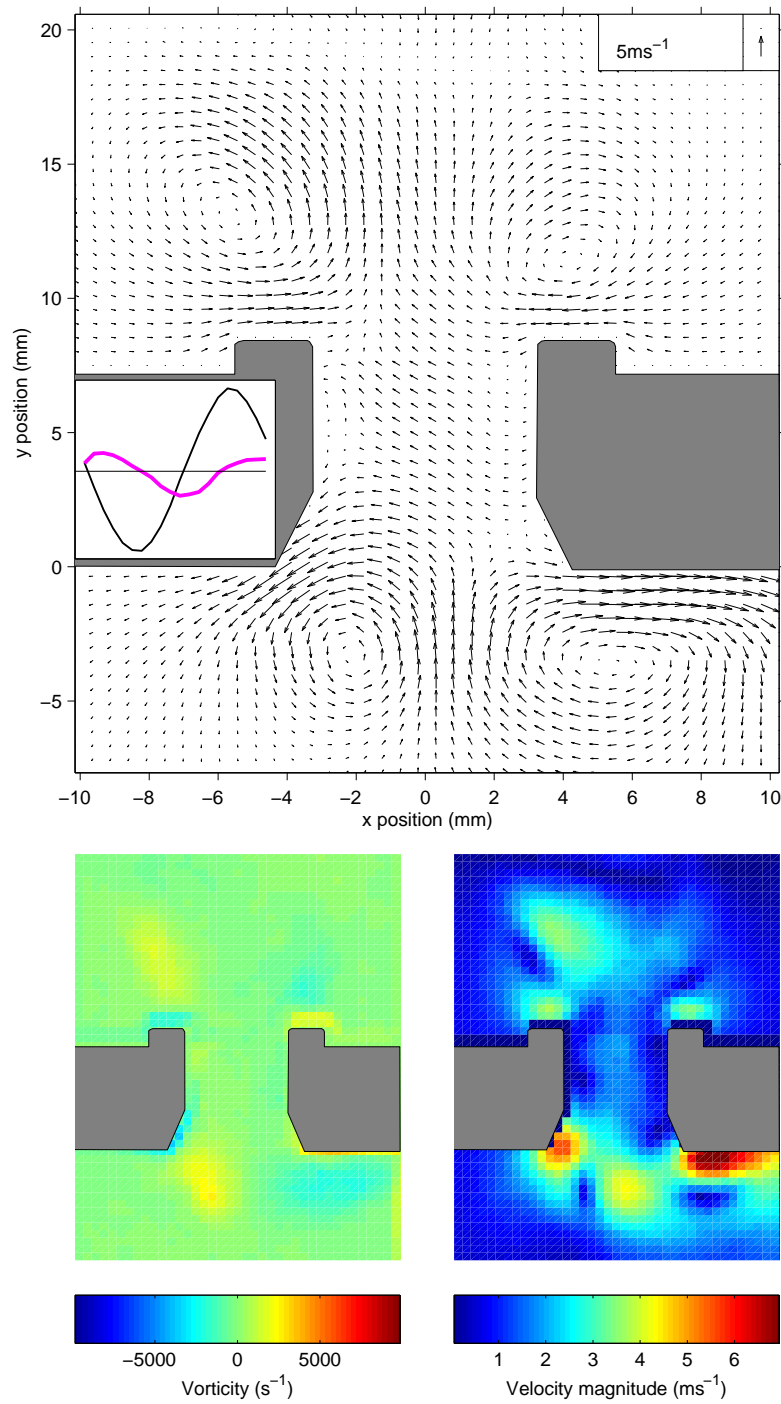


Figure 7.7: Flow decomposition for the undercut tonehole at  $\bar{p}_{an} = 1753\text{Pa}$ .



(b) Undercut tonehole,  $\bar{p}_{an} = 1753\text{Pa}$ ,  $\Phi_1(x, y)$

Figure 7.7 continued.  $a_1(t_i)$  is plotted inset into the vector map.



(c) Undercut tonehole,  $\bar{p}_{an} = 1753\text{Pa}$ ,  $\Phi_2(x, y)$

Figure 7.7 continued.  $a_1(t_i)$  and  $a_2(t_i)$  are plotted inset into the vector map.  
(Black)  $a_1(t_i)$ . (Magenta)  $a_2(t_i)$ .

Figures 7.1 to 7.7 show the flow decomposition at a number of values of  $\bar{p}_{an}$  (the RMS pressure measured at the pressure antinode in the tube), both for the square and undercut toneholes. A fuller collection of POD data is found on the accompanying CD. Compared with the termination PIV data, the region of interest is much bigger. The POD data is therefore presented in a similar fashion to the PIV data in chapter 5. Each numbered figure contains three sets of data labelled (a), (b) and (c), each of which consists of a vector map, a vorticity map and a velocity magnitude map. For each sound level and tonehole geometry, (a) gives the data for the cycle-averaged flow  $\tilde{\mathbf{u}}(x, y)$  (defined in equation 6.9), (b) gives the data for POD mode 1 and (c) the data for POD mode 2.

Parts (b) and (c) include both the spatial vector field  $\Phi_m(x, y)$  and the temporal coefficients  $a_m(t_i)$  for each POD mode. In part (b),  $a_1(t_i)$  is plotted inset into the vector map. In part (c),  $a_1(t_i)$  and  $a_2(t_i)$  are plotted inset into the vector map, with  $a_2(t_i)$  shown in magenta.

To give a sense of the relative velocities present in each part of the decomposition, (b) consists of velocity data obtained by multiplying  $\Phi_1(x, y)$  by the maximum value of  $a_1(t_i)$ . Likewise, (c) consists of velocity data obtained by multiplying  $\Phi_2(x, y)$  by the maximum value of  $a_2(t_i)$ . In (b) the scaling of the reference vector, the vorticity and the velocity magnitude is the same as that used for the PIV data at that sound level in chapter 5. (a) and (c) use a reduced scaling for the vector map and the velocity magnitude map.

Like for the velocity magnitude maps in chapter 5, the velocity magnitude map for POD mode 1 contains streamlines generated at fixed points in the flow. Again, these streamlines should be interpreted as showing the flow behaviour over a distance determined by the acoustic particle displacement at the point they are generated. The magenta streamlines are generated at evenly spaced points on a line across the top of the tonehole. The black streamlines are generated at evenly spaced points across the white line at the bottom of the tonehole. The black streamlines above the white line are generated using velocity data from  $\Phi_1(x, y)$  to show the form of the flow at the bottom of the tonehole during ejection. The black streamlines below the white line are generated using velocity data from  $-\Phi_1(x, y)$  to show the form of the flow at the bottom of the tonehole during suction.

### 7.3 Jet Driven Streaming

Part (a) of figures 7.1 to 7.7 gives the cycle-averaged flow  $\tilde{\mathbf{u}}(x, y)$  at the tonehole for a number of sound levels. This flow describes the jet driven streaming discussed in section 2.7.8 and observed in numerous studies of acoustic flow at discontinuities in

tubes [Rayleigh 45, Ingard 50, Rockliff 02a, Skulina 05a, Skulina 05b].

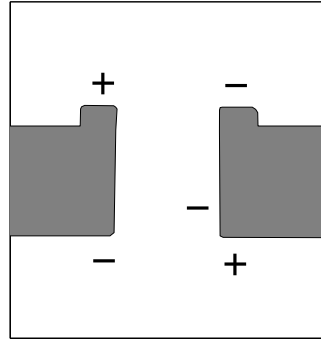


Figure 7.8: Vorticity sign of streaming flow.

Certain similarities are shared by the streaming maps for both geometries. The first similarity is the sign of the vorticity at different points in the flow. Take figure 7.2 (a) as an example. There is a region of negative vorticity at  $(-4,-1)$ , positive vorticity at  $(4,-1)$ , negative vorticity at  $(2,2)$ , positive vorticity at  $(-4,9)$  and negative vorticity at  $(4,9)$ . This pattern of the sign of vorticity at these locations is repeated for all the other sound levels and the undercut tonehole. It is summarised in figure 7.8. This pattern is due to the vortices formed by the oscillating flow (see section 5.3). During suction, the flow is drawn into the tonehole in an approximately diffuse fashion at the top while a vortex of negative vorticity forms at  $(-4,-1)$  and a vortex of positive vorticity forms at  $(4,-1)$ . During ejection, negative vortices form at  $(2,2)$  and  $(4,9)$ , while a positive one forms at  $(-4,9)$ . Averaged over the cycle, this gives rise to the observed vorticity of the streaming flow.

The second similarity between the streaming flows for the two toneholes is the development with increasing sound level. At the lowest levels (not shown) the streaming flow displays little clear structure. As the value of  $\bar{p}_{an}$  increases, vortices become apparent both at the top and bottom of the tonehole (see (a) in figure 7.1). This kind of streaming flow is also evident for certain sound levels at a termination (see section 6.5.2) and has been observed at an orifice [Ingard 50]. As  $\bar{p}_{an}$  increases further, a strong outward jet appears at the centre of the top of the tonehole, while air is drawn into the tonehole at the sides (see (a) in figures 7.2 to 7.7). The outward and inward streaming increases in strength with increasing  $\bar{p}_{an}$ . The bottom of the tonehole continues to be dominated by vortices, without a clearly defined outward jet. This is not the case for an orifice, where the streaming flow is symmetrical on either side [Ingard 50].



The final feature that all of the streaming maps share is a mean downward motion of the air inside the tonehole. It appears that air flows into the tonehole from the top, but not from the bottom. This seems unusual as true jet driven streaming should involve no net mass flux either in or out of the tube. This could be the result of some type of air current into the tube not caused by the imposed acoustic flow. A gravitational effect on the seeding particles can be ruled out as the experiment was performed the other way up to how the PIV data is presented.

There are also clear differences between the streaming flows for the two tonehole geometries. The first is that, at equivalent values of  $\bar{p}_{an}$ , the velocity magnitudes of the streaming effects for the undercut tonehole are considerably less than for the square tonehole. Compare (a) in figures 7.2 and 7.5 when  $\bar{p}_{an}$  is around 750Pa. The centre-line velocity of the outward jet at the top of the tonehole is roughly  $1.5\text{ms}^{-1}$  for the square tonehole and  $1\text{ms}^{-1}$  for the undercut. A similar difference can be seen in figures 7.3 and 7.6 (a) for the next highest value of  $\bar{p}_{an}$ . This is an interesting result, that the geometry of the internal edges of the tonehole can have a strong effect on the external streaming.

Another major difference is only evident for the two highest values of  $\bar{p}_{an}$ . The streaming maps for the square tonehole display a strong motion to the right for the outward flows, both at the top and bottom of the tonehole, as shown in figures 7.3 and 7.4 (a). This is not evident for the undercut tonehole at these levels (see figures 7.6 and 7.7 (a)). The right-ward motion at the bottom of the tonehole can be explained by the formation of the large attached vortex at (6,-2) during the suction phase of the cycle (see figure 5.4 (b)). This forces the flow emerging from the tonehole to the right because it is stronger than the vortex formed at the other side of the tonehole. The right-ward streaming motion at the top of the tonehole can be explained by the shedding of the larger vortex that forms at the upper-left edge of the tonehole during ejection. It was observed from figure 5.5 (d) that this shed vortex forces the flow emerging from the tonehole to the right late in the ejection phase. The effect is to introduce a right-ward direction to the resulting cycle-averaged flow.

An external streaming motion in the direction of the loudspeaker has been observed in previous studies of the flow outside a tonehole [Rockliff 02a, Skulina 05b]. These studies involved toneholes of considerably smaller height. Another streaming regime was observed at values of  $\bar{p}_{an}$  lower than those for which the external right-ward flow began, in which the external outward flow was found to move increasingly to the left as the sound level increased. In light of the above discussion on the internal streaming flow, it seems possible that the left-ward external streaming is caused by the presence of a larger attached vortex at the upper-left corner. Only when this vortex is shed is the streaming flow forced to the right.

## 7.4 POD Mode 1

Mode 1 of the POD is shown in part (b) of figures 7.1 to 7.7. The time coefficient  $a_1(t_i)$  is shown in the inset graph. These are highly sinusoidal at all values of  $\bar{p}_{an}$ , with none displaying a total harmonic distortion of more than 5% (evaluated with the first five harmonics above the fundamental). The spatial mode  $\Phi_1(x, y)$  soon begins to deviate from the low level case, with separated high velocity regions and areas of vorticity removed from the walls (see for example figure 7.3 (b)). At high values of  $\bar{p}_{an}$  the form of  $\Phi_1(x, y)$  at the bottom of the undercut tonehole maintains a similarity to the low level case. This can be seen in figure 7.6 (b).

## 7.5 POD Mode 2

Mode 2 of the POD is shown in part (c) of figures 7.1 to 7.7. Both  $a_2(t_i)$  and  $\Phi_2(x, y)$  show consistent features at all values of  $\bar{p}_{an}$  for both toneholes.  $a_2(t_i)$  has a roughly sinusoidal form, at the same frequency as  $a_1(t_i)$  and  $90^\circ$  out of phase. This is broadly the same behaviour of  $a_2(t_i)$  as observed at a tube termination (see section 6.5.2). Again, the maximum of  $a_2(t_i)$  occurs at the transition from the ejection phase to the suction phase. Sometimes  $a_2(t_i)$  displays a sudden discontinuity such as at  $i = 2$  for the square tonehole at  $\bar{p}_{an} = 760\text{Pa}$ , shown in figure 7.2 (c). Such discontinuities in  $a_2(t_i)$  are always accompanied by a discontinuity in  $a_3(t_i)$  at the same location (not shown), and the motions of modes 2 and 3 at these points seem to cancel each other out.

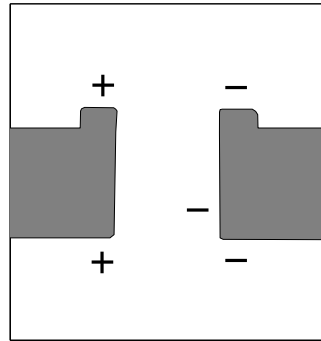


Figure 7.9: Vorticity sign of POD mode 2.

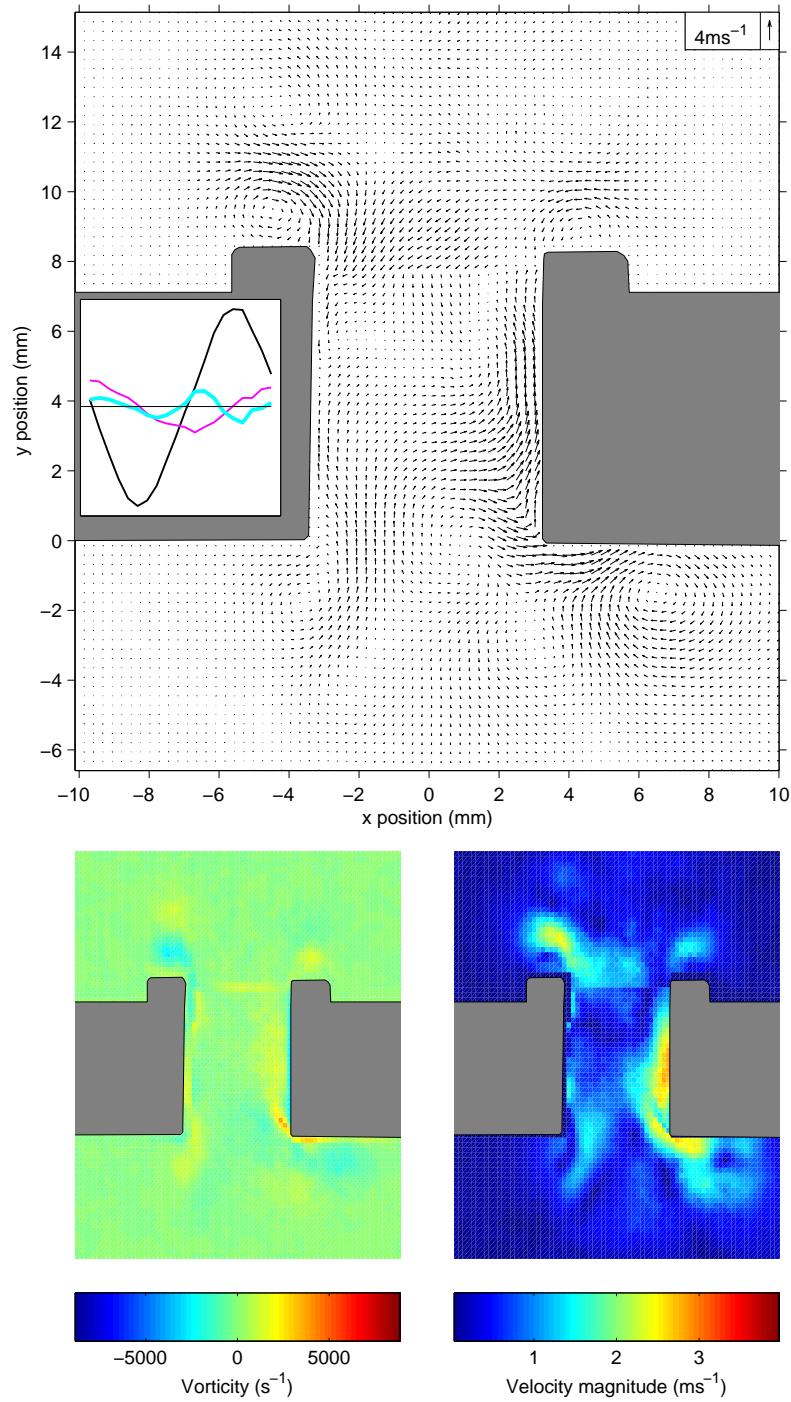


Figure 7.10:  $\Phi_3(x, y)$  for the square tonehole at  $\bar{p}_{an} = 1067 \text{ Pa}$ .  $a_1(t_i)$ ,  $a_2(t_i)$  and  $a_3(t_i)$  are plotted inset into the vector map. (Black)  $a_1(t_i)$ . (Magenta)  $a_2(t_i)$ . (Cyan)  $a_3(t_i)$ .

Like the mean flow,  $\Phi_2(x, y)$  displays a consistent pattern of vorticity at all values of  $\bar{p}_{an}$ . This pattern is shown in figure 7.9. This shows that, when  $a_2(t_i)$  is positive, mode 2 has the same vorticity sign as the cycle-averaged flow above the tonehole and inside the tonehole, and opposite vorticity sign below the tonehole (compare with figure 7.8).

As with the case of a tube termination (see chapter 6), the cycle-averaged flow and mode 2 must be considered together to understand the development of non-linear flow effects over the acoustic cycle. During the decelerating part of the suction phase and the accelerating part of the ejection phase  $a_2(t_i)$  is negative. In this half of the acoustic cycle, the vortices above the tonehole in mode 2 are acting to cancel out the vortices at this location in  $\tilde{\mathbf{u}}(x, y)$ . The vortices below the tonehole in mode 2 are at the same time acting to reinforce the vortices below the tonehole in  $\tilde{\mathbf{u}}(x, y)$ . After the maximum of ejection, the sign of  $a_2(t_i)$  switches to become positive. Mode 2 therefore now acts to reinforce the vortices above the tonehole and cancel the vortices below the tonehole in  $\tilde{\mathbf{u}}(x, y)$ . Thus the overall combined flow is created: vortices being formed below the tonehole from  $i \simeq 6$  to  $i \simeq 16$ , and vortices being formed above the tonehole from  $i \simeq 16$  to  $i \simeq 6$ .

In the real flow as described in chapter 5, for most sound levels the vortices are only evident from  $i \simeq 6$  to  $i \simeq 11$ , and from  $i \simeq 16$  to  $i \simeq 1$ . Figure 7.10 shows mode 3 of the POD for the square tonehole at  $\bar{p}_{an} = 1067\text{Pa}$ . Mode 3 acts to cancel out  $\tilde{\mathbf{u}}(x, y)$  and mode 2 at the bottom of the tonehole from  $i \simeq 12$  to  $i \simeq 15$ , thereby restoring the observed development of non-linear flow effects at that location. This cancelling behaviour of mode 3 is also observed above the tonehole for lower values of  $\bar{p}_{an}$  from  $i \simeq 2$  to  $i \simeq 5$ . Mode 3 also plays an important role at the values of  $\bar{p}_{an}$  for which vortex shedding occurs. Mode 2 then describes the shed vortex, whereas mode 3 describes the earlier formation of the vortex, as seen in figure 7.10 from  $i \simeq 15$  to  $i \simeq 18$ .

## 7.6 Energy Transfer

### 7.6.1 $e_1$ and $e_2$ against $\bar{u}_{an}$

In order to compare the energy transferred to non-linear flow effects by the two toneholes  $e_1$  and  $e_2$  are used, as defined by equations 6.12 and 6.15. In figure 7.11 these are plotted against  $\bar{u}_{an}$  (defined in equation 5.1) for the two toneholes. The percentage of kinetic energy per unit mass transferred into the higher modes of the POD and into streaming is consistently higher for the square tonehole.

There appears to be no discontinuity in the  $e_1$  data or sudden increase in the  $e_2$  data, which were associated with the transition to vortex shedding for the flow at a

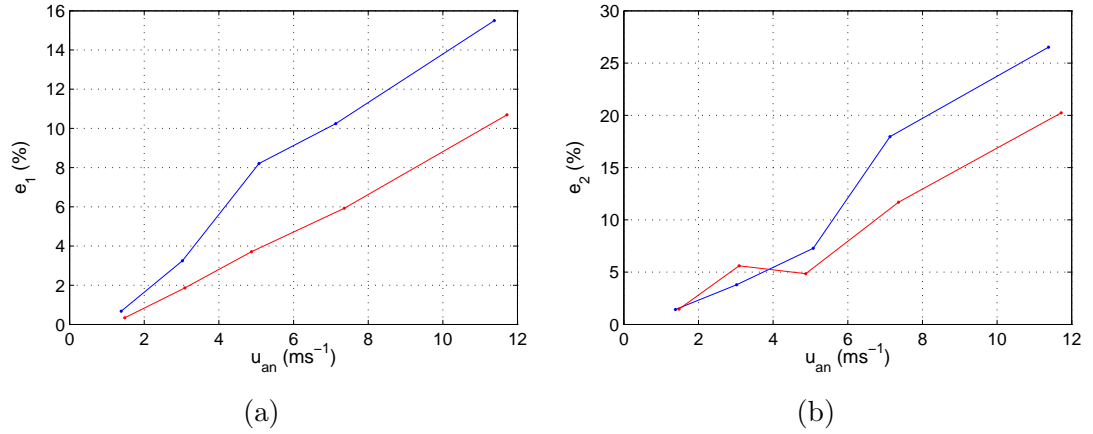


Figure 7.11: (a)  $e_1$  against  $\bar{u}_{an}$  for square and undercut toneholes. (b)  $e_2$  against  $\bar{u}_{an}$  for square and undercut toneholes. (Blue) square. (Red) undercut.

termination (see figure 6.9). Vortex shedding does occur at the toneholes in the range of  $\bar{u}_{an}$  studied. It may be that the discontinuity in the  $e_1$  data does not show up because of a lack of data points around the transition to vortex shedding.

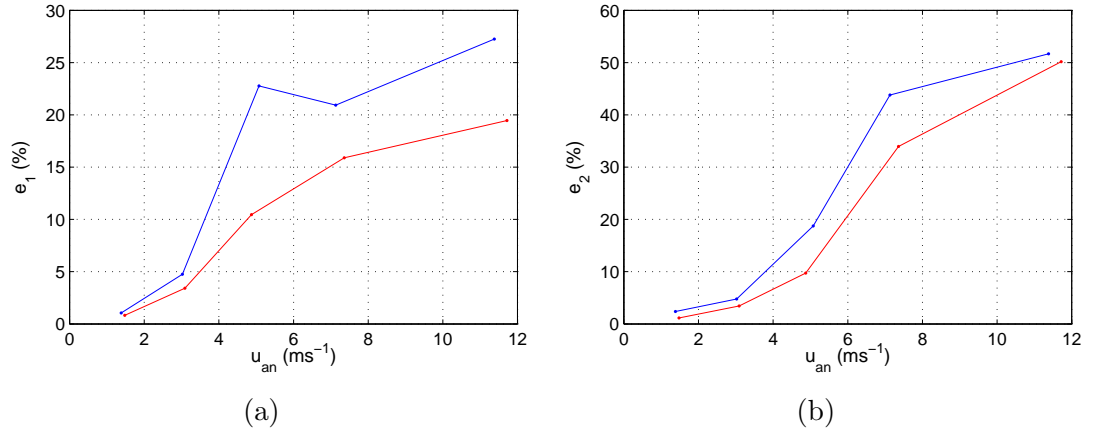


Figure 7.12: (a)  $e_1$  against  $\bar{u}_{an}$  for the area above the square and undercut toneholes. (b)  $e_2$  against  $\bar{u}_{an}$  for the area above the square and undercut toneholes. (Blue) square. (Red) undercut.

For the termination measurements, only the flow outside the end of the tube was measured. The observations of the flow around the tonehole (sections 7.3 and 7.5) suggest that the strength of non-linear flow effects relative to the acoustic flow is higher outside the tonehole than inside it. Including the area inside the tonehole in the calculation of  $e_1$  and  $e_2$  may ‘dampen out’ any variations in their value. An analysis of  $e_1$  and  $e_2$  for the area above the tonehole should provide results which are more similar to the termination results. These results are shown in figure 7.12 and

are more comparable to figure 6.9. Figure 7.12 (a) shows a dip in the  $e_1$  data for the square tonehole between  $\bar{u}_{an} = 5.1\text{ms}^{-1}$  and  $\bar{u}_{an} = 7.1\text{ms}^{-1}$ . The latter is the level at which vortex shedding from the outside of the tonehole begins. A discontinuity is not evident for the undercut  $e_1$  data, but it is possibly being missed due to the sparseness of data points. The  $e_2$  data for the flow above the toneholes is shown in figure 7.12 (b). The increase in  $e_2$  with the onset of vortex shedding is not as dramatic as for the terminations (see figure 6.9 (b)), but is clearer than for the whole flow around the tonehole (see figure 7.11 (b)). In the following section all  $e_1$  and  $e_2$  data are for the whole flow around the tonehole.

### 7.6.2 Strouhal number

It was found for flow around a step in a waveguide [Marx 08] and for flow outside a tube termination (see chapter 6) that  $e_1$  was strongly dependent on the Strouhal number of the flow. The Strouhal number is defined in equation 2.47. In the case of the flow around a tonehole, the characteristic velocity of the flow is taken to be  $\bar{u}_{an}$ , calculated using equation 5.1. The frequency in this case is the excitation frequency: 180Hz. The results in section 7.6.1 suggest that the characteristic length must be one that varies between the square and undercut tonehole geometries.

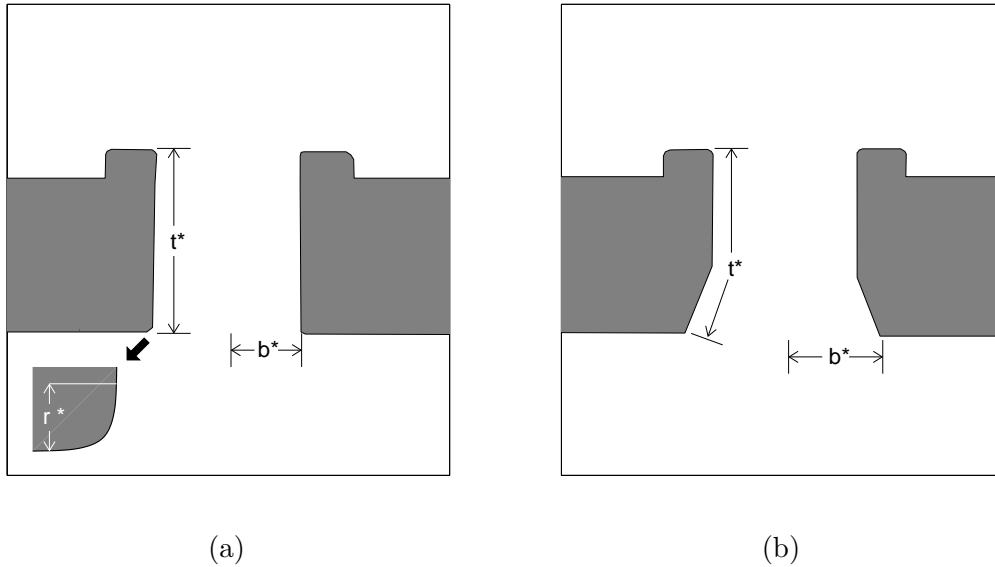
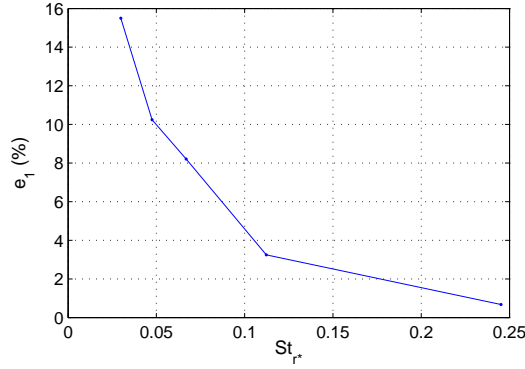


Figure 7.13: (a)  $t^*$ ,  $b^*$  and  $r^*$  for the square tonehole. (b)  $t^*$  and  $b^*$  for the undercut tonehole.

Dalmont et al found that the radius of curvature of the internal edges of the tonehole had a strong influence on its non-linear resistance [Dalmont 02]. This radius is shown as  $r^*$  in figure 7.13 (a). While  $r^*$  can be approximated for the square tonehole by

Figure 7.14:  $e_1$  against  $St_{r^*}$  for the square tonehole.

careful examination of photographs of the internal corner ( $r^* \simeq 0.3\text{mm}$ ), it is difficult to assign a value of  $r^*$  to the undercut tonehole. Figure 7.14 shows  $e_1$  against  $St_{r^*}$ , the Strouhal number defined using  $r^*$ , for the square tonehole. It shows that  $St_{r^*}$  is not the controlling Strouhal number for  $e_1$ .  $e_1$  only begins to grow significantly once  $St_{r^*}$  is less than 0.1. It is interesting to note that even the lowest sound pressure measured ( $\bar{p}_{an} = 207\text{Pa}$ ) gives a  $St_{r^*}$  of around 0.25. This suggests that at this lowest pressure we might expect to see some small-scale non-linear flow behaviour localised to the region just beside the internal corner of the tonehole. It was observed in section 5.3 that a small amount of boundary layer separation and reattachment was evident for the flow around the bottom-right corner of the square tonehole at  $\bar{p}_{an} = 207\text{Pa}$  (see figure 5.1 (d) and (g)).

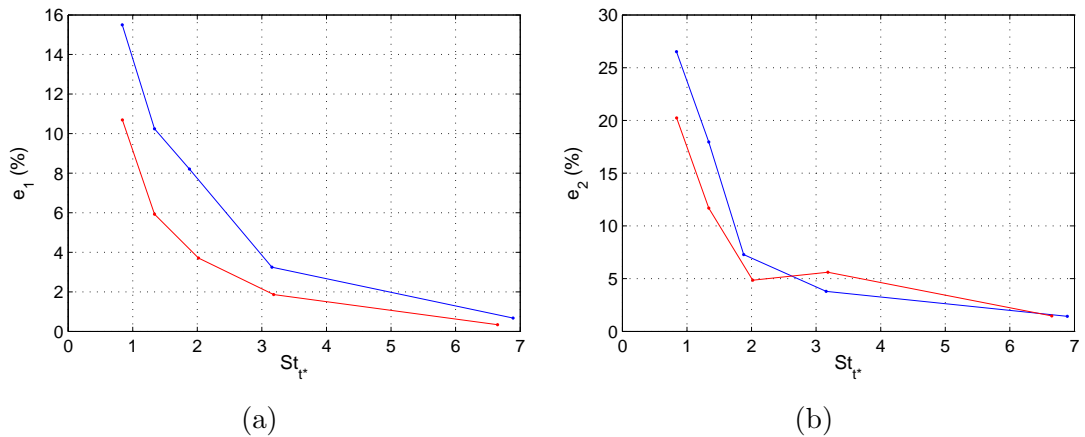
Figure 7.15: (a)  $e_1$  against  $St_{t^*}$  for the square and undercut toneholes. (b)  $e_2$  against  $St_{t^*}$  for the square and undercut toneholes. (Blue) square. (Red) undercut.

Figure 7.13 defines a length  $t^*$  which varies between the two tonehole geometries.

For the square tonehole  $t^* = t = 8.43\text{mm}$ , the tonehole height. For the undercut tonehole  $t^* = 8.7\text{mm}$ . Figure 7.15 shows  $e_1$  and  $e_2$  against  $St_{t^*}$ , the Strouhal number defined using  $t^*$ , for the two geometries. The two lines do not coincide, particularly in the case of  $e_1$ . Both  $e_1$  and  $e_2$  begin to increase rapidly as  $St_{t^*}$  becomes of the order 1. This means that the displacement amplitude of the flow is of the same order of magnitude as  $t^*$ . When  $St_{t^*}$  becomes less than 1 ( $\bar{p}_{an} = 1703\text{Pa}$ ) the separated flow no longer reattaches to the wall of the tonehole, as seen in figures 5.5 (c) and 5.10 (b).

The internal radius of a tube is used by some authors to define a Strouhal number [Disselhorst 80, Peters *et al* 93]. Half of the distance across the entrance to the tonehole,  $b^*$  is therefore defined in figure 7.13 as a characteristic length. For the square tonehole  $b^* = b = 3.27\text{mm}$ , half of the tonehole width. For the undercut tonehole  $b^* = 4.4\text{mm}$ . Figure 7.16 shows  $e_1$  and  $e_2$  against  $St_{b^*}$ , the Strouhal number defined using  $b^*$ . This seems to be the governing Strouhal number of the flow as the lines for both geometries coincide and start to grow rapidly at  $St_{b^*} \simeq 1$ . It is difficult to arrive at a physical interpretation of  $St_{b^*}$ . When  $St_{b^*} \simeq 1$  the displacement amplitude of the flow in the tonehole is roughly equal to half the width across the bottom of the tonehole.

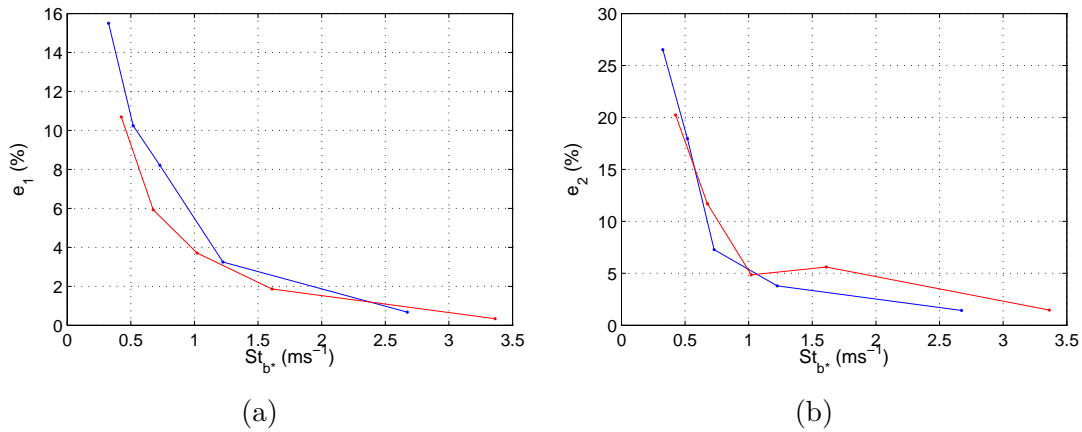


Figure 7.16: (a)  $e_1$  against  $St_{b^*}$  for the square and undercut toneholes. (b)  $e_2$  against  $St_{b^*}$  for the square and undercut toneholes. (Blue) square. (Red) undercut.

These results suggest that  $St_{b^*}$  is the governing Strouhal number of flow around a tonehole. To verify this would require that further measurements be made on geometries with different values of  $b^*$ . It is questionable however that the Strouhal number is completely independent of the height of the tonehole. This would seem to go against the observations of Keefe's experimental clarinet bodies [Keefe 83] described in section 5.2.3, and the discussion following figure 7.15. It is possible that the governing Strouhal number for non-linear flow at a tonehole is defined using both the height and entrance



radius in the numerator. To preserve non-dimensionality, another length would have to appear on the denominator, possibly the radius of the main bore of the instrument. A governing Strouhal number consisting of more than one spatial dimension was used by Fabre et al for the case of vortex shedding at the labium of an organ pipe [Fabre 96]. It may also be the case that the extent of non-linear flow around a tonehole is not solely dependent on one particular non-dimensional number. Smith and Swift found that, in the case of oscillating flow through a narrow channel at the end of a tube, the power transferred to non-linear effects was governed by three non-dimensional numbers, which were defined from the velocity amplitude of the flow and from the lengths of different features of the channel geometry [Smith 03].

## 7.7 Conclusion

PIV and POD have been applied to high amplitude oscillating flow around a tonehole. First, the cycle-averaged streaming flow was calculated. Stronger streaming flows were observed above the tonehole than below it. The external flows displayed behaviour similar to the streaming flows observed outside the open end of a tube. External streaming flow back in the direction of the loudspeaker was observed at high values of  $\bar{p}_{an}$  for the square tonehole. This behaviour was attributed to the asymmetrical vortex shedding which occurs on either side of the tonehole during ejection at these sound pressures. For a given value of  $\bar{p}_{an}$  the streaming velocities observed for the undercut tonehole were less than those for the square geometry.

When the cycle-averaged flow was subtracted from the total flow, mode 1 of the POD was found to approximately describe the acoustic flow, with more features of the non-linear flow becoming apparent at higher sound pressures. Mode 2 of the POD described the formation of vortices at different locations in the tonehole over the course of the acoustic cycle, but required to be viewed together with the cycle-averaged flow, for greater accuracy, mode 3, in order to describe the non-linear flow behaviour.

The energy transfer parameters  $e_1$  and  $e_2$  were found to increase with the sound pressure in the tube, and to be higher for the square tonehole at a given value of  $\bar{p}_{an}$ . This suggests that undercutting reduces the energy lost from the acoustic flow over the course of the acoustic cycle. When  $e_1$  and  $e_2$  were calculated using the region above the tonehole, discontinuities were found in the data for the square tonehole that signal the transition to vortex shedding. The location of these discontinuities is close to the location of the discontinuities in the data for the radiated sound:  $P_{rad}/\bar{p}_{an}^2$  versus  $\bar{p}_{an}$  and  $THD$  versus  $\bar{p}_{an}$  (see figures 5.14 (c) and 5.15 (b)). The conclusion is that the transition to vortex shedding from the top of the tonehole leads to a sudden increase in the generation of upper harmonics in the radiated sound spectrum.

An exact understanding of how to calculate quantitative values of power loss using the streaming velocity data and the velocity data from the POD modes greater than 1 is lacking. Particularly, it is not clear how the energies calculated from these two sets of velocity data are related. The relationship between the acoustic flow and the vortex formation modes is also complex. The rate of energy transfer from the acoustic flow to the vortex flow will depend on the rate of energy dissipation from the vortex motion. The vortices may also feed energy back into the acoustic flow at certain points in the acoustic cycle [Skulina 05a]. The definitions of  $e_1$  and  $e_2$  suggest that they may be linked to the minor loss coefficient  $K$  discussed in section 2.7.7, although any detailed comparison would need to take account of the issues raised above.

An attempt was also made in this chapter to identify the Strouhal number which dictates the strength of local non-linear flow effects at a tonehole. It was concluded that further investigation is required into this question. Knowledge of the non-dimensional flow parameters which influence the strength of local non-linear flow phenomena could be used to optimise the geometry of real woodwind instrument toneholes.

## Chapter 8

# Conclusion

Three out of the four thesis aims given in chapter 1 have been achieved, with the fourth aim partially achieved. Each of these is discussed here, as well as any potential extensions to the work which has been carried out.

### 8.1 Thesis Aims

#### 8.1.1 Clarinet model

Aim 1 was to construct an experimental clarinet model for which it is possible to perform PIV measurements on the entire flow in the region of the tonehole. Chapter 4 describes the design of a simplified clarinet model with one open tonehole, suitable for reproducing the lower notes on the clarinet and based on the dimensions of real instruments. The design allowed the insertion of tonehole pieces of various geometries. To perform PIV inside the tonehole it was necessary to make the main tube and tonehole rectangular in cross-section, with a glass window replacing the wall of the main tube in the region of the tonehole.

The resulting PIV data given in chapter 5 show a vast improvement over previous attempts to study the flow around a tonehole [Skulina 05b] in terms of optical access to the inside of the tonehole. Comparison with simulation results suggest that the rectangular cross-section model provides a flow field which is close to 2-dimensional.

#### 8.1.2 Undercutting and local non-linear flow effects

Aim 2 was to answer the questions of whether undercutting reduces local non-linear flow effects and, if so, how does it achieve this. The following evidence leads to the conclusion that undercutting does reduce local non-linear flow effects:

- The velocity and vorticity data obtained using PIV and presented in section 5.3 demonstrated that the oscillating flow around an undercut tonehole will produce non-linear effects of lower velocity, lower vorticity and lesser spatial extent than those produced by the flow around a square tonehole at an equivalent sound level. Observed non-linear flow behaviour included free shear layers, vortex formation and vortex shedding
- Results from an experiment to measure the radiated sound pressure (section 5.4) showed a greater radiated sound power for the undercut tonehole than for the square tonehole at the same value of input power. This suggests that the undercut tonehole converts less acoustic flow energy into energy used to drive the non-linear flow phenomena. The total harmonic distortion in the radiated pressure data for the undercut tonehole was also consistently less than that for the square geometry. The production of upper harmonics in the radiated spectra is associated with local non-linear flow effects.

The PIV results of section 5.3 show that undercutting a tonehole graduates the deceleration experienced by the flow as it negotiates the junction between the tonehole and the main bore. This reduces the extent of any boundary layer separation and the resulting non-linear flow phenomena, during both suction and ejection.

### 8.1.3 Proper Orthogonal Decomposition

Aim 3 was to extend the use of Proper Orthogonal Decomposition in analysing PIV data of high amplitude oscillating flows, and to assess its usefulness for measuring the strength of local non-linear flow effects. In chapter 6 Proper Orthogonal Decomposition (POD) was applied to PIV data of oscillating flow around the open end of a tube. After the cycle-averaged streaming flow was removed at each phase step, it was found that mode 1 of the POD described the acoustic motion, while the higher POD modes (together with the cycle-averaged flow) described the local non-linear flow effects. This distinction was found to be less clear at higher sound levels. Two parameters,  $e_1$  and  $e_2$ , were used to measure the kinetic energy per unit mass of the non-linear flow relative to that of the acoustic flow. These parameters were found to exhibit a dependence on the Strouhal number of the flow. They also reproduced the discontinuities observed in non-linear termination impedance data which signal the onset of vortex shedding from the end of the tube. They were therefore judged to be useful parameters for assessing the strength of local non-linear flow effects.

In chapter 7 the same POD analysis was applied to the tonehole PIV data from chapter 5, and was again found to approximately split the flow into acoustic and non-linear contributions.  $e_1$  and  $e_2$  were found to be consistently higher for the square

tonehole over the range of sound levels measured. This provided further evidence that undercutting reduces the strength of local non-linear flow effects at a tonehole.

#### 8.1.4 Tonehole geometry

Aim 4 was to investigate those aspects of tonehole geometry which are most significant in reducing local non-linear flow effects. It was noted in section 5.3 that the largest degree of boundary layer separation occurs at the internal edge of the tonehole, on the side of the excitation mechanism. Smoothing this corner should therefore have a greater reductive effect on local non-linear phenomena than smoothing the opposite edge. It was also observed that variations to the internal edge geometry of the tonehole can have significant influence on the flow outside the instrument (section 7.3).

An attempt was made at the end of chapter 7 to identify the dimension of the tonehole which should be used to construct the correct Strouhal number for the flow. The entrance radius of the tonehole was found to produce a suitable Strouhal number but it was concluded that, due to the complex geometry of a tonehole, the strength of local non-linear flow effects may rely on a Strouhal number comprised of more than one dimension of the tonehole, or that the flow may be governed by more than one non-dimensional number.

## 8.2 Future work

Studying a 2-dimensional flow with PIV does not provide results that can be used to calculate any quantities involving mass, such as kinetic energy. Circular geometries are preferable for this purpose because the circular symmetry can be used to integrate the 2-dimensional PIV data to obtain the volume or mass associated with each velocity vector [Skulina 05a]. Circular geometries are also those found in real woodwind instruments. The non-linear flow at the junction between a circular main tube and a circular tonehole may exhibit different features to those observed here.

Capturing PIV data of air flows through curved transparent surfaces is difficult because of flaring of the laser light and would be even more difficult at the point where the tonehole meets the main tube. 3-dimensional computational fluid dynamics therefore presents the best solution to the problem of obtaining full field velocity information from circular cross-section geometries.

Rough measurements of the internal sound pressure in a real clarinet have shown that toneholes may experience acoustic velocity amplitudes greater than  $25\text{ms}^{-1}$  during *fortissimo* playing. The results of this thesis suggest that vortex shedding from the tonehole may be present over the upper half of the musical dynamic range of the clarinet.

This would be a fascinating area for further study, where quasi-steady descriptions of the flow would be applicable.

This study has shown that undercutting reduces local non-linear flow effects at a tonehole. However, the question of the exact influence of these phenomena on the musical characteristics of a woodwind instrument is open. Energy losses due to local non-linear effects have been found to lower the maximum loudness of an instrument [Atig 04b]. In this study it was found that undercutting reduces the amount of input power necessary to sustain a note at a given radiated *SPL*. The exact influence of the energy losses on how a musical instrument will feel to a player is a topic for future research.

The observed higher harmonic generation in the radiated pressure spectrum may contribute to the timbre of real woodwind instruments. The directional characteristics of these harmonics would need to be studied as they were recorded in a reverberation chamber. It would also have to be asked whether they make a perceptible difference to the radiated spectrum of a real instrument, which contains higher harmonics generated at the reed.

POD has proved to be a useful tool in the study of high amplitude acoustic flows. More detailed work is required into the application of POD to acoustic flows, possibly looking at less complex velocity fields. An attractive study would be to apply POD to PIV data of a low amplitude standing wave in a closed tube containing more than one frequency component of known amplitude. The ability of POD to resolve these different components could be explored.

Finally, the relation between the geometry of different parts of the tonehole and the strength of non-linear effects should be explored. This would have to be done by varying all of the geometries - the height of the tonehole, the radius of the tonehole, the radius of curvature of the internal and external edges, the radius of the main tube - and finding the non-dimensional numbers which govern the energy lost to non-linear flow effects. While PIV would probably not be the optimum experimental technique for this kind of study due to the long times required to make the measurements and to process the data, it has proved itself to be an invaluable method for observing the detailed motions of local non-linear flow effects at a tonehole.

# Bibliography

- [Adrian (Editor) 93] R.J. Adrian (Editor). Selected papers on laser doppler velocimetry. New York: SPIE, 1993.
- [Atig 03] M. Atig, J.-P. Dalmont & J. Gilbert. *Impedance of pipe ends at high sound pressure levels*. Compte Rendus de l'Academie des Sciences - Mechanique, 2003.
- [Atig 04a] M. Atig. *Non-linéarité acoustique localisée a l'extrémité ouverte d'un tube*. PhD thesis, Université du Maine, Le Mans, 2004.
- [Atig 04b] M. Atig, J.-P. Dalmont & J. Gilbert. *Saturation mechanism in clarinet-like instruments, the effect of local non-linear losses*. Appl. Acoust., vol. 65, pages 1133–1154, 2004.
- [Bamberger 05] A. Bamberger. *Vortex sound of flutes using flow determination with Endo-PIV*. In Proceedings of Forum Acusticum, Budapest, Hungary, 2005.
- [Benade 76] A.H. Benade. Fundamentals of musical acoustics. Oxford University Press, 1976.
- [Benedict 80] R.P. Benedict. Fundamentals of pipe flow. John Wiley Sons, 1980.
- [Berkooz 93] G. Berkooz, P. Holmes & J.L. Lumley. *The proper orthogonal decomposition in the analysis of turbulent flows*. Annu. Rev. Fluid Mech., vol. 25, pages 539–537, 1993.
- [Berson 06] A. Berson, P. Blanc-Benon & M. Michard. *Encoulements secondaires aux extrémités du stack d'un réfrigérateur thermoacoustique: mesure des champs des vitesse oscillante à l'aide de la PIV*. In Proc. 6th French Conference on Acoustics, Tours, France, 2006.
- [BIAS 08] BIAS. *Brass Instrument Analysis System (BIAS)*, IWK, Austria, 2008. [Online] Available [http://www.bias.at/welcome\\_eng.htm](http://www.bias.at/welcome_eng.htm).
- [Bolt 49] R.H. Bolt, S. Labate & U. Ingard. *The Acoustic Reactance of Small Circular Orifices*. J. Acoust. Soc. Am., vol. 21(2), pages 94–97, 1949.

- [Boluriaan 03] S. Boluriaan & P.J. Morris. *Acoustic streaming: from Rayleigh to today*. International Journal of Aeroacoustics, vol. 2, pages 255–292, 2003.
- [Bruecker 04] C. Bruecker, M Treip & M. Kob. *Study of the vortex dynamics in a mechanical model of the vocal folds using Particle Image Velocimetry*. In Proceedings of the International conference on Voice Physiology and Biomechanics, Marseille, France, 2004.
- [Campbell 87] D.M. Campbell & C. Greated. The musician’s guide to acoustics. Oxford University Press, 1987.
- [Campbell 99] D.M. Campbell. *Nonlinear dynamics of musical reed and brass wind instruments*. Contemporary Physics, vol. 40(6), pages 415–431, 1999.
- [Dalmont 01] J.-P. Dalmont, C.J. Nederveen & N. Joly. *Radiation impedance of tubes with different flanges: numerical and experimental investigations*. J. Sound Vib., vol. 244(3), pages 505–534, 2001.
- [Dalmont 02] J.-P. Dalmont, C.J. Nederveen, V. Dubos, S. Ollivier, V. Meserette & E. te Slight. *Experimental determination of the equivalent circuit of an open side hole: linear and non-linear behaviour*. Acustica, vol. 88, pages 567–577, 2002.
- [Dantec 98] Dantec. *Safex Fog Generator - User’s guide*. Dantec Measurement Technology A/S, October 1998.
- [Degroot 07] A. Degroot, R. MacDonald, O. Richoux, B. Gazangel & M. Campbell. *Suitability of laser Doppler velocimetry for the calibration of pressure microphones*. Applied Acoustics, 2007. In press.
- [Dickens 07] P. Dickens, J. Smith & J. Wolfe. *Improved precision in measurements of acoustic impedance spectra using resonance-free calibration loads and controlled error distribution*. J. Acoust. Soc. Am., vol. 121(3), pages 1471–1481, 2007.
- [Disselhorst 80] J.H.M. Disselhorst & L. Van Wijngaarden. *Flow in the exit of open pipes during acoustic resonance*. Journal of Fluid Mechanics, vol. 99(2), pages 293–319, 1980.
- [Esposito 03] E Esposito & M. Marassi. *Quantitative assessment of air flow from professional bass reflex systems ports by Particle Image Velocimetry and laser doppler anemometry*. In Proceedings of the Stockholm Musical Acoustics Conference, 2003.
- [Fabre 96] B. Fabre, A. Hirschberg & Wijnands A. P. J. *Vortex Shedding in Steady Oscillation of a Flue Organ Pipe*. Acustica, vol. 82, pages 863–877, 1996.



- [Fletcher 98] N.T. Fletcher & T.D. Rossing. The physics of musical instruments. Springer-Verlag, New York, 1998.
- [Fuks 99] L. Fuks. *From Air to Music: Acoustic, Physiological and Perceptual Aspects of Reed Wind Instrument Playing and Vocal-Ventricular Fold Phonation*. PhD thesis, Royal Institute of Technology, Stockholm, 1999.
- [Graftieaux 01] L. Graftieaux, M. Michard & Grosjean N. *Combining PIV, POD and vortex identification algorithms for the study of unsteady turbulent swirling flows*. Meas. Sci. Technol., vol. 12, pages 1422–1429, 2001.
- [Grant 97] I. Grant. *Particle image velocimetry: a review*. Proc. Instn. Mech. Engrs., vol. 211(C), pages 55–76, 1997.
- [Greenham 03] A.C. Greenham. *Clarinet Toneholes: A Study of Undercutting and its Effects*. PhD thesis, London Metropolitan University, 2003.
- [Hann 97] D.B. Hann & C.A. Greated. *Measurement of the acoustic particle velocity using particle image velocimetry*. Acustica, vol. 83, pages 354–358, 1997.
- [Hino 76] M. Hino & S. Sawamoto. *Experiments on transition to turbulence in an oscillatory pipe flow*. J. Fluid Mech., vol. 75, pages 193–207, 1976.
- [Hirschberg 94] A. Hirschberg, J. Gilbert, A.P.J. Wijnands & A.M.C. Valkering. *Musical aero-acoustics of the clarinet*. Journal de Physique IV, vol. 4, pages C5–559–568, 1994.
- [Hirschberg 95] A. Hirschberg, J. Kergomard & G. Weinreich. *Mechanics of musical instruments - cism courses and lectures no.355*. Springer - Verlag, Wein, New York, 1995.
- [Ingard 50] U. Ingard & S. Labate. *Acoustic circulation effects and the nonlinear impedance of orifices*. Journal of the Acoustical Society of America, vol. 22(2), pages 211–218, 1950.
- [Ingard 67] U. Ingard & H. Ising. *Acoustic nonlinearity of an orifice*. Journal of the Acoustical Society of America, vol. 42(1), pages 6–17, 1967.
- [Keane 90] R.D. Keane & R.J. Adrian. *Optimisation of particle image velocimeters part1: double pulsed systems*. Meas. Sci. Technol., vol. 1, pages 1202–1215, 1990.
- [Keane 92] R.D. Keane & R.J. Adrian. *Theory of cross-correlation analysis of PIV images*. Applied Scientific Research, vol. 49, pages 191–215, 1992.

- [Keefe 82a] D.H. Keefe. *Experiments on the single woodwind tone hole*. J. Acoust. Soc. Am., vol. 72(3), pages 688–699, 1982.
- [Keefe 82b] D.H. Keefe. *Theory of the single woodwind tone hole*. J. Acoust. Soc. Am., vol. 72(3), pages 676–687, 1982.
- [Keefe 83] D.H. Keefe. *Acoustic streaming, dimensional analysis of nonlinearities, and tone hole mutual interactions in woodwinds*. J. Acoust. Soc. Am., vol. 73(5), pages 1804–1820, 1983.
- [Kinsler 00] L.E. Kinsler, A.R. Frey, A.B. Coppens & J.V. Sanders. *Fundamentals of acoustics*. John Wiley & Sons, New York, 2000.
- [Kostas 05] J. Kostas, J. Soria & Chong M.S. *A comparison between snapshot POD analysis of PIV velocity and vorticity data*. Experiments in Fluids, vol. 38, pages 146–160, 2005.
- [Levine 48] H. Levine & J. Schwinger. *On the Radiation of Sound from an Unflanged Circular Pipe*. Phys. Rev, vol. 74, pages 383–406, 1948.
- [Marx 08] D. Marx, H. Bailliet & J.-C. Valière. *Analysis of the Acoustic Flow at an Abrupt Change in Section of an Acoustic Waveguide Using Particle Image Velocimetry and Proper Orthogonal Decomposition*. Acustica, vol. 94(1), pages 54–65, 2008.
- [Melling 97] A. Melling. *Tracer particles and seeding for particle image velocimetry*. Meas. Sci. Technol., vol. 8, pages 1406–1416, 1997.
- [Merchant 08] N.D. Merchant, 2008. Private communication.
- [Merkli 75] P. Merkli & H. Thomann. *Transition to turbulence in oscillating pipe flow*. J. Fluid Mech., vol. 68, pages 567–575, 1975.
- [Morse 86] P.M. Morse & K.U. Ingard. *Theoretical acoustics*. Princeton University Press, 1986.
- [Nederveen 98a] C.J. Nederveen. *Acoustical aspects of woodwind instruments*. Northern Illinois University Press, DeKalb, Illinois. 2nd Edition, 1998.
- [Nederveen 98b] C.J. Nederveen, J.K.M. Jansen & R.R. van Hassel. *Corrections for Woodwind Tone-Hole Calculations*. Acta Acustica, vol. 84, pages 957–966, 1998.
- [Neubauer 07] J. Neubauer, Z. Zhang, R. Miraghaie & D.A. Berry. *Coherent structures of the near field flow in a self-oscillating physical model of the vocal folds*. J. Acoust. Soc. Am., vol. 121(2), pages 1102–1118, 2007.
- [Nomura 60] Y. Nomura, I. Yamamura & S. Inawashiro. *On the acoustic radiation from a flanged circular pipe*. J. Phys. Soc. Japan, vol. 15, pages 510–517, 1960.

- [Petculescu 02] A. Petculescu & L.A. Wilen. *Oscillatory flow in jet pumps: Nonlinear effects and minor losses*. J. Acoust. Soc. Am., vol. 113(3), pages 1282–1292, 2002.
- [Peters *et al* 93] M.C.A.M. Peters *et al.* *Damping and reflection coefficient measurements for an open ended pipe at low mach and low helmholtz numbers*. J. Fluid Mech., vol. 256, pages 499–534, 1993.
- [Pierce 81] A.D. Pierce. *Acoustics: An introduction to its physical principles and applications*. McGraw-Hill Book Company, Inc., New York, 1981.
- [Raffel 98] M. Raffel, C.E. Willert & J. Kompenhans. *Particle image velocimetry*. Springer - Verlag, Berlin, Heidelberg, 1998.
- [Rayleigh 45] J.W.S. Rayleigh. *The theory of sound: Vol ii*. Dover, New York, 1945.
- [Richards 82] W.B. Richards & A.H. Benade. *Second-harmonic sound generation at woodwind tone holes*. J. Acoust. Soc. Am., vol. 71, page S91, 1982.
- [Richter 07] A. Richter, 2007. Private communication.
- [Riley 98] K.F. Riley, M.P. Hobson & S.J. Bence. *Mathematical methods for physics and engineering*. Cambridge University Press, 1998.
- [Rockliff 02a] D. Rockliff. *Application of Particle Image Velocimetry to the Measurement of Non-Linear Effects generated by High-Intensity Acoustic Fields*. PhD thesis, University of Edinburgh, 2002.
- [Rockliff 02b] D. Rockliff, D.J. Skulina, D.M. Campbell & C.A. Greated. *PIV Measurement of acoustic velocities at woodwind instrument toneholes*. In Proceedings of the Institute of Acoustics meeting, Salford, UK, 2002.
- [Sirovich 87] L. Sirovich. *Turbulence and the dynamics of coherent structures, parts I-III*. Quarterly of Applied Math., vol. XLV, pages 561–582, 1987.
- [Sivian 35] L.J. Sivian. *Acoustic Impedance of Small Orifices*. J. Acoust. Soc. Am., vol. 7, pages 94–101, 1935.
- [Skulina 02] D.J. Skulina, D. Rockliff, D.M. Campbell & C.A. Greated. *Measurement of the acoustic velocities at woodwind instrument toneholes using particle image velocimetry*. In Proceedings of Forum Acusticum Conference, Seville, Spain, 2002.
- [Skulina 03] D.J. Skulina, D.M. Campbell & C.A. Greated. *Measurement of the Termination Impedance of a Tube using Particle Image*

- Velocimetry*. In Proceedings of the Stockholm Musical Acoustics Conference, 2003.
- [Skulina 05a] D.J. Skulina. *A Study of Non-linear Acoustic Flows at the Open End of a Tube using Particle Image Velocimetry*. PhD thesis, University of Edinburgh, 2005.
- [Skulina 05b] D.J. Skulina, R. MacDonald & D.M. Campbell. *PIV applied to the measurement of the acoustic particle velocity at the side hole of a duct*. In Proceedings of Forum Acusticum Conference, Budapest, Hungary, 2005.
- [Smith 03] B.L. Smith & G.W. Swift. *Power dissipation and time-averaged pressure in oscillating flow through a sudden area change*. J. Acoust. Soc. Am., vol. 113 (5), pages 2455–2463, 2003.
- [Sveen 04] J. K. Sveen. *An introduction to MatPIV v.1.6.1*. Eprint no. 2, ISSN 0809-4403, Dept. of Mathematics, University of Oslo, 2004. <http://www.math.uio.no/~jks/matpiv>.
- [Tonddast-Navæi 05] A. Tonddast-Navæi. *Acoustic particle-image velocimetry development and applications*. PhD thesis, Open University, 2005.
- [Tritton 99] D.J. Tritton. *Physical fluid dynamics*. Clarendon Press, Oxford, 1999.
- [van Walstijn 02] M. van Walstijn. *Discrete-Time Modelling of Brass and Reed Woodwind Instruments with Application to Musical Sound Synthesis*. PhD thesis, University of Edinburgh, 2002.
- [Visualisation 08] Separation Visualisation, 2008. [Online image] Available [http://en.wikipedia.org/wiki/Image:Flow\\_separation.jpg](http://en.wikipedia.org/wiki/Image:Flow_separation.jpg).
- [Ward-Smith 80] A.J. Ward-Smith. *Internal fluid flow*. Clarendon Press, 1980.
- [Webber 02] G.A. Webber, R.A. Handler & L. Sirovich. *Energy dynamics in a turbulent channel flow using the Karhunen-Loève approach*. Int. J. Numer. Meth. Fluids, vol. 40, pages 1381–1400, 2002.
- [Westerweel 94] J. Westerweel. *Efficient detection of spurious vectors in particle image velocimetry data*. Exp. Fluids, vol. 16, pages 236–247, 1994.

# Publications

## Journal papers

A. Degroot, R. MacDonald, O. Richoux, B. Gazengel & M. Campbell, *Suitability of laser Doppler velocimetry for the calibration of pressure microphones*, Applied Acoustics, Volume 69, Issue 12, December 2008, Pages 1308-1317.

## Conference papers

A. Degroot, R. MacDonald, D.M. Campbell, B. Gazengel, & O. Richoux. *Etalonnage de microphones par Vélocimétrie Laser Doppler*. In Proceedings of the 8th Conference of the French Acoustical Society, Tours, France, 2006.

R. MacDonald, & D.M. Campbell. *Non-linear losses at woodwind toneholes*. In Proceedings of the Institute of Acoustics Spring Conference, Southampton, UK, 2006.

D. J. Skulina, R. MacDonald & D.M. Campbell. *PIV applied to the measurement of the acoustic particle velocity at the side hole of a duct*. In Proceedings of Forum Acusticum Conference, Budapest, Hungary, 2005.

D. J. Skulina, R. MacDonald & D.M. Campbell. *Visualisation of acoustic flows around a square duct side hole using PIV* In Proceedings of the Scottish Fluid Mechanics Meeting, Edinburgh, UK, 2005.